

MULTIPLICITY OF TIGHT ULTRA LOW MASS SYSTEMS

DIPLOMARBEIT



seit 1558

FRIEDRICH-SCHILLER-UNIVERSITÄT JENA
PHYSIKALISCH-ASTRONOMISCHE FAKULTÄT

eingereicht von: Andrea Mehner
geb. am: 12.08.1981 in Berlin

Thüringer Landessternwarte Tautenburg, Juni 2007

1. Gutachter: Prof. Dr. Artie P. Hatzes
 2. Gutachter: Prof. Dr. Peter H. Hauschildt
- Tag der Verleihung des Diploms:

Abstract

A number of scenarios for the formation of brown dwarfs are currently being discussed. Binary properties constrain these scenarios. While many imaging surveys were carried out to find visuell binaries, few surveys were conducted to find short-period binaries. By deriving the frequency of short-period binary brown dwarfs, the importance of momentum transfer and tidal interactions for the formation of binary brown dwarfs can be studied.

A radial velocity survey is the most efficient way to find short-period brown dwarf binaries. In this work, high-resolution spectra of 27 very-low mass stars and brown dwarfs were analyzed. The data was taken with UVES at the VLT (Paranal, Chile) in the years 2001 to 2004. Parts of this data were already analyzed by Guenther and Wuchterl (2003). For the work presented here, all data from the years 2001 to 2004 was used. Additionally, the accuracy of the radial velocity measurement was improved.

Two spectroscopic binaries were confirmed. It was shown that there is no additional binary with a period of $\lesssim 40$ days in this sample. By improving the accuracy of the measurements and increasing the number of spectra, the binary candidate, LHS 292, turned out not to be a binary. Thus, the binary frequency is $7.4 \pm 1.4\%$. This frequency supports the solar-like formation scenario of very low-mass stars and brown dwarfs and it shows that momentum transfer during the formation is not of great importance.

To study the effects of magnetic fields on the atmospheres of brown dwarfs, I observed the brown dwarf LP 944-20 with EFOSC2 on the 3.6 m telescope in La Silla, Chile. LP 944-20 is an ideal object for this purpose. The magnetic field strength at the surface of LP 944-20 may be nearly 1 kG, even in quiescence. There are no significant variations, neither in the equivalent widths of the $H\alpha$ and Na D emission lines nor the temperature. It can be concluded that LP 944-20 has a very homogeneous atmosphere. It is highly unlikely that spots or other prominent surface features exist on this object.

Contents

1. Background	1
1.1. The discovery of brown dwarfs	1
1.2. Why searching for binary brown dwarfs?	1
2. What are brown dwarfs?	4
2.1. Defining the term "brown dwarf"	4
2.1.1. Star or brown dwarf? - The hydrogen-burning limit and the lithium-test	4
2.1.2. Planet or brown dwarf? - The deuterium-burning limit	5
2.2. Physical properties of brown dwarfs	5
2.2.1. Evolutionary tracks	5
2.2.2. Radius and gravity	6
2.2.3. Temperature and luminosity	7
2.2.4. Density and pressure	8
2.2.5. Energy transportation mechanisms	8
2.2.6. Magnetic field, rotation and activity	8
2.3. Atmosphere and spectral type classification	9
2.3.1. M-dwarfs	11
2.3.2. L-dwarfs	11
2.3.3. T-dwarfs	11
3. The formation of brown dwarfs	13
3.1. How do brown dwarfs form?	13
3.2. Brown dwarf formation scenarios	14
3.2.1. Turbulent fragmentation	14
3.2.2. Embryo-ejection	14
3.2.3. Gravitational instabilities in disks	15
3.2.4. Photo-erosion of pre-existing cores in H II regions	16
3.2.5. Binary disruption	16
4. Binary systems as a diagnostic tool for understanding the formation of brown dwarfs	18
4.1. Observations	18
4.1.1. High-resolution imaging	18
4.1.2. High-resolution spectroscopy	19
4.1.3. Astrometry	20
4.1.4. Photometric monitoring	20

4.2. Properties of very low-mass star and brown dwarf binary systems	21
4.2.1. The binary frequency	21
4.2.2. Separation distribution	21
4.2.3. Mass ratio distribution	23
4.2.4. The brown dwarf desert	24
4.2.5. Possible planet formation in brown dwarf disks	25
4.3. Other means of testing the different formation scenarios	25
5. Observation and data reduction	28
5.1. Sample	28
5.2. UV-Visual Echelle Spectrograph	30
5.3. Reduction of the UVES echelle frames	32
6. Results of the UVES observations	34
6.1. Spectral Types	34
6.2. Temperatures	37
6.3. Masses	38
6.4. Radial velocities	41
6.4.1. The spectroscopic binaries	45
6.4.2. The visuell binaries	46
6.4.3. Other objects with possible radial velocity variations	48
6.5. Mass limits of companions	52
7. The atmosphere of the highly active brown dwarf LP 944-20	54
8. Conclusions	61
A. IRAF CL script for the radial velocity measurement	I
B. Radial velocity variations	XVII
C. Graphs for the radial velocity variation measurements	XXII
Bibliography	LXVII

1. Background

1.1. The discovery of brown dwarfs

The theoretical existence of brown dwarfs was first proposed in 1963, by Shiv S. Kumar. He demonstrated that in a stellar core below a certain mass hydrogen-burning no longer takes place. Below this mass limit electron degeneracy provides the hydrostatic equilibrium against gravitational collapse. Evolutionary calculations yield a mass of $\approx 0.075 M_{\odot}$ for the hydrogen-burning minimum mass. The term "brown dwarf", for objects below the hydrogen-burning limit, was proposed by Tarter in 1975.

In the 1980s an intensive search began to find these low mass objects, but none of the candidates were proven to be a brown dwarf. An important step in the discovery of brown dwarfs was the lithium-test, proposed by Rebolo et al. in 1992. The lithium-test makes use of the fact that most brown dwarfs are too cool to burn lithium in distinction to main sequence stars. It was not until 1995 that the existence of brown dwarfs was incontrovertibly proven by the demonstration of the brown dwarf nature of PP1 15 by Basri et al. (1995). In the same year, the T-dwarf Gliese 229B, in orbit around the M-dwarf Gliese 229A, was found by Nakajima et al. (1995) and Teide 1 was proven to be a brown dwarf by Rebolo et al. (1995).

Now hundreds of brown dwarfs have been discovered. They are found at star-formation sites, as cluster members and as free-floating objects in the field. To mention are the 2MASS (Two Micron All Sky Survey) and DENIS (Deep Near Infrared Survey) surveys in the near-infrared and the SDSS (Sloan Digital Sky Survey) survey in the optical, which discovered many brown dwarfs.

Some scientist speculated that brown dwarfs might be an important constituent of the dark matter. Based on the frequency of detection, it is estimated that brown dwarfs are as common as hydrogen-burning stars. However, because brown dwarfs are much lighter than stars they are not the dominant constituent of the universe's mass.

1.2. Why searching for binary brown dwarfs?

One of the main open questions in the field of star formation is the formation of brown dwarfs. Brown dwarfs are objects with intermediate masses between stars and planets. Their mass is not sufficient to support stable hydrogen fusion. Different formation scenarios explaining the formation of these low-mass objects are being discussed. Current research focuses on finding out which of these scenarios are realistic and which are not. An important diagnostic in this context is the frequency of long-period, as well as short-period brown dwarf binaries. Binary properties are closely related to the formation

processes. Therefore, comparing the predicted with observed binary properties is a good means of testing the different scenarios.

Many studies have been carried out using high-spatial-resolution imaging to find binary systems among very low-mass stars and brown dwarfs. Due to limited angular resolution, these surveys are only sensitive to binary separations of a ≥ 1 AU. Only a few studies were done to find spectroscopic binaries at separations a < 1 AU. Therefore, the statistics concerning spectroscopic binaries are very poor. While the detection of radial velocity variations in high-resolution spectroscopic surveys implies a close binary frequency of 17 – 30% (Jeffries & Maxted 2005), only five spectroscopic binaries have been found so far.

Knowing the statistical properties of close brown dwarf binaries would give a better insight into the formation of these objects. Observed close binary properties could be compared with the predictions of the different scenarios. The frequency distribution for separations a < 1 AU also provides information about the importance of tidal interactions and momentum transfer. When searching for spectroscopic binaries, one has a likely chance to find eclipsing binary systems, which make it possible to test the evolutionary models of brown dwarfs.

High-resolution spectra of 27 old brown dwarfs and very low-mass stars were taken with UVES at the VLT (Paranal, Chile). Accretion disks around young brown dwarfs imply that objects at the sub-stellar border do not show any indication, at the beginning of their evolution, that they will end up as brown dwarfs or as very low-mass stars. Therefore, the statistical properties are expected to change only smoothly at the sub-stellar border. On this account, the sample contains brown dwarfs as well as very low-mass stars. Another reason is that it is very difficult to say if an object at the sub-stellar border is a brown dwarf or a very low-mass star. Old brown dwarfs and very low-mass stars are ideal objects in a search for spectroscopic binaries because old objects should not have significant radial velocity variations caused by stellar activity.

Some of the data was already analyzed by Guenther and Wuchterl (2003). Their analysis was improved by using more data. Also, a higher accuracy of the radial velocity measurement was achieved. Guenther and Wuchterl (2003) measured the radial velocity by crosscorrelating the spectra with template spectra. In this work, the radial velocity was measured with a new method. The radial velocity is determined by fitting model spectra to the observed spectra. This method gives an increase in accuracy by a factor of roughly 5 - 10, allowing to detect companions of smaller masses than in the previous analysis. The accuracy of the radial velocity measurement is about 0.2 km/s. This level of accuracy makes it possible to find brown dwarf companions down to the mass of Jupiter. The detection of planets around brown dwarfs would give an insight into the formation of brown dwarfs and the formation of planetary systems. Yet, so far no planet around a brown dwarf has been found by means of radial velocity measurements.

The immediate aim of this work was to find the frequency of brown dwarf companions to very low-mass stars and brown dwarfs, in a sample of 27 objects. Based on the detected radial velocity variations, upper limits for possible orbiting companions were calculated for all objects. Furthermore, spectral types, temperatures and masses of all objects were derived.

In order to find out if brown dwarfs have spots, which could mimic a companion, the brown dwarf LP 944-20 was observed over several rotation periods with EFOSC2 on the 3.6 m telescope in La Silla, Chile.

This work is structured as follows:

Chapter 2 discusses the definition of brown dwarfs. It is described how they differ from stars and from planets. Their physical properties are explained, such as their radii, temperatures, densities, the magnetic field, etc. Also, their atmospheric features and their spectral type classification are described.

Chapter 3 presents five different brown dwarf formation scenarios; turbulent fragmentation, dynamical ejection, gravitational instabilities in disks, photo-erosion and binary disruption. The pros and cons of these scenarios are discussed.

One way of testing the different scenarios are the binary properties of brown dwarfs. Chapter 4 examines observed brown dwarf binary properties, such as the binary frequency, the separation distribution and the mass ratio distribution. These properties are compared to predictions of numerical simulations. Also, the brown dwarf desert and planet formation around brown dwarfs are discussed. Other means of testing the formation scenario are described, such as the initial mass function, kinematics, spatial distribution and circumstellar disks.

Chapter 5 presents the sample that is analyzed in this work. The setup of the UV-Visual Echelle Spectrograph (UVES) at the VLT is explained. Also, the data reduction is described.

The results of the UVES observations are presented in chapter 6. The results include the measurements of spectral types, temperatures, masses and radial velocities. From the radial velocities, conclusions concerning possible companions are made. Upper mass limits for possible companions are calculated. The properties of the three known visual binaries in the sample are presented.

Chapter 7 describes the observation of the highly active brown dwarf LP 944-20, with EFOSC2 at the 3.6 m telescope in La Silla. The spectrographic setup, the data reduction and the analysis are explained. Finally, the results are presented.

Chapter 8 gives a conclusion of the work.

In appendix A the IRAF CL script for the radial velocity measurement is given. Appendix B shows the radial velocity variations of each object. Appendix C shows all graphs from where the radial velocities were measured. The objects are listed in alphabetical order.

2. What are brown dwarfs?

2.1. Defining the term "brown dwarf"

Brown dwarfs have intermediate masses between stars and planets. They are objects with masses between $0.012 M_{\odot}$ and $0.075 M_{\odot}$ or $13 M_{Jup}$ and $80 M_{Jup}$, respectively. A mass of $0.075 M_{\odot}$ is required for hydrogen-burning and a mass below $0.012 M_{\odot}$ is associated with gaseous planets. These mass limits depend, to a certain level, on the metallicity. Unlike normal stars, during their evolution brown dwarfs never reach the phase of hydrogen-burning in equilibrium. During the collapse of a molecular cloud, the cores of brown dwarfs get very dense. Before the temperature in the core is large enough for hydrogen-burning to take place, the collapse is stopped by the pressure of degenerated electrons. Electrons obey the Pauli exclusion principle. They are forbidden from occupying identical quantum states, therefore, the electrons will successively fill up the lowest available energy states. Those electrons that are forced into higher energy levels contribute to the degeneracy pressure $P_{degeneracy} \propto \rho^{5/3}$.

There is considerable debate about the definition of sub-stellar objects, such as brown dwarfs and planets. What should be the criteria to distinguish very low-mass stars from brown dwarfs and brown dwarfs from planets? First, there is the fusion or mass criteria, classifying stars as hydrogen-burning objects, brown dwarfs as deuterium-burning objects, and planets as not burning either. This fusion criteria has consequences for the planet definition because free-floating objects have been found with masses lower than the deuterium-burning minimum mass of $13 M_{Jup}$ (Zapatero Osorio et al. 2000). Should there be a new name for these objects? Another criteria to distinguish between the objects could be their different formation process. Brown dwarfs are classified as objects that form like hydrogen-burning stars, but do not have sufficient mass to burn hydrogen. Planets are objects formed in accretion disks. This second criteria is very problematic because the formation history of low-mass objects is not well understood. Also, it is difficult to distinguish between a high-mass planet that was ejected out of a planetary system and a very low-mass brown dwarf that never burned deuterium.

2.1.1. Star or brown dwarf? - The hydrogen-burning limit and the lithium-test

The defining characteristic of a star is the hydrogen-burning in equilibrium. One way to ascertain that an object is a brown dwarf is the demonstration that hydrogen fusion has not occurred in its core. To distinguish very low-mass stars from brown dwarfs, Rafael Rebolo proposed the lithium-test in 1992. Lithium-burning through the ${}^7\text{Li}(p,\alpha){}^4\text{He}$ reaction occurs at slightly lower temperatures than hydrogen-burning. The predicted

minimum mass for lithium-burning is $\sim 0.06 M_{\odot}$. The timescale for the destruction of lithium in the lowest-mass stars is about 10^8 yr. Because brown dwarfs are fully convective objects, ${}^7\text{Li}$ from the atmosphere will be mixed with the interior through convection zones. The evolutionary timescale of these objects is many orders of the convective timescale. Therefore, these objects are fully mixed and have identical abundances in their interior and their atmosphere. If the temperature is sufficiently high in the interior, ${}^7\text{Li}$ will be destroyed by thermal protons. Therefore, the presence of lithium in a fully convective object older than 10^8 yr signifies the lack of hydrogen-burning and, thus, identifies the object as a brown dwarf. This test is not applicable for the identification of sub-stellar objects in young star-forming regions, where even stars had no time to burn their lithium. Also, it is not applicable for brown dwarfs with masses between ~ 0.06 and $0.075 M_{\odot}$.

2.1.2. Planet or brown dwarf? - The deuterium-burning limit

In 2003, the IAU adopted the deuterium-burning minimum mass as the official distinction between brown dwarfs and planets. The so-called opacity-limited minimum mass for fragmentation is of a few Jupiter masses, which is in the same range as the deuterium-burning minimum mass of $\sim 0.013 M_{\odot}$. The deuterium-burning minimum mass corresponds to maximum central temperatures of $T_c \sim 10^6$ K. The deuterium-test can be used in a similar manner as the lithium-test. Brown dwarfs, in contrast to planets, burn their deuterium through the ${}^2\text{D}(p,\gamma){}^3\text{He}$ process. The typical timescale for deuterium-burning in main sequence stars is $t \lesssim 10^7$ yr. Thus, sub-stellar objects older than $t \sim 10^7$ yr, which have deuterium in their atmosphere, are planets. In contrast to the lithium-test, the deuterium-test is difficult to use in practice.

There is certainly an overlap in the masses of the most massive planets and the least massive brown dwarfs in the mass range of $\sim 1 - 10 M_{Jup}$. A very low-mass brown dwarf that never burned deuterium could be mistaken for a massive planet. To distinguish a very low-mass brown dwarf from a massive planet, one could make use of the signatures that their different formation histories would leave, such as different abundance patterns of the atmosphere. A planet formed in a circumstellar disk will have a larger abundance of metals in its atmosphere than a brown dwarf formed like a star. Heavy elements in the planet interior will also affect its mechanical structure, for example its mass - radius relationship, which also could be observed.

2.2. Physical properties of brown dwarfs

2.2.1. Evolutionary tracks

In figure 2.1 the evolution in the Hertzsprung-Russel diagram of very low-mass stars and brown dwarfs is shown. At early times the tracks are nearly vertical. As the objects become degenerate, T_{eff} and L decline. At later age the tracks go into a diagonal, corresponding to a constant radius. The lower open white circle indicates the point where an object of $0.075 M_{\odot}$ stops contracting. All objects with lower masses are brown

dwarfs. The shaded area signifies the lithium depletion. The upper white circle shows the point where a $0.075 M_{\odot}$ object has depleted 90% of its lithium.

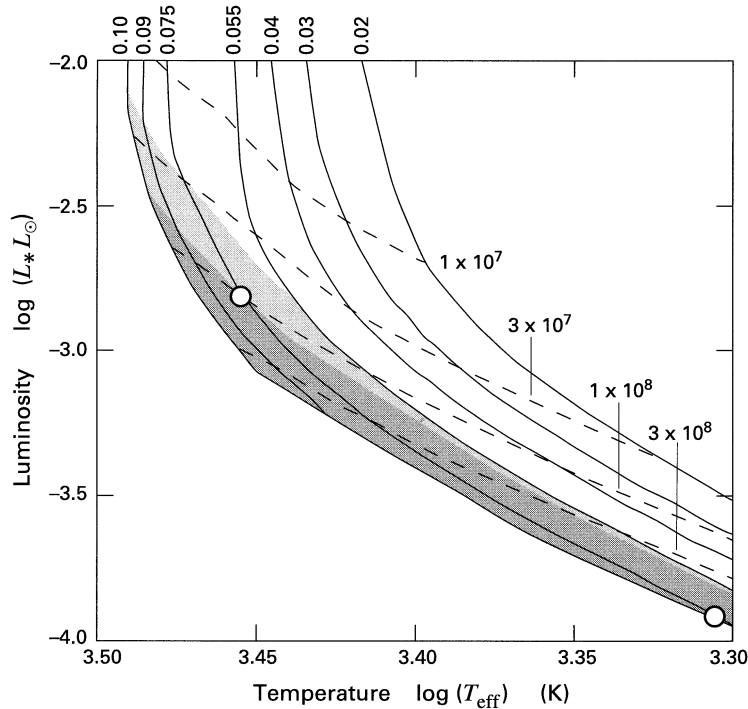


Figure 2.1.: Evolutionary tracks of very low-mass stars and brown dwarfs. (Stahler et al. 2004)

2.2.2. Radius and gravity

Due to the degeneration in brown dwarfs, there is only a very weak mass dependence of the radius. The energy of the degenerated particles is comparable to the gravitational potential energy. Degenerated objects shrink with increasing mass, having a radius - mass relation of $R \propto M^{-1/3}$. However, the Coulomb pressure is negative. This causes the radius to deviate from this relation. With decreasing mass, the Coulomb pressure is characterized by a radius - mass relation of $R \propto M^{1/3}$. This leads to an almost constant radius of brown dwarfs of about $R \sim 1 R_{Jup} \approx 0.1 R_{\odot}$. Lighter brown dwarfs have slightly larger radii.

The surface gravity $g = Gm/R^2$ for brown dwarfs range from $\log(g) \approx 5.5$ to $\log(g) \approx 3.5$ (g in cms^{-2}). For comparison, Jupiter has $\log(g) \approx 3.4$ and the Earth $\log(g) \approx 3.0$ (g in cms^{-2}).

2.2.3. Temperature and luminosity

The central temperature in brown dwarfs is by definition less than the critical hydrogen-burning temperature of about 3×10^6 K. A planet like Jupiter has a central temperature of $T_c \simeq 10^4$ K.

The effective temperature of a brown dwarf depends on his age. The only energy available in brown dwarfs is the heat from the collapse of the gas cloud. With age this energy gets radiated away and the brown dwarf gets cooler and fainter. A brown dwarf of $0.075 M_\odot$ and an age of 1 Myr has an effective temperature of ~ 2900 K. The coolest temperatures observed so far are around 700 K. It is expected that future surveys, for instance with VISTA (Visible and Infrared Survey Telescope for Astronomy), will detect even cooler brown dwarfs.

Because of their low effective temperatures, brown dwarfs are not very luminous. The absolute V magnitudes are around +17 mag and fainter. While they are very faint in the optical, they are brighter in the near infrared. Brown dwarfs, at temperatures of about 1500 K, radiate nearly 90% of their energy at wavelengths long-ward of $1 \mu\text{m}$, and even up to 99% if dust is present in the atmosphere.

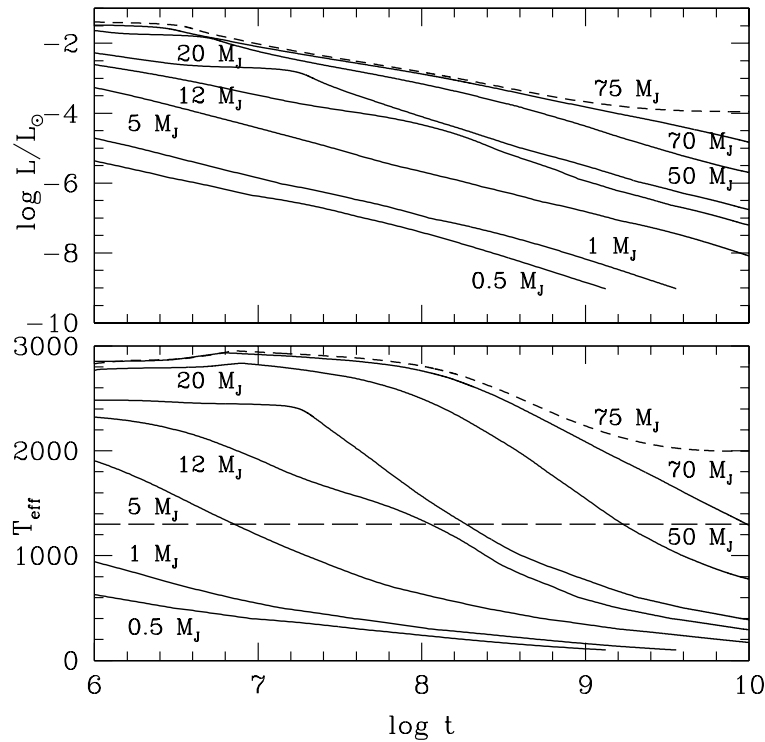


Figure 2.2.: Evolution of the luminosity L and the effective temperature T_{eff} as a function of time (in years) for different masses. The short-dashed line indicates the stellar/sub-stellar border. The long-dashed line indicates the border from L- to T-dwarfs. (Baraffe et al. 2003)

2.2.4. Density and pressure

The central density in sub-stellar objects range from a density of $\rho_c \simeq 10^3 \text{ gcm}^{-3}$, at the hydrogen-burning limit, to $\rho_c \simeq 10 \text{ gcm}^{-3}$, for masses of Jupiter. The pressure in brown dwarfs is mainly caused by degenerated electrons and is about 10^6 Pa .

2.2.5. Energy transportation mechanisms

Below a minimum mass of $m_{conv} \sim 0.3 - 0.4 M_\odot$, depending on the metallicity, the inner radiative core vanishes. Objects with masses lower than this minimum mass are entirely convective. In convective objects the transportation of mass from the core to the surface leads to a fully mixed object.

If the density is high enough and the temperature low enough, electron conductivity becomes important. Brown dwarfs that are old enough develop a conductive core.

2.2.6. Magnetic field, rotation and activity

The solar magnetic field generation is explained by the $\alpha\Omega$ - dynamo and depends on shearing motions at the radiative/convective transition zone. Very low-mass stars and brown dwarfs are fully convective objects. Therefore, the magnetic field generation through the $\alpha\Omega$ - dynamo does not work for these objects.

Still, radio observations show that some late M- and L-dwarfs are able to generate magnetic fields in the order of 0.1 to 1 kG (Berger 2006). Radio emission arises from gyroresonance or coherent processes and is, therefore, a direct indicator of magnetic fields. The magnetic dynamo in convective objects could be generated by turbulent motions associated with the internal convection (Durney et al. 1993). Another possibility is the generation of a large-scale magnetic field by an α^2 - dynamo. In an α^2 - dynamo the helicity is generated by the action of the Coriolis force on the convective motions in a rotating, stratified fluid. Fields of fully convective objects are expected to be distributed on a global scale. According to these calculations, they should not be concentrated in small spots (Chabrier et al. 2006, Dobler et al. 2006).

Fully convective objects are rapid rotators with rotation velocities of $\sim 20 - 30 \text{ kms}^{-1}$, corresponding to rotation periods of a few hours. Also, young solar-type stars rotate rapidly but disk interactions and stellar winds slow down their rotation. The reason for the rapid rotation of objects near and below the sub-stellar boundary could be that their field distribution does not lead to much magnetic braking.

For stars, there is a connection between the rotation and the magnetic activity at the surface. The more rapid the rotation the more active the object, arguing for a magnetic field generation by an $\alpha\Omega$ - dynamo. This connection between rotation and activity does not apply to very low-mass stars. Activity leads to emission in spectral lines, such as $H\alpha$, or to coronal X-rays. Emission in spectral lines and X-ray emission are caused by the dissipation of magnetic fields in the atmosphere. They are, therefore, secondary indicators of magnetic fields and provide information about the influence of magnetic fields on the atmosphere.

There is a drop in the fraction of active objects from $\sim 30\%$, for M-dwarfs, to $\sim 5\%$, for L-dwarfs (Berger 2006). The ratio $\log(L_{Radio}/L_{X-ray})$ drops from ~ -15.5 , for spectral types earlier than M7, to ≥ -12 , for spectral types later than M7, as can be seen in figure 2.3. Also, at about spectral type M7 a significant drop in the $H\alpha$ activity occurs. This transition is likely due to the increasingly neutral atmospheres. The ionization level in the atmosphere of these objects becomes so low that there is no coupling between the magnetic field and the gas. In this case, the motion of the gas does not twist up the field and, therefore, there is no dissipation to heat the upper atmosphere. Also, the transition to a turbulent dynamo could have an effect on the activity.

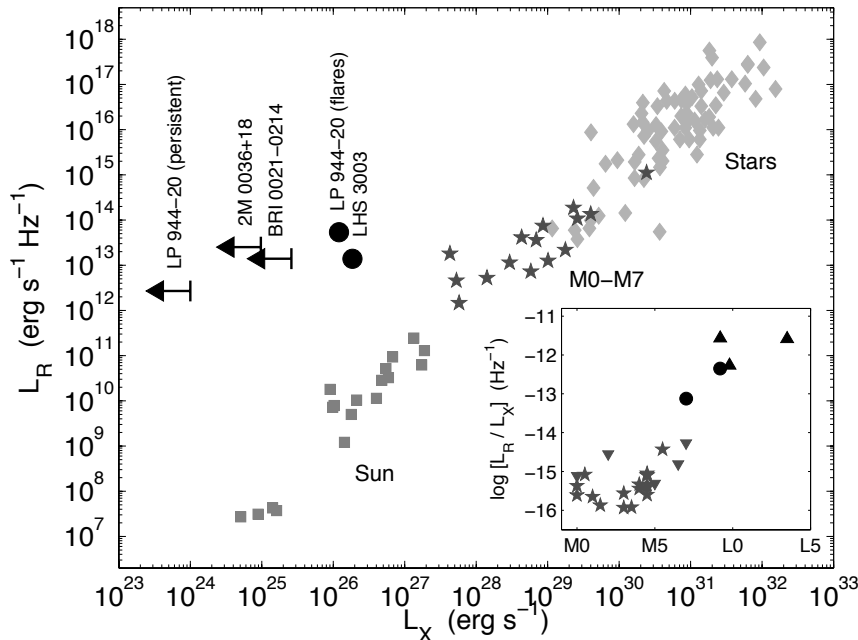


Figure 2.3.: Radio versus X-ray luminosity. The late M and L dwarfs clearly violate the correlation between L_R and L_X . (Berger 2006)

2.3. Atmosphere and spectral type classification

For brown dwarfs the mass - spectral type relation depends on the age of the object. Brown dwarfs cool with age and go to later spectral types with time. Thus, the spectral type of these objects only gives an information about the combination of mass and age. A massive brown dwarf starts its life with a temperature of about 2900 K and goes through all the spectral classes from late M on, while lighter brown dwarfs start at later spectral classes.

Characteristic atmospheric features are used to classify the spectral types of stellar and sub-stellar objects. These spectral classes provide a temperature scale. Atmospheres of brown dwarfs are very cool. Molecular hydrogen and other molecules appear at temper-

atures lower than $T \simeq 5 \times 10^3$ K. Brown dwarfs have temperatures of 2900 K and less. Thus, in the atmospheres of brown dwarfs molecules form. For $T < 1800$ K dust particles condense out of the photosphere. This leads to strong changes of the spectrum, which can be used for a spectral type classification.

Brown dwarfs are generally divided in two spectral classes, L and T, with some late M-dwarfs also being brown dwarfs. There is no monotonic relation between the spectral types L and T and the effective temperature, like for main sequence stars where later spectral types correspond to cooler objects. For late L to mid T spectral types the temperature is nearly constant. These spectral types are probably as equally influenced through dust properties as through effective temperatures. The figures 2.5 and 2.6 show optical and near infrared spectra of late M- to late T-dwarfs.

Observations will soon make it possible to observe even fainter and lower-mass objects. A new spectral class will be needed. For Jovian-like atmospheres with $T_{eff} \lesssim 600$ K, the dominant equilibrium form of nitrogen is NH_3 . For $T_{eff} \lesssim 150$ K and $T_{eff} \lesssim 80$ K, H_2O and NH_3 condense near and below the photosphere and water and ammonia bands disappear completely. The letter Y was reserved for objects whose temperatures resemble Jupiter's.

Figure 2.4 shows a near-infrared color - color plot of M-, L- and T-dwarfs. T-dwarfs exhibit bluer colors than L-dwarfs. This fact can be explained by the hypothesis that the dust grains grow rapidly at such low temperatures as in T-dwarfs. The dust grains sink to deeper layers of the atmosphere where they partially sublime and no longer affect the emitted spectrum.

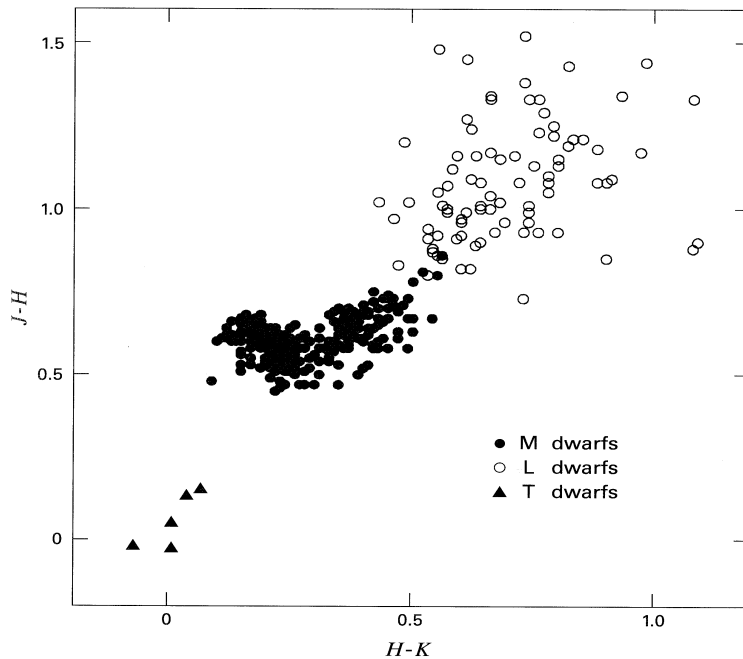


Figure 2.4.: Near-infrared color - color plot of M-, L- and T-dwarfs. (Stahler et al. 2004)

2.3.1. M-dwarfs

Below $T_{eff} \lesssim 4000$ K, most of the hydrogen is bound in H_2 and most of the carbon in CO. Oxygen is bound in molecules such as TiO, VO and H_2O , with some amounts also in OH. Therefore, the energy distribution of solar-abundance M-dwarfs is determined by the absorption of TiO and VO in the optical and H_2O and CO in the near-infrared. Metal oxides and metal hydrides like FeH, CaH and MgH are also present. There is no true continuum. Below $T_{eff} \sim 2800$ K, for mid M-dwarfs, the atmosphere gets gradually depleted by grain condensation of a number of molecules, for example, VO and TiO. VO and TiO band-strength indices can be used to classify the spectral types of M-dwarfs.

2.3.2. L-dwarfs

L-dwarfs cover more or less the temperature region from 2100 to 1300 K. They can be either very low-mass hydrogen burning stars or brown dwarfs. The TiO and VO molecular features seen in M-dwarfs have gradually disappeared. The main spectral characteristics of L-dwarfs in the optical are metal-hydride-lines, such as CrH, FeH, CaH and strong neutral alkali-metal-lines like Na I, K I, Rb I and Cs I. In the near-infrared, the spectra are characterized by strong bands of H_2O and bands of FeH and CO. At a temperature of $T \lesssim 1800$ K, the elements Al, Ca, Mg, Si, Ti, Fe and V are removed gradually from the gaseous atmosphere by condensation into grains (e.g. Al_2O_3 , $CaTiO_3$, $CaSiO_3$, $MgSiO_3$, etc.) and the spectral features of these elements will eventually disappear.

For synthetic spectra of L-dwarfs, so-called DUSTY-models are used. These models assume that dust grains are suspended in the atmosphere. The spectral shapes cannot be modeled unless the formation, scattering and absorption of dust grains are taken into account. The main effect of dust is the decreasing of line strengths. Therefore, the main difference of the COND (no dust) and the DUSTY models lies in the strengths of the lines. These two models are two extreme cases. The true spectrum for L dwarfs will be somewhere in between.

2.3.3. T-dwarfs

T-dwarfs cover the temperature region from 1300 to 800 K. All T-dwarfs are believed to be sub-stellar. Below a temperature $T_{eff} \approx 1800$ K, CO dissociates and the dominant form of carbon becomes CH_4 . As the temperature decreases, methane causes strong absorption bands in the near-infrared. By late T spectral types, H_2O is a major absorber in the near-infrared and the two prominent lines of Na I and K I in the optical part of the spectrum have grown very wide. The proto-type for a methane T-dwarf is Gl 229B.

Theoretical spectra of mid to late T-dwarfs are calculated with the so-called COND-models, assuming that the dust grains have settled below the photosphere and therefore do not affect the emergent spectrum.

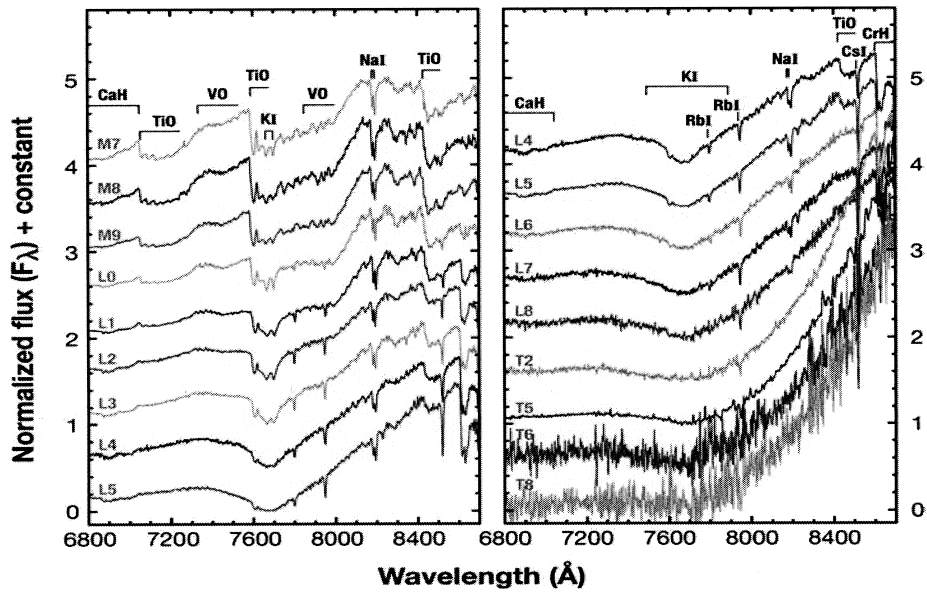


Figure 2.5.: Optical spectra from 6800 to 8700 Å for late M- through late T-dwarfs. (Kirkpatrick et al. 2005)

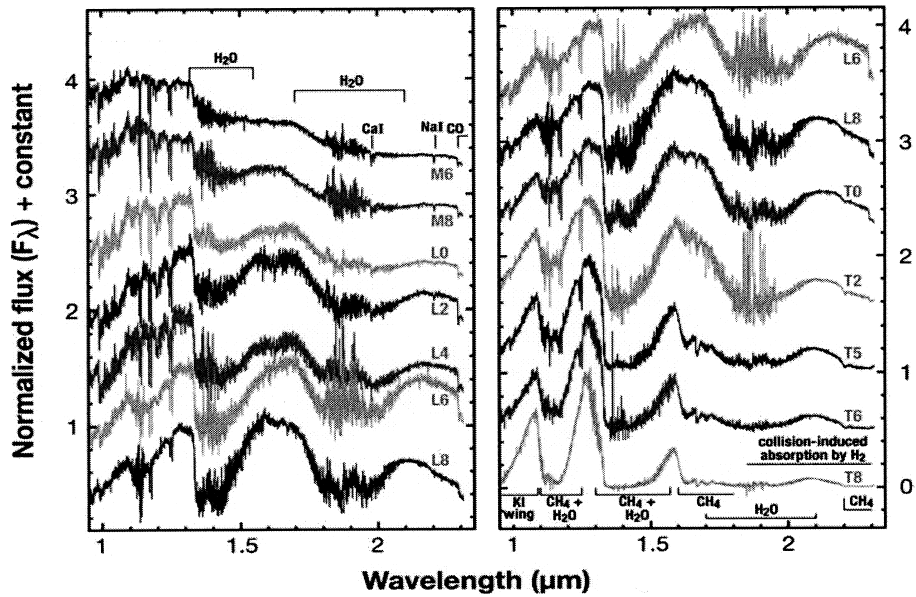


Figure 2.6.: Near-infrared spectra from 0.95 to 2.3 μm for mid M- to late T-dwarfs. (Kirkpatrick et al. 2005)

3. The formation of brown dwarfs

3.1. How do brown dwarfs form?

There is no widely accepted explanation for the formation of objects intermediate between stars and planets. Standard gravitational collapse and fragmentation of molecular clouds cannot easily explain the formation of brown dwarfs. Brown dwarfs could form like stars if the density of interstellar matter is locally very high. Whether such regions exist is not known. Because of the difficulty in explaining the formation of brown dwarfs with stellar formation models, alternative scenarios have been developed. As will be shown below, the binary properties are an important diagnostic in order to test these different scenarios.

The standard star formation model explains the formation of stars through the collapse of molecular cloud cores. Because of small density perturbations in a molecular cloud, dense self-gravitating cores form and collapse. In these dense cores the formation of stars occurs. When the rate at which the gravitational potential energy is released exceeds the rate at which the gas can cool, the opacity limit for fragmentation occurs. The opacity limit results in the formation of fragments of a few Jupiter masses. The material with higher angular momentum will settle in a disk around the object, which continues to accrete material from the disk and will eventually reach stellar masses. Hydrogen-burning provides the pressure that supports the star against its own gravity.

The standard planet formation model is the core-accretion model. Dust particles in the disk coagulate into planetesimals. Rock and ice cores of a few Earth masses form when these planetesimals crash together. The cores accrete gas out of the disk and grow to about Jupiter size.

Based on their statistical properties, which appear to form a continuum with those of low-mass hydrogen-burning stars, it can be argued that brown dwarfs form basically like hydrogen-burning stars and not like planets. For instance, the initial mass function appears to be continuous across the hydrogen-burning limit. Brown dwarfs appear to be homogeneously mixed with stars in clusters. Also, disks, accretion and outflows indicate that brown dwarfs are formed by a similar formation mechanism to that of stars (e.g. Apai et al. 2004, Muzerolle et al. 2005).

For a collapse of a sufficiently low-mass core, the slow increase in the central temperature and the fast increase in the central density will cause the gas to become partially degenerate before the central temperature can reach the hydrogen-burning temperature. During the contraction, all electrons are freed from their nuclei by the heat. Because of the Pauli exclusion principle many electrons are forced to occupy very high energy states. The object becomes degenerate and the degeneracy pressure in the core opposes the gravitational collapse.

It is to note that there is no reason why higher-mass brown dwarfs cannot form from the collapse of dense cloud cores, like low-mass stars do. On the other hand, deuterium-burning objects at the lower mass limit for brown dwarfs may be formed like planets by condensation from a circumstellar disk.

3.2. Brown dwarf formation scenarios

Different formation scenarios for brown dwarfs are under discussion. Here, five different scenarios will be presented; turbulent fragmentation, dynamical ejection, gravitational instabilities in disks, photo-erosion and binary disruption. These mechanisms do not necessarily exclude each other. Their relative importance may depend on the environment.

3.2.1. Turbulent fragmentation

Brown dwarfs may form like stars by the collapse of a molecular cloud but do not become stars because they form out of relatively small cores. This could be achieved by turbulent fragmentation in molecular clouds, as suggested by Padoan and Nordlund in 2002. This scenario seems to be supported by many observational facts that show a continuum in statistical properties across the sub-stellar border.

In the turbulent fragmentation scenario, a highly nonlinear density and velocity field is generated in the cloud by supersonic turbulence. Shocks cause the formation of dense filaments. Along these filaments there are places where the local densities are high enough for gravity to overwhelm the turbulent, thermal and magnetic pressure support. In turbulent fragmentation simulations, gas flows collide, are compressed and form gravitationally unstable cores. These simulations can form cores as small as $\sim 0.003 M_{\odot}$ (Padoan & Nordlund 2004). In addition, magnetic fields most likely play an important role in the fragmentation and collapse process.

When multiple systems form by fragmentation, the minimum separation should be a ~ 10 AU due to the opacity limit. Closer binaries require dynamical or hydrodynamical hardening mechanisms. The small number of wide binaries observed could be explained by dynamical decay of these weakly bound systems at a later time in their evolution.

3.2.2. Embryo-ejection

In the "embryo-ejection" scenario, dynamical interaction in small-N clusters eject stellar embryos from the cloud before they can accrete enough mass to become more massive stars. This scenario was suggested by Reipurth and Clarke in 2001.

The formation of very low-mass objects begins like that for stars but in the context of small-N clusters of objects. In the cluster the sub-stellar cores are competing for the accretion material and the one which grows the slowest will be the most likely ejected. The lowest mass member tends to be driven out by mass segregation and will accrete even less material because of the lower gas densities in the outer regions of the cloud. This process drives it farther out and so forth. Also, if all members have nearly equal masses these systems are so instable that dynamical scattering will dissolve such systems.

Proto-stars, which get ejected due to dynamical interactions out of their dense gaseous environment before they have time to accrete to stellar masses, end up as brown dwarfs. Thus, brown dwarfs could be addressed as failed stars.

Many numerical simulations have been carried out to simulate the dynamical evolution in star-forming regions and to model the embryo-ejection scenario. Hydrodynamical collapse calculations were carried out, for example, by Bate et al. (2002, 2003, 2005) and numerical N-body simulations by Sterzik and Durisen (2003), Delgado-Donate et al. (2003), and Umbreit et al. (2005). In these numerical simulations the production of very low-mass stars and brown dwarfs is high. Some of these simulations show significant differences in their theoretical predictions to the observed properties of very low-mass stars and brown dwarfs. Some ejection scenarios, such as from Reipurth and Clarke (2001), propose that objects are ejected with high velocities out of a dense region and thus would make it less likely to find them in star-forming clusters with a low escape velocity. Also, numerical models, such as Umbreit et al. (2005), predict higher velocities for brown dwarfs than for stars. Yet, observations show similar distributions of velocities and similar spatial positions for stars and brown dwarfs. Dynamical calculations for certain models, such as from Sterzik and Durisen (2003) and Bate et al. (2003), imply that ejection might occur with velocities too small to be observable. Close collisions that are required for the ejection of fragments would truncate the disks and thus limit their lifetime. However, observations show similar disk properties as for T Tauri stars. In simulations, some of the brown dwarfs retain low-mass disks with $M_{Disk} \lesssim 0.010 M_{\odot}$ and $R_{Disk} \lesssim 40$ AU after ejection, from which they continue to accrete. There are huge differences between the simulations and the observations concerning the binary statistics. Simulations produce binary frequencies of less than 10%, whereas the observed binary frequency is at least 20%. Wide binary systems challenge the ejection scenario because these systems should be easily disrupted by such a vehement process. Additionally to the high binary frequency observed, the ejection scenario has difficulties in explaining wide brown dwarf companions around solar-type stars. More about binary properties will be explained in chapter 4.

The requirements for the ejection mechanism are very general. Also, the formation probability in numerical simulations is very high. Therefore, it is likely that this scenario occurs in nature. The question is how often it occurs compared with relatively undisturbed stellar formation.

3.2.3. Gravitational instabilities in disks

Disk fragmentation can occur when gravitational instabilities in circumstellar disks form. Lin et al. (1998) proposed that the encounter between two proto-stellar disks might increase the Jeans mass locally, making the formation of a very low-mass object possible. Jiang et al. (2004) suggested that brown dwarfs could be formed by gravitational instabilities in circumbinary disks and are removed afterwards through dynamical interaction with their parent star.

Gravitational instabilities in circumstellar disks could happen, for example, through dynamical interactions with a passing star or another disk, through tidal or spiral insta-

bilities, or if the disk does not have time to relax towards an equilibrium state. Only at large radii of ~ 100 AU can fragments of a disk contract and cool sufficiently fast to condense out. At smaller radii the temperature and the surface-density of the disk are higher. Thus, the fragments are unable to cool radiatively sufficiently fast to condense out. Instead, they bounce and are shredded by tidal forces. This may explain the almost complete absence of brown dwarfs, the so-called brown dwarf desert, in close (≤ 3 AU) orbits around solar-like stars. The disk mass necessary to produce such objects as brown dwarfs is $\sim 0.1 M_{\odot}$. Thus, the disk fragmentation scenario appears capable of producing brown dwarfs in disks around some massive stars, which have massive enough disks. However, it does not explain brown dwarf companions around very low-mass stars.

In a dense proto-cluster, impulsive interactions between disks, or between a disk and a naked star, should be common. Therefore, it should be possible that some brown dwarf companions around stars form by disk fragmentation at large radii.

3.2.4. Photo-erosion of pre-existing cores in H II regions

Hester et al. (1996) suggested the formation of very low-mass stars and brown dwarfs based on photo-erosion in the vicinity of O or B stars, whose strong UV fields erode the outer layers of proto-stellar cores before they reach stellar masses.

Photo-erosion occurs when a pre-stellar core of a few $0.1 M_{\odot}$ is compressed and eroded by the ionizing radiation front of a nearby massive O or B star. When the compression wave from the O or B star reaches the center of the pre-stellar core, a proto-star is created, which then grows by accretion. The compression wave is reflected and propagates outwards. It then meets the inward propagating ionization front. Shortly after, the ionization front encounters gas, which is so tightly bound to the proto-star that it cannot be stripped by ionization. All the material interior to the ionization front at that time ends up in the proto-star.

This mechanism produces very low-mass stars for initial conditions, which are likely to be realized in nature. Binary formation is possible if the initial core was fragmented. However, this mechanism is also very inefficient because it requires the presence of massive young stars and a very massive initial core to form a brown dwarf. Thus, brown dwarfs could form by this formation mechanism in high-mass dense star formation environments, such as Orion, but not in low-mass star-forming environments, such as Taurus or Chamaeleon I, which also harbor brown dwarfs. Therefore, photo-erosion cannot be a universal mechanism for very low-mass stars and brown dwarf formation. It can only be responsible for a few very low-mass objects.

3.2.5. Binary disruption

Goodwin et al. (2007) proposed that brown dwarfs are initially binary companions that form by gravitational fragmentation at large radii ($R \gtrsim 100$ AU) in proto-stellar disks of low-mass stars. These systems are then disrupted by gentle velocity perturbations due to passing stars. This model implies that most stars and brown dwarfs form in multiple systems, which are then rapidly and gently disrupted by tidal encounters in clusters.

This hypothesis yields a continuum of statistical properties at the stellar/substellar border. The binary disruption model does not have the difficulty of forming very low-mass pre-stellar cores, as has the turbulent fragmentation mechanism. Also, because the systems are gently disrupted, it does not have certain problems of the embryo-ejection scenario, such as a high velocity dispersion, the stripping of the disks or hardening mechanisms for binary systems.

Because fragmentation can only take place at the outer parts of the disk, close brown dwarf binary systems are unlikely to form by disk fragmentation. However, a low-mass fragment, which condenses out of a disk, may undergo secondary fragmentation, producing a close binary system. A gentle disruption could separate the binary system from the star, without destroying it. This could be tested by comparing the frequency of binary brown dwarf systems around low-mass stars in young star-forming regions with the frequency in the field.

4. Binary systems as a diagnostic tool for understanding the formation of brown dwarfs

Multiple star systems are common in the Galaxy. The physical properties of the components in these systems are significantly influenced by dynamical and evolutionary processes. This makes it possible to put constraints to the different formation scenarios due to observed properties of very low-mass star and brown dwarf binaries. Different formation scenarios produce, for example; different multiplicity frequencies, different distribution functions for separations, different mass ratios, and different variations of these quantities with primary mass. In particular, the predictions of the standard scenario and the embryo-ejection scenario are sufficiently different as to be tested by observations. Also, important constraints on the formation mechanisms could be made if the binary properties of very low-mass stars and brown dwarfs depend on their formation environment.

If very low-mass stars and brown dwarfs appear to continue the binary properties for low-mass and solar-type stars, it would imply that they are formed through the same processes as stellar binaries. If there is no continuousness it would suggest a different formation mechanism.

In section 4.1, different techniques for the search of binary systems are presented. The pros and cons of these techniques are discussed. In section 4.2, some binary properties of very low-mass stars and brown dwarfs are described in detail. In section 4.3, other means of testing the different formation scenarios are discussed.

4.1. Observations

4.1.1. High-resolution imaging

Searches for very low-mass binaries have been carried out mostly through high-resolution imaging surveys (e.g. Boy et al. 2003, Burgasser et al. 2003, Close et al. 2003, Siegler et al. 2005, Kraus et al. 2005, Boy et al. 2006), using ground- and space-based facilities (either the Hubble Space Telescope or adaptive optics). The studies are in agreement about the general properties of very low-mass binaries. They find a binary frequency of $\sim 15\%$ for separations $a \geq 1$ AU. The frequency of wide binary systems with a semi-major axis greater than 15 AU is estimated to be $\lesssim 5\%$. The binary companions tend to have nearly equal masses. In contrast, companions to the more massive low-mass stars show a wider range of both separations and mass ratios.

Direct imaging is only sensitive enough to detect binary separations larger than 1 AU, which correspond to very large orbital periods. In the case that orbital parameters, such as the period, have not been observed yet, the masses can only be determined indirectly, using evolutionary tracks. If the orbital period is known, the sum of the masses $M_1 + M_2$ can be determined. If the stars' motion with respect to the stellar background is known, it can also be determined how the total mass is divided between the two components.

4.1.2. High-resolution spectroscopy

Imaging surveys cannot resolve tightly bound systems. Brown dwarfs in the field and in nearby associations with separations of a $\lesssim 1 - 3$ AU cannot be detected by them. To detect these close binary systems high-resolution spectroscopy has to be used. Presently, only a small number of high-resolution surveys have been carried out. This is because the required high-resolution spectroscopy of very faint objects has not been available for long. Additionally, more observing time is needed on a large telescope in order to detect a short-period system with spectroscopy than a large-period system using imaging (adaptive optics). From the limited observational facts, the close binary frequency is estimated to be $\sim 17 - 30\%$ (Jeffries & Maxted 2005). In comparison, stellar-mass stars have a binary fraction of $\sim 14\%$ for companions with distances of $\lesssim 1 - 3$ AU. So far only five spectroscopic binaries have been found.

Gibor Basri and Eduardo Martin were the first to confirm a spectroscopic binary. In 1999 they found PPl 15 to have a companion with an orbital period of 5.8 days. PPl 15 is a member of the Pleiades open cluster and has an age of ~ 115 Myr. The masses are estimated to be between 60 and 70 M_{Jup} and the eccentricity of the orbit is estimated to be 0.4. Since then, some spectroscopic surveys of very low-mass stars and brown dwarfs were conducted. These surveys are summarized in table 4.1. Reid et al. (2002) observed 39 very low-mass stars and brown dwarfs and found two spectroscopic binaries and another object with significant radial velocity variation. Guenther and Wuchterl (2003) detected 2 spectroscopic binaries (one of them already detected by Reid et al. 2002) among 25 very low-mass stars and brown dwarfs in the field. Kenyon et al. (2005) found evidence for 4 close binaries in a sample of 57 very low-mass stars and brown dwarfs in the young Sigma Ori cluster. Joergens (2006a) found 2 radial velocity variables among 12 very low-mass stars and brown dwarfs in the Cha I star-forming region. Gibor Basri and Ansgar Reiners (2006) determined 6 ± 2 binary systems out of 53 observed very low-mass stars and brown dwarfs in the field. Kurosawa et al. (2006) obtained high-resolution spectra of 14 brown dwarfs and very low-mass stars in the Upper Scorpius OB association and three brown dwarf candidates in the ρ Ophiuchi dark cloud core. They found that 4 out of 17 objects show significant radial velocity variations. However, each object was only observed twice.

With high-resolution spectroscopy only a mass-function $f(M) = M_2^3 \sin^3 i / (M_1 + M_2)^2$ can be derived for spectroscopic single-lined systems. If one knows the primary mass M_1 , a lower mass limit for the companion can be derived. For spectroscopic double-lined systems, the ratio of the stars' masses M_1/M_2 and the sum of the masses $(M_1 + M_2) \sin^3 i$ can be determined. If a double-lined system is eclipsing, the inclination i can be determined

and the absolute masses M_1 and M_2 can be derived.

Table 4.1.: Spectroscopic surveys of very low-mass stars and brown dwarfs

Survey	Spectral Type	Sample (# of objects)	Binary Frequency (%)
Reid et al. (2002)	M6 - L0.5	39	6...8
Guenther et al. (2003)	M5.5 - L1.5	25	12^{+4}_{-4}
Kenyon et al. (2005)	0.03 - 0.35 M_{\odot}	57	7...19
Joergens (2006a)	M2.5 - M8	12	17
Basri et al. (2006)	M5 - L5	53	11^{+7}_{-4}
Kurosawa et al. (2006)	M5 - M8.5	17	24^{+16}_{-13}

4.1.3. Astrometry

Only one component of an astrometric binary can be observed. The position of this component wobbles, due to the gravitational influence from its invisible companion. Due to proper motion astrometric binaries appear to follow a sinusoidal path across the sky. Astrometric monitoring leads to the determination of the orbital period and to mass constraints. Only a mass function $f(M) = M_3^3 \sin^3 i / (M_1 + M_2)^2$ can be determined if no additional data, such as radial velocity measurements, is available. The astrometric method is sensitive to nearby binary systems with large orbital separations.

4.1.4. Photometric monitoring

Stassun et al. (2006) found the object 2MASS J0535218-054608 in the Orion Nebula to be an eclipsing binary. It is the first known eclipsing binary system of two brown dwarfs. Because it is a member of the Orion Nebula it is only a few million years old. The objects have masses of $M_1 = 0.054 \pm 0.005 M_{\odot}$ and $M_2 = 0.034 \pm 0.003 M_{\odot}$. The radii are $R_1 = 0.669 \pm 0.034 R_{\odot}$ and $R_2 = 0.511 \pm 0.026 R_{\odot}$, which is consistent with models that predict that young brown dwarfs are significantly larger in their early stages. The temperatures were derived to $T_1 = 2650 \pm 100$ K and $T_2 = 2790 \pm 105$ K. Their finding that the smaller brown dwarf is the brighter one is not consistent with theoretical models. This fact can be explained with a different age of the two brown dwarfs, which might be brought together through dynamical interactions or, alternatively, by incorrect theoretical models. For instance, magnetic fields might alterate the physical structure of these objects.

Eclipsing binary systems are very rare. Therefore, the best method to find short-period systems are spectroscopic surveys. However, the light curve of an eclipsing binary system is a valuable supplement to spectroscopic data. From the light curve the inclination i can be determined, making it possible to calculate the absolute masses M_1 and M_2 of a double-lined spectroscopic binary system. The light curve of an eclipsing binary system provides the relative dimensions of the orbit. Together with the spectroscopic data, the absolute values of the orbit and the radii can be derived.

4.2. Properties of very low-mass star and brown dwarf binary systems

4.2.1. The binary frequency

The binary frequency is the best way of testing the two leading formation scenarios, the turbulent fragmentation scenario and the embryo-ejection scenario. Dynamical ejection is a very vehement process and binary systems are very likely to disrupt. Therefore, the ejection hypothesis predicts a low binary fraction. Some close binary brown dwarfs might be ejected from a multiple system without disruption if the other components of the system are widely separated or if the eccentricity of the orbit is low. Smoothed particle hydrodynamical and numerical simulations of decaying N-body clusters indicate a binary fraction of less than 10% and, thus, under-predict the observed binary frequency.

Those systems of brown dwarfs, which can be resolved by high-resolution imaging, have a frequency of at least 15%, while close brown dwarf binaries are estimated to have a frequency of $\sim 17 - 30\%$ (Jeffries & Maxted 2005), which still has to be tested. This close binary frequency would be larger than for G-dwarfs ($\sim 14\%$) or M-dwarfs ($\sim 10\%$). The overall multiplicity for brown dwarfs was estimated by Jeffries and Maxted, using Monte Carlo simulations and published radial velocity surveys, to be $\sim 32 - 45\%$. G-dwarfs have an overall binary fraction of up to 65%, M2 to M5 dwarfs of $42 \pm 9\%$.

4.2.2. Separation distribution

The few brown dwarf binaries produced in smoothed particle hydrodynamical simulations of the embryo-ejection scenario have separations below 10 AU. Also, numerical simulations of decaying N-body clusters indicate a maximum separation of a ~ 10 AU.

Umbreit et al. (2005) investigated the decay of accreting triple systems. In figure 4.1, the semi-major distribution for two different accretion types and a constant mass system is shown. Their simulations show that for accreting systems the semi-major axis is narrower and the peak is at lower values than for constant mass systems. Therefore, the influence of accretion in the brown dwarf formation can be observed. The more the momentum of the bodies is reduced, the narrower the semi-major axis distribution becomes. Also, the peak of the distribution shifts to smaller separations. Therefore, observing spectroscopic binaries constrains the importance of momentum transfer during the formation. If one finds a semi-major axis distribution which is very narrow and peaks at small separations this would mean that there is a small amount of momentum transfer. If the decline of the binary frequency is steep at small separations it would also argue against an importance of tidal interactions.

Figure 4.2 shows the semi-major axis distribution of brown dwarf binaries obtained from simulations of accreting triple systems by Umbreit et al. (2005) in comparison to the observed volume-limited sample distribution of Bouy et al (2003)¹. The two distributions match very well. The model predicts that the distribution decreases to

¹As can be seen in figure 8.1, I found a somewhat different semi-major axis distribution using the same data from Bouy et al. (2003).

smaller semi-major axis. Because of the detection limit, it is not clear whether the observed distribution will decrease. The aim of this work is to find the binary frequency beyond this detection limit for imaging surveys in a sample of very low-mass stars and brown dwarfs.

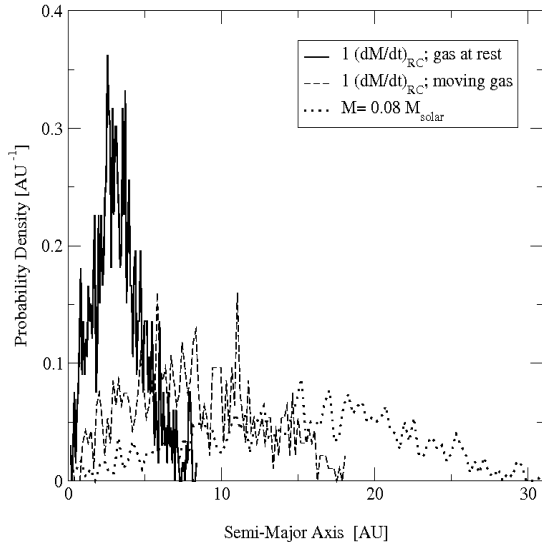


Figure 4.1.: Semi-major axis distribution for different kinds of accretion as well as for constant mass systems. (Umbreit et al. 2005)

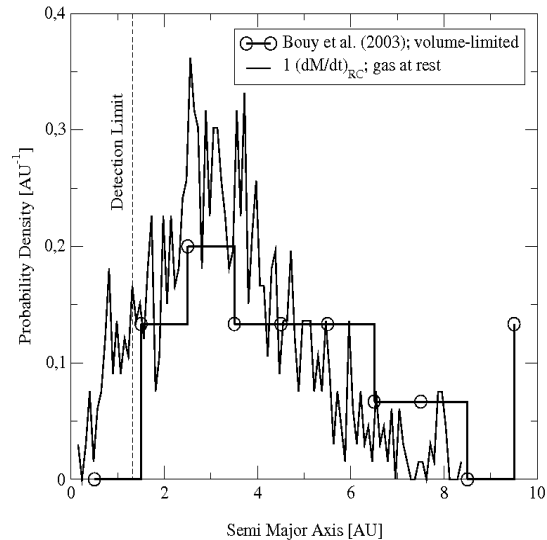


Figure 4.2.: Semi-major axis distribution obtained from simulations of decaying triple systems compared with the observed volume-limited sample of Bouy et al. (2003). (Umbreit et al. 2005)

Observationally, compared to higher mass stars, the separation of very low-mass star binaries is closer. The peak of the distribution is found near ~ 4 AU. However, there is incompleteness in observations at separations $\lesssim 3$ AU. The separation distribution of young systems suggests a distribution peaked towards wider separations, compared with old field binary systems.

Until recently, no very low-mass star and brown dwarf binaries with separations of $a \geq 15$ AU were found. This was taken as evidence for the embryo-ejection scenario because a wide binary would easily be disrupted by the strong dynamical interactions. However, recently some wide binary candidates, up to 240 AU, were found in the field (e.g. Martín et al. 1998, Forveille et al. 2004, Golimowski et al. 2004, Phan-Bao et al. 2005, Billères et al. 2005) and in young associations (e.g. Luhman et al. 2004, Chauvin et al. 2005, Luhman et al. 2005). The fraction of wide binary systems is estimated to be about 5%. In comparison, the binary frequency of field M-dwarfs in the mass range from $0.25 - 0.5 M_{\odot}$ for separations of 25 - 300 AU is 12%. These wide multiple systems challenge the ejection models. Some theoretical ejection models, such as from Bate and

Bonnell (2005), produce some wide brown dwarf binaries with separations ≥ 60 AU. To explain the apparent deficit of wide binaries within the standard star formation model, one could argue that this deficit could be produced by dynamical interactions in small-N clusters after the main accretion phase.

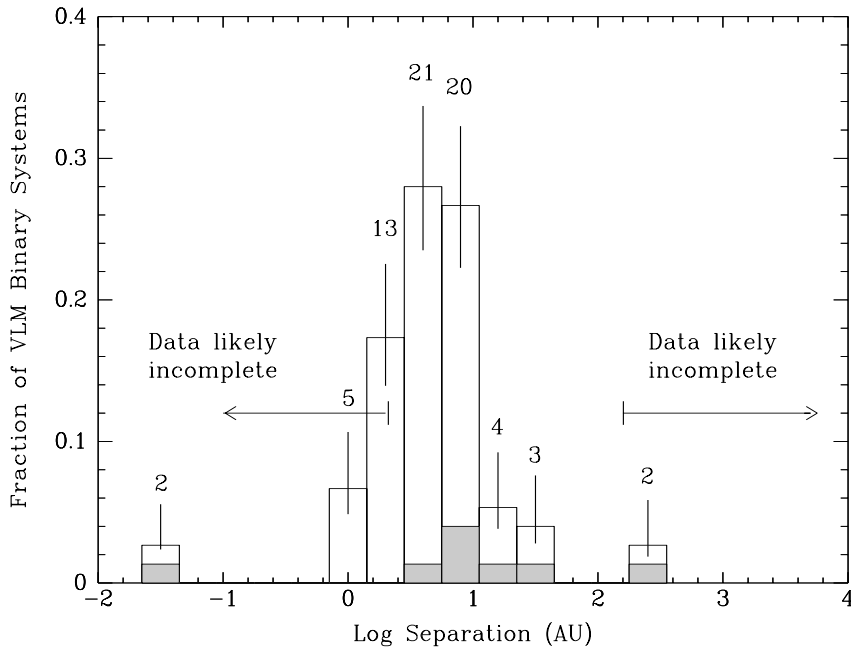


Figure 4.3.: Distribution of orbital semi-major axes of very low-mass binary systems. The shaded area represents the systems with ages < 10 Myr. (Burgasser et al. 2006)

4.2.3. Mass ratio distribution

The mass ratio distribution also puts constraints on the formation models. For instance, the embryo-ejection hypothesis predicts a tendency towards more equal masses in binary systems.

According to the currently available data, it appears that small mass ratios among solar-type binaries are more common than with very low-mass binaries. Among very low-mass dwarf binaries, 77% have a mass ratio of $q = M_2 / M_1 \gtrsim 0.8$ (Burgasser et al. 2006). The mass ratio distribution of younger systems shows a distribution peaked towards smaller mass ratios than that of the older field binaries. However, the statistics are largely incomplete due to instrument detection limits. Also, the masses were derived from imaging and thus depend on evolutionary tracks and model spectra.

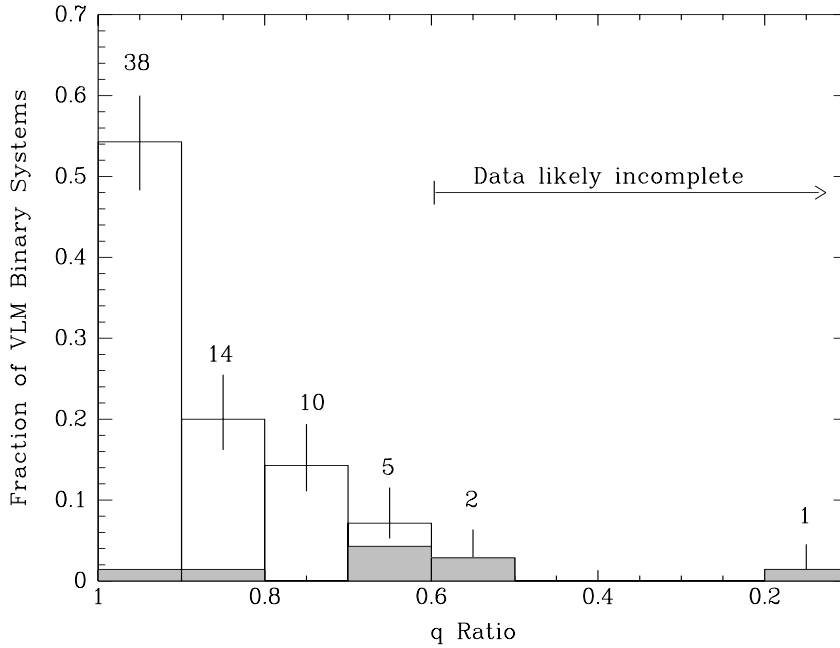


Figure 4.4.: Distribution of mass ratios q for very low-mass binary systems. The shaded area represents the systems with ages < 10 Myr. (Burgasser et al. 2006)

4.2.4. The brown dwarf desert

Radial velocity surveys have revealed very few brown dwarfs among companions of solar-type stars at small separations. For separations less than 3 AU, the frequency of brown dwarf companions is smaller than 1% (e.g. Marcy & Butler 2000). In comparison, the frequency of stellar companions for these separations is about 14% (Duquennoy & Mayor 1991) and the frequency of giant planets around solar-type stars is about $5 \pm 2\%$ (Grether & Lineweaver 2006). At wider separations, brown dwarfs are found with a frequency that is consistent with the relative number of brown dwarfs among isolated objects. Also, brown dwarf companions are more common around low-mass stars. Therefore, there only seems to be a deficiency of brown dwarfs around solar-type stars at small distances.

The knowledge of binary systems are of fundamental importance for the understanding of the star formation process. The explanation of this so-called brown dwarf desert could provide a better understanding about the formation of brown dwarfs in general. Therefore, the brown dwarf desert has attained much interest. The disk masses of solar-type stars are mostly too small for the formation of brown dwarfs through gravitational instabilities.

A possible explanation of the brown dwarf desert is that fragments of a disk can only cool sufficiently fast to condense out at large radii. At smaller radii the fragments bounce and are shredded by tidal forces (Whitworth & Stamatellos 2006). Another explanation

could be that orbital migration causes the brown dwarf desert. Orbital migration might depend on the ratio between the disk mass and the mass of the planet. For a brown dwarf companion of a solar-type star, the orbital migration would become so strong that such an object would fall into the star (Armitage & Bonnell 2003). The scaled-down situation implies that there should be a giant planet desert around brown dwarfs.

4.2.5. Possible planet formation in brown dwarf disks

In the standard model, the formation of giant planets starts with the formation of a rocky core, which subsequently accretes gas from the circumstellar disk. The fact that young brown dwarfs have accretion disks with estimated masses of a few Jupiter masses makes planet formation in their disks possible. Also, the first steps of planet formation, such as grain growth, crystallization and dust settling, were observed in brown dwarf disks (Apai et al. 2005).

The most likely place for a planet to form is the snow radius of the disk. It is interesting that the surface density at the snow radius is similar for disks of brown dwarfs and stars. At radii larger than the snow radius, the frequency of planet formation declines with the decreasing surface density until the surface density is too low for planets to form. A planet formed at the snow radius will be pulled in by tidal interactions and possibly migration due to disk - planet interactions. Therefore, most of the massive planets around brown dwarfs are expected to have periods of 40 days or less. The lower limit for an orbiting period is around 15 hours; for smaller distances the planet would be tidally disrupted.

There are indications of a giant planet companion to the brown dwarf 2MASSW J1207334-393254 (Chauvin et al. 2005). The mass of this companion was derived to be about $5 M_{Jup}$. The semi-major axis was determined to be ≥ 55 AU. Besides this object, no planet of a brown dwarf has been found yet.

4.3. Other means of testing the different formation scenarios

Comparing predicted binary frequencies with the observed one might be the best way to test the standard and the ejection scenario as possible formation mechanisms for brown dwarf formation. However, there are other means of testing the different formation scenarios. In the following, some of the properties are discussed, which also constrain the different formation scenarios under discussion.

Initial mass function

The initial mass function relates the relative number of stars to their mass. If the initial mass function would continue across the sub-stellar border, it would imply a common formation history for stars and brown dwarfs.

It is very difficult to derive a unique initial mass function for brown dwarfs because their mass - luminosity relation is a function of age. The age of individual field brown dwarfs cannot be determined and, thus, the mass cannot be derived. Only in star-forming regions is the age of brown dwarfs known and the initial mass function can be derived.

Observations of brown dwarfs in star-forming regions yield an initial mass function that appears to be continuous across the hydrogen-burning limit, implying that brown dwarfs form like stars.

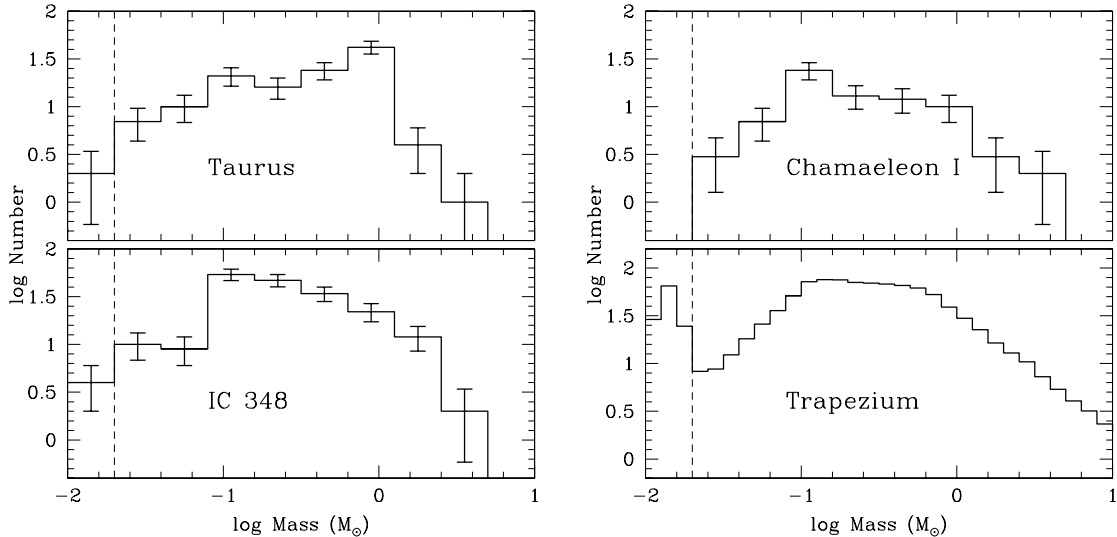


Figure 4.5.: Initial mass functions for Taurus, IC 348, Chamaeleon I and Trapezium. (Luhman et al. 2007)

Kinematics and spatial distribution

Some models for the embryo-ejection scenario predict that brown dwarfs have higher velocity dispersions than stars (e.g. Reipurth & Clarke 2001). Therefore, in star-forming regions brown dwarfs should be more widely distributed than objects with stellar masses. Additionally, the radial velocity distribution function of brown dwarfs should be broader than that of stars. Observations in young star-forming regions, such as Chamaeleon (Joergens & Guenther 2001), show that radial velocities of brown dwarfs are similar to those of stars. Also, brown dwarfs appear to be homogeneously mixed with hydrogen-burning stars (e.g. Luhman 2004b). However, there are new ejection models, which predict that the difference in the kinematics between brown dwarfs and stars are so small that it is almost impossible to detect them. According to these models the main difference is not the velocity but the time of the ejection. Brown dwarfs are ejected at an earlier stage of the evolution than stars.

The observed kinematic properties and spatial distribution are consistent with a common formation mechanism for stars and brown dwarfs. However, they are also consistent with some of the ejection models (e.g. Bate et al. 2003).

Circumstellar disks

The collapse of a cloud core produces a circumstellar disk, due to angular momentum conservation. Infrared excesses have been found in young brown dwarfs down to their lower mass limit of $13 M_J$, which indicate that brown dwarfs have disks (e.g. Apai et al. 2004).

Disk fractions of stars and brown dwarfs appear to be similar. The disk masses derived from observations range from 0.4 to $10 M_{Jup}$ (e.g. Klein et al. 2003). In some of these disks grain growth and settling was observed. Through observations of equivalent widths of $H\alpha$ emission lines, it is known that brown dwarfs accrete material. Accretion rates decrease continuously with mass from stars to brown dwarfs (see figure 4.6). Also, forbidden line emissions are seen, which implies that they have outflows.

The finding of similar disk characteristics for young brown dwarfs and classical T Tauri stars support a common formation history. However, these results do not exclude other formation scenarios. For instance, during formation through embryo-ejection the inner regions of disks can survive.

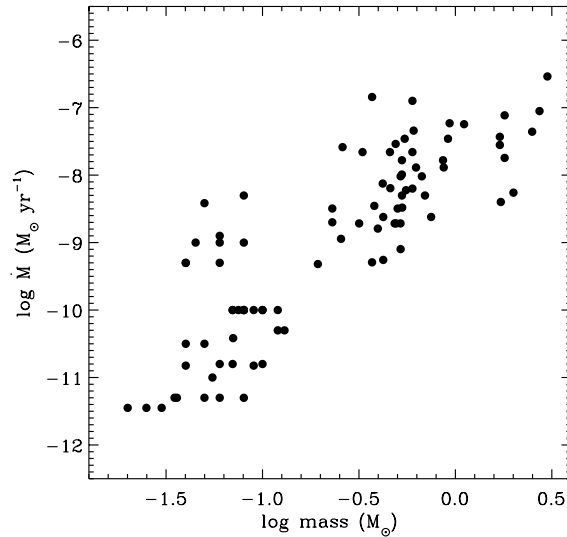


Figure 4.6.: Mass accretion rate as a function of mass. (Luhman et al. 2007)

5. Observation and data reduction

5.1. Sample

In the previous chapters it was shown that a number of different brown dwarf formation scenarios are being discussed. It was shown how binary properties can be used as a diagnostic tool for understanding the formation of brown dwarfs. By deriving the frequency of short-period binary brown dwarfs, the importance of momentum transfer for the formation of brown dwarf binaries can be studied. A radial velocity survey is the most efficient way to find short-period brown dwarf binaries. In this chapter the sample and the data reduction of this present work are presented. In the next chapter the results are shown.

High-resolution spectra of 27 very low-mass stars and brown dwarfs were taken with the cross-dispersed echelle spectrograph UVES at the VLT (Paranal, Chile). The sample contains the most luminous very low-mass stars and brown dwarfs in the southern hemisphere. The objects have spectral types between M6 and L2 and masses $M \leq 0.1 M_{\odot}$. Their V-band magnitude is 15 to 20 mag. Six of these objects are classified as brown dwarfs. Most of the objects are old objects in the field within a radius of 25 pc from our sun. The intrinsic radial velocity variability of old very low-mass stars and old brown dwarfs is very low. Therefore, these objects are highly suitable targets for a search for companions based on radial velocity variation measurements. Four objects are in Upper Scorpius. Upper Scorpius is the OB association closest to our sun. This association lies at a distance of ~ 145 pc and has an age of ~ 5 Myr.

The presence of circumstellar disks around brown dwarfs shows that these very low-mass objects do not show any indications in their earlier stages about whether they will end up as hydrogen-burning stars or as brown dwarfs. Therefore, though most of the objects are very low-mass stars and not brown dwarfs, it is possible to make a conclusion about the binary statistics of such low-mass objects.

The targets were, with some exceptions, observed for at least three nights. Two consecutive spectra were taken for most of the objects, making it possible to calculate the error from the scatter of these two consecutive measurements. The original aim of the survey was to find companions to brown dwarfs and very low-mass stars down to planet sizes. If brown dwarfs and very low-mass stars have giant planets, their periods are estimated to be smaller than 40 days. Because the probability to detect such a planet is highest if the sampling of the observation matches the orbital period, the time-span of the observation for most of the objects is equal or larger than 30 to 70 days.

Table 5.1 lists the observed targets, their spectral types, the number of spectra taken, the observed time-span Δt and the signal to noise of each spectra. The signal to noise was calculated in a region of pseudo-continuum using the IRAF task SPLIT.

Table 5.1.: Sample

Name	Spectral Type ¹	No. of spectra	Δt [d]	S/N
2MASS J08320451-0128360	L1.5	7	56	9, 8, 6, 10, 15, 20, 17
2MASS J09522188-1924319 ²	M7	3	60	39, 29, 22
2MASS J12372705-2117481	M6	7	53	42, 33, 47, 28, 37, 25
2MASSW J2013510-313651	M6	6	72	36, 23, 27, 27, 24, 58
2MASS J20491972-1944324	M7.5	6	28	15, 12, 22, 16, 17, 22
2MASS J20520861-2318096	M7.5	6	28	28, 31, 36, 37, 33, 38
2MASS J21130293-1009412 ³	M6	6	28	20, 13, 15, 18, 21, 16
2MASSW J2135146-315345	M6	6	73	15, 12, 11, 20, 14, 19
2MASSW J2147446-264406	M7.5	6	76	15, 23, 31, 19, 13, 18
2MASSW J2202112-110946	M6.5	6	28	21, 22, 29, 28, 27, 24
2MASSW J2206228-204705 ⁴	M8	6	28	41, 26, 41, 35, 49, 42
2MASS J23062928-0502285	M7.5	1	1	9
BRI B0021-0214	M9.5	6	42	25, 16, 18, 17, 20, 41
BR B0246-1703	M8	4	35	14, 14, 13, 12
BR B1104-1227	M6	3	57	36, 68, 28
DENIS-P J0021.0-4244	M9.5	4	44	18, 14, 15, 13,
DENIS-P J1047.5-1815	L2.5	6	32	14, 13, 10, 15, 12, 15
LHS 2065	M9	6	32	43, 23, 18, 30, 31, 41
LHS 2397a ⁵	M8	8	52	43, 24, 44, 24, 34, 23, 30, 22
LHS 292	M6.5	10	784	18, 19, 21, 18, 15, 19, 18, 16, 18, 19
LHS 3566	M8.5	6	72	15, 15, 35, 21, 17, 19
LP 944-20	M9	23	841	56, 37, 45, 51, 55, 32 24, 19, 43, 11, 22, 21, 30, 30, 23, 28, 29, 21, 36, 25, 31, 32, 26
TVLM 868-110639	M9	6	27	18, 22, 11, 9, 33, 23
UScoCTIO 55 ⁶	M5.5	6	27	19, 19, 29, 25, 28, 20
UScoCTIO 75	M6	6		26, 21, 40, 28, 26, 23
UScoCTIO 85	M6	6	37	31, 38, 23, 14, 30, 25
UScoCTIO 100	M7	6		30, 33, 26, 26, 26, 24

¹ Literature value² SB2 (Reid et al. 2002)³ SB2 (Guenther et al. 2003)⁴ Visuell binary (Close et al. 2003)⁵ Visuell binary (Freed et al. 2003)⁶ Visuell binary (Kraus et al. 2005)

Because the observed objects are very red, a spectrograph setting was used which covers the wavelength region 6600 - 10600 Å using the red arm of the UVES spectrograph. This wavelength region contains the telluric band at 6860 - 6930 Å, which is used as a secondary wavelength reference for the radial velocity measurements. Variations of these telluric lines are caused by the wind in the Earth's atmosphere and are of the order of about 20 m/s (e.g. Balthasar et al. 1982). As will be shown in chapter 6, the typical accuracy of the radial velocity measurement is 0.2 km/s. Thus, the telluric lines are suitable as secondary wavelength reference.

The spectra have been taken with a slit width of 1.2". The spectral resolution obtained is $\lambda/\Delta\lambda = 40,000$. The seeing was $\leq 1.2''$.

5.2. UV-Visual Echelle Spectrograph

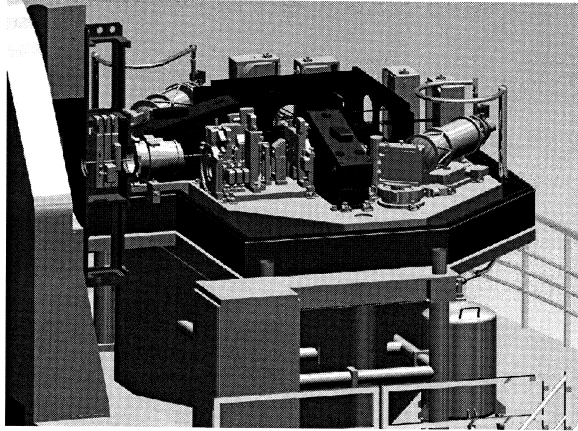
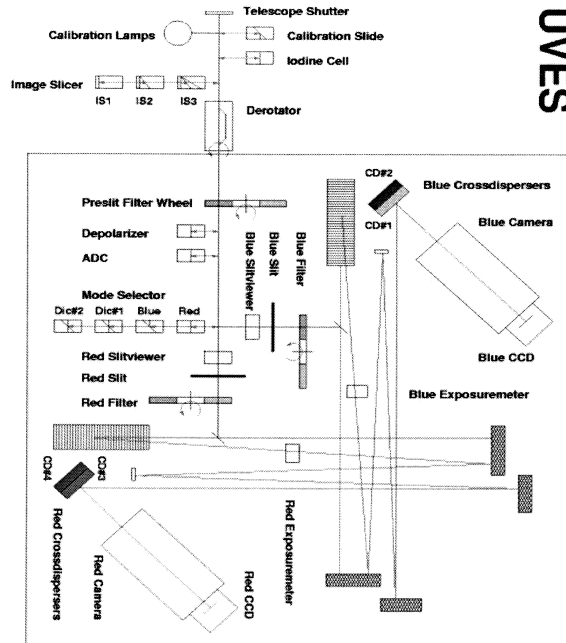


Figure 5.1.: 3-dim CAD view of UVES. (ESO UVES User Manual, 2006)

The UV- and Visual Echelle Spectrograph UVES is located at the Nasmyth platform B of the second Unit Telescope (Kueyen) of the VLT. The VLT is operated by the European Southern Observatory at Paranal, Chile. UVES is a cross-dispersed echelle spectrograph. An echelle spectrograph contains two dispersive elements. In the case of UVES both are gratings, one is the echelle-grating and the other is the crossdisperser grating, which separates the echelle orders. The order separation for the crossdisperser grating corresponds to 10 arcsec.

The light coming from the telescope first passes through the calibration unit which contains calibration lamps, an integrating sphere, relay optics and a mirror slide. The next device is the derotator, which compensates for field rotating. It is an Abbe-Koenig type silica prism that incorporates a lens to create a parallel beam. The slit was positioned so that it was always perpendicular to the horizon. In this way light loss due to differential atmospheric refraction was avoided without using the ADC (two counter-rotating prisms, which compensate for atmospheric dispersion). There is a pupil stop, which is required because the telescope is not baffled. The pupil stop reduces the sky-background.



UVES

Figure 5.2.: Schematic overview of UVES. (ESO UVES User Manual, 2006)

A mode selector is used to choose which arm to operate. One can select the red arm (going straight) or the blue arm (reflected to the right). The red arm operates in the wavelength region 420 - 1100 nm and the blue arm in 300 - 500 nm. Also, the beam can be split and both arms can be used simultaneously. Because the objects in our sample are very red, only the red arm was used.

After the mode selector there is the red and blue slit, respectively. In both spectrograph arms, the beams are reflected by a mirror to the main collimators. The design of the two arms is of the white-pupil type with 200 mm pupils. The collimators each consist of two off-axis parabolic mirrors and two flat mirrors. The collimated beams are dispersed by the echelle R4 gratings. The echelle gratings are 84 cm long and 21 cm wide. These echelle gratings are the largest ever made of this type. They are made of two aligned gratings because single gratings of this size cannot be made.

To maximize the efficiency they are operated in quasi-Littrow mode. This means the angle of incidence and diffraction are equal but in a different plane. About 1% of the light hits the 14 mm gap between the echelle mosaics and is reflected to the exposure meters, which are used to monitor the flux of the observed star. From the echelle gratings the light is sent back to the main collimators and from there the dispersed beams fall on the cross-disperser units. The cross-disperser units are grating turrets with two different gratings mounted back-to-back between which one can choose. The angle of the grating has to be set in accordance to the required wavelength of the central echelle order. From the cross-disperser units the echelle spectra enter the cameras and are recorded on the

CCD detectors. There is one chip (2k x 4k, EEV CCD-44) in the blue arm and two chips (2k x 4k, EEV CCD-44 and MIT/ll CCID-20) in the red arm.

The factors affecting the resolving power are the image quality of the optics, such as the focus and the alignment, CCD effects, such as chip tilt, diffusion of photo-electrons and charge transfer as well as the echelle dispersion. The image quality over the entire spectral range is better than 20 - 30 μm over the full CCD. The maximum resolution is 80,000 in the blue arm, for a slit of 0.4", and 110,000 in the red arm, for a slit of 0.3". The spectral resolution is about 40,000 when a 1 arcsec slit is used. Objects as faint as 18 to 20 mag can be observed with UVES.

5.3. Reduction of the UVES echelle frames

A CCD reduction, to remove the instrumental signatures from the two-dimensional UVES echelle frames, was done with the echelle package of IRAF. For the measurement of the radial velocity, eventually only the frames of the MIT/LL CCID-20 chip were used because this chip has a higher quantum efficiency and less fringing than the second chip.

For every epoch a master bias frame was produced. A bias frame is the read-out of the CCD detector with zero integration time and a closed shutter. All CCD exposures have an offset in order to prevent any problems with the A/D converter during the read-out, in case of counts that are too low. This offset is called bias and needs to be subtracted from all CCD exposures because these electrons were not created by photons from the source. Many bias frames were averaged, thus reducing effects of the read-out noise. Bad pixels were corrected using the procedure CCDPROC. Therefore, a bad pixel mask was created, that is a file containing the positions of all bad lines, bad columns and individual bad pixels. The bad pixels were corrected by linear interpolation from neighboring lines and columns. Because the structure of the bias is only a gradient on the chip, the bias frames were smoothed. Then the overscan was subtracted in order to obtain the master bias.

A master flat was produced from a set of standard flat-fields. A flat-field is a spectrum obtained from a light source without spectral features. It provides information about the response of the detector, such as variations in sensitivity from pixel to pixel, the echelle order shape (blaze function), the presence of bad columns on the detector, fringing, the structures introduced by imperfections of the slit geometry, etc. Science frames need to be corrected through division by the master flat-field. The master frame was created by taking the medium of many flat-field exposures, thus correcting for so-called cosmic rays. These can be genuine cosmic rays but most are locally produced by the decay of radioactive atoms, which are, for example, present in the telescope optics. The bias and overscan were then subtracted. A correction for bad pixels was applied. Finally, the procedure APFLATTEN was used, which models both the profile and overall spectrum shape and removes it from the flat-field, leaving only pixel to pixel variations.

The reference emission-line lamp for the wavelength calibration was a ThAr arc-lamp. The wavelengths of the emission lines are accurately known and are used to transform pixel space into wavelength space. When measuring the radial velocity, additionally, the

telluric lines were used for a more accurate wavelength calibration.

Standard stars are stars for which the flux at each wavelength interval is known. They can be used to determine the response curve of the instrument. This provides a relative flux calibration. Here, the standard star HD 60753, with a spectral type B2III, was used.

From the science spectra the master bias and the overscan were subtracted. Then the frames were divided through the master flat. Scattered light was corrected using the procedure APSCATTER. Scattered light is caused by the scattering and reflections at the optical components of the spectrograph. The amount of scattered light is determined by measuring the flux between the orders. To remove the scattered light the orders of the spectrum have to be found. This was done for one spectrum of a bright star with the procedure APALL and the parameters of the orders were saved to database for later reference. Using the reference spectrum the position of the spectral orders in each frame were again derived, allowing for shifts of the whole spectrum on the detector. APSCATTER was used to measure and fit the scattered light in between the orders and subtract it from the spectra. Bad pixels were corrected using the procedure CCDPROC. Cosmic rays were corrected using the task COSMICRAYS. The detected cosmic rays were replaced by the average of the surrounding pixels. With the procedure APALL the orders were extracted. The spectrum spans over several columns on the detector. With APALL they were added to a one-dimensional spectrum. Simultaneously, the sky was subtracted, that is the light which falls into the spectrograph besides the light of the object. With the procedure ECIDENTIFY, the ThAr emission lines of one spectrum were identified interactively and the dispersion relation in the spectrum was determined. The results were saved for further reference. The procedure ECREIDENTIFY was used to reidentify the features in all other ThAr spectra with the help of the reference spectrum and to determine a dispersion relation for each spectra. With the procedure REFSPECTRA, each science frame was assigned to a reference ThAr spectrum. This ThAr spectrum was then used to calculate the dispersion solution of the object spectra. With the procedure DISPCOR, the object spectra were dispersion corrected. To correct for the CCD sensitivity variations in the science frames, a flat-field was reduced exactly like a science spectrum as described before, only the sky subtraction was omitted. The science spectra were divided by this frame. With the procedure SCOMBINE, the orders were merged together. The average of pixels at the same dispersion coordinate was taken. Then the spectra were corrected for the extinction of the atmosphere using the procedure CALIBRATE. The factor of the extinction correction is $10^{0.4 \times \text{airmass} \times \text{extinction}}$, where the extinction value is an interpolated value from an extinction file, which had to be specified. Finally, the spectra were flux calibrated with the standard star HD 60753. The true flux of HD 60753 was divided by the observed one. All science spectra were multiplied with this factor and, thus, the true fluxes of the objects were obtained.

6. Results of the UVES observations

6.1. Spectral Types

The spectrum of M-dwarfs is characterized by the presence of molecular TiO bands. The TiO band-strengths are primarily temperature dependent. They can be used to classify the spectral types of M-dwarfs. The TiO band-strengths are barely visible at spectral type K7 and increase steadily until they dominate the spectrum among late M-dwarfs. For the latest M spectral types, the strength of the TiO bands decreases, because the atmosphere gets gradually depleted of Ti due to condensation.

Band-strengths can be quantified using indices. Indices are defined as $\text{Index} = F_W / F_{Cont}$. F_W is the mean flux measured in a region that contains an atomic or molecular feature and F_{Cont} is the mean flux in a nearby region that approximates the local pseudo-continuum. Here the indices TiO 5 and VO-a were chosen for the determination of the spectral type, because of all available indices they do correlate best with the spectral type (Cruz & Reid 2002). Table 6.1 shows in which wavelength regions F_W and F_{Cont} have to be measured in order to calculate the indices TiO 5 and VO-a.

Table 6.1.: Indices TiO 5 and VO-a

Index	F_W	F_{Cont}
TiO 5	7126 - 7135 Å	7042 - 7046 Å
VO-a	Sum of 7350 - 7370 Å and 7550 - 7570 Å	7430 - 7470 Å

The spectral type relations from Cruz and Reid (2002) were used for the determination of the spectral types of the observed objects.

The spectral type relations for TiO 5 are:

$$\text{Sp} = -10.775 \times (\text{TiO 5}) + 8.2, \text{ for } \text{TiO 5} \leq 0.75 \text{ and } \text{Sp} = \text{K7} - \text{M7} \quad (6.1)$$

$$\text{Sp} = 5.673 \times (\text{TiO 5}) + 6.221, \text{ for } \text{TiO 5} \geq 0.3 \text{ and } \text{Sp} \geq \text{M7} \quad (6.2)$$

The spectral type relations for VO-a are:

$$\text{Sp} = 10.511 \times (\text{VO-a}) - 16.272, \text{ for } \text{Sp} \leq \text{M9} \quad (6.3)$$

$$\text{Sp} = -7.037 \times (\text{VO-a}) + 26.737, \text{ for } \text{Sp} \geq \text{M9} \quad (6.4)$$

Both indices are double-valued. TiO 5 reverses in strength at about M7 and VO-a at about M9. The fact that the two indices reverse at different spectral types allows the calculation of the spectral type. In the end, only the index TiO 5 is used to assign a

spectral type to each object because the VO bands are more diffuse and, thus, not as precise. Nevertheless, VO-a was crucial to find out which of the two possible spectral types derived with the index TiO 5 is the correct one. The spectral type of each object was obtained by rounding the value derived with TiO 5 to the nearest half sub-class. The uncertainty of the derived spectral types is, therefore, ± 0.25 sub-classes. Table 6.2 lists the index values for TiO 5 and VO-a and the resultant spectral types for both indices. The last column contains the spectral type that was assigned to each object as described above. The derived spectral types are, within one subclass, in accordance with the literature values given in table 5.1.

Figure 6.1 shows the spectral type against TiO 5 and against VO-a for all objects. The two red points indicate the two different spectral types derived for 2MASSW J2202112-110946. This object shows a change in spectral type from M6.476, during the first two observation days, to M5.598, during the third observation day. This corresponds to an increase of the effective temperature of about 134 K. The inspection of the Ca II line at 8662.14 Å showed that this increase of temperature is due to a flare, as can be seen in figure 6.2.

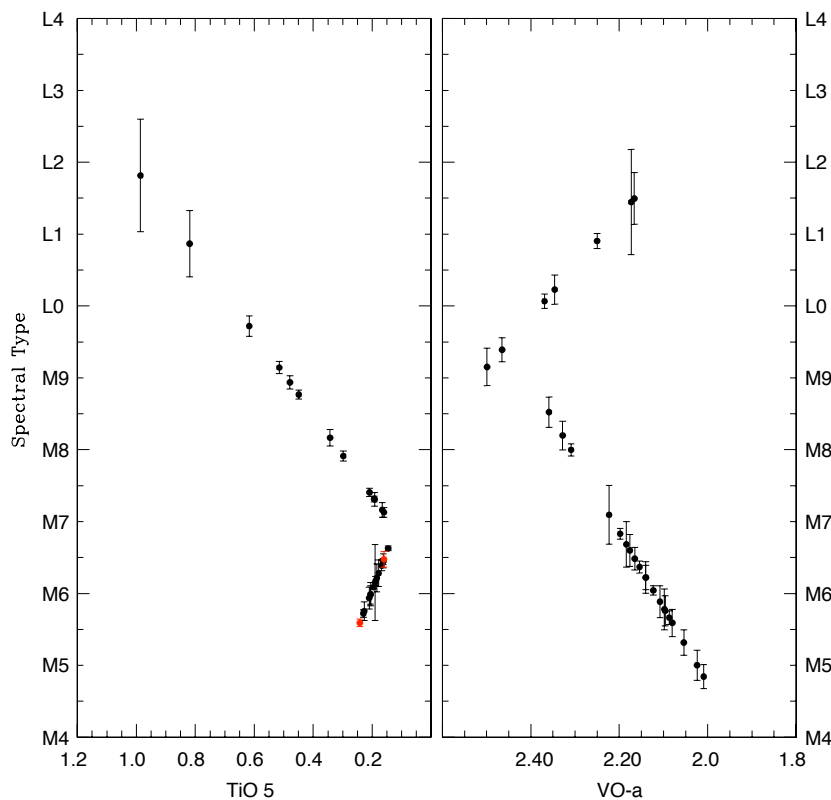


Figure 6.1.: TiO 5 and VO-a spectral type calibration.

Table 6.2.: Spectral types

Name	TiO 5	Spectral Type derived with TiO 5	VO-a	Spectral Type derived with VO-a	Spectral Type ¹
2MASS J08320451-0128360	0.986±0.138	L1.815±0.783	2.173±0.104	L1.446±0.732	L2
2MASS J09522188-1924319	0.196±0.002	M6.088±0.022	2.154±0.008	M6.369±0.084	M6
2MASS J12372705-2117481	0.210±0.014	M5.937±0.151	2.123±0.006	M6.043±0.063	M6
2MASSW J2013510-313651	0.188±0.006	M6.174±0.065	2.096±0.020	M5.759±0.210	M6
2MASS J20491972-1944324	0.162±0.009	M6.454±0.097	2.184±0.030	M6.684±0.315	M6.5
2MASS J20520861-2318096	0.163±0.004	M6.444±0.043	2.087±0.009	M5.664±0.095	M6.5
2MASS J21130293-1009412	0.168±0.007	M6.390±0.075	2.080±0.018	M5.591±0.189	M6.5
2MASSW J2135146-315345	0.178±0.017	M6.282±0.183	2.108±0.021	M5.885±0.221	M6.5
2MASSW J2147446-264406	0.166±0.018	M7.163±0.102	2.223±0.039	M7.094±0.410	M7
2MASSW J2202112-110946	0.160±0.010	M6.476±0.108	2.140±0.021	M6.222±0.221	M6.5
2MASSW J2206228-204705	0.160±0.012	M7.129±0.068	2.198±0.007	M6.831±0.074	M7
2MASS J23062928-0502285	0.193±0.007	M7.316±0.040	2.309±0.008	M7.998±0.084	M7.5
BRI B0021-0214	0.617±0.025	M9.721±0.142	2.250±0.015	L0.904±0.106	M9.5
BR B0246-1703	0.209±0.010	M7.407±0.057	2.328±0.019	M8.198±0.260	M7.5
BR B1104-1227	0.206±0.012	M5.980±0.129	2.176±0.021	M6.600±0.221	M6
DENIS-P J0021.0-4244	0.515±0.015	M9.143±0.085	2.346±0.029	L0.228±0.204	M9
DENIS-P J1047.5-1815	0.819±0.081	L0.869±0.460	2.166±0.051	L1.495±0.359	L1
LHS 2065	0.479±0.016	M8.938±0.091	2.465±0.024	M9.391±0.169	M9
LHS 2397a	0.298±0.012	M7.912±0.068	2.359±0.020	M8.523±0.210	M8
LHS 292	0.146±0.003	M6.627±0.032	2.165±0.015	M6.484±0.158	M6.5
LHS 3566	0.192±0.017	M7.310±0.096	2.098±0.027	M5.780±0.284	M7.5
LP 944-20	0.449±0.011	M8.768±0.062	2.499±0.037	M9.152±0.260	M9
TVLM 868- 110639	0.343±0.020	M8.167±0.113	2.369±0.014	L0.066±0.099	M8
UScoCTIO 55	0.227±0.012	M5.754±0.129	2.009±0.016	M4.845±0.168	M6
UScoCTIO 75	0.230±0.005	M5.722±0.054	2.024±0.020	M5.002±0.210	M5.5
UScoCTIO 85	0.184±0.018	M6.217±0.194	2.140±0.016	M6.222±0.168	M6
UScoCTIO 100	0.205±0.015	M5.991±0.162	2.054±0.017	M5.318±0.179	M6

¹ The errors are ± 0.25 subclasses

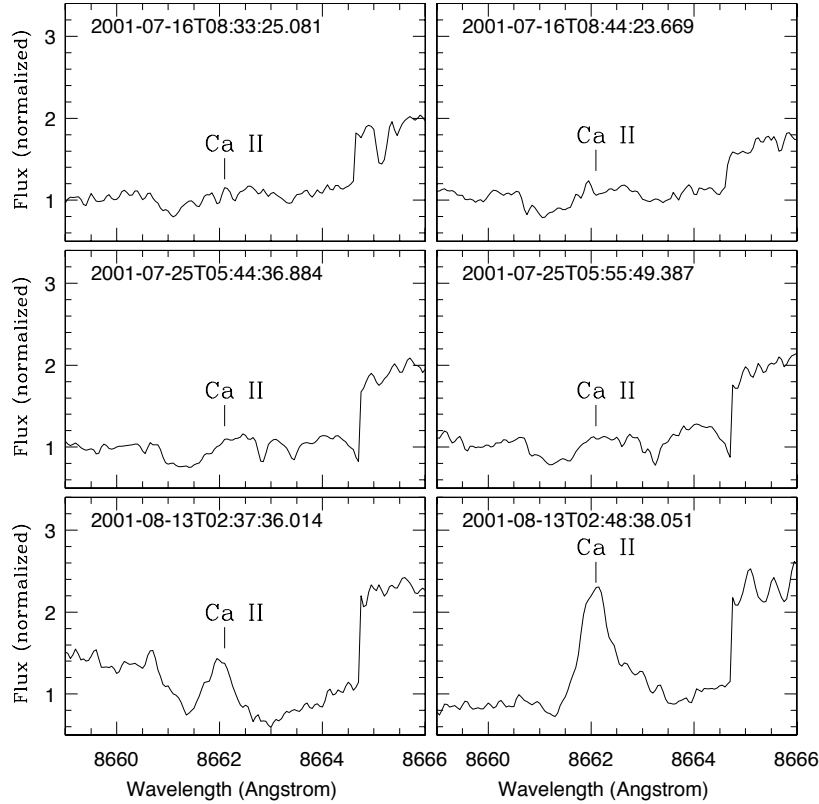


Figure 6.2.: Ca II line at 8662.14 Å of 2MASSW J2202112-110946 showing a flare-like event.

6.2. Temperatures

To determine the temperature, a temperature - spectral type relation was derived by interpolating the data from Golimowski et al. (2004). The fit of the data with a polynomial of third order, as seen in figure ??, gives the relation:

$$T_{\text{eff}} = 3980.65 - 266.96 \times \text{Sp} + 12.16 \times \text{Sp}^2 - 0.30 \times \text{Sp}^3. \quad (6.5)$$

The derived temperatures of the objects are listed in table 6.3. The errors of the temperatures given there refer to the 0.25 subclasses error in calculating the spectral types. The real variation of the temperature of these objects is only about 10 to 40 K over the whole disk. Only 2MASSW J2202112-110946 has a temperature variation of about 134 K, which is due to a flare. The amazingly constant temperatures of these objects show that observed radial velocity variations are unlikely to be due to activity like spots on these objects.

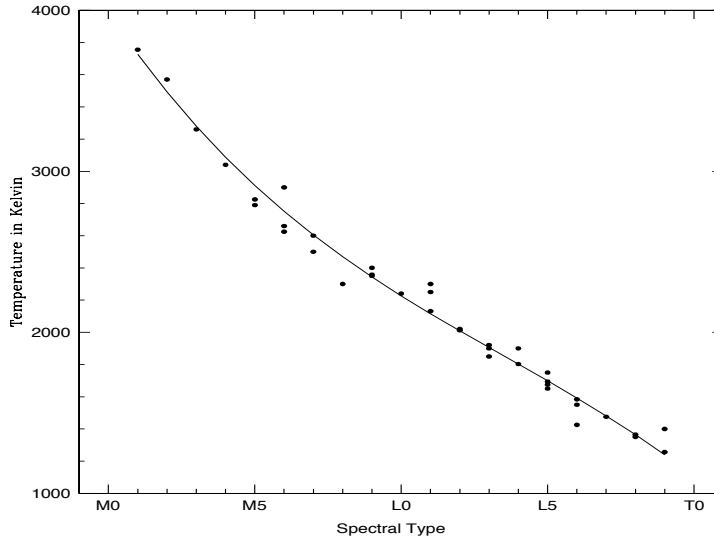


Figure 6.3.: Temperature - spectral type relation derived with data from Golimowski et al. (2004).

6.3. Masses

The object masses were calculated using the models from Chabrier et al. (2000) and Baraffe et al. (2003). Figure ?? shows the mass - temperature relations for the COND and DUSTY models for different ages. The COND models assume a rapid settling of the grains below the photosphere. Therefore, there is no grain absorption near the photosphere. In contrast, in the DUSTY models dust grains are suspended in the atmosphere.

Most of the observed objects have masses $M \geq 0.08 M_{\odot}$. In this mass range there are only marginal differences between the COND and the DUSTY models. For ages ≥ 1 Gyr there are also only very small mass differences for objects with the same temperature but with different ages. Object masses for an age of 0.5 Gyr are about $\lesssim 0.01 M_{\odot}$ smaller than an older object with the same temperature. Only for objects with ages of 0.1 Gyr are the derived masses significantly different from masses of older objects. For instance, for spectral type M6, masses calculated for an age of 0.1 Gyr are about $\sim 0.03 M_{\odot}$ smaller than for an age of 0.5 Gyr.

For free-floating brown dwarfs it is not possible to derive the age and, therefore, the mass exactly. However, it is very unlikely that field objects are much younger than 0.5 Gyr. Therefore, the masses for the field objects were calculated for an age of 1 Gyr using the DUSTY model. The maximum error would be $\lesssim 0.01 M_{\odot}$ when calculating the masses with the models for an age of 0.5, 5 or 10 Gyr or using the COND model.

The relation between the temperature and the mass for an age of 1 Gyr and the DUSTY model is given through the equation:

$$M_1^D = -0.156 + 2.809 \times 10^{-4} \times T_{\text{eff}} - 1.252 \times 10^{-7} \times T_{\text{eff}}^2 + 2.055 \times 10^{-11} \times T_{\text{eff}}^3. \quad (6.6)$$

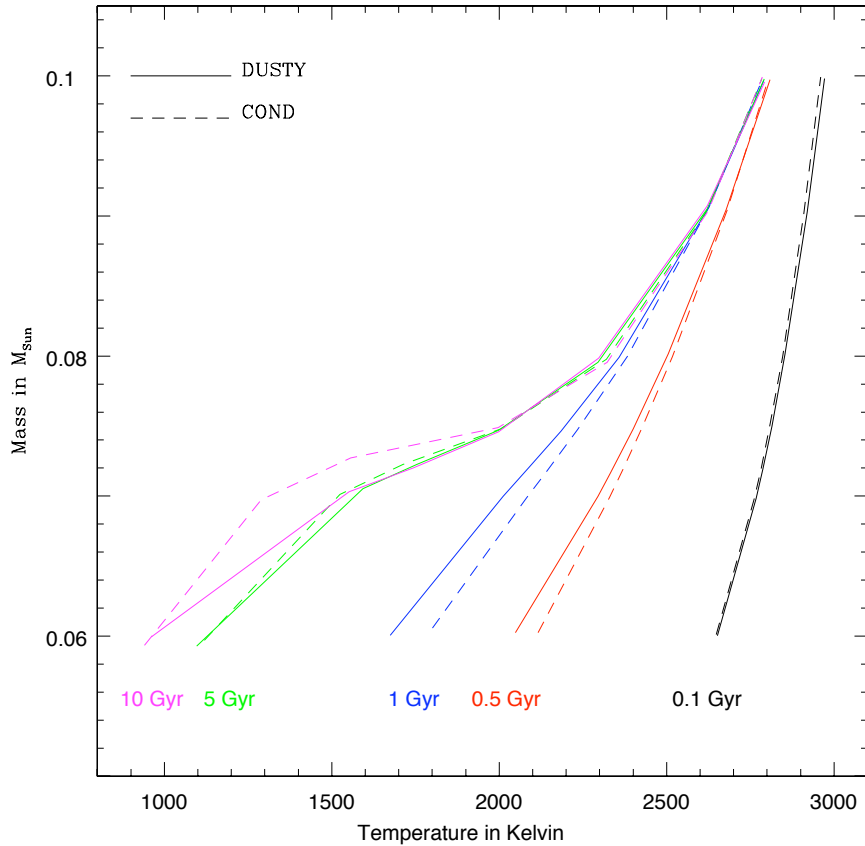


Figure 6.4.: Mass - temperature relation for different ages with the COND and DUSTY models. Derived with the models from Chabrier et al. (2000) and Baraffe et al. (2003).

Because Upper Scorpius is a star forming region with an age of 5 Myr, the masses for the four objects in Upper Scorpius were calculated with the DUSTY model for an age of 0.1 Gyr (no model with a younger age was available). The relation between the temperature and the mass in this case is:

$$M_{0.1}^D = -3.566 + 4.227 \times 10^{-3} \times T_{\text{eff}} - 1.668 \times 10^{-6} \times T_{\text{eff}}^2 + 2.222 \times 10^{-10} \times T_{\text{eff}}^3. \quad (6.7)$$

The age for LP 944-20 is estimated to be between 320 and 659 Myr (see chapter 7). Therefore, the mass was calculated with the DUSTY model for 0.5 Gyr. The corresponding mass - temperature relation is:

$$M_{0.5}^D = -0.105 + 1.885 \times 10^{-4} \times T_{\text{eff}} - 8.342 \times 10^{-8} \times T_{\text{eff}}^2 + 1.506 \times 10^{-11} \times T_{\text{eff}}^3. \quad (6.8)$$

The derived masses are listed in table 6.3.

Table 6.3.: Temperature and mass

Name	Spectral Type	T_{eff} [K]	Mass [M_{\odot}]
2MASS J08320451-0128360	L2	2010±210	0.07
2MASS J09522188-1924319	M6	2750±150	0.10
2MASS J21130293-1009412	M6.5	2680±160	0.09
2MASS J12372705-2117481	M6	2750±150	0.10
2MASSW J2013510-313651	M6	2750±150	0.10
2MASS J20491972-1944324	M6.5	2680±160	0.09
2MASS J20520861-2318096	M6.5	2680±160	0.09
2MASSW J2135146-315345	M6.5	2680±160	0.09
2MASSW J2147446-264406	M7	2600±160	0.09
2MASSW J2202112-110946	M6.5	2680±150	0.09
2MASSW J2206228-204705	M7	2600±160	0.09
2MASS J23062928-0502285	M7.5	2540±160	0.09
BRI B0021-0214	M9.5	2280±180	0.08
BR B0246-1703	M7.5	2540±160	0.09
BR B1104-1227	M6	2750±150	0.10
DENIS-P J0021.0-4244	M9	2340±180	0.08
DENIS-P J1047.5-1815	L1	2120±200	0.07
LHS 2065	M9	2340±180	0.08
LHS 2397a	M8	2470±170	0.08
LHS 292	M6.5	2680±160	0.09
LHS 3566	M7.5	2540±160	0.09
LP 944-20 ¹	M9	2340±180	0.07
TVLM 868- 110639	M8	2470±170	0.08
UScoCTIO 55	M6	2750±150	0.07
UScoCTIO 75	M5.5	2830±150	0.08
UScoCTIO 85	M6	2750±150	0.07
UScoCTIO 100	M6	2750±150	0.07

¹ For mass and temperature by other authors, see chapter 7.

6.4. Radial velocities

Spectroscopic binaries are binaries which cannot be spatially resolved and, therefore, visually appear to be single stars. They are detected to be binaries through radial velocity variations. These are determined from the Doppler shift of their spectral features. In some cases, two sets of spectral lines can be observed with a variable Doppler shift in each. Such a system is called a double-lined spectroscopic binary (SB2). When one star is much brighter than the other the spectrum of the fainter star is lost in the spectrum of the brighter one. This type of system is called single-lined spectroscopic binary (SB1). In the spectra of a single-lined spectroscopic binary, the binary nature is still detectable from the variable Doppler shift of the single lines.

The probability of detecting radial velocity variability of a binary system depends on the accuracy of the measurement and the time-span of the observations. The longer the time-span the larger the binary separation that can be found. The efficiency of finding spectroscopic binaries is the highest when the observational time-span is at least half the orbital period.

To calculate the radial velocities of the observed objects a FORTRAN program was written, which fits the observed spectra with templates. The templates used are spectra calculated by Peter Hauschildt. They were calculated for temperatures of 2000, 2300 and 2600 K and a $\log(g) = 5.5$ (g in cms^{-2}). These template spectra were calculated with the so-called COND model. In this model there are no dust grains suspended in the atmosphere.

For the determination of the radial velocity of an object it is important that the template contains the same lines as the observed spectrum. It is less important that the strength of the lines is the same. In practice it is known that templates with deeper lines are better than those with shallower ones. When deriving the radial velocity one could either use observed or calculated spectra of an object with similar spectral type. The problem with brown dwarfs is that they are very faint. It is, therefore, very difficult to obtain a spectrum of high signal to noise ratio. Because theoretical spectra are noise-free they are much better templates than observed spectra, even if the strengths of individual lines differ from the observed ones.

For each object the template was selected which matches closest the temperature of the object. For the measurements of the Doppler shifts, two wavelength regions were chosen. The criteria, for selecting these wavelength regions, were that they are not affected by telluric lines and that they have strong absorption features. The first region contains the wavelengths from 6935 to 7160 Å, with strong TiO bands at 7054.5, 7059.2, 7087.9, 7093.1, 7124.9, 7125.6 and 7130.4 Å. VO produces a more diffuse absorption. There are band-heads in this region at 6951.6, 7011.0, 7070.2 and 7131.7 Å. The second region is the wavelength region from 7660 to 8100 Å, with the atomic K I lines at 7664.9 and 7699.0 Å and the Rb I lines at 7800.2 and 7947.6 Å. There is also a Ba I line at 7911.3 Å.

Figure 6.5 and 6.6 show the chosen wavelength regions with the most prominent band-heads and lines.

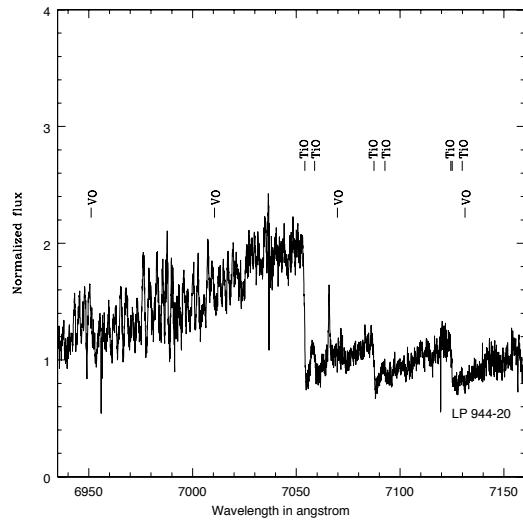


Figure 6.5.: Wavelength region 6935 to 7160 Å.

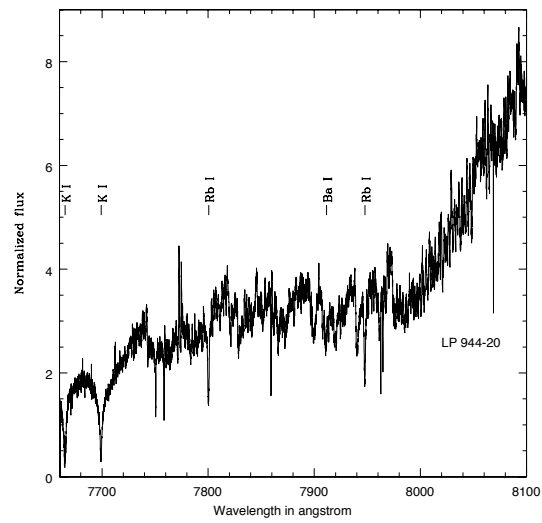


Figure 6.6.: Wavelength region 7660 to 8100 Å.

The wavelengths of the templates were selected to be 6800 - 7300 Å and 7550 - 8250 Å, respectively. In figure 6.7 and figure 6.8 parts of a template (black) and a corresponding science spectrum (red) are shown. In this case the template is a calculated spectrum for a temperature of 2300 K, whereas the science spectrum is one of the spectra obtained of LP 944-20, which has a temperature of approximately 2300 K.

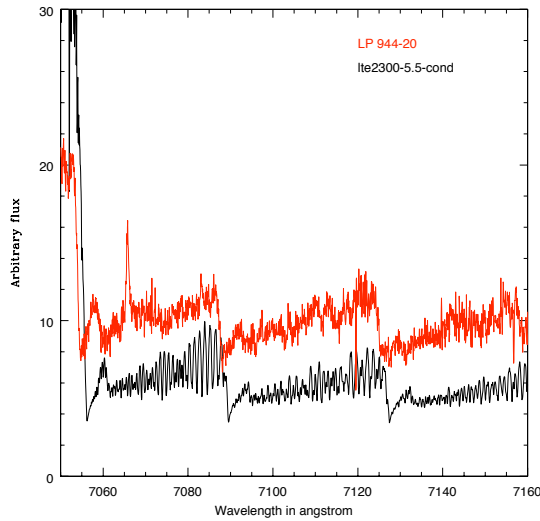


Figure 6.7.: Part of the first selected region (6935 - 7160 Å).

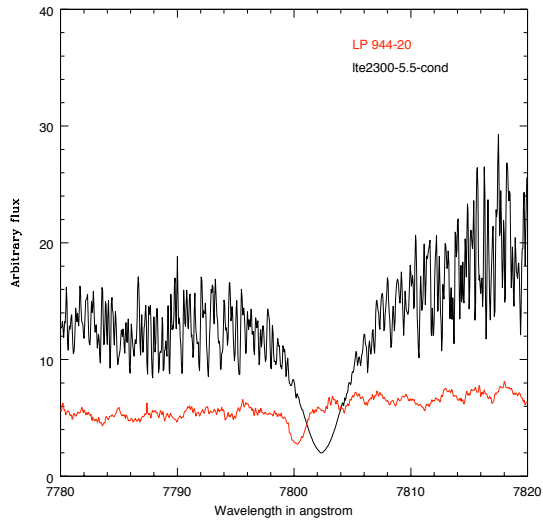


Figure 6.8.: Part of the second selected region (7660 - 8100 Å).

The program shifts the selected part of the spectrum against the appropriate template in steps of one pixel. For each step the difference between the observed spectrum and the template is calculated by subtracting the value of the two spectra for all pixels and then adding up all these differences. In this way, for each pixel-step one value (the sum of the differences) was obtained. An interpolation between all values of the sum of the differences was done in steps of 1/100th pixel. This data was displayed as a graph from where the radial velocity was derived by determining the minimum with a Gaussian fit using the IRAF procedure SPLOT. One example can be seen in figure 6.9. The results do not change if no interpolation is carried out because SPLOT also does an interpolation when fitting the profile. Therefore, the fitted Gaussian function does not differ if the data is oversampled or not.

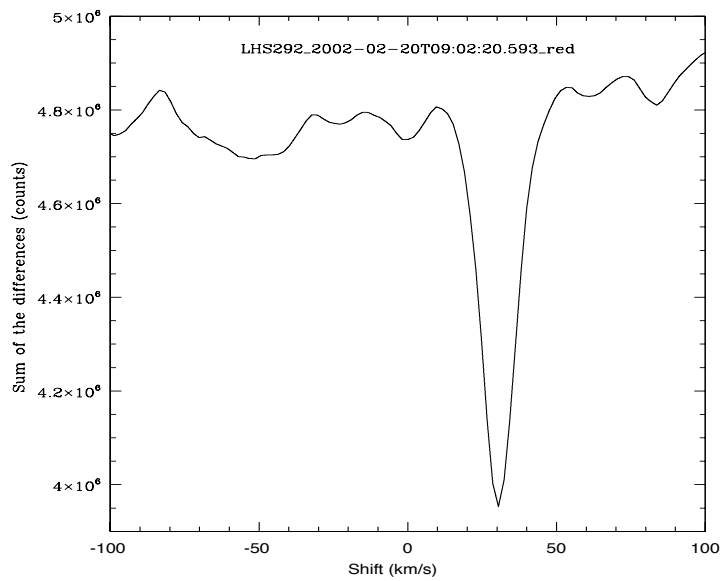


Figure 6.9.: Sum of the differences plotted over the shift for LHS 292. From curves like this the radial velocity was derived by determining the minimum by a Gaussian fit.

Guiding errors or differences in the light path of the calibration lamps and the stellar spectra lead to errors of the wavelength calibration. To achieve a high wavelength and therefore high radial velocity precision, the telluric O₂ lines of the B-band, which is centered at 6880 Å, were used as a secondary wavelength reference. The lines were cross-correlated with the spectra and the obtained shift was taken into account for the calculation of the radial velocity measurement.

With the procedure RVCORRECT, the Heliocentric Julian Date was derived from the Universal Time. Because of the Earth's orbit around the Sun, the Earth can be several light minutes closer or further away from the observed object. Therefore, the time of observation was corrected for the light travel difference to the Sun. RVCORRECT was

also used to apply a heliocentric correction to the observed radial velocities. The observed radial velocity was corrected for the rotation of the Earth (diurnal velocity), the motion of the Earth about the Earth - Moon barycenter (lunar velocity), the motion of the Earth - Moon barycenter about the Sun (annual velocity), and the motion of the Sun (solar velocity). The correction does not include the perturbation of the other planets and also not the nutation. The accuracy of this correction is better than 0.005 km/s.

Different errors were taken into account for deriving the overall error of the radial velocity measurement. First, for each spectrum two different sections were used to obtain the radial velocity. This provides two values for the radial velocity for each spectrum, making it possible to calculate an error of the measurement. Additionally, every Gaussian fit was made three times at different positions around the minimum, providing an error. The error from the secondary wavelength calibration was also taken into account. With a few exceptions, two consecutive spectra of each object were taken. This provides an error of the radial velocities from the scatter of these two measurements. A radial velocity accuracy of 0.1 km/s to 1.4 km/s was achieved, depending of the S/N of the individual spectra. This precision is sufficient to detect objects down to a few Jupiter masses. The fit in the wavelength region 7660 to 8100 Å is better than the fit in the wavelength region 6935 to 7160 Å because in the former one atomic spectral lines are fitted against each other, whereas in the latter one the TiO band-heads are fitted, which are less precise.

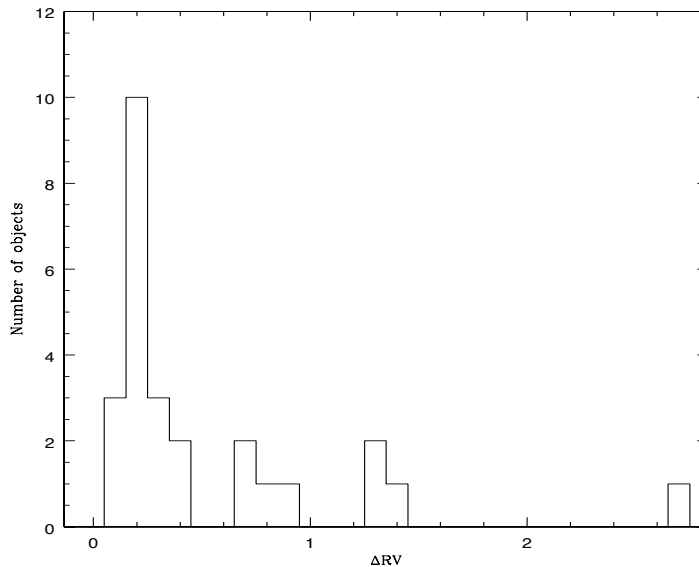


Figure 6.10.: Accuracy of the radial velocity measurement.

The amplitude of the radial velocity variation of a planet orbiting a brown dwarf is much larger than the same planet orbiting a star due to the smaller mass of the brown dwarf. If brown dwarfs have giant planets, their orbital periods should be between 15 hours and 40 days. A period of 40 days corresponds to a planet which formed at the snow

radius. Planets with an orbital period smaller than 15 hours would be tidally disrupted, due to their small distance to the primary object. A planet of $1 M_{Jup}$ in a circular orbit of 40 days around a $0.07 M_{\odot}$ brown dwarf would induce radial velocity variations with an amplitude of 0.2 km/s. An object at the stellar/sub-stellar border with a mass of $0.013 M_{\odot}$ around the same object would induce a radial velocity variation of 2.4 km/s. A companion of $0.07 M_{\odot}$ in circular orbit around a $0.07 M_{\odot}$ brown dwarf with a period of 40 days would cause a radial velocity variation of 9.0 km/s. For smaller periods or larger eccentricities the radial velocity variations would be even larger.

A criteria had to be found when the observed radial velocity variations are significant. The average of the radial velocity of two consecutive spectra was taken. The standard deviation over the whole observational time-span of these averaged radial velocities was calculated and compared with the error of the single radial velocity measurements. A radial velocity variability is classified as significant if the scattering of the measured radial velocity, over the whole observation period, is at least two times larger than the scatter of the single data points. This is a very conservative method. That means that the measured radial velocity variation was classified as significant if the measured variation was larger than 95.4% (2σ) of what would be measured randomly assuming no radial velocity variation and a normal distribution with the given uncertainty for that object. Thus, an object which shows 2σ variations is very likely to be variable.

In the following, the spectroscopic and visuell binaries in this sample are discussed.

6.4.1. The spectroscopic binaries

Two spectroscopic binaries, 2MASS J21130293-1009412 and 2MASS J09522188-1924319, were confirmed. This yields a close binary frequency of 7.4%. The sampling error is $\sigma = \sqrt{np(1-p)}$, where n is the number of objects and p the binary probability. Thus, the close binary frequency of this sample is $7.4 \pm 1.4\%$.

2MASS J09522188-1924319

Reid et al. (2002) found 2MASS J09522188-1924319 to be a spectroscopic binary. Also, in the UVES data it can be clearly seen that it is a spectroscopic binary. The variation of the radial velocity is $\sigma_{RV} = 4.48$ km/s. That variation is significantly larger than the error of the measurement $\Delta RV = 0.19$ km/s. In the graphs one can see one prominent line with a bulge. Therefore, it can be concluded that one of the objects is brighter than the other. Using evolutionary tracks from Chabrier et al. (2000), the mass derived for the primary, based on the UVES data, is $0.1 M_{\odot}$. The mass for the companion is set to be $0.09 M_{\odot}$. A round orbit and an inclination of $i = 52^{\circ}$ are assumed. With equation 6.14 one can then calculate an upper limit for the orbital period of $P \leq 19.4$ d.

2MASS J21130293-1009412

Guenther and Wuchterl (2003) found 2MASS J21130293-1009412 to be a binary. In the graph of the sum of the differences it can be very clearly seen that it is a binary. On the third night of observation one sees two peaks with a difference in radial velocity

of $\sigma_{RV} = 5.99$ km/s. The error of the measurement is only $\Delta RV = 0.20$ km/s. The two peaks have about the same strength. This indicates that the objects have equal luminosities and therefore equal masses. From the UVES data, a mass of the primary of $0.09 M_{\odot}$ was derived using evolutionary tracks from Chabrier et al. (2000). Assuming a round orbit and an inclination of $i = 52^{\circ}$, this yields (equation 6.14) an upper limit for the orbital period of $P \leq 13.2$ d.

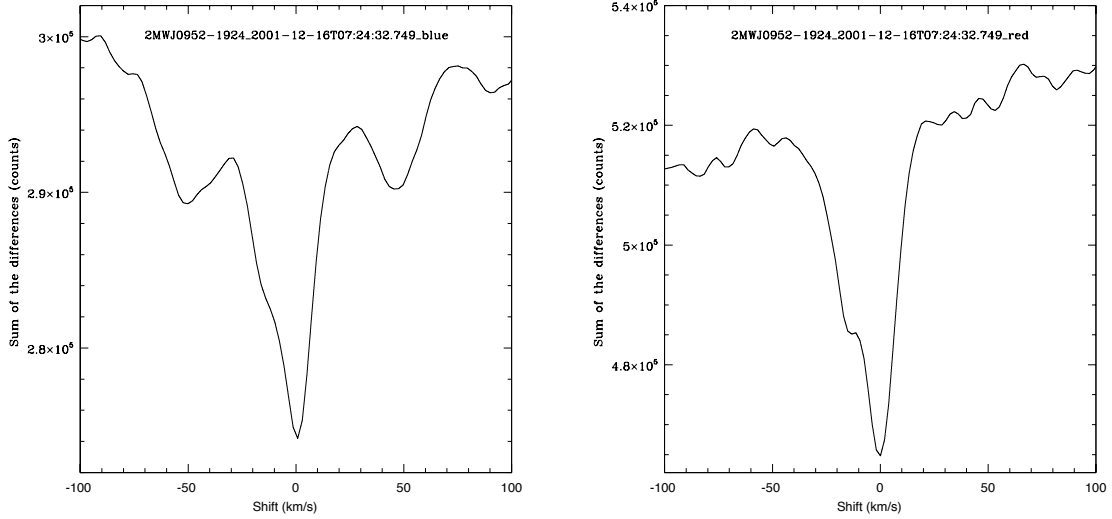


Figure 6.11.: Graphs of the sum of the differences for 2MASS J09522188-1924319 for both selected regions.

6.4.2. The visuell binaries

There are three known visuell binaries in the sample. All of them were detected to be visuell binaries after the UVES data were taken.

2MASSW J2206228-204705

Close et al. (2003) found 2MASSW J2206228-204705 to be a visuell binary. The distance of this object was estimated to be 26.7 ± 4.5 pc. The projected separation is 4.4 ± 0.7 AU. The period was estimated to be 22^{+10}_{-5} yr. Both objects have a spectral type of M8 and the masses are estimated to be $0.092 M_{\odot}$ and $0.091 M_{\odot}$. In the UVES data no significant radial velocity variation can be seen.

LHS 2397a

The binary nature of LHS 2397a was revealed by Freed et al. (2003). This field object lays at a distance of 14.3 ± 0.4 pc. The projected separation is 3.86 ± 0.18 AU. The period is estimated to be 22 ± 3 yr. The primary has a spectral type of M8 and the

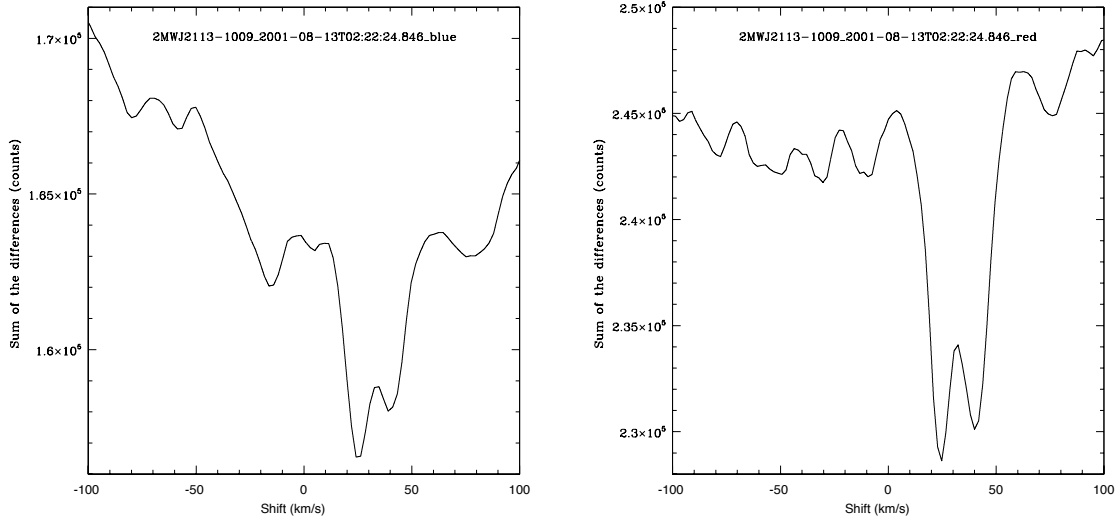


Figure 6.12.: Graphs of the sum of the differences for 2MASS J21130293-1009412 for both selected regions.

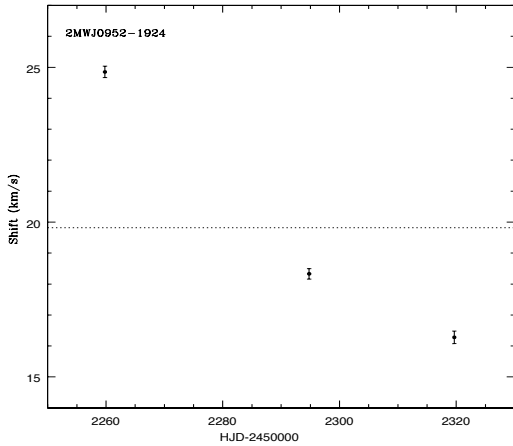


Figure 6.13.: Radial velocities of 2MASS J09522188-1924319.

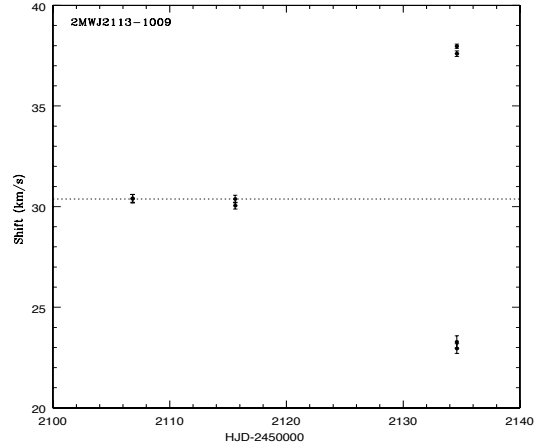


Figure 6.14.: Radial velocities of 2MASS J21130293-1009412. On the third night of observation the radial velocity values of both peaks are shown.

spectral type of the companion was estimated to be L7.5. The masses were derived to be $0.090 M_{\odot}$ and $0.068 M_{\odot}$.

In the UVES data, this object has a radial velocity variation of 1σ . One can see in the graph of the sum of the differences that the peak is somewhat broadened and there are

little bumps in the wings of the peak that do change. The radial velocity measurements show a variability that implies that the telescope sometimes points on the primary star and sometimes on the companion.

Knowing that this object is a binary, the sensitivity of this work can be tested. A binary with object masses of $0.090 M_{\odot}$ and $0.068 M_{\odot}$ and a separation of about 4 AU is on the limit of being detectable.

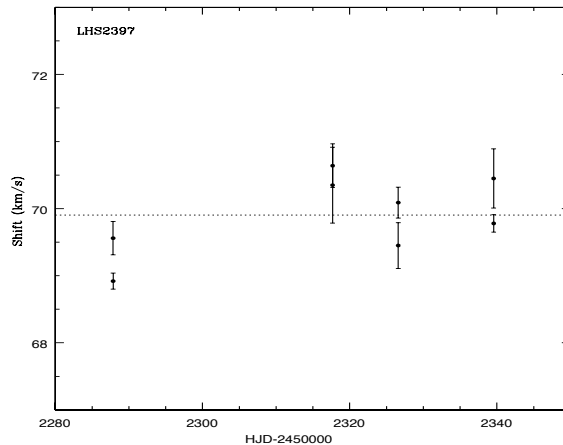


Figure 6.15.: Radial velocities of LHS 2397a.

UScoTIO 55

This object in Upper Scorpius was found to be a binary by Kraus et al. (2005). The distance is 14.5 ± 2 pc. The projected separation is 17.63 ± 0.09 AU. They determined the masses to be $0.1 \pm 0.03 M_{\odot}$ and $0.07 \pm 0.02 M_{\odot}$. The spectral types are estimated to be M5.5 and M6. The period is estimated to be 225 yr. In the UVES data the radial velocities do not show any variability.

6.4.3. Other objects with possible radial velocity variations

Besides the two spectroscopic binaries discussed above, no hints of a brown dwarf companion to any other object were found. Nevertheless, there are some objects which have radial velocity variations that might be real. More data is needed to find out if these variations could have been caused by wide companions, clouds, spots or planet companions. The possibility of existing spots on brown dwarfs will be discussed in chapter 7. Observed variations could be related to dust bands or large clouds. Brown dwarfs are fully convective objects. Therefore, sunken particles are brought up to the atmosphere again. Because of the complexity of the convection process, the dust might not be equally distributed across the surface of the brown dwarf. These clouds could cause radial velocity variations, thus, mimicking a companion.

Besides the known spectroscopic binaries in this sample, 2MASSW J2202112-110946 has the highest radial velocity variation ($\sigma_{RV} = 0.83$ km/s). This is a very active object. On the third night of observation a flare was observed. Therefore, it is possible that the observed radial velocity variation is due to stellar activity.

For 2MASS J20491972-1944324, 2MASSW J2135146-315345 and 2MASSW J2147446-264406 radial velocity variations can be seen of the order of 0.34 - 0.54 km/s. The graphs of these three objects are very good, therefore, the variations could be real. More spectra should be taken of these objects.

In table 6.4 the objects are listed with variation of at least 2σ . In the first and the second column the name and spectral type of the objects are given. The third column shows the error of the radial velocity measurement (Δ_{RV}) and the fourth column the radial velocity variation (σ_{RV}). Table 6.5 lists the objects with variations between 1 and 2σ and table 6.6 shows the objects with constant radial velocity.

Some of the graphs are very good and true radial velocity variations can be detected by the shape of the curve, even when the scatter of the overall data points is only a little bit larger than the scatter of a single data point. On the other side, there are objects with very noisy curves. These objects have a risk of accidentally being classified as objects with radial velocity variations. Also, there are some objects in the sample which have only been observed for one or two nights. Therefore, nothing can be said about a likely binary nature of these objects. Table 6.7 lists the objects, which, after studying both the radial velocity measurements and the shape of the curves, were classified as having radial velocity variations.

LHS 292

Based on the first three spectra taken, the object LHS 292 was listed as an spectroscopic binary candidate by Guenther and Wuchterl (2003). For this work more spectra of this object were available. Also, the accuracy of the radial velocity measurement was improved. A radial velocity variability of 1σ was found but this variability is too small to be caused by a close brown dwarf companion.

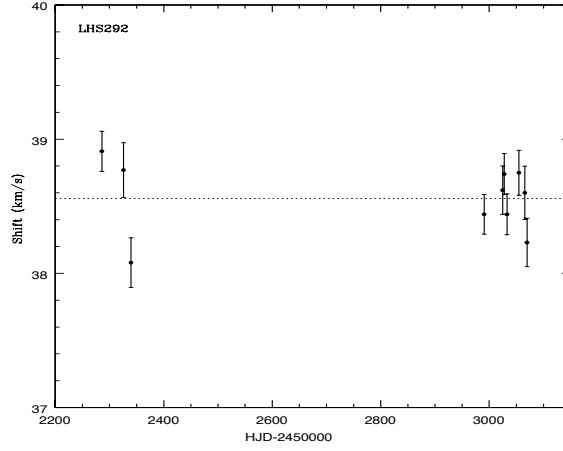


Figure 6.16.: Radial velocities of LHS 292

Table 6.4.: Objects with variations larger than 2σ

Name	Spectral Type	ΔRV [kms^{-1}]	σRV [kms^{-1}]
2MASS J21130293-1009412 ¹	M6.5	0.195 ± 0.061	5.990
2MASS J09522188-1924319 ²	M6	0.185 ± 0.018	4.475
2MASSW J2202112-110946	M6.5	0.137 ± 0.106	0.833
BR B0246-1703	M7.5	0.221 ± 0.075	0.580
2MASSW J2147446-264406	M7	0.159 ± 0.092	0.535
2MASSW J2135146-315345	M6.5	0.181 ± 0.064	0.390
2MASS J20491972-1944324	M6.5	0.114 ± 0.044	0.338

¹ SB2 (Guenther et al. 2003)

² SB2 (Reid et al. 2002)

Table 6.5.: Objects with variations between 1 and 2σ

Name	Spectral Type	ΔRV [kms^{-1}]	σRV [kms^{-1}]
2MASS J08320451-0128360	L2	1.294 ± 0.508	1.902
TVLM 868- 110639	M8	0.692 ± 0.497	1.620
DENIS-P J0021.0-4244	M9	0.396 ± 0.163	0.608
LHS 2397a ¹	M8	0.300 ± 0.152	0.533
LHS 3566	M7.5	0.183 ± 0.019	0.264
LHS 292	M6.5	0.172 ± 0.021	0.260

¹ Visuell binary (Freed et al. 2003)

Table 6.6.: Objects with constant radial velocities

Name	Spectral Type	ΔRV [$km s^{-1}$]	σRV [$km s^{-1}$]
BR B1104-1227	M6	0.110±0.039	0.093
UScoCTIO 55 ¹	M6	0.174±0.042	0.110
2MASS J20520861-2318096	M6.5	0.226±0.032	0.170
2MASS J12372705-2117481	M6	0.270±0.080	0.218
LHS 2065	M9	0.268±0.153	0.245
2MASSW J2206228-204705 ²	M7	0.177±0.099	0.251
UScoCTIO 85	M6	0.389±0.170	0.506
DENIS-P J1047.5-1815	L1	0.798±0.283	0.526
2MASSW J2013510-313651	M6	0.672±0.781	0.695
LP 944-20	M9	1.261±0.918	1.175
UScoCTIO 75	M5.5	1.309±0.923	1.609
UScoCTIO 100	M6	0.921±0.865	1.712
BRI B0021-0214	M9.5	2.759±1.240	2.182

¹ Visuell binary (Kraus et al. 2005)

² Visuell binary (Close et al. 2003)

Table 6.7.: Objects with radial velocity variations, which are likely to be real

Name	Spectral Type	ΔRV [$km s^{-1}$]	σRV [$km s^{-1}$]
> 2 σ variations			
2MASS J21130293-1009412 ¹	M6.5	0.195±0.061	5.990
2MASS J09522188-1924319 ²	M6	0.185±0.018	4.475
2MASSW J2202112-110946	M6.5	0.137±0.106	0.833
2MASSW J2147446-264406	M7	0.159±0.092	0.535
2MASSW J2135146-315345	M6.5	0.181±0.064	0.390
2MASS J20491972-1944324	M6.5	0.114±0.044	0.338
1 - 2 σ variations			
LHS 2397a ³	M8	0.300±0.152	0.533
LHS 292	M6.5	0.172±0.021	0.260

¹ SB2 (Guenther et al. 2003)

² SB2 (Reid et al. 2002)

³ Visuell binary (Freed et al. 2003)

6.5. Mass limits of companions

Based on the σRV -values, that is the standard deviation of the measured radial velocities over the whole observational time-span, upper mass limits for possible companions were derived. The σRV -values depend on different values like the eccentricity of the orbit, the node angle, the inclination of the orbit, the orbital period of the planet and, when less than one orbital period is observed, the orbital phase when the first observation was taken.

Here, only a case with typical parameters will be discussed. Therefore, the calculated upper limits can only serve as guidelines for a typical companion mass that can be excluded. A round orbit, that is $e = 0$, is assumed. The orbital period is set to 40 days, which corresponds to a separation of $a \leq 0.1$ AU. Calculations for smaller periods or higher eccentricities yield smaller masses.

Kepler's third law relates the two masses to their period of revolution and the size of their relative orbit:

$$\frac{a^3}{T^2} = (M_1 + M_2) \times \frac{G}{4\pi^2}, \quad (6.9)$$

with a the semi-major axis of their relative orbit, T the period, M_1 and M_2 the masses of the two objects and G the gravitational constant.

The semi-major axis a_1 fulfills the following equation:

$$a_1 \sin i = 86400 \times T \times K \times \sqrt{1 - e^2} / (2\pi), \quad (6.10)$$

where T is the period in days, $K = \frac{1}{2} \times (RV_{max} - RV_{min})$ in km/s and e is the eccentricity.

With a_1 and a_2 being the semi-major axes of the orbits and M_1 and M_2 their masses, one can calculate a_1 from

$$a = a_1 + a_2 \quad (6.11)$$

and

$$M_1 \times a_1 = M_2 \times a_2 \quad (6.12)$$

to be

$$a_1 = a \times \frac{M_2}{M_1 + M_2}. \quad (6.13)$$

The substitution of a in equation 6.13, with the value for a derived from equation 6.9, yields an equation for a_1 . After inserting this equation for a_1 in equation 6.10 and putting in all known constants, one gets the equation:

$$\frac{M_2 \sin i}{(M_1 + M_2)^{2/3}} = \left(\frac{3.985 \times 10^{-20}}{T^2} \right)^{1/3} \times \frac{86400 \times T \times K \times (1 - e^2)^{1/2}}{2\pi}, \quad (6.14)$$

where M_1 and M_2 are in M_\odot , T is in days and K is in km/s.

Because only a few points of a supposable orbit were observed, RV_{max} and RV_{min} are unknown. However, from the observed data $\sigma_{Experiment}$ is known. With

$$\sigma_{Theorie} = K/\sqrt{2} \stackrel{!}{=} \sigma_{Experiment}, \quad (6.15)$$

K, in equation 6.14, was substituted with $\sqrt{2} \times \sigma_{Experiment}$. Then the obtained equation was solved for $M_2 \sin i$, using an inclination $i = 52^\circ$.

As can be seen in table 6.8, a brown dwarf companion with an orbital period of $P \leq 40$ d can be excluded for all objects but the two confirmed spectroscopic binaries.

Table 6.8.: Upper mass limits for companions, assuming a circular orbit and an orbital period of 40 days.

Name	Mass [M_\odot]	σRV [$km s^{-1}$]	Upper limits for $M_2 \sin i$ [M_{Jup}]
2MASS J08320451-0128360	0.07	1.902	8.4
2MASS J12372705-2117481	0.10	0.218	1.10
2MASSW J2013510-313651	0.10	0.695	3.7
2MASS J20491972-1944324	0.09	0.338	1.6
2MASS J20520861-2318096	0.09	0.170	0.8
2MASSW J2135146-315345	0.09	0.390	1.9
2MASSW J2147446-264406	0.09	0.535	2.6
2MASSW J2202112-110946	0.09	0.833	4.1
2MASSW J2206228-204705	0.09	0.251	1.2
BRI B0021-0214	0.08	2.182	10.7
BR B0246-1703	0.09	0.580	2.8
BR B1104-1227	0.10	0.093	0.5
DENIS-P J0021.0-4244	0.08	0.608	2.8
DENIS-P J1047.5-1815	0.07	0.526	2.2
LHS 2065	0.08	0.245	1.1
LHS 2397a	0.08	0.533	2.4
LHS 292	0.09	0.260	1.3
LHS 3566	0.09	0.264	1.3
LP 944-20	0.07	1.135	5.0
TVLM 868- 110639	0.08	1.620	7.7
UScoCTIO 55	0.07	0.110	0.4
UScoCTIO 75	0.08	1.609	7.6
UScoCTIO 85	0.07	0.506	2.1
UScoCTIO 100	0.07	1.712	7.5

7. The atmosphere of the highly active brown dwarf LP 944-20

Recently several brown dwarfs have been found with strong magnetic fields. To study the effects of magnetic fields on the atmospheres of brown dwarfs, the brown dwarf LP 944-20 was observed with EFOSC2 on the 3.6 m telescope in La Silla, Chile. The aim of this observation run was to find out if LP 944-20 has spots and whether these are related to the magnetic field. Regarding searches of companions around brown dwarfs by means of radial velocity measurements, the question if brown dwarfs have stellar spots is very important. This is because, in principle, stellar spots can cause radial velocity variations. Because of the weak ionization of brown dwarf atmospheres, which leads to a very low coupling between the magnetic field and the atmosphere, it is possible that even strong magnetic fields do not lead to spots on brown dwarfs. The strength of the coupling between the gas and the magnetic field can be described with the magnetic Reynolds number $R_m = lv/\eta$, where l is a length scale, v is a velocity scale and η is the magnetic diffusivity of the gas. The magnetic Reynolds number R_m is a dimensionless number, which describes how efficiently a gas interacts with a magnetic field. When $R_m \ll 1$, there is no interaction between the gas and the magnetic field. When $R_m \gg 1$, the magnetic field is frozen in the gas. While for the Sun R_m near sunspots is estimated to be 10^4 to 10^6 (Priest 1982), for old brown dwarfs R_m lies in the range of 10^{-10} to 10^{-20} (Gelino et al. 2002).

The brown dwarf LP 944-20 has a parallactic distance of 5.0 pc (Tinney 1996). Its spectral type is M9 (Tinney 1996). Space velocities suggest that LP 944-20 is a member of the Castor moving group. Therefore, it has an age of 320 ± 80 Myr, implying a mass of around $0.05 M_\odot$ (Ribas 2003). However, there is the possibility that LP 944-20 does not belong to the Castor moving group. Tinney (1998) derived the age of this object by comparing the equivalent width of Li I with theoretical models. He estimates an age of 475 - 650 Myr, which corresponds to a mass of $0.056 - 0.064 M_\odot$. Literature values for its effective temperature vary between 2000 and 2400 K. In this work a temperature of 2300 K, using the UVES spectra and the models from Chabrier et al. (2000), was derived. Like other ultra-cool dwarfs, LP 944-20 rotates very fast. It has a $v \sin i = 30$ km/s (Tinney et al. 1998), corresponding to a rotation period of $P \leq 4.5$ h. No infrared-excess emission has been found, implying that this object has no disk (Apai et al. 2002).

LP 944-20 is an ideal object to study the effects of magnetic fields on brown dwarf atmospheres. LP 944-20 lies in the vicinity of our Sun and is fairly bright, which makes it easy to observe. An X-ray flare was detected with Chandra (Rutledge et al. 2000). This suggested for the first time that brown dwarfs have magnetic fields, which can release energy through a flare. Berger et al. (2001) found a persistent radio emission

from LP 944-20 at 4.9 and 8.5 GHz, which is most likely gyrosynchrotron emission. The quiescent magnetic field strength was derived by Berger (2006) to be < 95 G. During flares, a magnetic field strength of 135 G was inferred. The radio emission is probably produced in a region of $\sim 1 - 2 R_{BD}$ above the stellar surface. Thus, depending on the field configuration, the magnetic field strength at the surface may be nearly 1 kG even in quiescence. For comparison, our Sun has a global averaged magnetic field of ~ 1 G (Lin et al. 1999). Like other ultra-cool dwarfs, LP 944-20 violates the X-ray - radio emission relation for normal stars. Its radio emission is 4 to 5 orders of magnitude brighter than expected from the X-ray emission (see figure 2.3).

Tinney and Tolley (1999) observed LP 944-20 in two passbands centered at 8570 Å (B1) and 8725 Å (B2). The band B1 lies on a strong TiO feature. This band decreases with decreasing temperature, due to condensation and therefore depletion of Ti from the atmosphere. They detected a photometric variability of 0.04 mag in the B1-B2 colors. These brightness variations signify T_{eff} variations of 20 K over the entire visible surface. Significant radial velocity variations in the optical were detected with the VLT/UVES (Martín et al. 2006). The variations were of an amplitude of 3.5 km/s. However, in the newly reduced data the radial velocity variation was only in the order of 1.2 km/s and within the error bars (see figure 7.1).

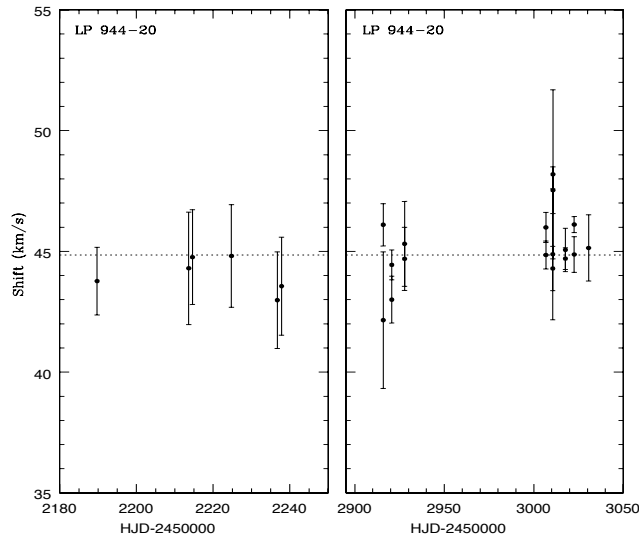


Figure 7.1.: Radial velocities of LP 944-20 derived from the UVES data.

The difference between the old and the new reduction is that in the old reduction the radial velocity was determined by fitting individual lines (Li, K, Rb, Na) with Gaussian functions (private communication). The new reduction takes all absorption features into account. It is thus possible that the radial velocity of some individual lines differ from the radial velocity of the whole ensemble of lines and molecular bands. Such effects are well known on the Sun. Near-infrared observations, with the KECK/NIRSPEC spectrograph

(Martín et al. 2006), showed only a variation in the order of 0.36 km/s. In case of a companion, variations should also be seen in the near-infrared. Because LP 944-20 is very constant in the near-infrared, it can be ruled out that LP 944-20 has a companion. Together with the fact that LP 944-20 does not have a disk, it can be concluded that any variability seen must be due to the atmosphere of this object.

Observation

I performed a low-resolution ($\lambda/\Delta\lambda = 450$) spectroscopic time-series over two nights with the ESO Faint Object Spectrograph and Camera Version 2 (EFOSC2) at the 3.6 m telescope in La Silla, Chile. Grism #5, covering the wavelength region from 5200 - 9350 Å, was used. The slit-width was set to 1.2". The seeing was better than 0.8" throughout the whole observation run. The grism covers the wavelength regions of the TiO bands and the H α emission line. It was therefore possible to map out the temperature distribution on the surface and relate it to stellar activity.

LP 944-20 was observed during the night from the 29th to the 30th of November, in which 14 spectra were taken, and during the night from the 30th of November to the 1st of December 2006, in which 16 spectra were taken. During both nights LP 944-20 was observed for six hours. The period of LP 944-20 is estimated to be $P \leq 4.5$ h. This means that over the two nights several rotation periods were observed, making it possible to find out how stable surface features are.



Figure 7.2.: 3.6 m telescope in La Silla, Chile. (ESO webpage, 2006)

Data reduction

A standard data reduction was performed with IRAF. The frames were corrected for bad pixels and cosmic rays were removed. The spectra were divided by internal flat-fields, which were taken after each exposure. The CCD has very strong fringing in the redder part, making it necessary to use internal flats. However, even after the flat-fielding there is still strong fringing left for wavelengths longward of 7200 Å. The scattered light was subtracted. The spectra were obtained with the nodding technique. That is, two consecutive spectra were recorded on different columns of the CCD. Through this nodding technique the sky and the bias can be removed by subtracting each frame by the consecutive frame. The spectra were extracted and a wavelength calibration was performed. Finally, the spectra were corrected for extinction and a flux calibration with the flux-standard star EG 21 was applied. Figure 7.3 shows a reduced spectra of LP 944-20.

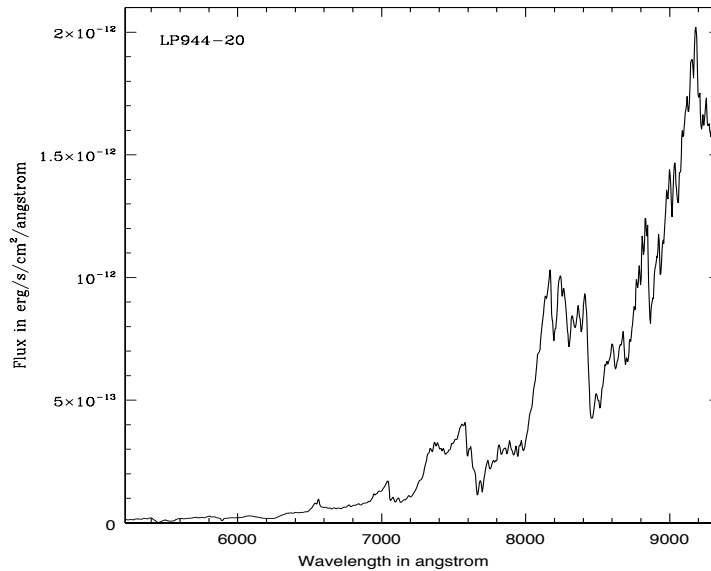


Figure 7.3.: Spectra of LP 944-20 taken with EFOSC2 on the 3.6m.

Results of the observations of LP 944-20

The temperature of LP 944-20 was calculated by measuring the index TiO 5 as described in chapter 6. The observation with EFOSC2 shows that there are only small temperature variations of about 20 K (see figure 7.4). This is consistent both with the photometric variability found by Tinney and Tolley (1999) and the UVES data (see figure 7.5). The temperature variation of LP 944-20, derived with the UVES data, is less than 20 K. The variation of 20 K is too small to be caused by large star-spots.

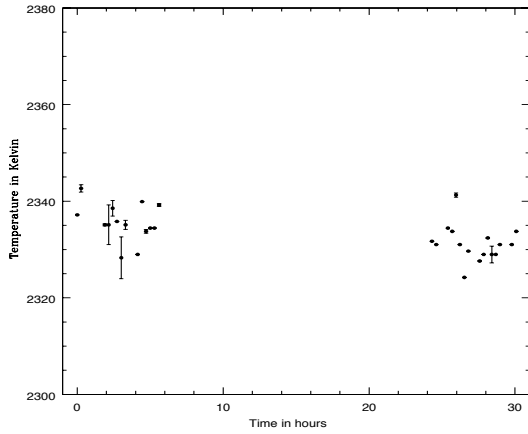


Figure 7.4.: Temperature variations of LP 944-20 observed with EFOSC2.

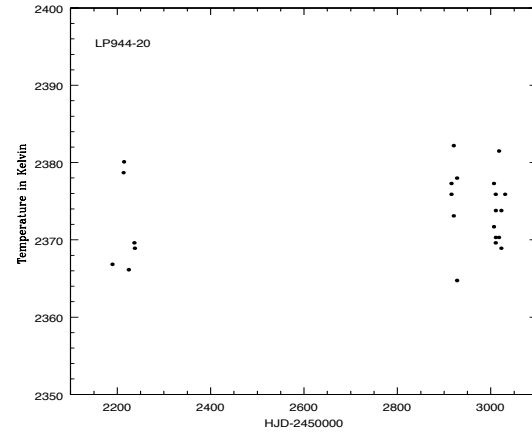


Figure 7.5.: Temperature variation of LP 944-20 observed with the UVES data.

Because there is no real continuum in the spectrum of an M-dwarf, it is difficult to measure the equivalent widths of the $H\alpha$ and Na D lines in a consistent manner. To find a criteria for what part of the spectrum belongs to the lines and what part does not, the pseudo-continuum around these lines was fitted with a polynomial. Then the spectrum was divided by this polynomial, thus resulting in a normalized spectrum. Taking the value one as continuum, it was then possible to measure the equivalent width consistently.

In figure 7.8, the $H\alpha$ equivalent width is plotted against time. The $H\alpha$ equivalent width is fairly constant. There are only variations of about 8 \AA of the $H\alpha$ equivalent width, which is a very small value for an active object. No periodical trend can be seen. In figure 7.9, the equivalent width of the Na D line is plotted against time. Also, the equivalent width of the Na D line has only very small variations of 4 \AA .

Figure 7.10 shows the $H\alpha$ equivalent width plotted against the temperature. No correlation can be seen. In figure 7.11 it can be seen that the Ca II line at 8662.14 \AA of LP 944-20 is in emission.

Conclusion

LP 944-20 is a very constant object, despite its enormous magnetic field strength. There are no significant variations in the $H\alpha$ and Na D equivalent widths. Also there are no significant temperature variations. In conclusion, it can be said that the atmosphere of LP 944-20 must be very homogeneous. It is very unlikely that spots or other prominent features exist on this object despite its strong magnetic field. Thus, a brown dwarf with a large magnetic field is, because of the low magnetic Reynolds numbers, completely different from an active star. While some brown dwarf have strong magnetic fields, these fields have essentially no influence on the structure of the atmosphere.

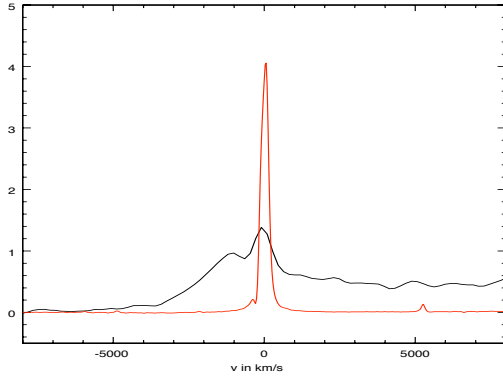


Figure 7.6.: $H\alpha$ line of LP 944-20 (black) overplotted by the $H\alpha$ line of the T Tauri star DR Tau (red) for comparison.

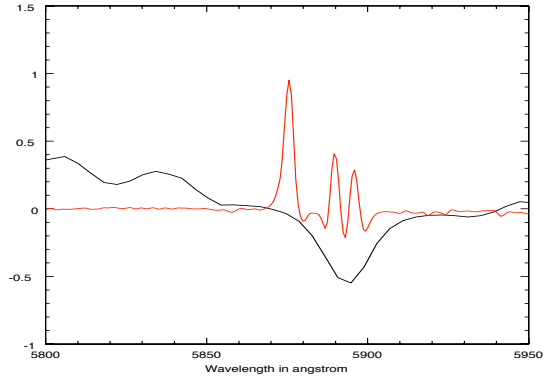


Figure 7.7.: Na D line of LP 944-20 (black) overplotted by the Na D line of the T Tauri star DR Tau (red).

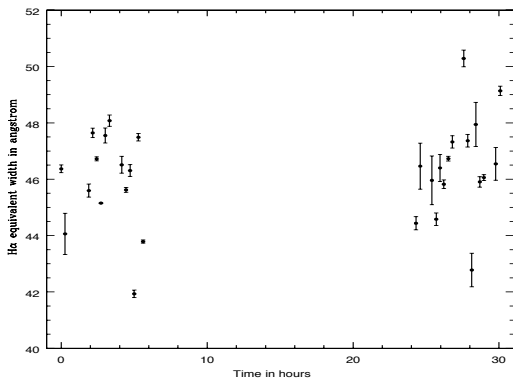


Figure 7.8.: $H\alpha$ equivalent width against time.

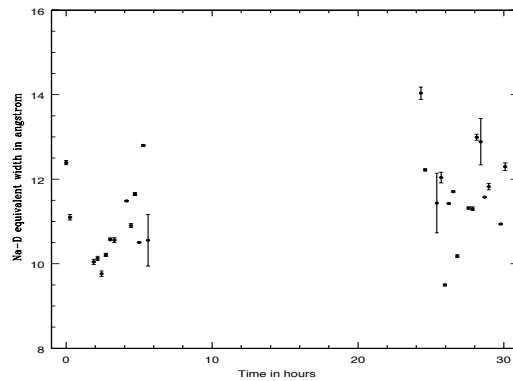


Figure 7.9.: Sodium equivalent width against time

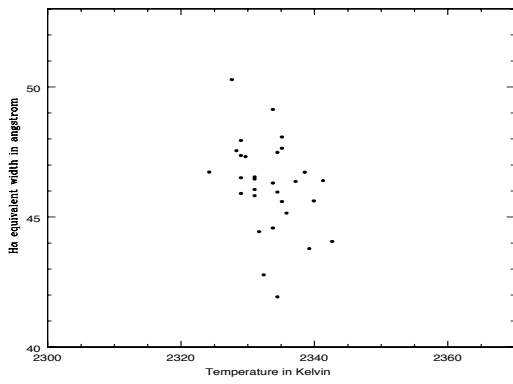


Figure 7.10.: $H\alpha$ against temperature.

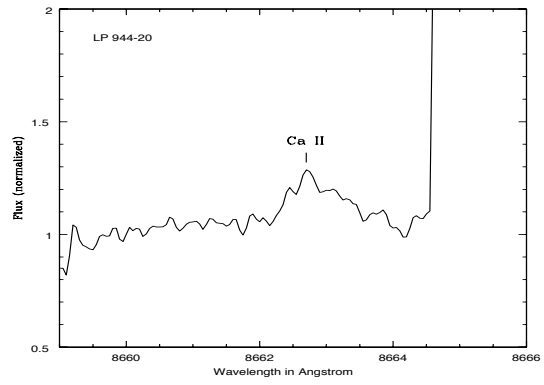


Figure 7.11.: Ca II line at 8662.14 Å of LP 944-20 from a UVES spectrum.

8. Conclusions

The aim of this work was to determine the frequency of brown dwarf companions to very low-mass stars and brown dwarfs, within a sample of 27 objects. The radial velocities were measured by fitting the spectra with templates. As templates, spectra were used that were calculated with the so-called COND models. With this new method, the accuracy of the radial velocity measurement is about 0.2 km/s. This is an improvement by a factor of roughly 5 - 10 from the previous analysis by Guenther and Wuchterl (2003), which utilized crosscorrelation. This precision makes it possible to find companions with masses down to Jupiter masses. The sensitivity of this measurement is very high. So much so, that even the binary nature of the visuell binary LHS 2397a, with a separation of almost 4 AU, was detected.

It is to note that for measurements of radial velocities, using crosscorrelation, spectral lines are necessary. The fitting method used in this work can also derive radial velocities with the help of molecular band-heads. This makes this method very suitable for radial velocity measurements of late-type objects, which have spectra that are dominated by molecular bands.

Two spectroscopic binaries, 2MASS J21130293-1009412 and 2MASS J09522188-1924319, were confirmed. It was shown that brown dwarf companions with periods $\lesssim 40$ days can be excluded for all other objects. Additionally, it was shown that the brown dwarf binary candidate LHS 292 is not a binary. This yields a close binary frequency of $7.4 \pm 1.4\%$. This frequency shows that momentum transfer during the formation is not of great importance.

Besides the two spectroscopic binaries, four objects show radial velocity variations larger than 2σ . For one of these objects, 2MASSW J2202112-110946, a flare was observed, making it likely that the variation is due to stellar activity. For the other three objects the observed variations of 0.34 to 0.54 km/s are too small to be caused by close brown dwarf companions. These variations could be due to a wide companion, an orbiting planet or changeable surface features, such as clouds. These variation could also be random. However, the probability that they are real is larger than 95.4%. Upper limits for possible orbiting companions, based on the detected radial velocity variations, were calculated for all objects. A circular orbit and an orbital period of 40 days were assumed. The radial velocity variations of 0.34 to 0.54 km/s, of the three objects mentioned above, lead to upper mass limits between 1.3 and 4.1 M_{Jup} .

Along with the measurement of the radial velocities, spectral types, temperatures and masses of all objects were derived. The calculated spectral types are within one sub-class in agreement with the literature values. The temperatures of the objects vary over the whole observational time-span of the order of 10 to 40 K.

To find out if there is a possible relation between surface features, such as spots and

the magnetic field, I observed the extremely active brown dwarf LP 944-20 over several rotation periods with EFOSC2 on the 3.6 m telescope in La Silla, Chile. The analysis of the observation shows that, despite its strong magnetic field, it is very unlikely that this object has large spots or other dominant surface features. This can be explained by the fact that the conductivity in the outer atmospheres of brown dwarfs is so low that there is no interaction with the magnetic field.

Figure 8.1 is the best summary of my work. The plot shows the semi-major axis distribution of brown dwarfs and very low-mass stars. The black line is the result of the high-resolution imaging survey done by Bouy et al. (2003). This survey was sensitive for separations $a > 1$ AU. The black bar represents my work, which extends the results by Bouy et al. (2003) to smaller separations. I find a close binary frequency of $7.4 \pm 1.4\%$, which hints at a rather small multiplicity frequency for brown dwarfs and very low-mass stars with orbital separations of $a \lesssim 1$ AU. This finding affirms the current observational results, which support a star-like formation of brown dwarfs. However, additional formation mechanisms might play a small role, as they probably do with stars, but they are probably not essential for the formation of brown dwarfs.

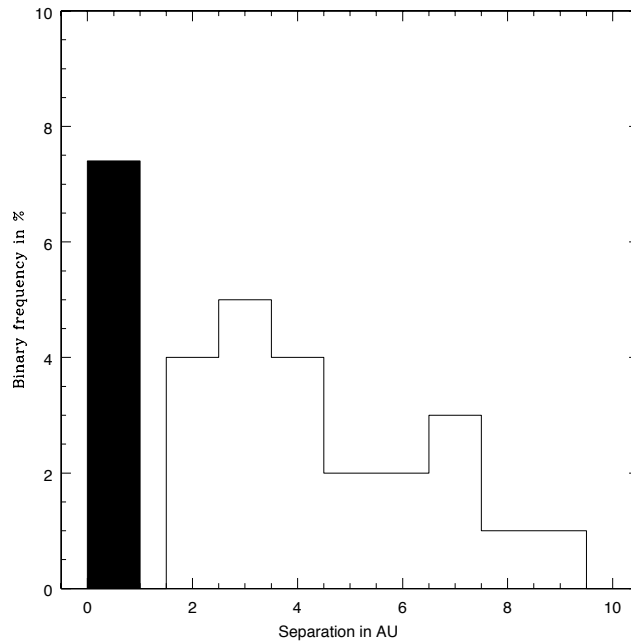


Figure 8.1.: Semi-major axis distribution of brown dwarf binaries. The black line represents the work obtained from the volume-limited sample distribution of Bouy et al. (2003). The black bar represents my work.

Appendix A.

IRAF CL script for the radial velocity measurement

```
# -----  
procedure radial_velocity (inimage,temimage)  
# -----  
  
string inimage {prompt="object frames"}  
string temimage {prompt="templates"}  
  
struct *list1  
struct *list2  
  
begin  
    file infile  
    file temfile  
    string in  
    string tem  
    real telu1  
    real telu2  
    real telu3  
    real telu4  
    real telu5  
    real telu6  
    real telu7  
    real telu8  
    real telu9  
    real mx  
    real mx1  
    real mx2  
    real sx
```

```

real sxx
real fmx
real fmx1
real fmx2
real hjd
real vhelio

# --- temporary files
infile = mktemp ("tmp")
temfile = mktemp ("tmp")
# --- transforming the lists of frames into temporary files
sections(inimage, option="root", > infile)
sections(temimage, option="root", > temfile)
list1 = infile
list2 = temfile
# --- processing the frames in a loop
print("*****")
while (fscan(list1,in) !=EOF){
if (fscan(list2, tem) == EOF){
    print (" Not enough second frames ")
    return
}
print("-----")
print(" ")
print(" This program measures the")
print(" RV for spectra taken with")
print(" ")
print("      --- UVES --- ")
print(" ")
print(" Current Frame:      ",in)
print("-----")

# -----
imdelete("duma", verify=no)
imdelete("dumb", verify=no)
imdelete("summe1.imh", verify=no)
imdelete("summe2.imh", verify=no)
imhead(in)
imhead(tem)

# -----
# --- fit of the telluric lines
scopy("filename.imh","duma",w1=6860,w2=6930)
fit1d("duma","dumb",interactive=yes,order=3,type="ratio")

```

```

fxcor("dumb","telu_lines_6900.imh",width=100,maxwidth=50,
      window=100,cuton=5,cutoff=1500)
print("Velocity computed from shift ?")
scan(telu7)
fxcor("dumb","telu_lines_6900.imh",width=100,maxwidth=50,
      window=100,cuton=5,cutoff=1500)
print("Velocity computed from shift ?")
scan(telu8)
fxcor("dumb","telu_lines_6900.imh",width=100,maxwidth=50,
      window=100,cuton=5,cutoff=1500)
print("Velocity computed from shift ?")
scan(telu9)

# --- mean
sx=telu7+telu8+telu9
mx1=sx/3
# --- standard deviation (sample)
telu7=telu7-mx1
telu8=telu8-mx1
telu9=telu9-mx1
telu7=telu7*telu7
telu8=telu8*telu8
telu9=telu9*telu9
sx=telu7+telu8+telu9
sxx=sx/2
fmx1=sqrt(sxx/3)*1.32

# -----
# --- Fitprogramm
# -----

fit(tem,in)

onedspec
sinterp("summe1.dat","", "summe1.imh")
sinterp("summe2.dat"," ", "summe2.imh")
# --- radial velocity 6935-7160
splot summe1.imh
print ("Velocity computed from shift ?")
scan(telu1)
splot summe1.imh
print ("Velocity computed from shift ?")
scan(telu2)
splot summe1.imh
print ("Velocity computed from shift ?")

```

```

    scan(telu3)
# --- radial velocity 7550-8250
    splot summe2.imh
    print ("Velocity computed from shift ?")
    scan(telu4)
    splot summe2.imh
    print ("Velocity computed from shift ?")
    scan(telu5)
    splot summe2.imh
    print ("Velocity computed from shift ?")
    scan(telu6)

# -----
# --- mean
    sx=telu1+telu2+telu3+telu4+telu5+telu6
    mx=sx/6
# --- standard deviation (sample)
    telu1=telu1-mx
    telu2=telu2-mx
    telu3=telu3-mx
    telu4=telu4-mx
    telu5=telu5-mx
    telu6=telu6-mx
    telu1=telu1*telu1
    telu2=telu2*telu2
    telu3=telu3*telu3
    telu4=telu4*telu4
    telu5=telu5*telu5
    telu6=telu6*telu6
    sx=telu1+telu2+telu3+telu4+telu5+telu6
    sxx=sx/5
    fmx=sqrt(sxx/6)*1.11

# --- correction with telluric lines
    mx2=mx-mx1
    fmx=fmx*fmx
    fmx1=fmx1*fmx1
    fmx2=sqrt(fmx+fmx1)

# --- output
    print("The mean of VOBS is:")
    print(mx2)
    print("The standard deviation of VOBS is:")
    print(fmx2)

```

```
# -----  
    hedit(in,fields="VOBS",value=mx2,add=yes)  
    rvcorrect(images=in)  
    print("HJD?")  
    scan(hjd)  
    print("VHELIO?")  
    scan(vhelio)  
    hedit(in,fields="HJD",value=hjd,add=yes)  
    hedit(in,fields="VHELIO",value=vhelio,add=yes)  
    hedit(in,fields="HJD",value=hjd,add=yes)  
    }  
  
# --- Clean  
    list1= ""  
    list2= ""  
    delete (infile, verify=no)  
    delete (temfile, verify=no)  
end
```


The Fortran program fit.f

```
c -----  
  
      program fit  
  
c -----  
c --- Declarations  
      implicit none  
      character*80      imagel , image2 , errmsg  
      integer          i , ii , iii , k  
      integer          im1 , im2 , axlen ( 7 ) , naxis , dtype , ier  
      real             ncols , nlines , nbands  
      real             pix1 ( 0 : 100000 ) , pix2 ( 0 : 100000 )  
      double precision d3pix1 ( 0 : 1 , 0 : 1 , 0 : 100000 ) ,  
      double precision d3pix2 ( 0 : 1 , 0 : 1 , 0 : 100000 )  
      double precision lambda , lambda1 , lambda2  
      double precision alpha , omega , a , b , d , e , f , g , n  
      double precision summe ( 0 : 1000000 )  
      double precision sigmamin  
      double precision c , iimin , v  
      double precision x ( 0 : 100000 ) , xmed , med1 , med2 , medf , medf1  
      double precision t , m  
      double precision y ( 0 : 1000000 , 0 : 100 )  
      double precision beta ( 0 : 2 ) , gamma ( 0 : 2 )  
  
c -----  
c                               IRAF  
c -----  
c --- Get first image  
      call clargc ( 1 , imagel , ier )  
      if ( ier .ne. 0 ) then  
          write ( * , '( ''_template_image_ : _ '' , $ ) )  
          read ( * , * ) imagel  
      endif  
  
c --- Imopen first image  
      call imopen ( imagel , 3 , im1 , ier )  
      if ( ier .ne. 0 ) goto 9999  
      call imgsiz ( im1 , axlen , naxis , dtype , ier )  
      if ( ier .ne. 0 ) goto 9999
```

```

ncols = axlen(1)
nlines = axlen(2)
nbands = axlen(3)

c —— Import the values of the input-frames into 3d array
do 30 i = 1, nbands
  do 20 ii = 1, nlines
    call imgl3r (im1, pix1, ii, i, ier)
    if (ier .ne. 0) goto 9999
    do 10 iii = 1, ncols
      d3pix1(i, ii, iii)=DBLE(pix1(iii))
10      continue
20      continue
30      continue

write(6,*) ncols, nlines, nbands
open (unit=1, file='template.dat', status='old')
do 70 i = 1, ncols
  lambda=6.750D+3+((DBLE(i)-1.0D0)*5.0D-2)
  write(1,*) lambda, d3pix1(1,1,i)
70  continue
close (unit=1)

c —— Get second image
call clargc (2, image2, ier)
if (ier .ne. 0) then
  write (*, '( '_spectrum_image_:_' , $)')
  read (*,*) image2
endif

c —— Imopen for second image
call imopen (image2, 3, im2, ier)
if (ier .ne. 0) goto 9999
call imgsiz (im2, axlen, naxis, dtype, ier)
if (ier .ne. 0) goto 9999

ncols = axlen(1)
nlines = axlen(2)
nbands = axlen(3)

c —— Import the values of the input-frames into 3d array
do 60 i = 1, nbands
  do 50 ii = 1, nlines
    call imgl3r (im2, pix2, ii, i, ier)

```

```

        if (ier .ne. 0) goto 9999
        do 40 iii = 1, ncols
            d3pix2(i, ii, iii)=DBLE(pix2(iii))
40         continue
50         continue
60         continue

        write(6,*) ncols, nlines, nbands
        open (unit=1, file='spectrum.dat', status='old')
        do 80 i = 1, ncols
            lambda=6.7820D+3+((DBLE(i)-1.0D0)*5.0D-2)
            write(1,*) lambda, d3pix2(1,1,i)
80         continue
        close (unit=1)

c -----
c                               Constants
c -----
c ----- Speed of light (km/s)
c = 299792.5

c -----
c ----- Fit of the wavelength region 6935-7160 Angstrom
c -----
c ----- Selecting part of the template
        open (unit=1, file='template1.dat', status='old')
        alpha=6.800D+3
        omega=7.300D+3
        a=(alpha-6.750D+3)/(5.0D-2)+2.0D+0
        b=(omega-6.750D+3)/(5.0D-2)+2.0D+0
        do 110 i=a,b
            lambda=6.750D+3+((DBLE(i)-1.0D0)*5.0D-2)
            write(1,*) lambda, d3pix1(1,1,i)
110         continue
        close (unit=1)

c ----- Selecting part of the spectrum
        open (unit=1, file='spectrum1.dat', status='old')
        alpha=6.935D+3
        omega=7.160D+3
        d=(alpha-6.7820D+3)/(5.0D-2)+2.0D+0
        e=(omega-6.7820D+3)/(5.0D-2)+2.0D+0
        do 120 i=d,e
            lambda=6.7820D+3+((DBLE(i)-1.0D0)*5.0D-2)

```

```

        write(1,*)lambda,d3pix2(1,1,i)
120  continue
      close (unit=1)

c —— Normalization
      k=2
      beta(1)=7.000D+3
      gamma(1)=7.050D+3
      beta(2)=7.050D+3
      gamma(2)=7.100D+3

      medf1=0.0
      do 230 ii=1,k
c —— Median of the template
      f=(beta(ii)-6.750D+3)/(5.0D-2)+2.0D+0
      g=(gamma(ii)-6.750D+3)/(5.0D-2)+2.0D+0
      n=g-f+1.0
      do 180 i=1,n
180  x(i)=d3pix1(1,1,f+i-1)
      continue

      call MEDIAN(X,N,XMED)
      med1=xmed

c —— Median of the spectrum
      f=(beta(ii)-6.7820D+3)/(5.0D-2)+2.0D+0
      g=(gamma(ii)-6.7820D+3)/(5.0D-2)+2.0D+0
      n=g-f+1.0
      do 200 i=1,n
200  x(i)=d3pix2(1,1,f+i-1)
      continue

      call MEDIAN(X,N,XMED)
      med2=xmed

      medf=med2/med1
      medf1=medf1+medf
230  continue
c —— Factor to multiply the template with
      medf1= medf1/(DBLE(k))

      a=a-1
      b=b-1
      d=d-1

```

```

e=e-1

open (unit=1, file='template3.dat', status='old')
do 220 i=a,b
    lambda=6.750D+3+((DBLE(i)-1.0D+0)*5.0D-2)
    d3pix1(1,1,i)=medf1*d3pix1(1,1,i)
    write(1,*)lambda,d3pix1(1,1,i)
220 continue
close (unit=1)

c -----
c ----- Fit
c -----
c ----- Sum
    sigmamin=10000000.0D+0
    do 1170 ii=a,b-e+d
        summe(ii)=0.0D+0
        do 1340 i=0,e-d
            summe(ii)=summe(ii)+DABS(d3pix1(1,1,ii+i)-d3pix2(1,1,d+i))
1340 continue
1170 continue
c ----- Subpixel shifting
    t=99.0
    do 240 iii=0,t
        do 250 ii=a,b-e+d
            if (summe(ii) .gt. summe(ii+1)) then
                y(ii,iii)=(summe(ii)-summe(ii+1))*((DBLE(ii)+1.0D+0)-(DBLE(ii)
&+DBLE(iii))/(DBLE(t)+1.0D+0)))+summe(ii+1)
            else if (summe(ii) .lt. summe(ii+1)) then
                y(ii,iii)=(summe(ii+1)-summe(ii))*((DBLE(ii)+DBLE(iii))/(DBLE(t)
&+1.0D+0)-DBLE(ii))+summe(ii)
            else if (summe(ii) .eq. summe(ii+1)) then
                y(ii,iii)=summe(ii)
            end if
250 continue
240 continue

c -----
c ----- Wavelength --> km/s
c ----- Calculated with averaged wavelength: (d+e)/2
    open (unit=1, file='summel.dat', status='old')
    do 870 ii=a,b-e+d
        do 860 m=0,t
            lambda=6.750D+3+((DBLE(ii)+DBLE(m))/(DBLE(t)+1.0D+0)-1.0D+0)*0.05)
            lambda1=6.7820D+3+((DBLE(d)-1.0D+0)*0.05)

```

```

        lambda2=6.7820D+3+((DBLE(e)-1.0D+0)*0.05)
        v=c*((lambda1+lambda2)/2.0D+0-((lambda+lambda2-(lambda1+lambda2)
&/2.0D+0))/1.0004D+0)/((lambda+lambda2-(lambda1+lambda2)/2.0D+0))/
&1.0004D+0
        write(1,*) v,y(ii,m)
860  continue
870  continue
      close (unit=1)

c -----
c —— Fit of the wavelength region 7660–8100 Angstrom
c -----
c —— Selecting part of the template
      open (unit=1, file='template2.dat', status='old')
      alpha=7.550D+3
      omega=8.250D+3
      a=(alpha-6.750D+3)/(5.0D-2)+2.0D+0
      b=(omega-6.750D+3)/(5.0D-2)+2.0D+0
      do 1110 i=a,b
          lambda=6.750D+3+((DBLE(i)-1.0D0)*5.0D-2)
          write(1,*) lambda,d3pix1(1,1,i)
1110  continue
      close (unit=1)

c —— Selecting part of the spectrum
      open (unit=1, file='spectrum3.dat', status='old')
      alpha=7.660D+3
      omega=8.100D+3
      d=(alpha-6.7820D+3)/(5.0D-2)+2.0D+0
      e=(omega-6.7820D+3)/(5.0D-2)+2.0D+0
      do 1120 i=d,e
          lambda=6.7820D+3+((DBLE(i)-1.0D0)*5.0D-2)
          write(1,*) lambda,d3pix2(1,1,i)
1120  continue
      close (unit=1)

c -----
c —— Normalization
      k=2
      beta(1)=7.820D+3
      gamma(1)=7.870D+3
      beta(2)=7.980D+3
      gamma(2)=8.030D+3
      medf1=0.0

```

```

    do 1230 ii=1,k
c —— Median of the templates
    f=(beta(ii)-6.750D+3)/(5.0D-2)+2.0D+0
    g=(gamma(ii)-6.750D+3)/(5.0D-2)+2.0D+0
    n=g-f+1.0
    do 1180 i=1,n
        x(i)=d3pix1(1,1,f+i-1)
1180    continue

    call MEDIAN(X,N,XMED)
    med1=xmed

c —— Median of the spektrums
    f=(beta(ii)-6.7820D+3)/(5.0D-2)+2.0D+0
    g=(gamma(ii)-6.7820D+3)/(5.0D-2)+2.0D+0
    n=g-f+1.0
    do 1200 i=1,n
        x(i)=d3pix2(1,1,f+i-1)
1200    continue

    call MEDIAN(X,N,XMED)
    med2=xmed

    medf=med2/med1
    medf1=medf1+medf
1230    continue
c —— Factor to multiply the template with
    medf1= medf1/(DBLE(k))

    a=a-1
    b=b-1
    d=d-1
    e=e-1

    open (unit=1, file='template4.dat', status='old')
    do 1220 i=a,b
        lambda=6.750D+3+((DBLE(i)-1.0D+0)*5.0D-2)
        d3pix1(1,1,i)=medf1*d3pix1(1,1,i)
        write(1,*)lambda,d3pix1(1,1,i)
1220    continue
    close (unit=1)

c _____
c —— Fit

```

```

c -----
c ---- Sum
      sigmamin=10000000.0D+0
      do 1170 ii=a,b-e+d
            summe(ii)=0.0D+0
            do 1340 i=0,e-d
                  summe(ii)=summe(ii)+DABS(d3pix1(1,1,ii+i)-d3pix2(1,1,d+i))
1340      continue
1170      continue
      close (unit=1)
c -----
c ---- Subpixel shifting
      t=99.0
      do 1240 iii=0,t
            do 1250 ii=a,b-e+d
                  if (summe(ii) .gt. summe(ii+1)) then
                        y(ii,iii)=(summe(ii)-summe(ii+1))*(DBLE(ii)+1.0D+0-(DBLE(ii)
&+DBLE(iii)/(DBLE(t)+1.0D+0)))+summe(ii+1)
                  else if (summe(ii) .lt. summe(ii+1)) then
                        y(ii,iii)=( summe(ii+1)-summe(ii))*(DBLE(ii)+DBLE(iii)/(DBLE(t)
&+1.0D+0)-DBLE(ii))+summe(ii)
                  else if (summe(ii) .eq. summe(ii+1)) then
                        y(ii,iii)=summe(ii)
                  end if
1250      continue
1240      continue
c -----
c ----- Wavelength --> km/s
c ----- Calculated with averaged wavelength: (d+e)/2
      open (unit=1, file='summe2.dat', status='old')
      do 1870 ii=a,b-e+d
            do 1860 m=0,t
                  lambda=6.750D+3+((DBLE(ii)+DBLE(m))/(t+1.0D+0)-1.0D+0)*0.05)
                  lambda1=6.7820D+3+((DBLE(d)-1.0D+0)*0.05)
                  lambda2=6.7820D+3+((DBLE(e)-1.0D+0)*0.05)
                  v=c*((lambda1+lambda2)/2.0D+0-((lambda+lambda2-(lambda1+lambda2)
&/2.0D+0))/1.0004D+0)/((lambda+lambda2-(lambda1+lambda2)/2.0D+0))/
&1.0004D+0
                        write(1,*) v,y(ii,m)
1860      continue
1870      continue
      close (unit=1)
c -----

```

```

c                                     Clean up
c -----
c ----- Clean up
      call imclos (im1, ier)
      if (ier.ne.0) goto 9999
      stop
      call imclos (im2, ier)
      if (ier.ne.0) goto 9999
      stop

c ----- Error exit
9999 call imemsg (ier, errmsg)
      write (*, '( "Error: ", a80)') errmsg
      stop
      end

c -----
c ----- MEDIAN
c -----
c ----- This program calculates the median of the values.

      SUBROUTINE MEDIAN(X,N,XMED)

      implicit none

      integer          np,j,mm
      double precision big,afac,amp,x(20000)
      double precision xmed,a,eps,ap,am,sum,sumx
      double precision xp,xm,xx,dum,aa,n

c -----
c ----- Parameters
      BIG=1.E30
      AFAC=1.5
      AMP=1.5

c -----
      A=0.5*(X(1)+X(N))
      EPS=ABS(X(N)-X(1))
      AP=BIG
      AM=-BIG
1     SUM=0.
      SUMX=0.

```

```

NP=0
NM=0
XP=BIG
XM=-BIG
DO 11 J=1,N
  XX=X(J)
  IF (XX.NE.A)THEN
    IF (XX.GT.A)THEN
      NP=NP+1
      IF (XX.LT.XP)XP=XX
    ELSE IF (XX.LT.A)THEN
      NM=NM+1
      IF (XX.GT.XM)XM=XX
    ENDIF
    DUM=1./ (EPS+ABS (XX-A))
    SUM=SUM+DUM
    SUMX=SUMX+XX*DUM
  ENDIF
11 CONTINUE
  IF (NP-NM.GE.2)THEN
    AM=A
    AA=XP+MAX(0.,SUMX/SUM-A)*AMP
    IF (AA.GT.AP)AA=0.5*(A+AP)
    EPS=AFAC*ABS(AA-A)
    A=AA
    GO TO 1
  ELSE IF (NM-NP.GE.2)THEN
    AP=A
    AA=XM+MIN(0.,SUMX/SUM-A)*AMP
    IF (AA.LT.AM)AA=0.5*(A+AM)
    EPS=AFAC*ABS(AA-A)
    A=AA
    GO TO 1
  ELSE
    IF (MOD(N,2).EQ.0)THEN
      IF (NP.EQ.NM)THEN
        XMED=0.5*(XP+XM)
      ELSE IF (NP.GT.NM)THEN
        XMED=0.5*(A+XP)
      ELSE
        XMED=0.5*(XM+A)
      ENDIF
    ELSE
      IF (NP.EQ.NM)THEN

```

```
      XMED=A
    ELSE IF (NP.GT.NM)THEN
      XMED=XP
    ELSE
      XMED=XM
    ENDIF
  ENDIF
ENDIF
```

c ——— The output is XMED, which is the median

```
      RETURN
    END
```

c _____
c MEDIAN
c _____

Appendix B.

Radial velocity variations

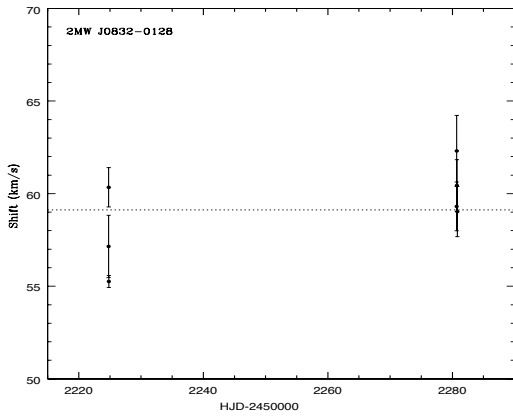


Figure B.1.: 2MASS J08320451-0128360

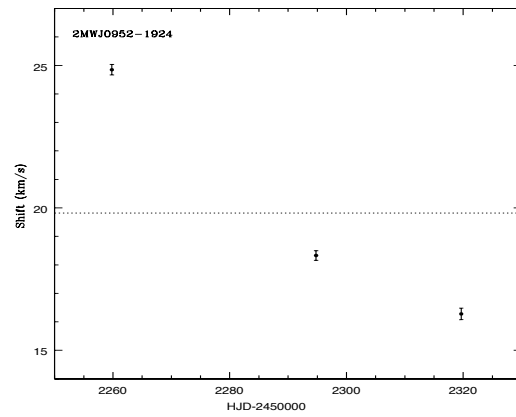


Figure B.2.: 2MASS J09522188-1924319

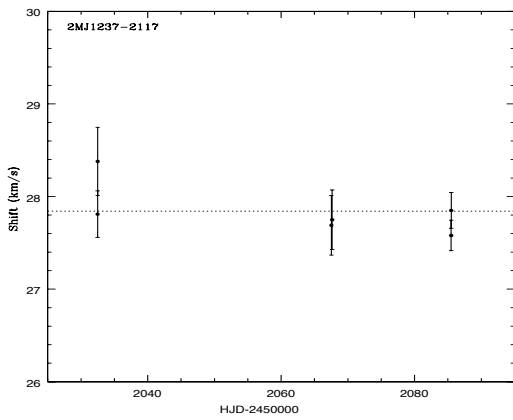


Figure B.3.: 2MASS J12372705-2117481

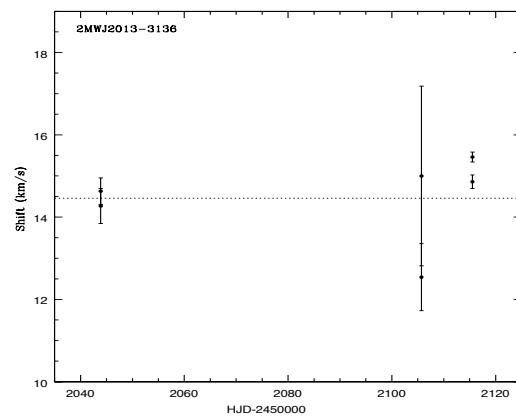


Figure B.4.: 2MASSW J2013510-313651

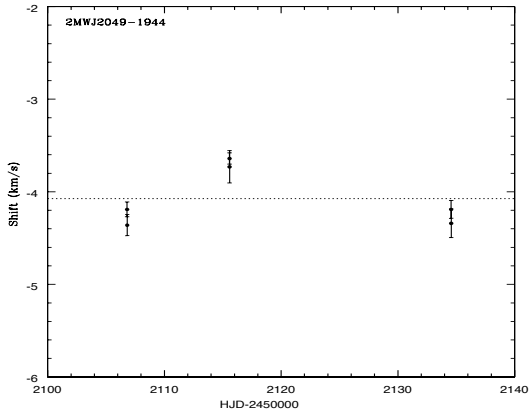


Figure B.5.: 2MASS J20491972-1944324

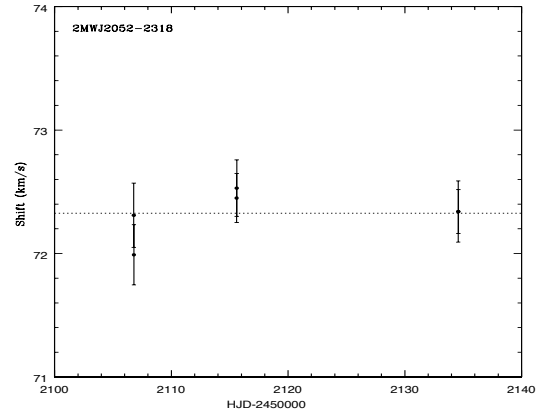


Figure B.6.: 2MASS J20520861-2318096

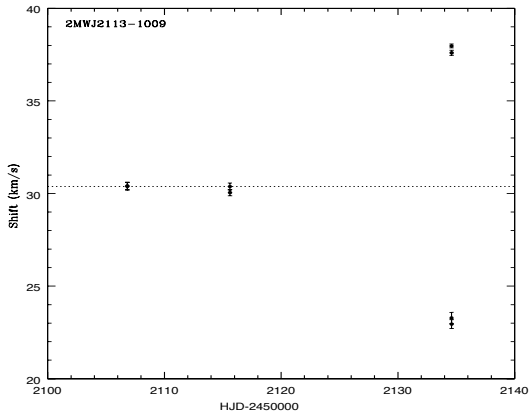


Figure B.7.: 2MASS J21130293-1009412

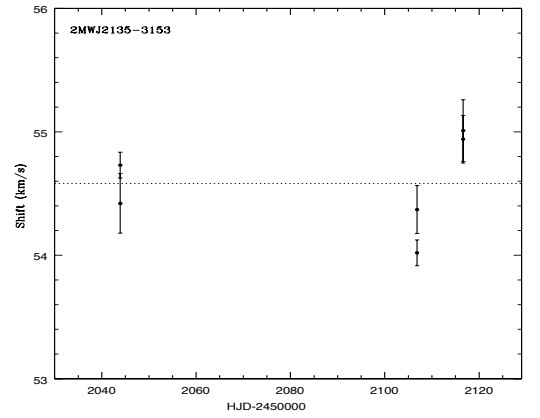


Figure B.8.: 2MASS J2135146-315345

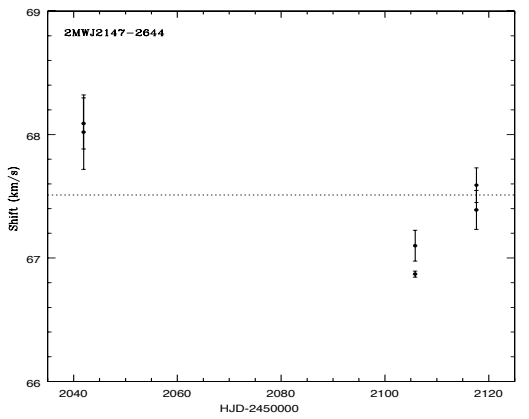


Figure B.9.: 2MASS J2147446-264406

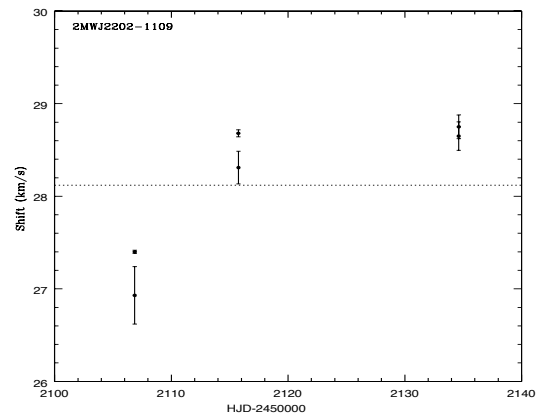


Figure B.10.: 2MASS J2202112-110946

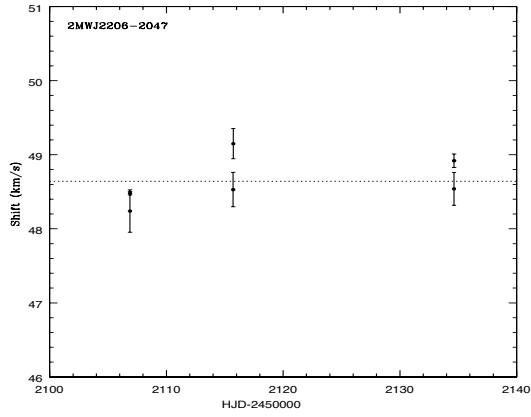


Figure B.11.: 2MASS J2206228-204705

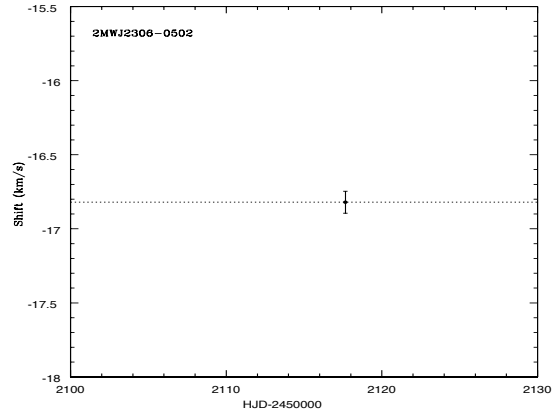


Figure B.12.: 2MASS J23062928-0502285

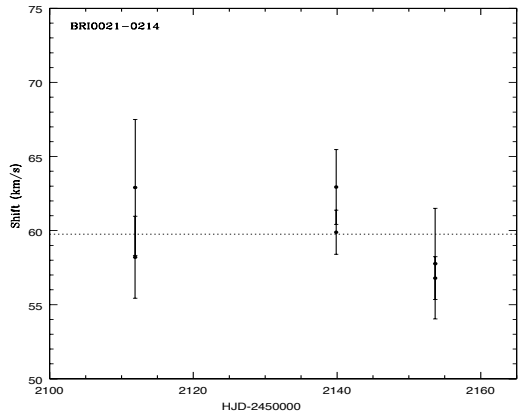


Figure B.13.: BRI B0021-0214

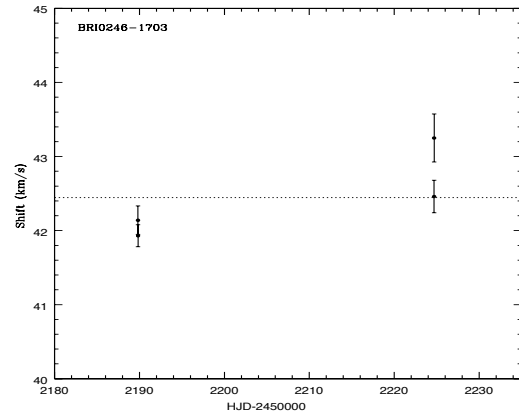


Figure B.14.: BRI B0246-1703

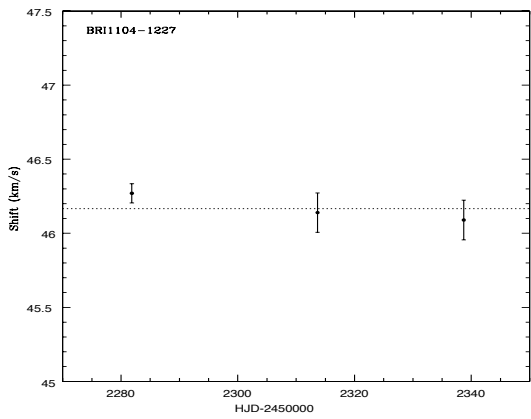


Figure B.15.: BRI B1104-1227

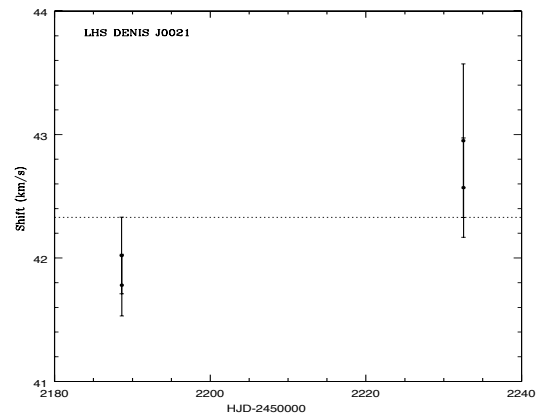


Figure B.16.: DENIS-P J0021.0-4244

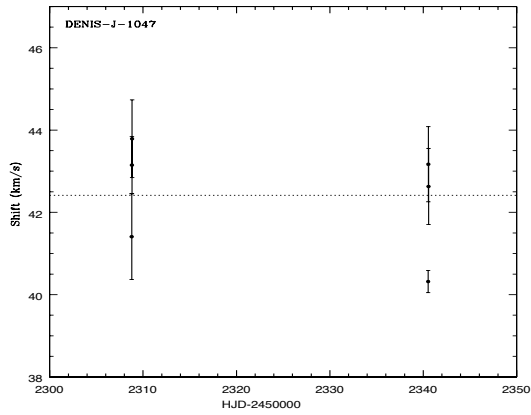


Figure B.17.: DENIS-P J1047.5-1815

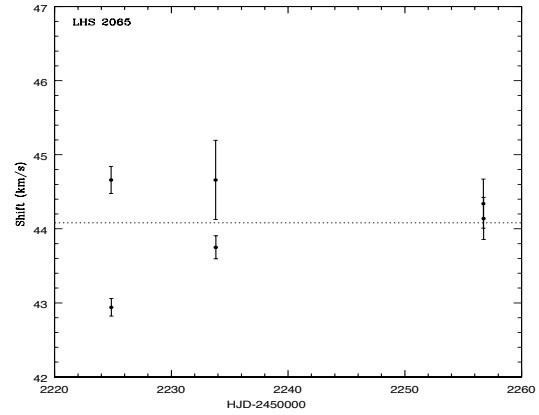


Figure B.18.: LHS 2065

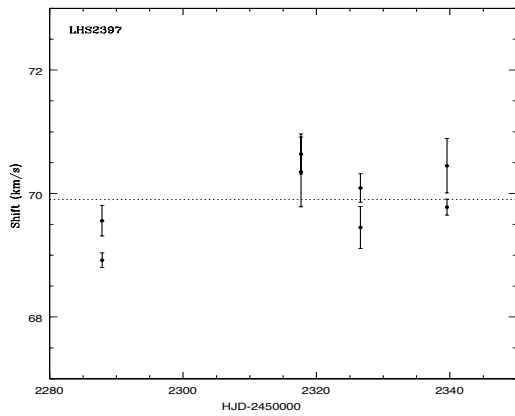


Figure B.19.: LHS 2397

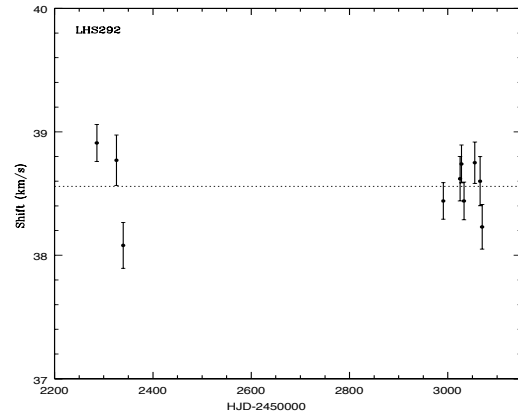


Figure B.20.: LHS 292

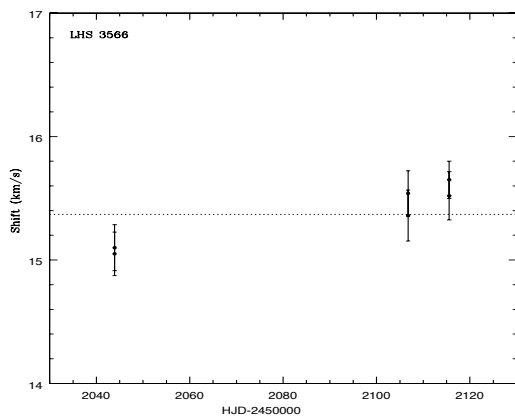


Figure B.21.: LHS 3566

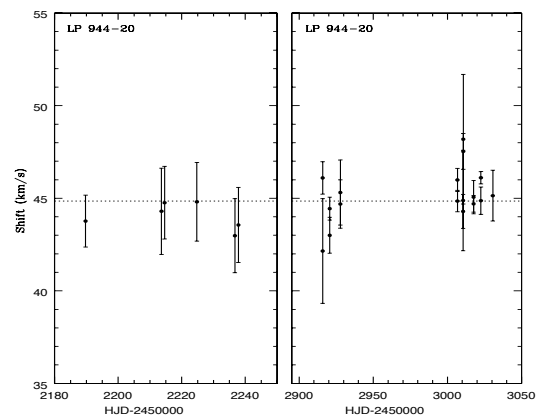


Figure B.22.: LP 944-20

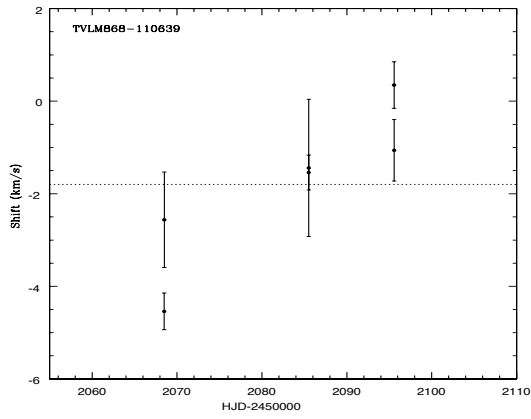


Figure B.23.: TVLM 868-110639

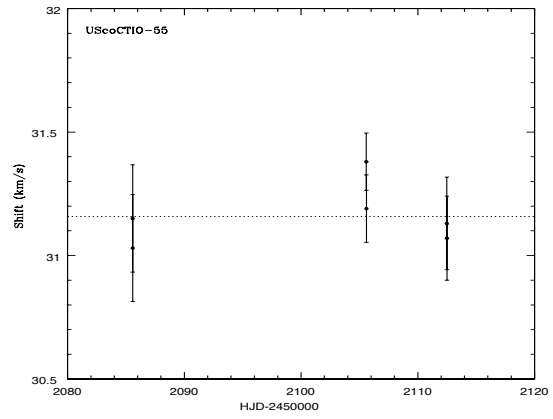


Figure B.24.: UScoCTIO 55

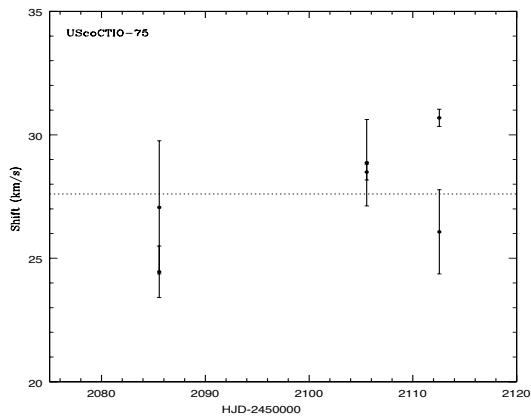


Figure B.25.: UScoCTIO 75

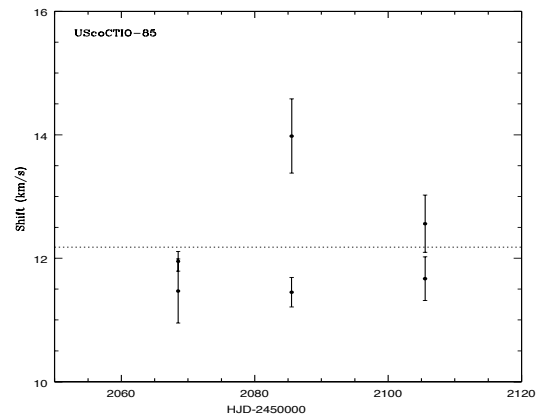


Figure B.26.: UScoCTIO 85

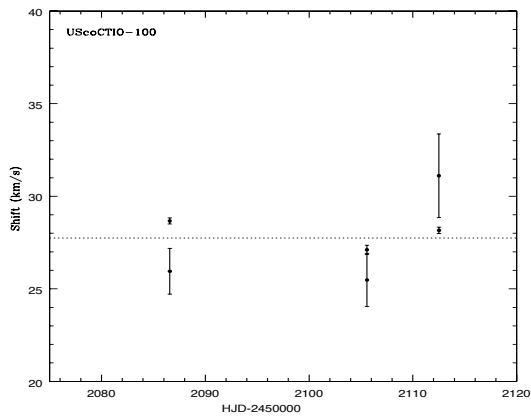
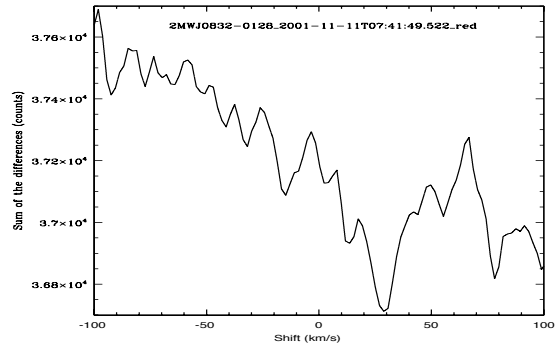
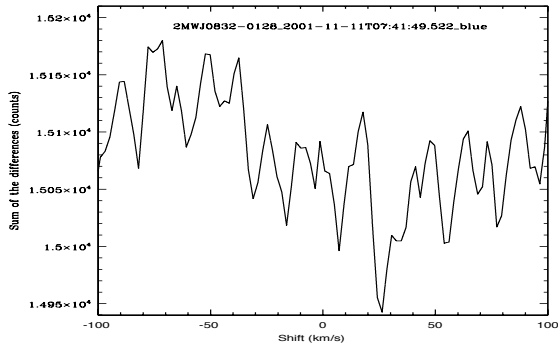
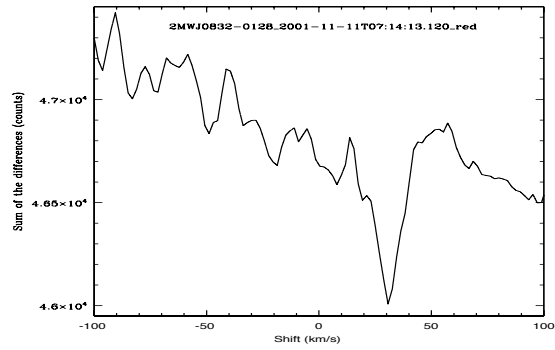
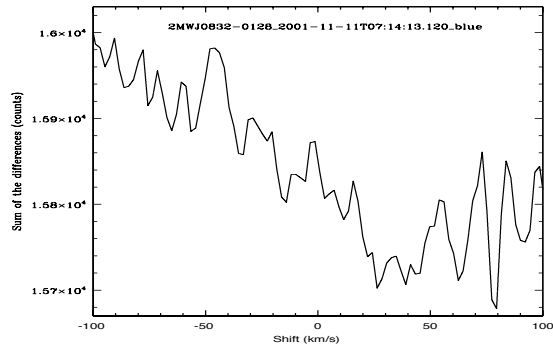
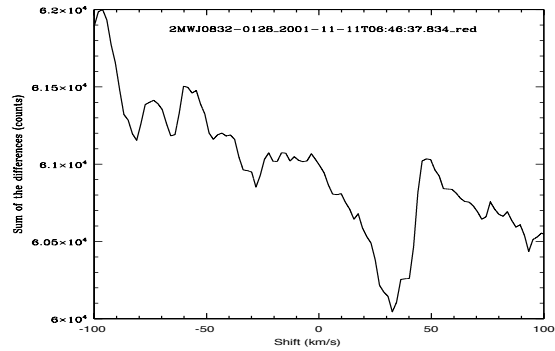
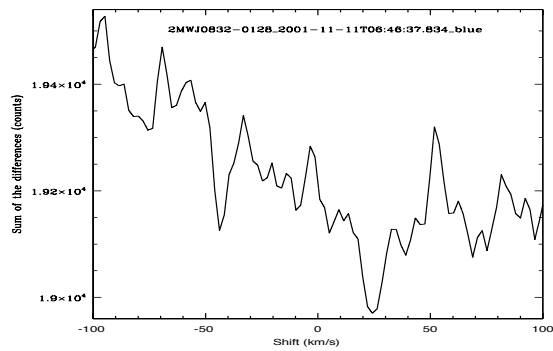


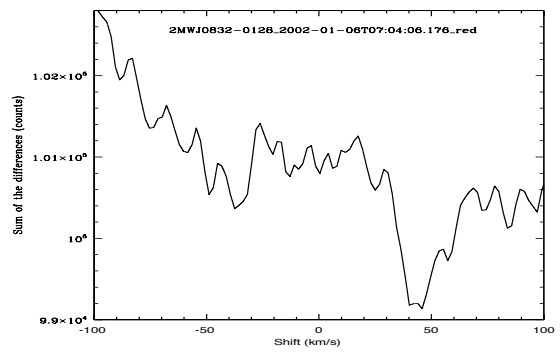
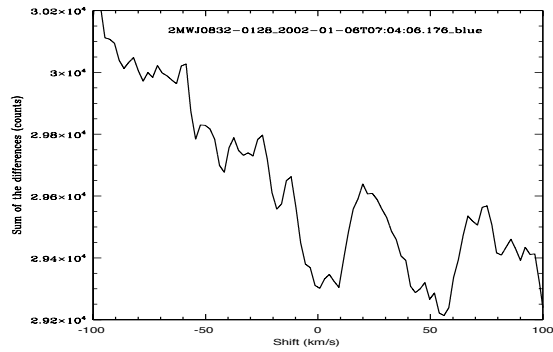
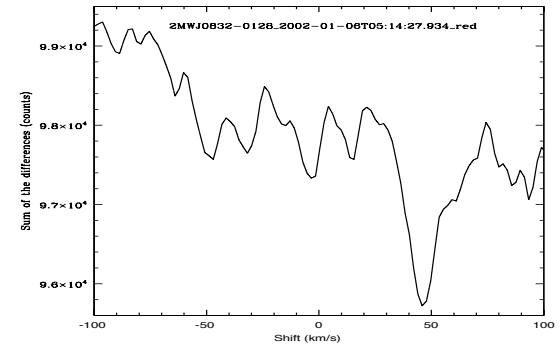
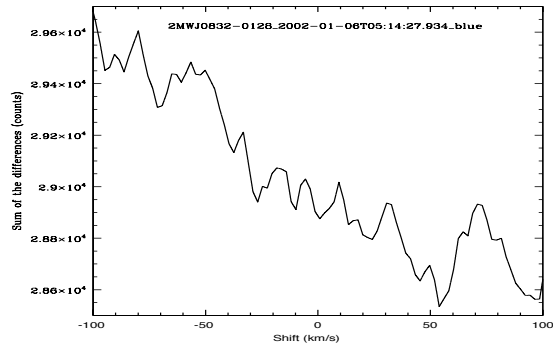
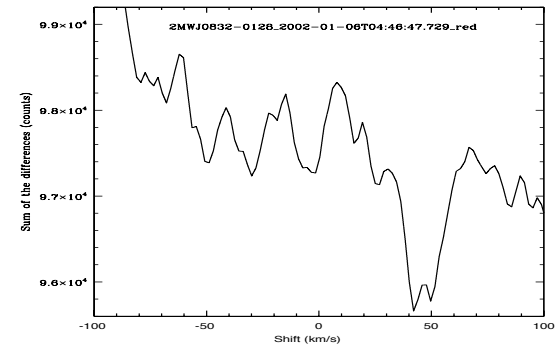
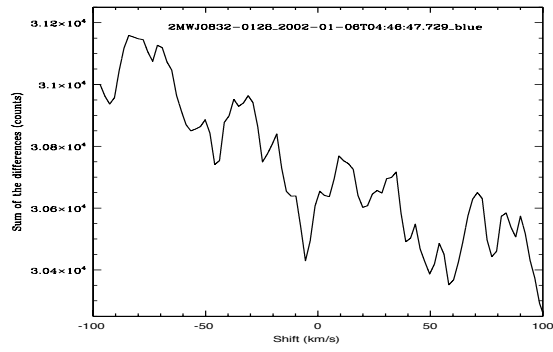
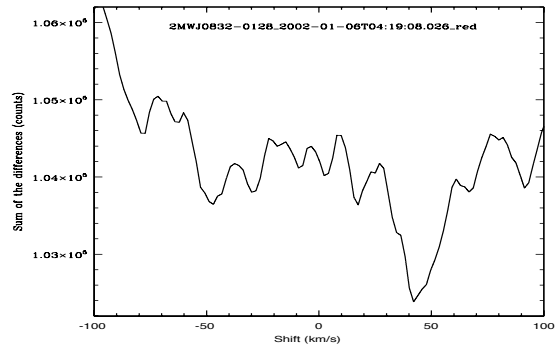
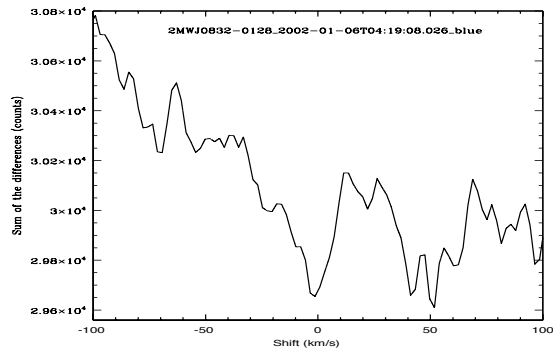
Figure B.27.: UScoCTIO 100

Appendix C.

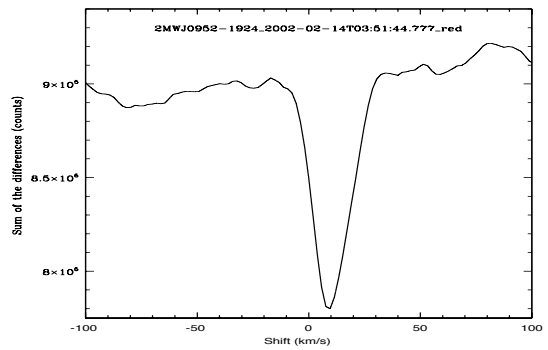
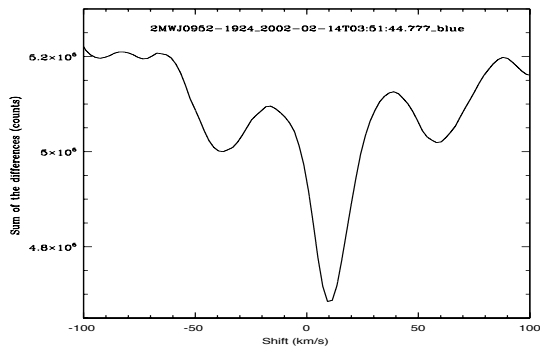
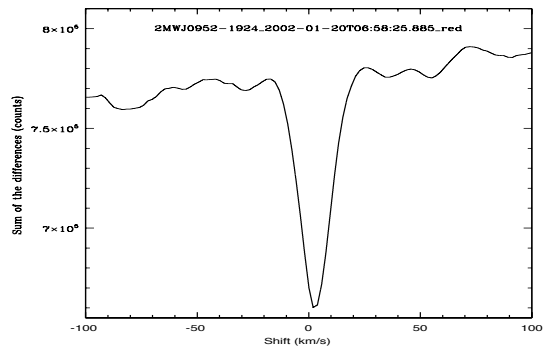
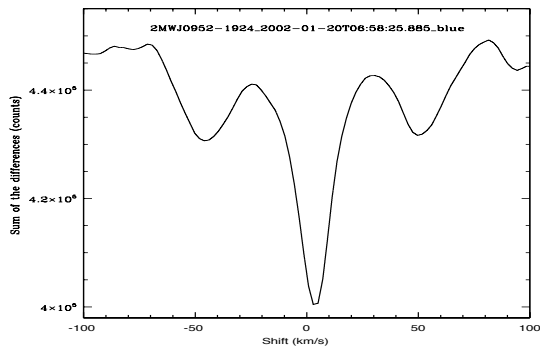
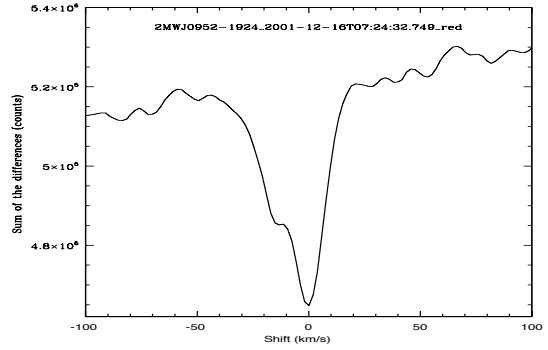
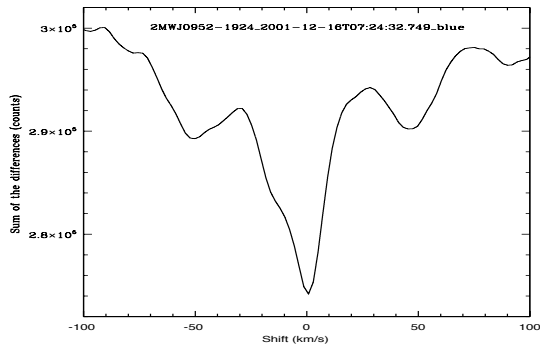
Graphs for the radial velocity variation measurements

2MASS J08320451-0128360

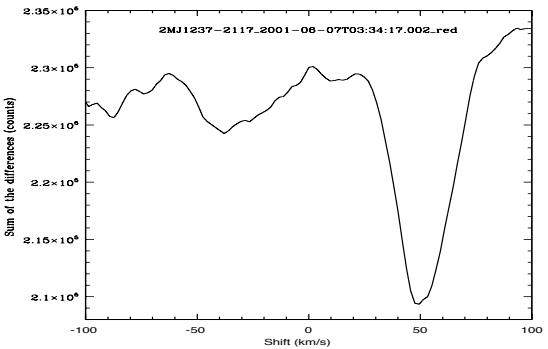
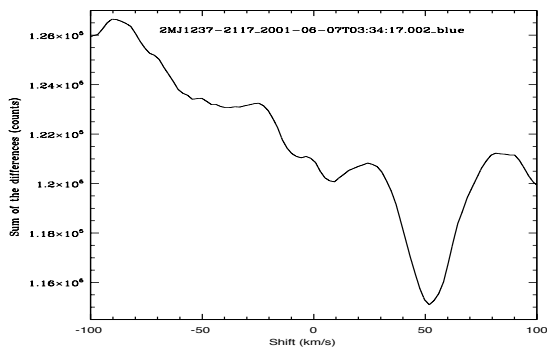
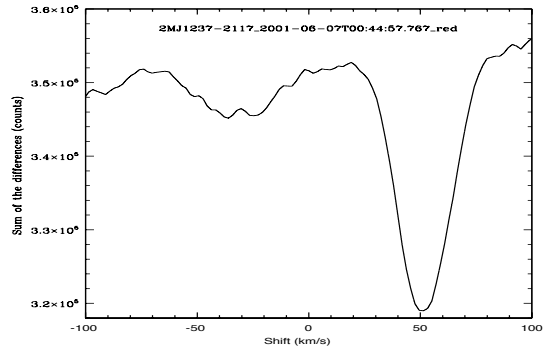
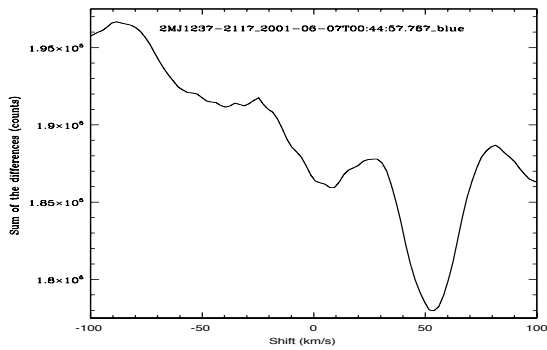
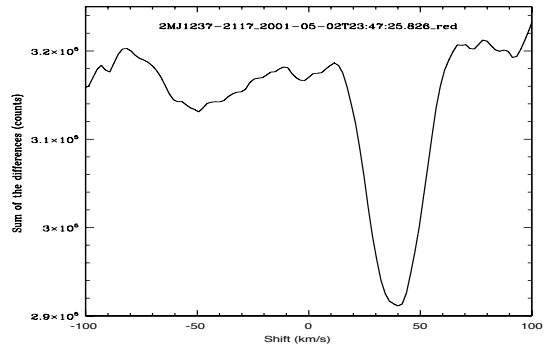
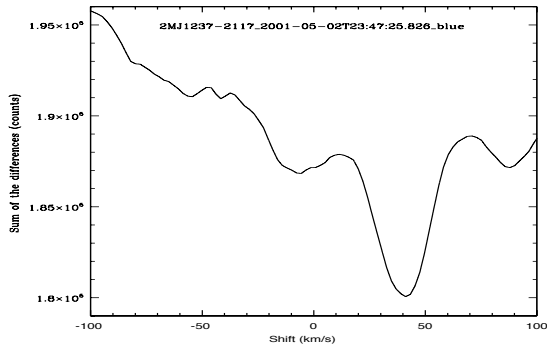
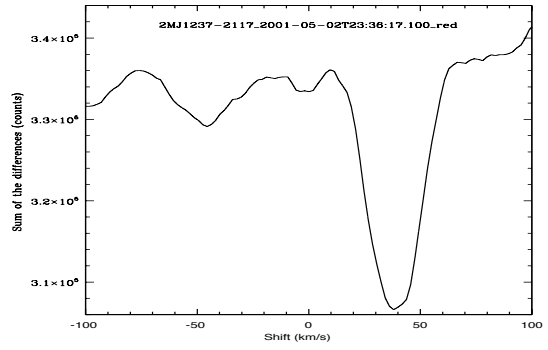
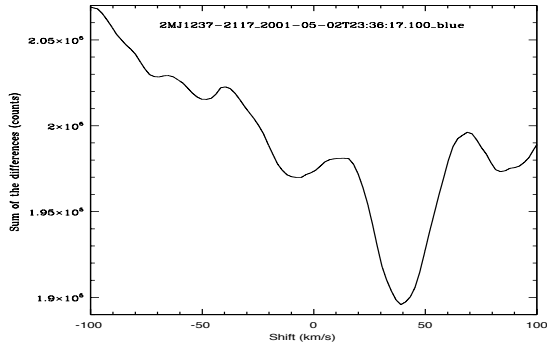


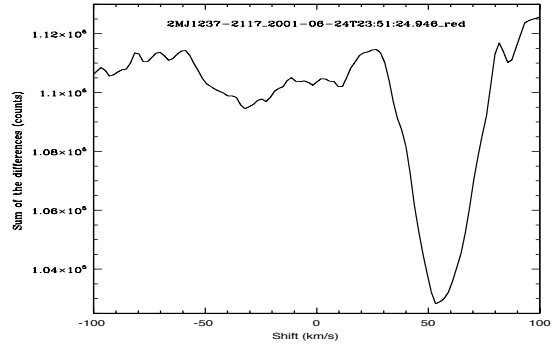
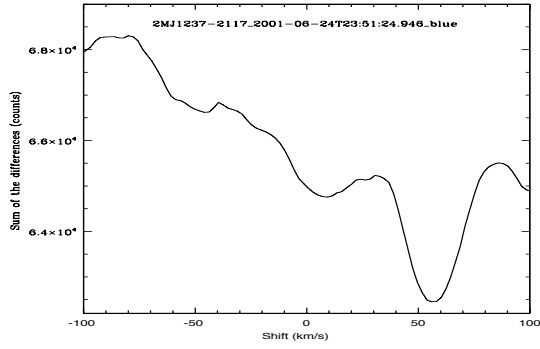
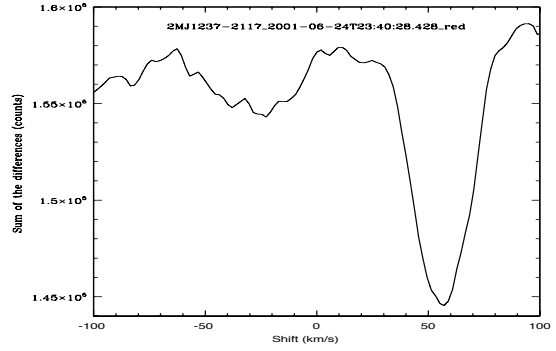
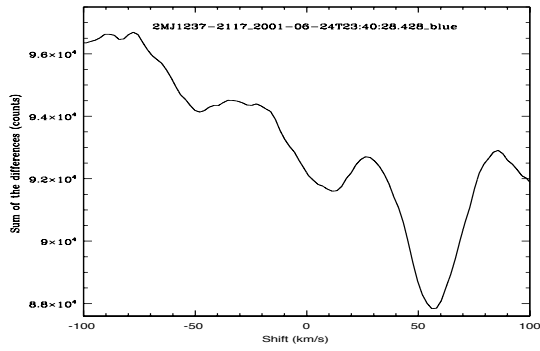


2MASS J09522188-1924319

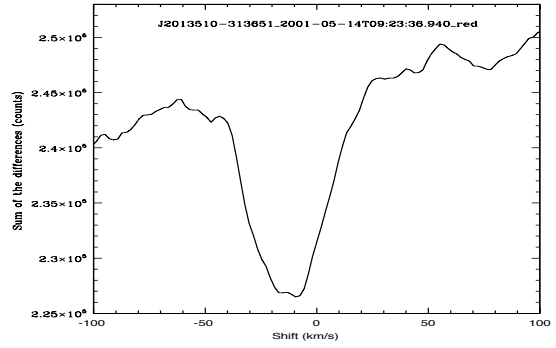
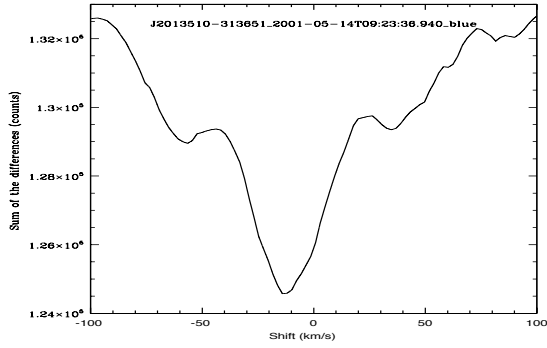
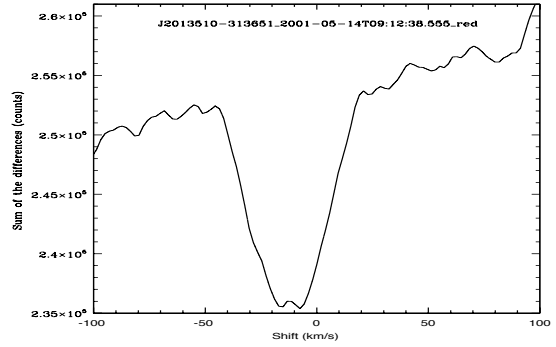
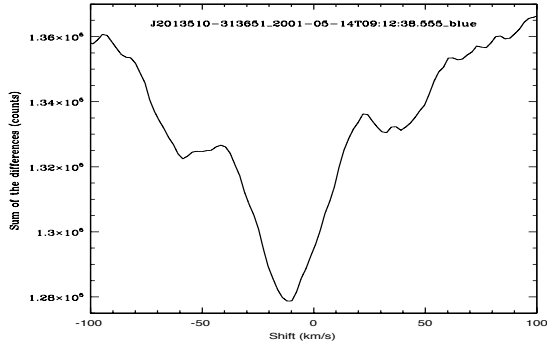


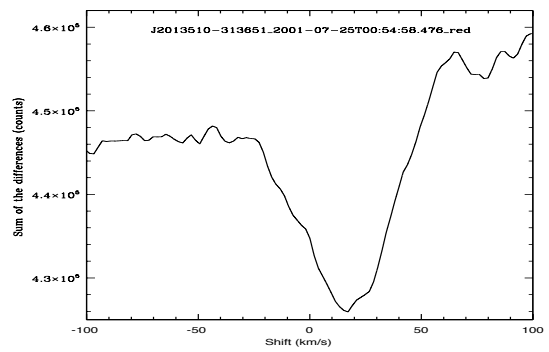
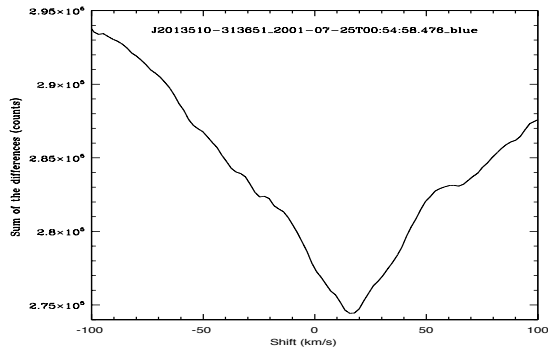
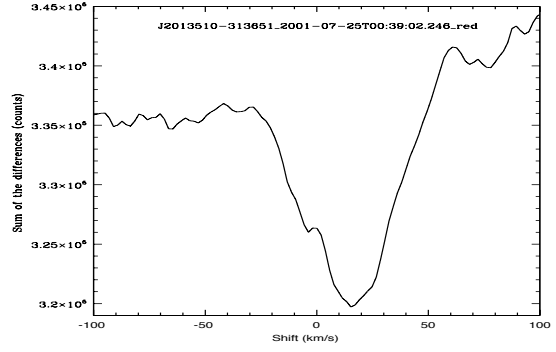
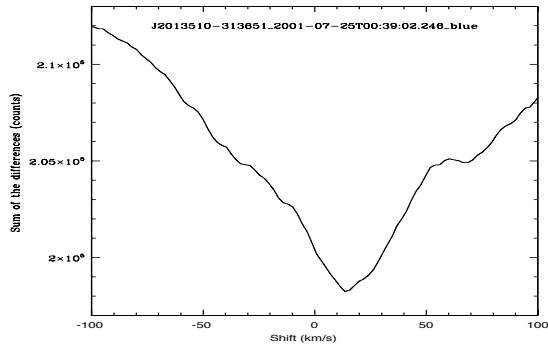
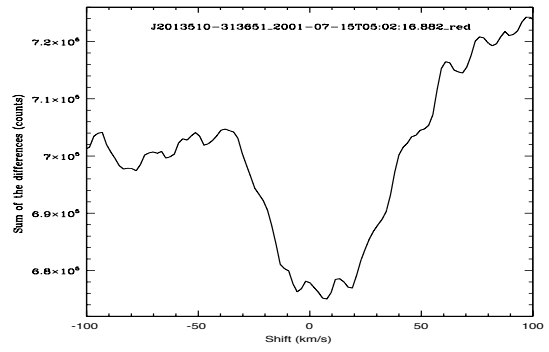
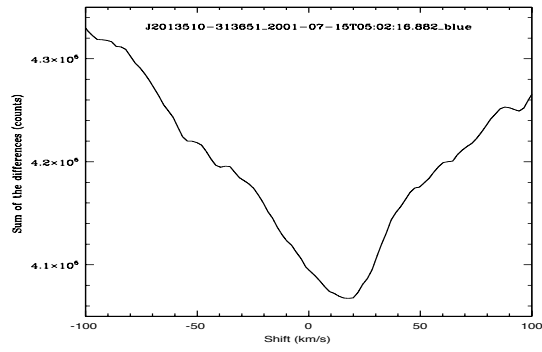
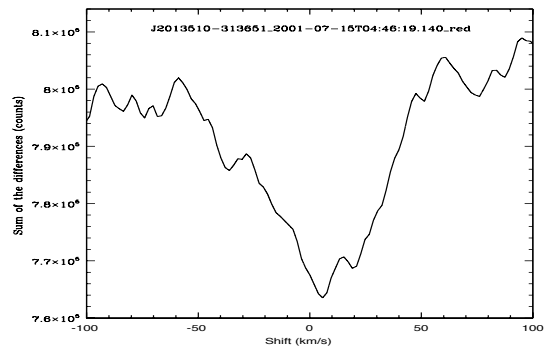
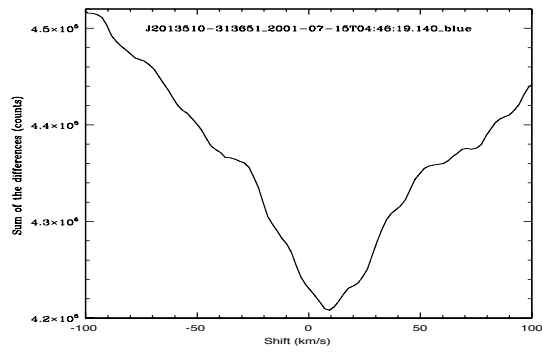
2MASS J12372705-2117481



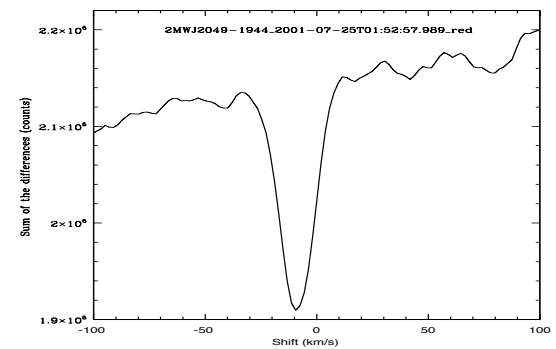
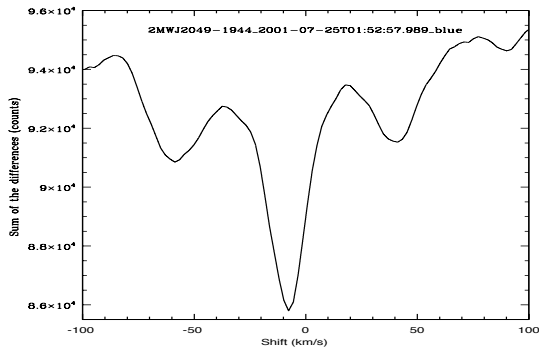
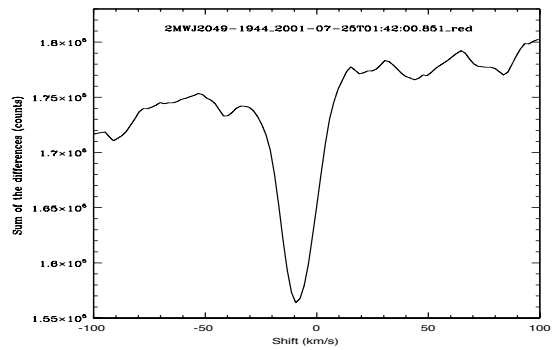
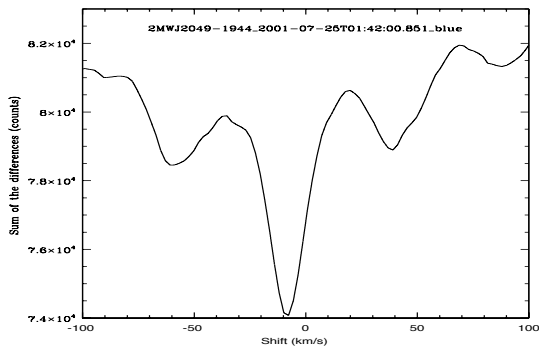
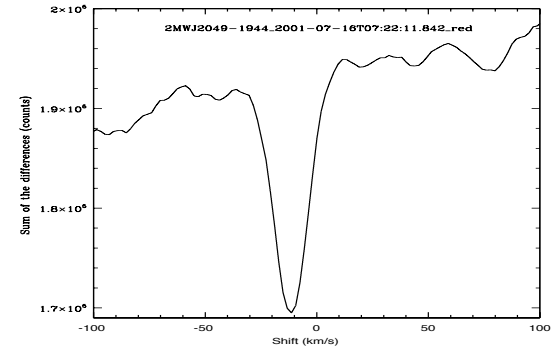
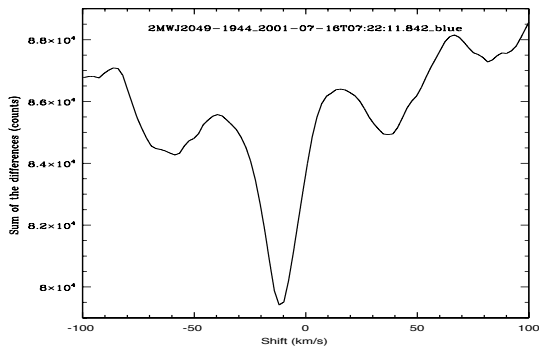
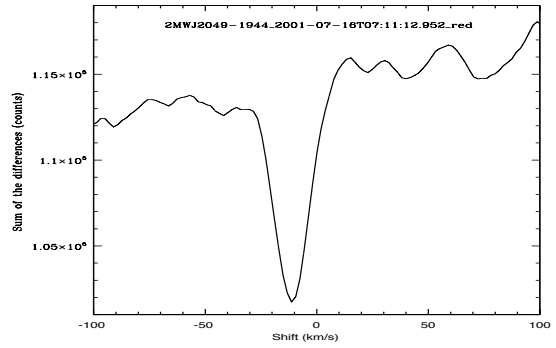
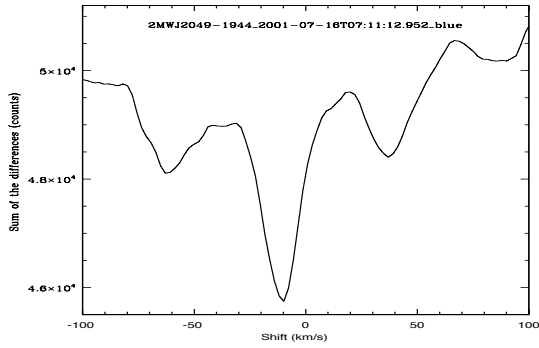


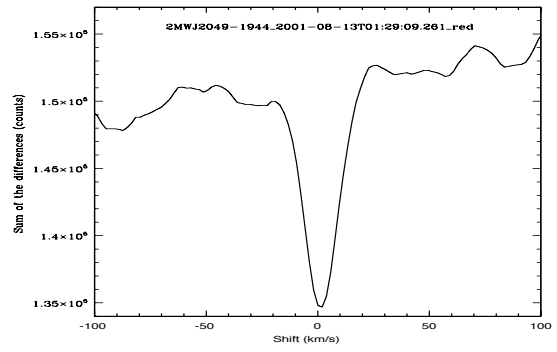
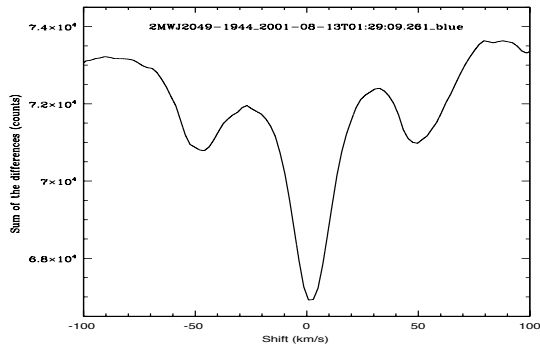
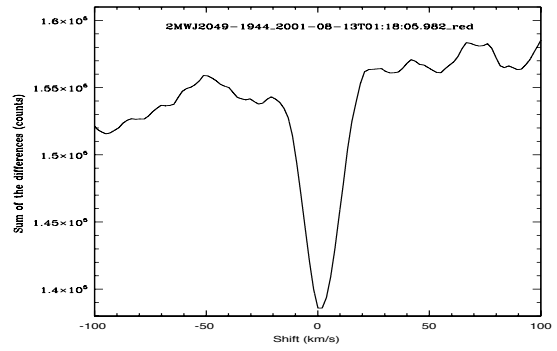
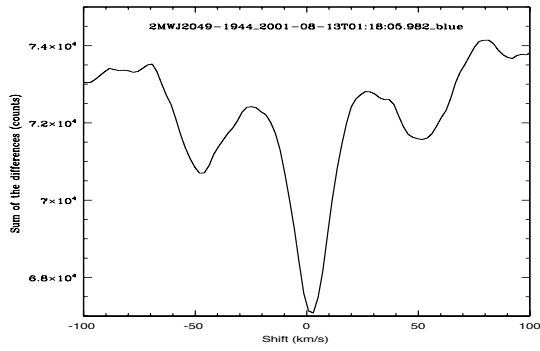
2MASSW J2013510-313651



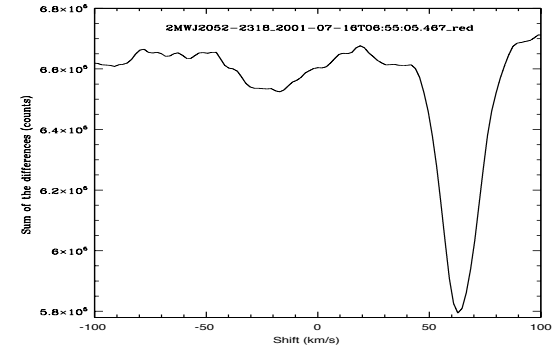
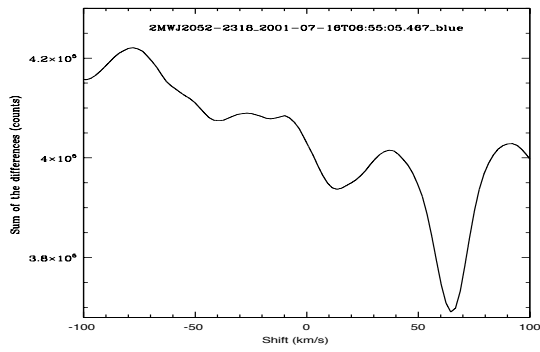
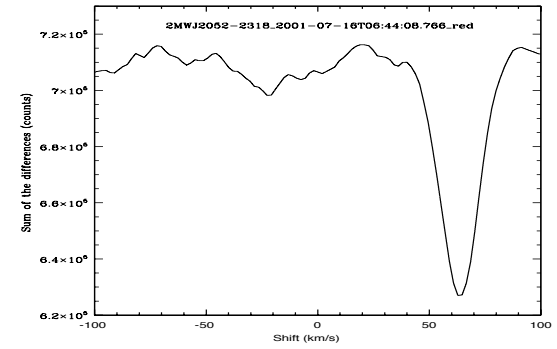
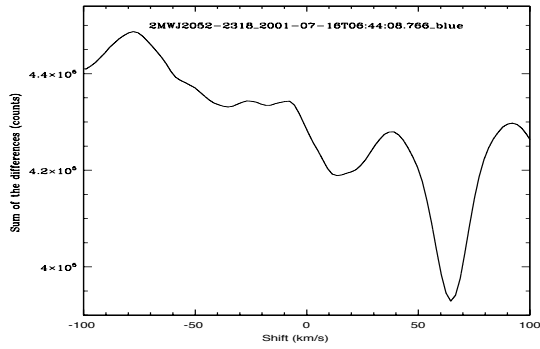


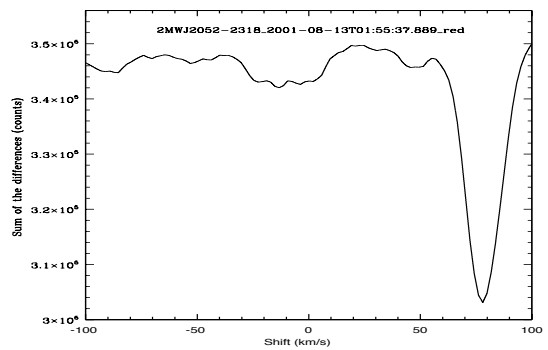
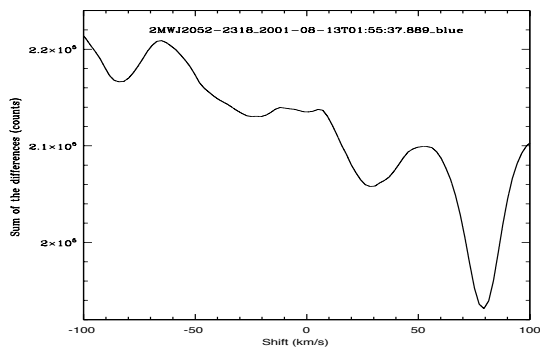
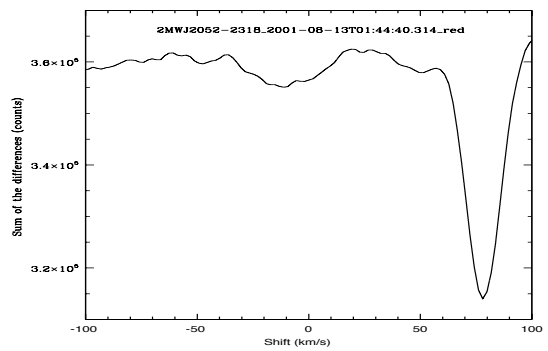
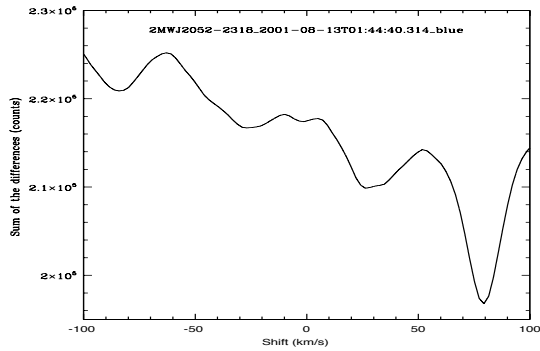
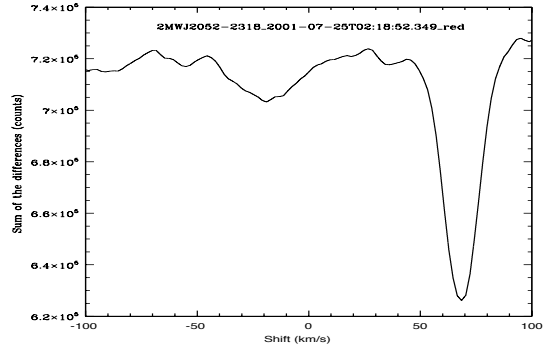
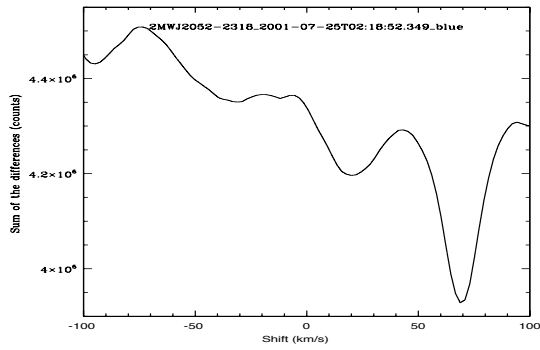
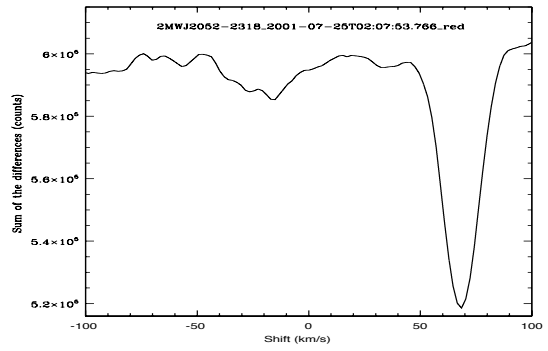
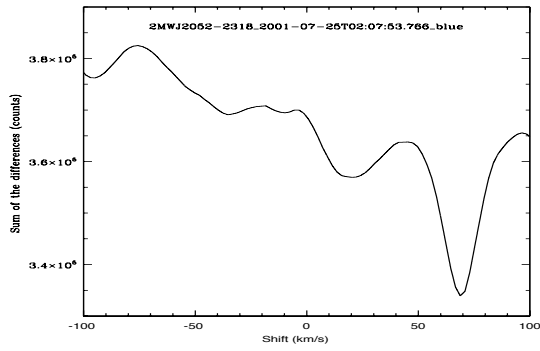
2MASS J20491972-1944324



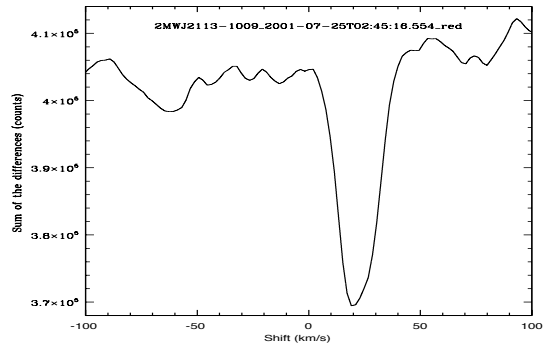
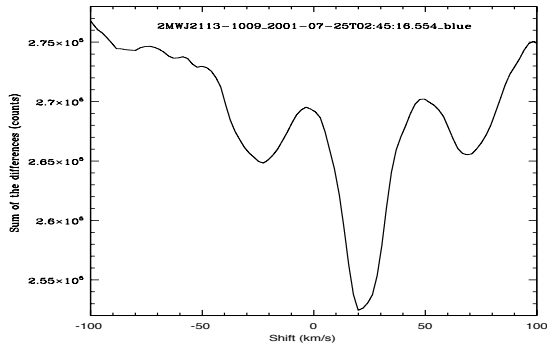
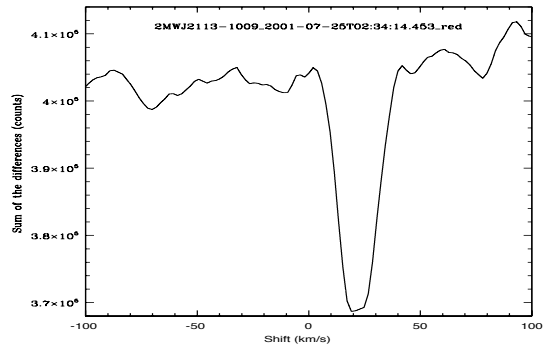
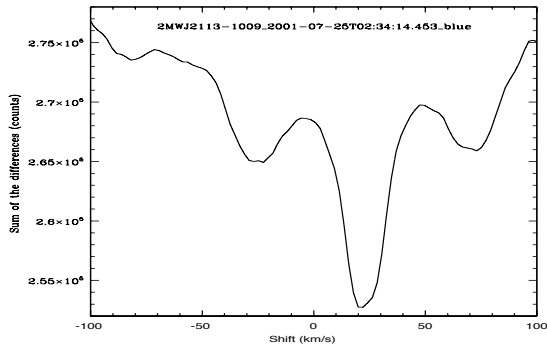
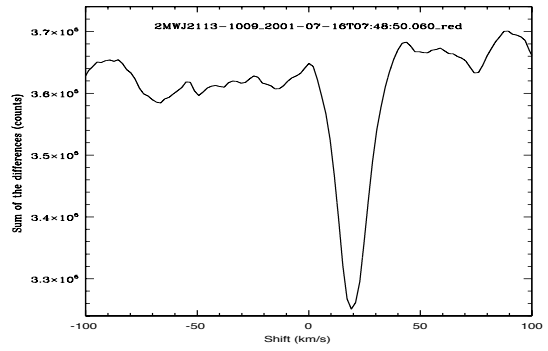
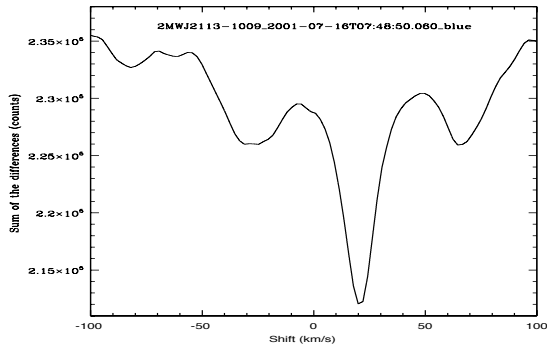
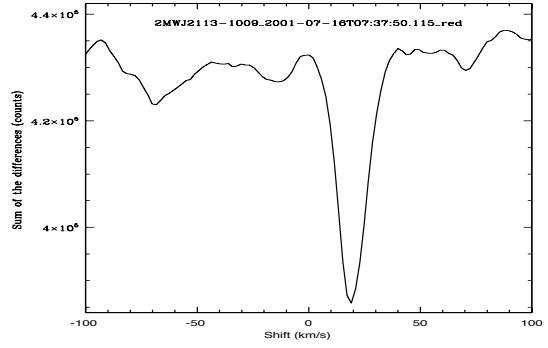
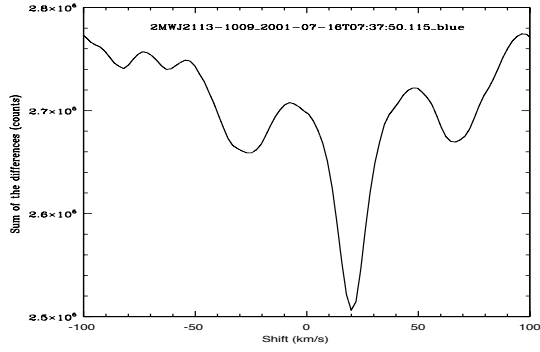


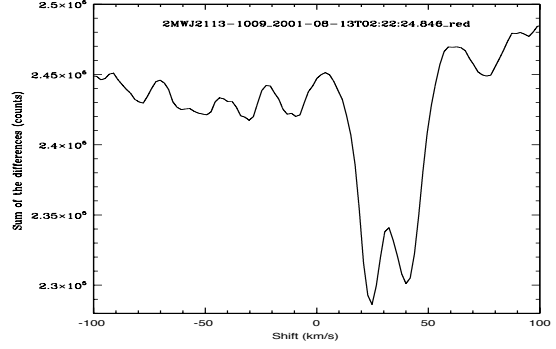
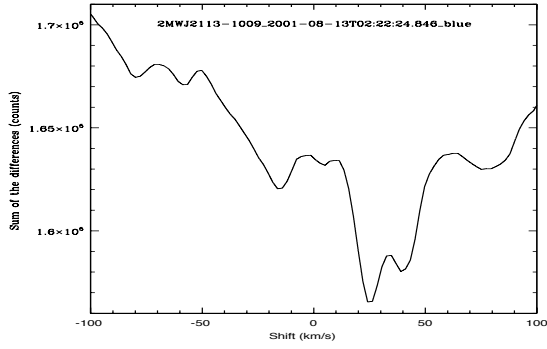
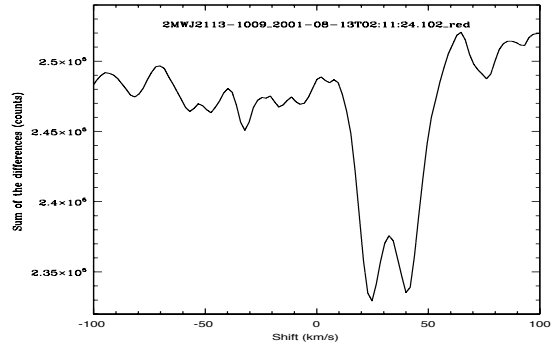
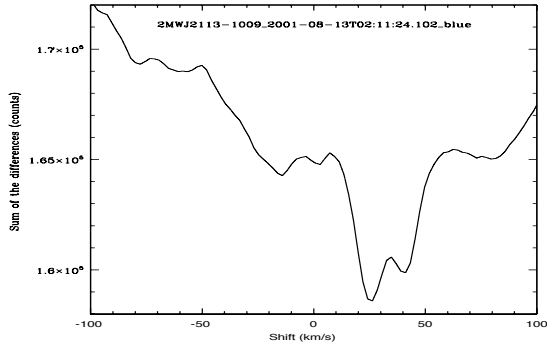
2MASS J20520861-2318096



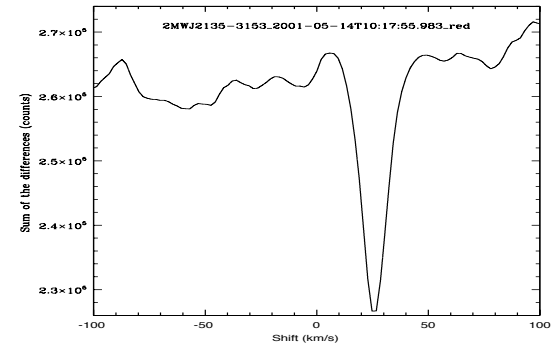
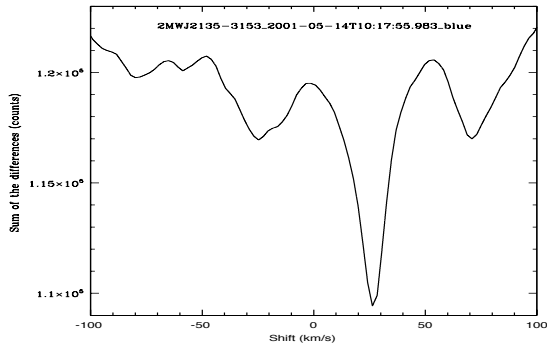
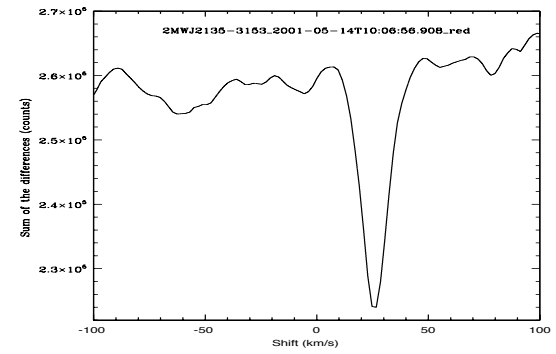
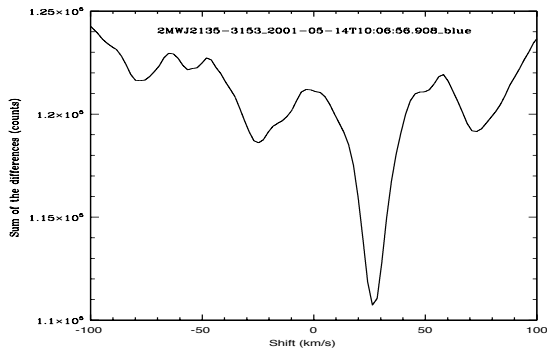


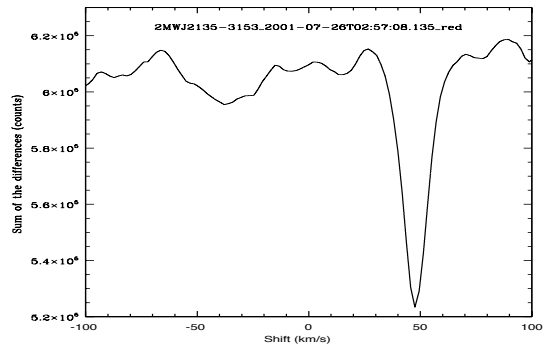
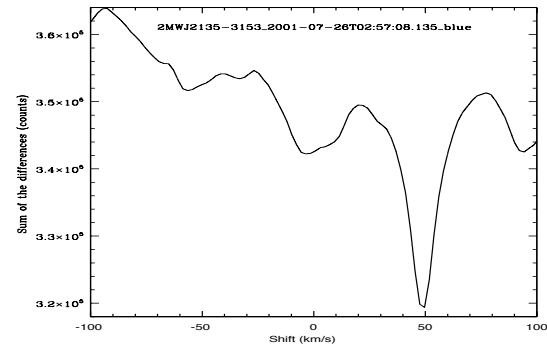
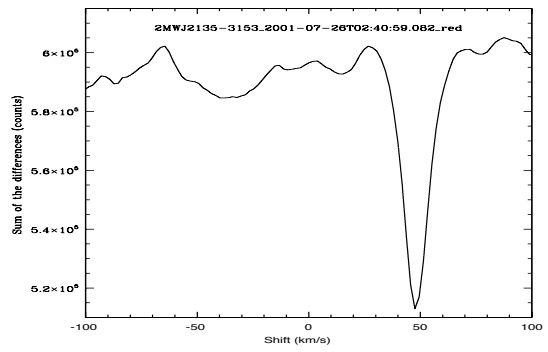
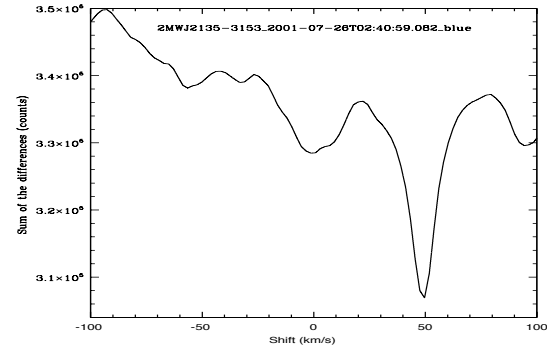
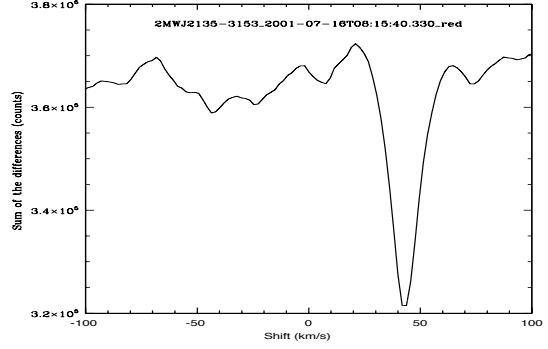
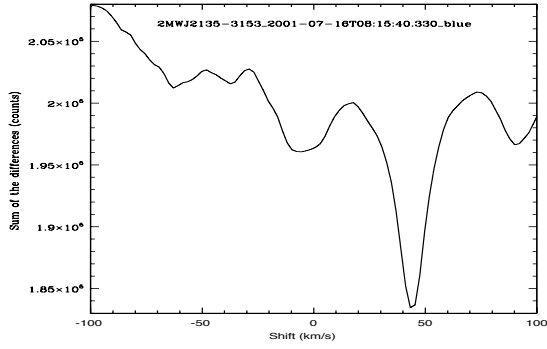
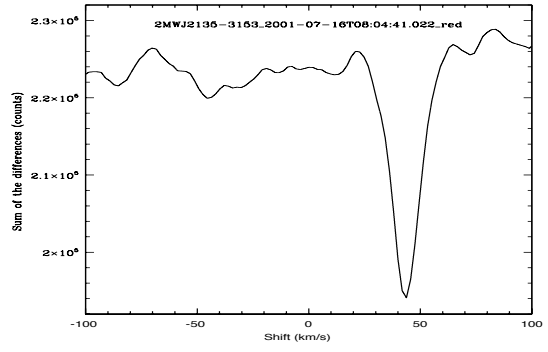
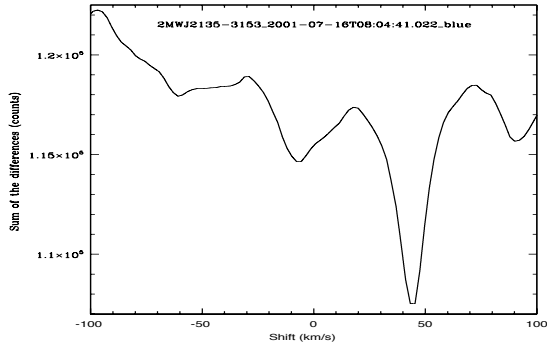
2MASS J21130293-1009412



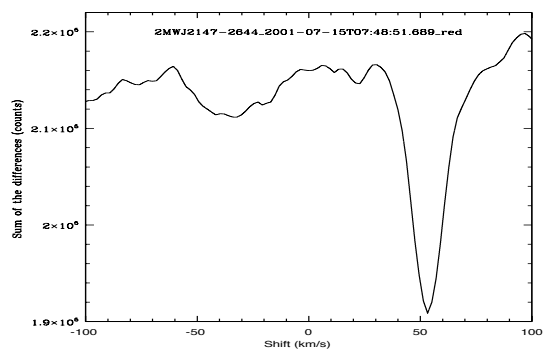
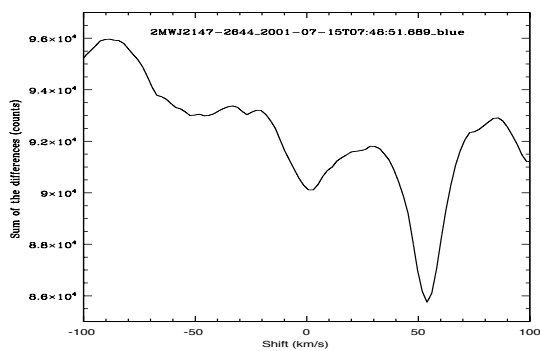
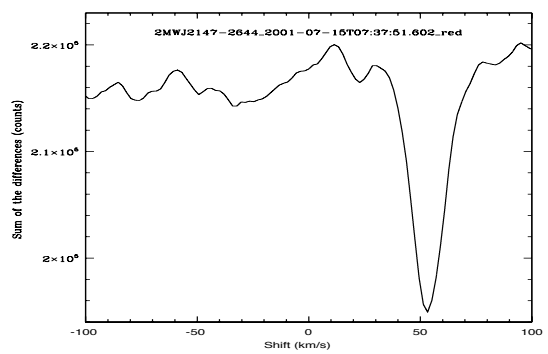
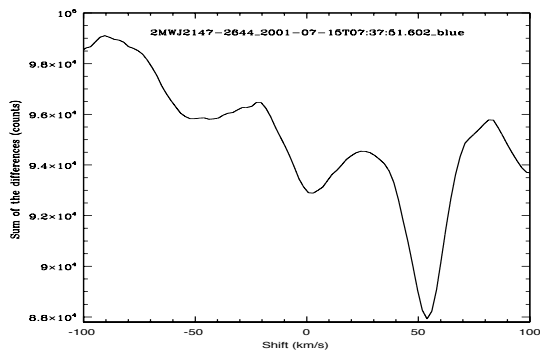
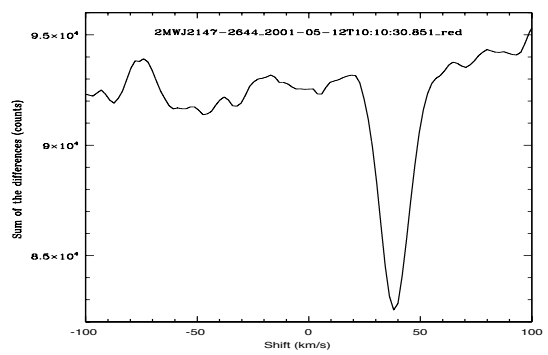
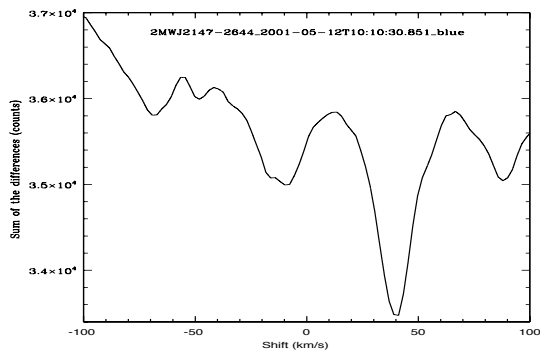
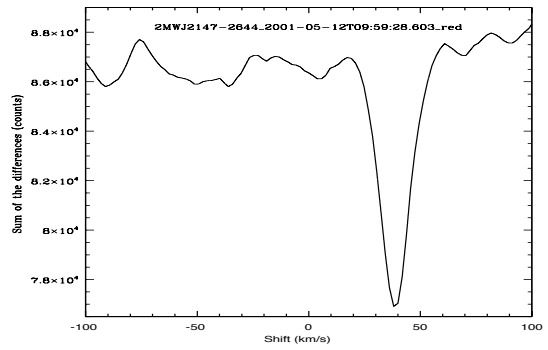
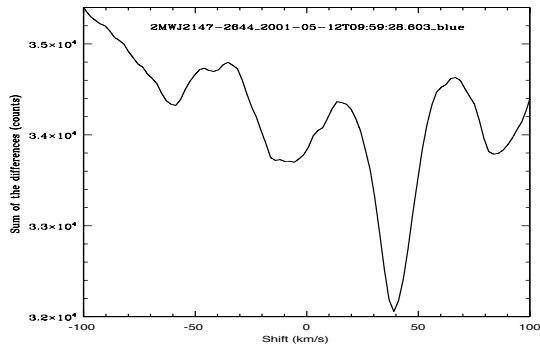


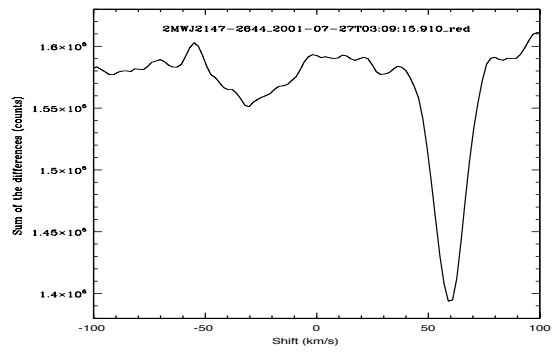
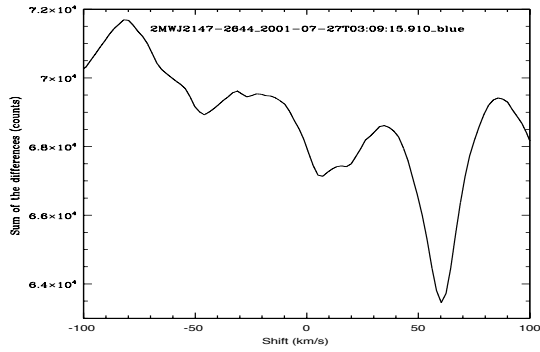
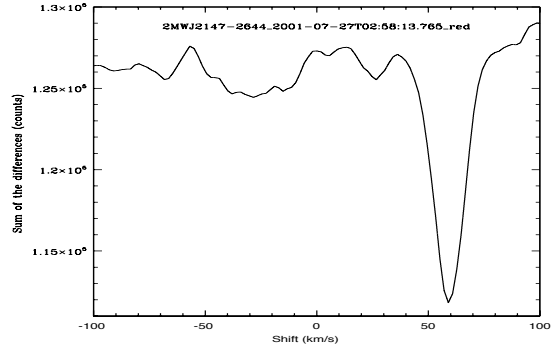
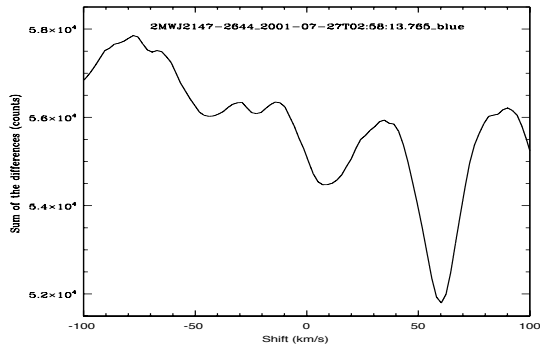
2MASS J2135146-315345



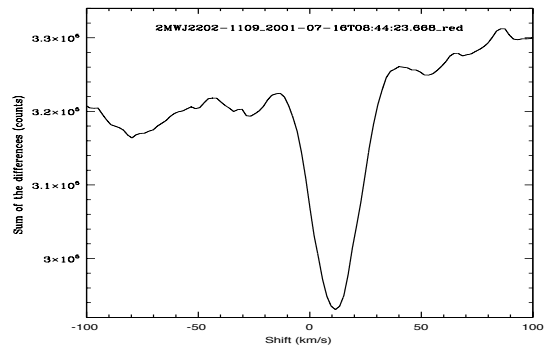
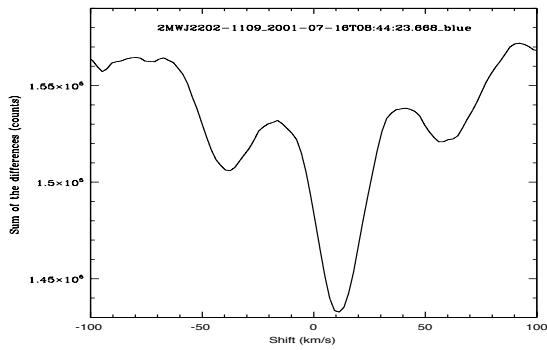
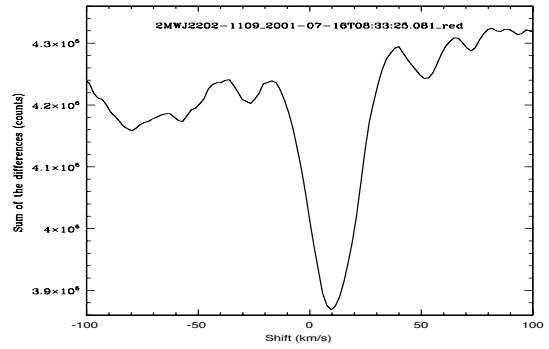
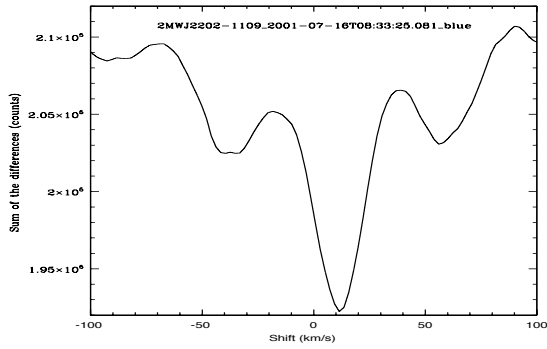


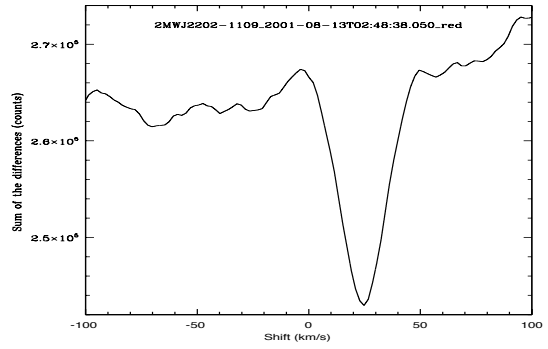
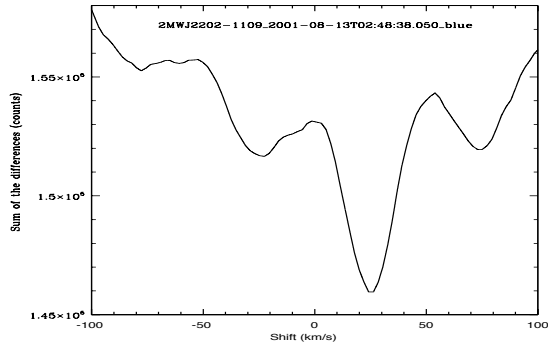
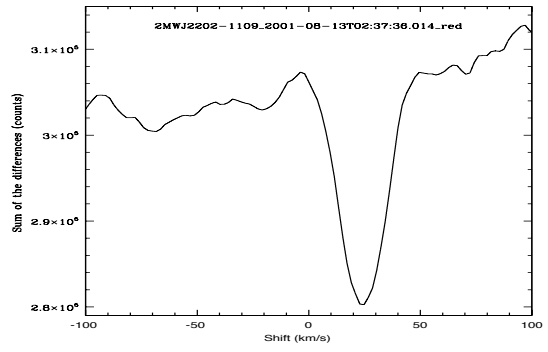
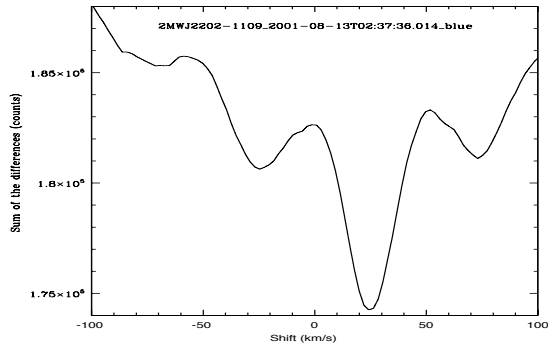
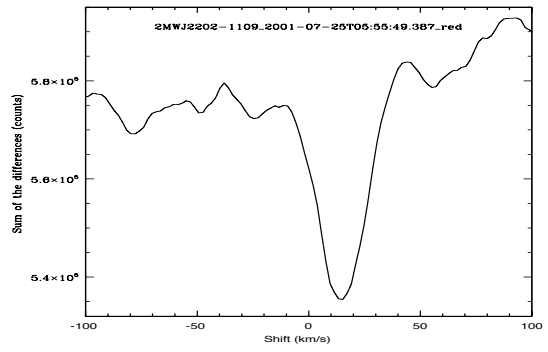
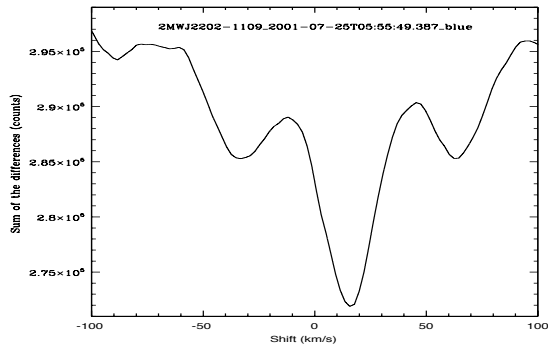
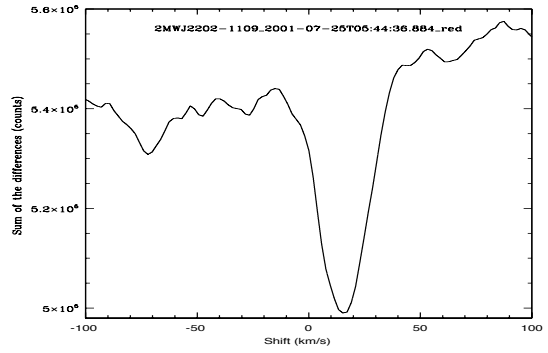
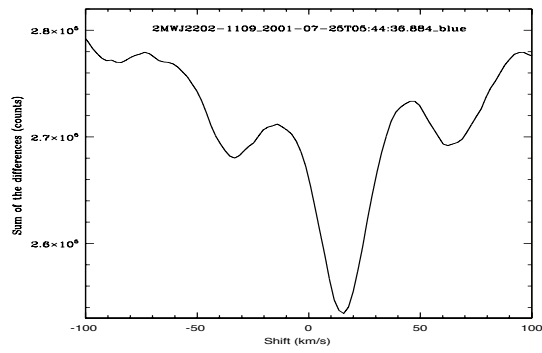
2MASS J2147446-264406



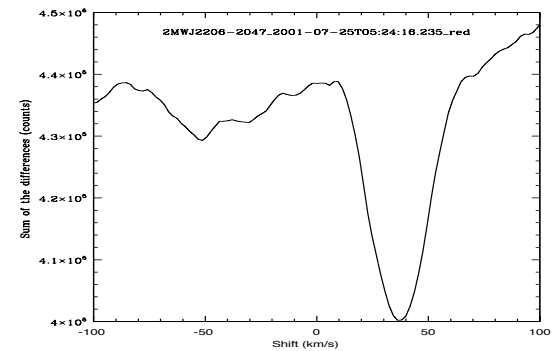
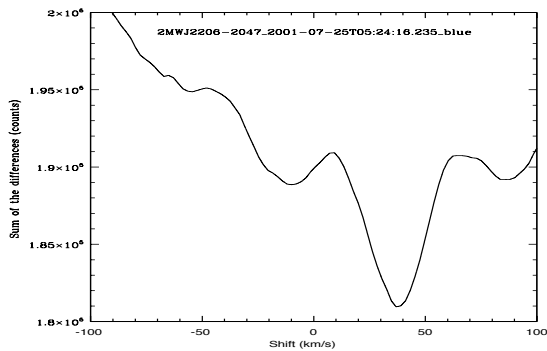
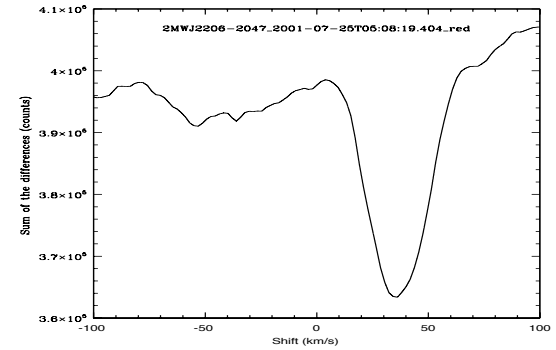
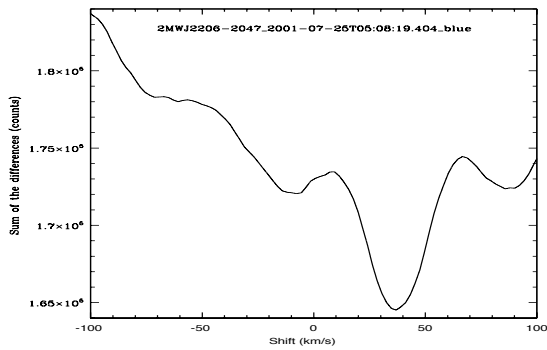
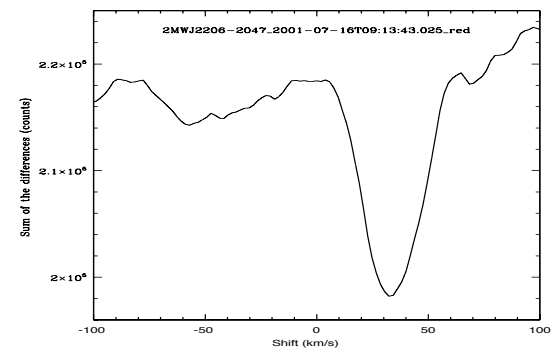
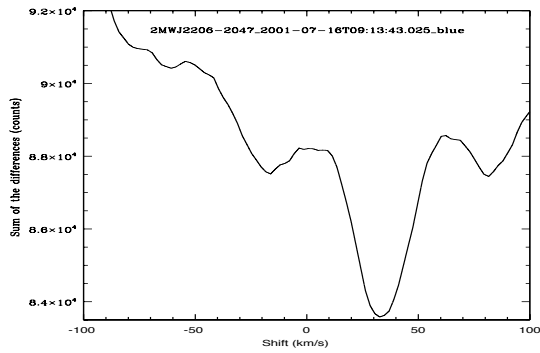
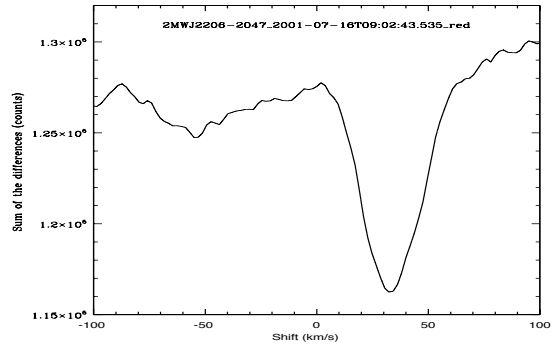
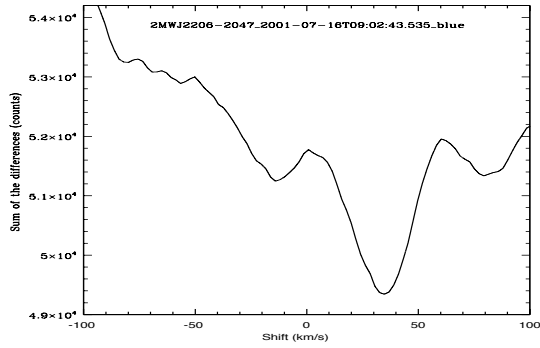


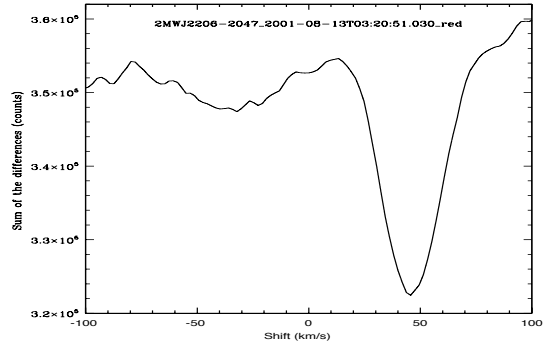
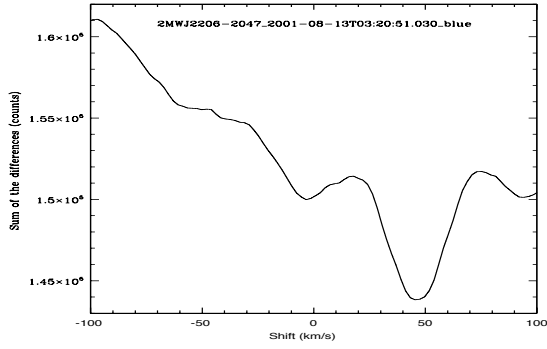
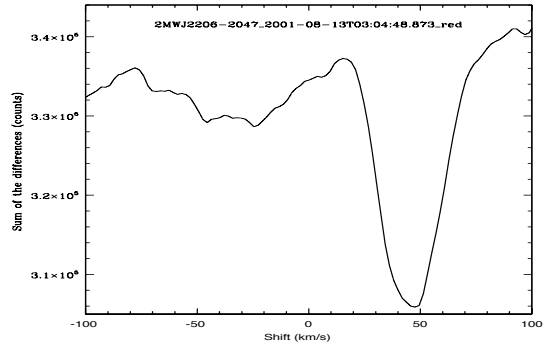
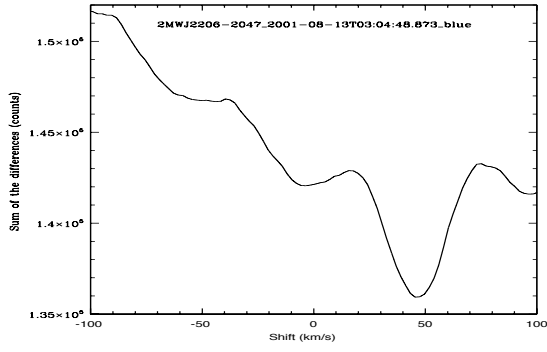
2MASS J2202112-110946



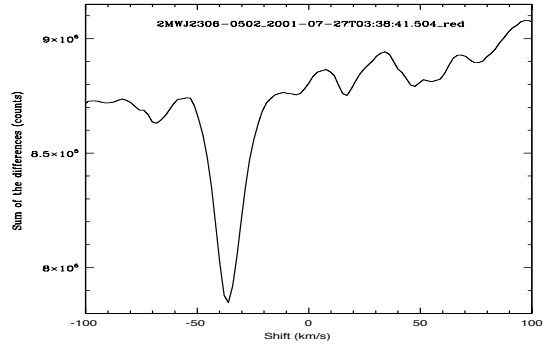
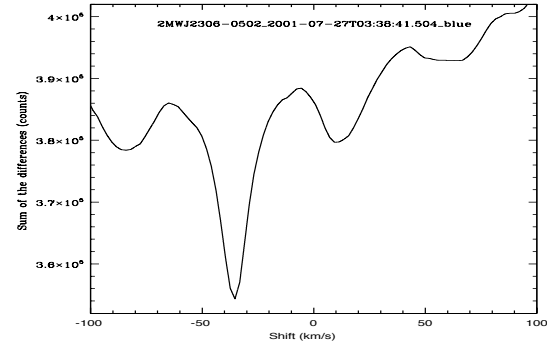
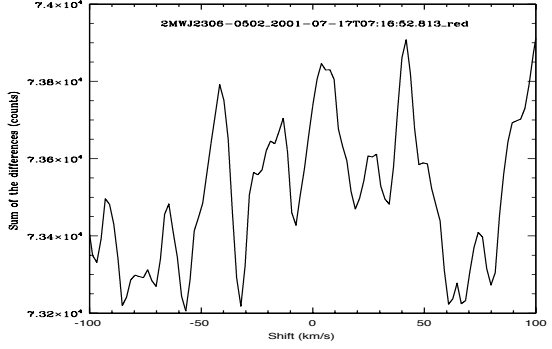
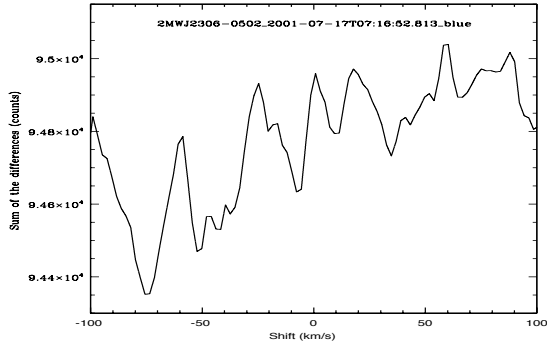


2MASS J2206228-204705

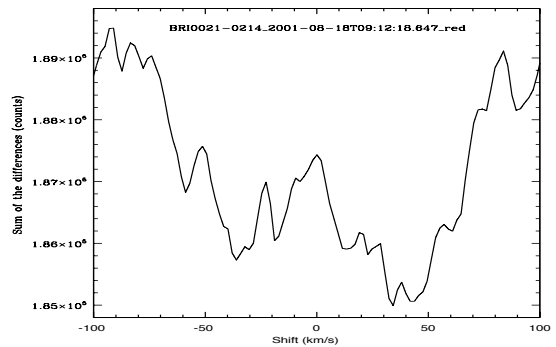
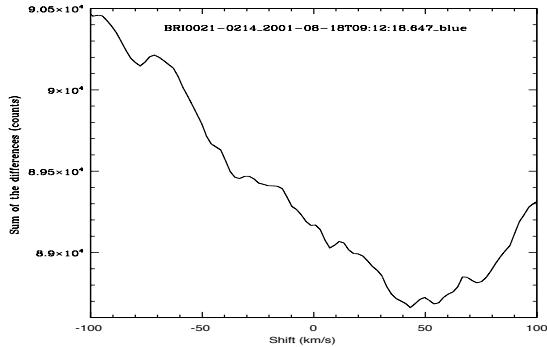
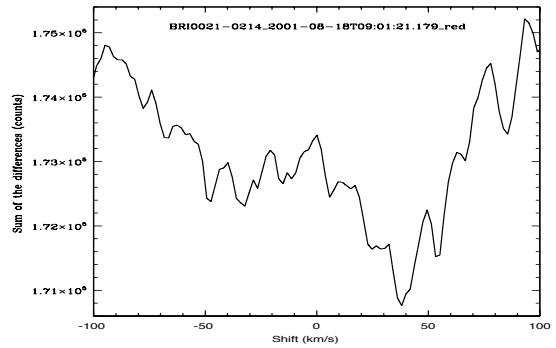
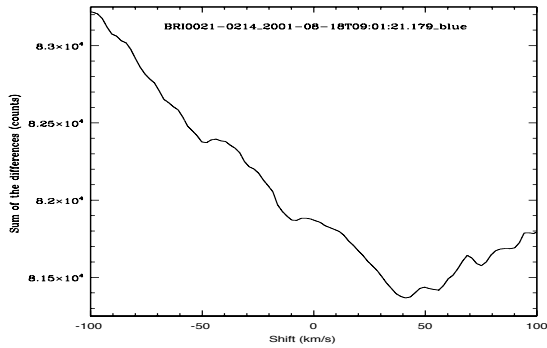
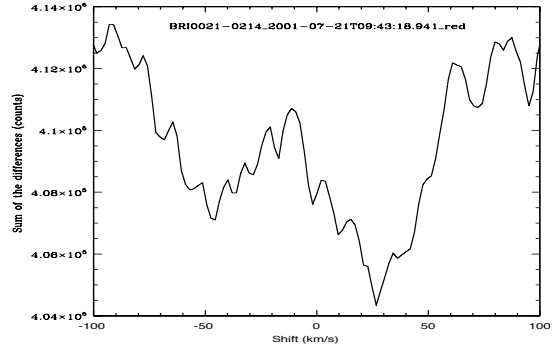
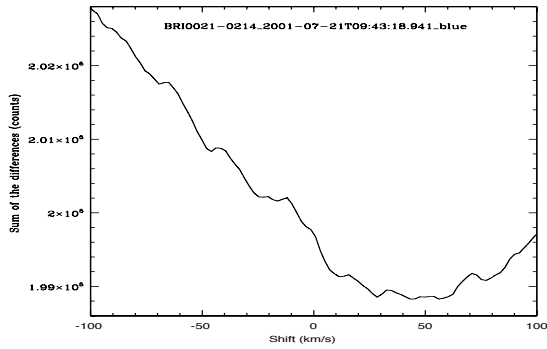
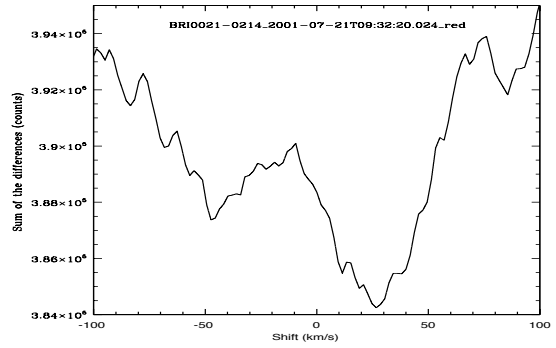
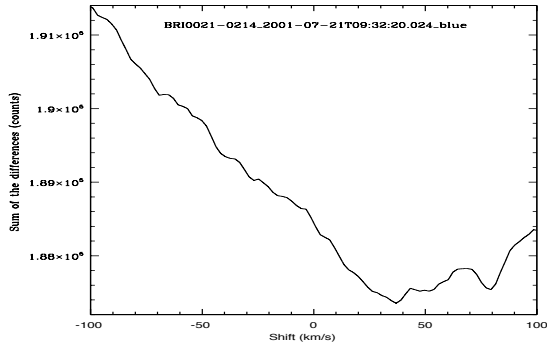


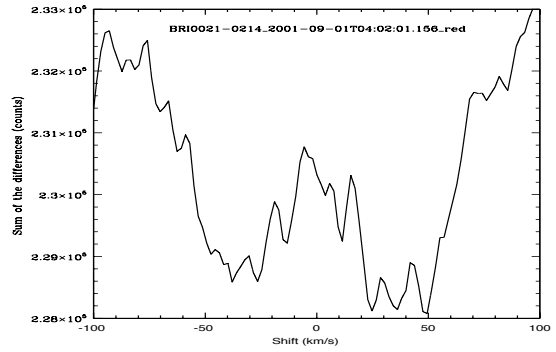
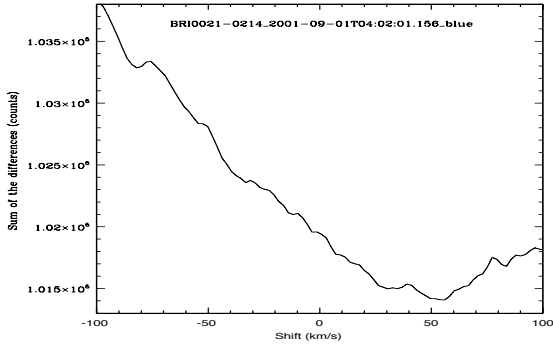
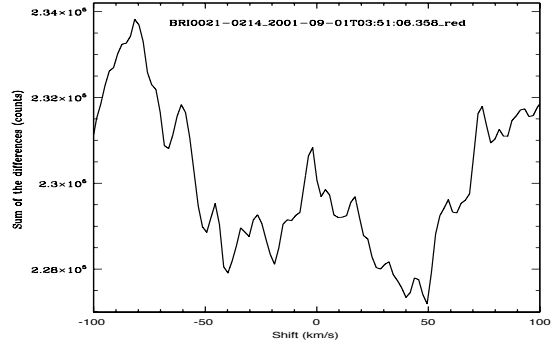
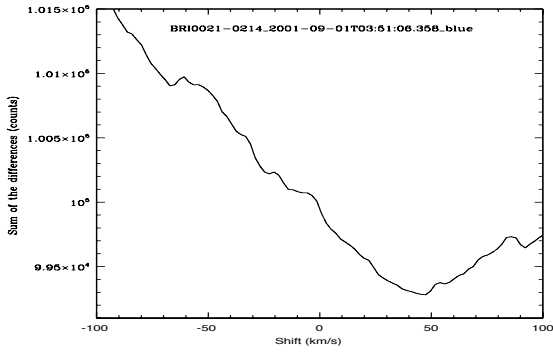


2MASS J23062928-0502285

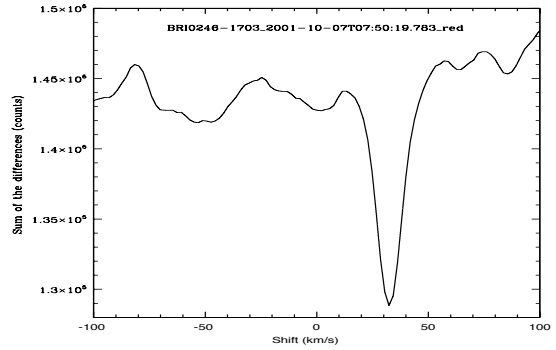
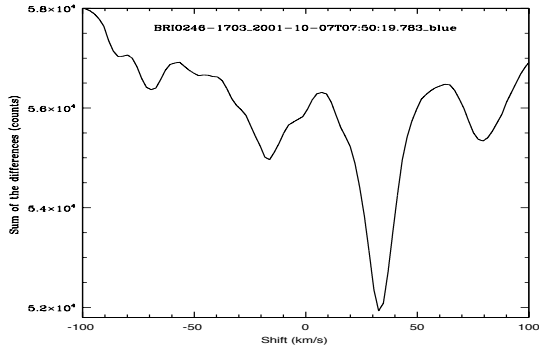
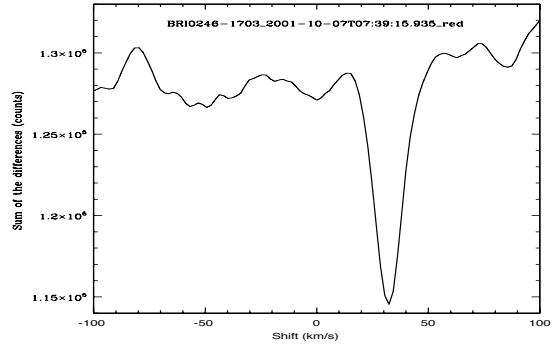
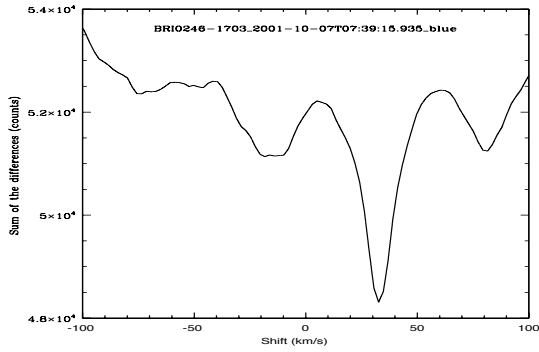


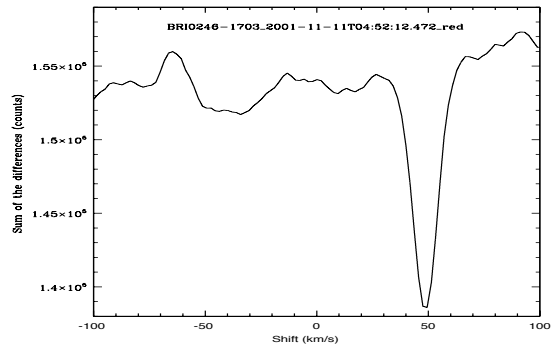
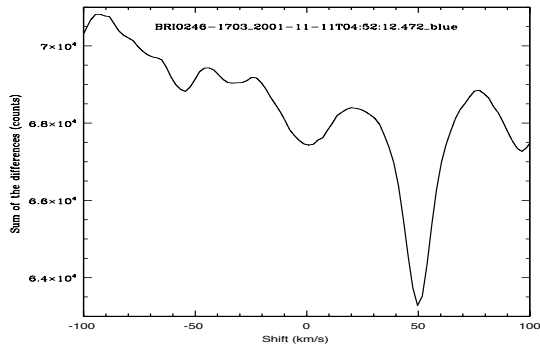
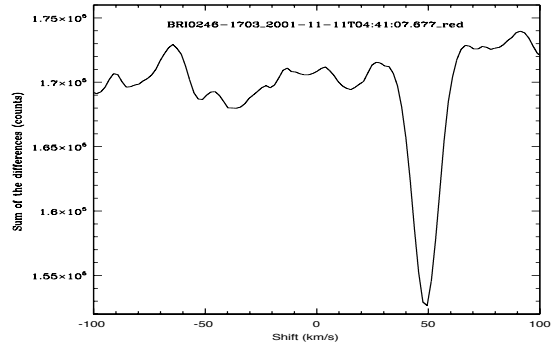
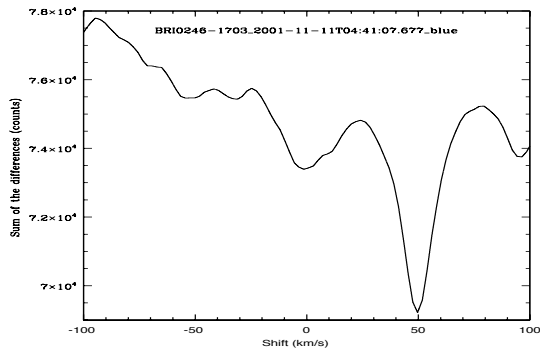
BRI B0021-0214



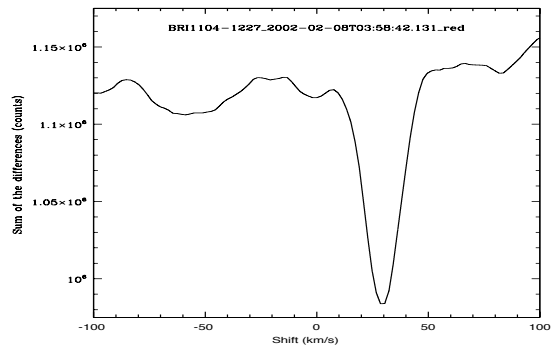
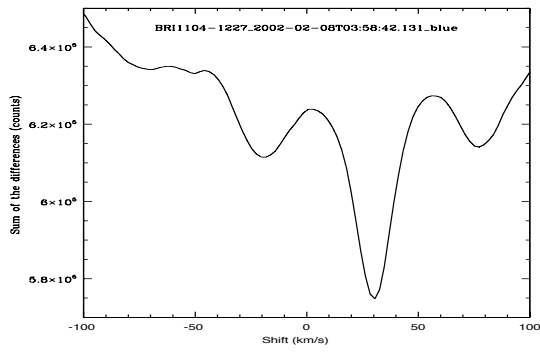
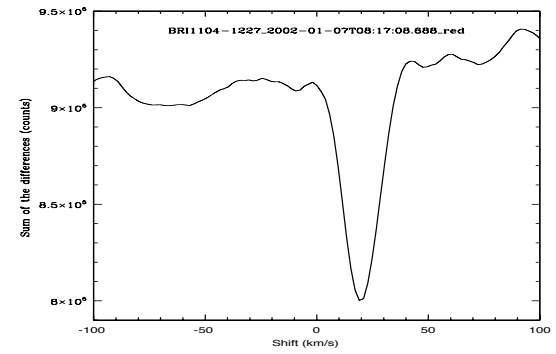
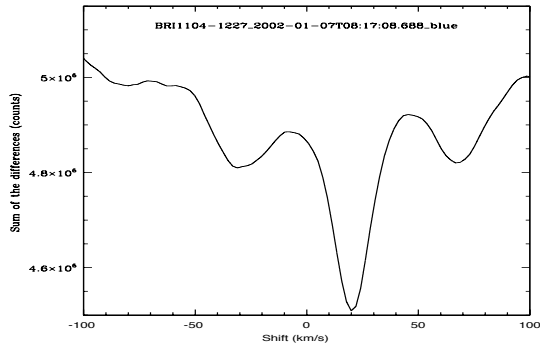


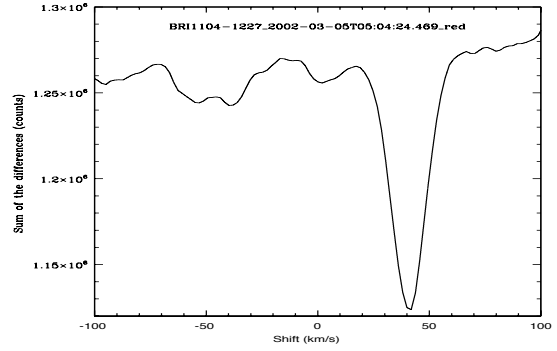
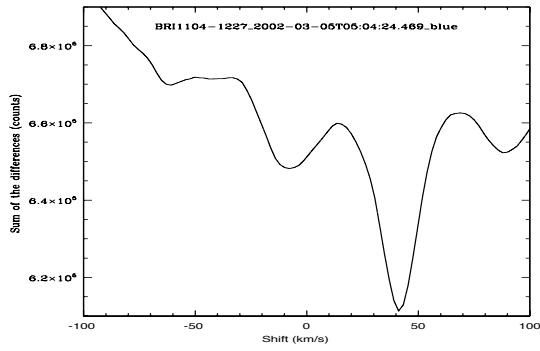
BRI B0246-1703



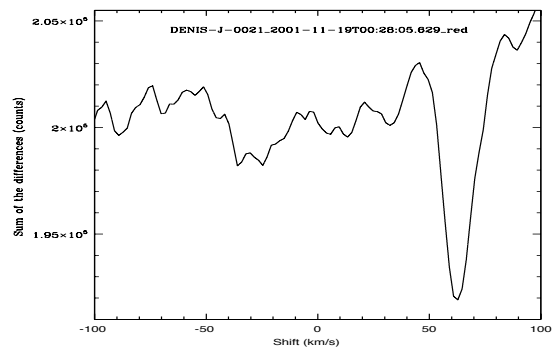
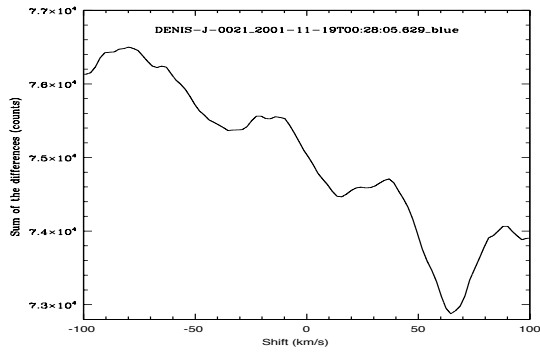
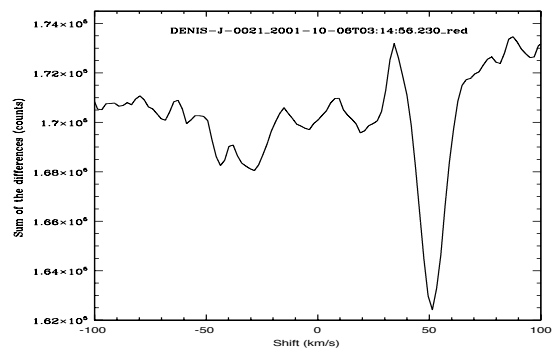
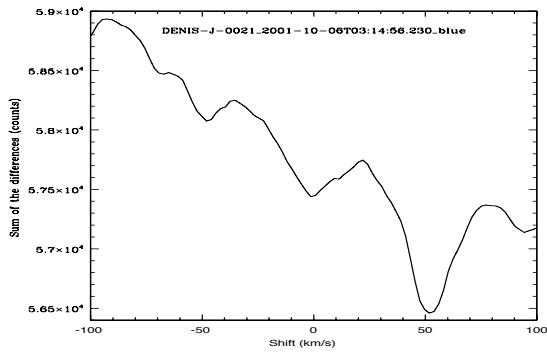
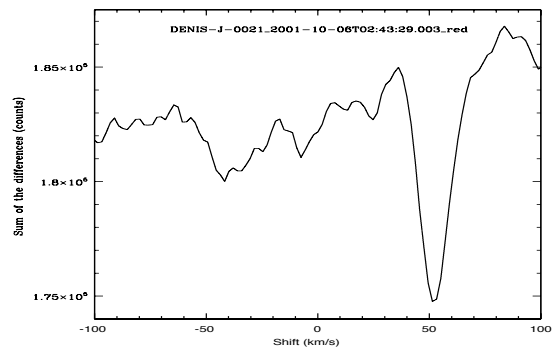
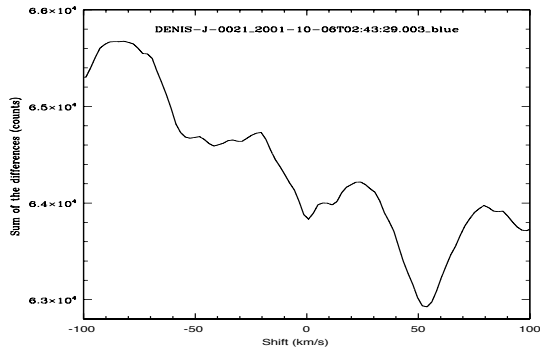


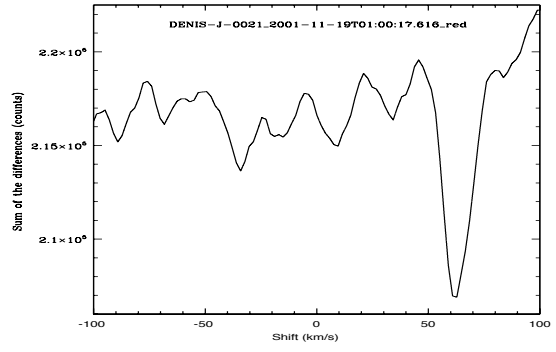
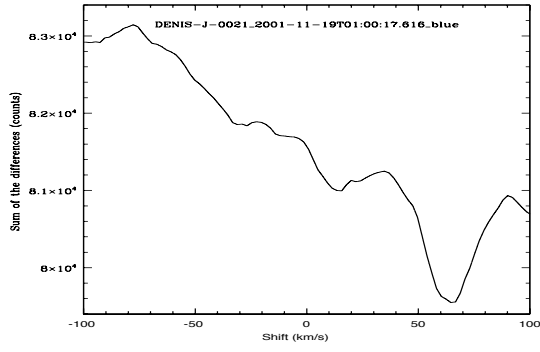
BRI B1104-1227



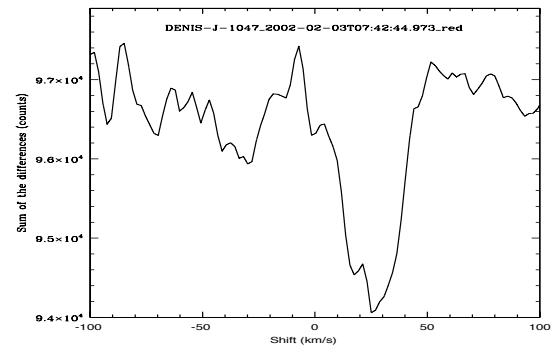
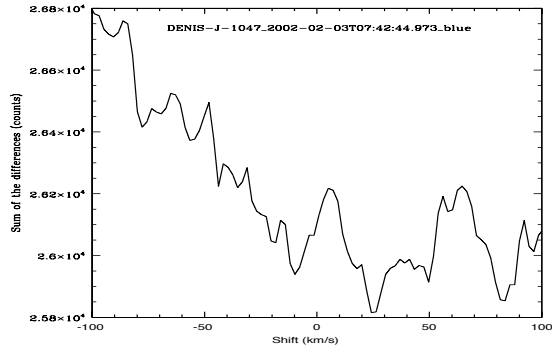
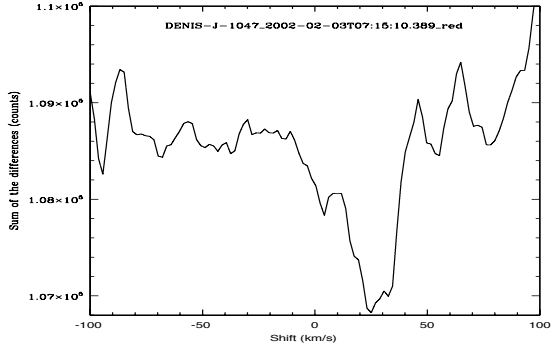
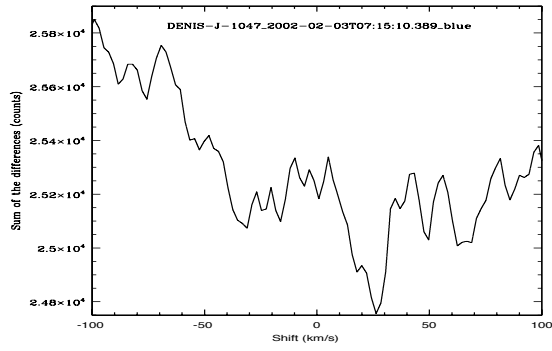
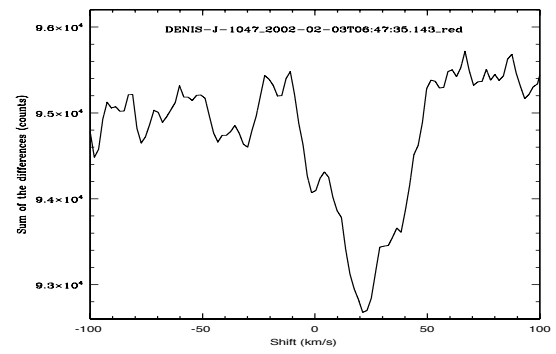
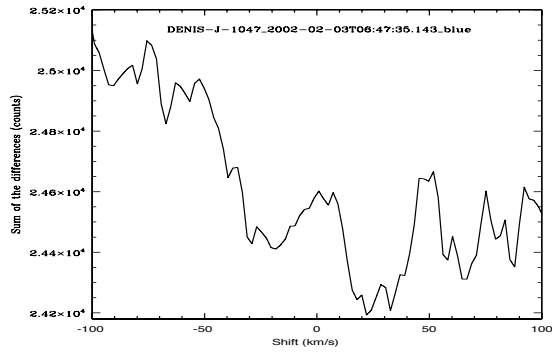


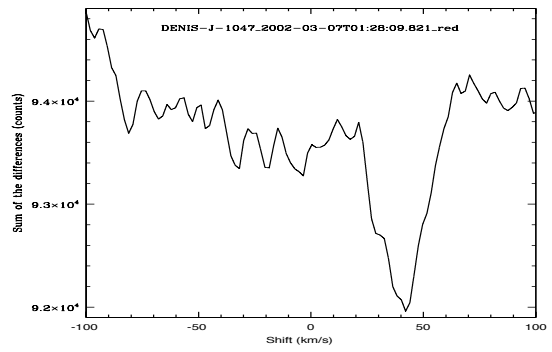
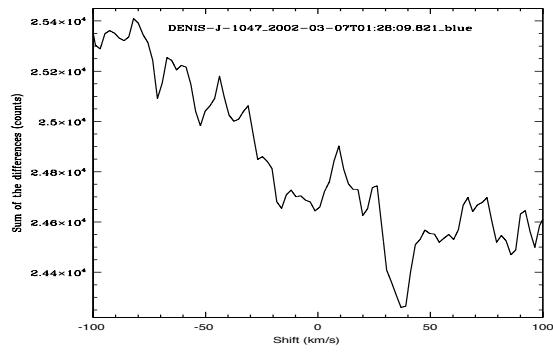
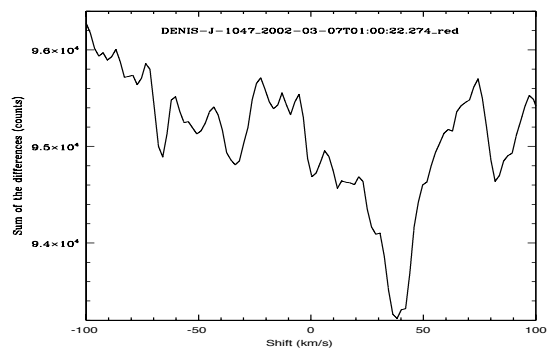
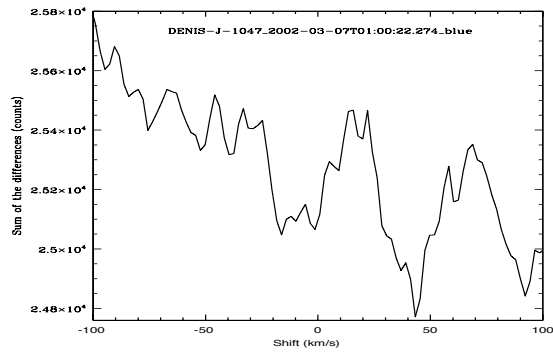
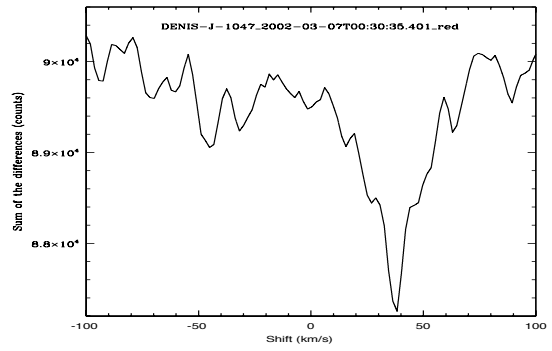
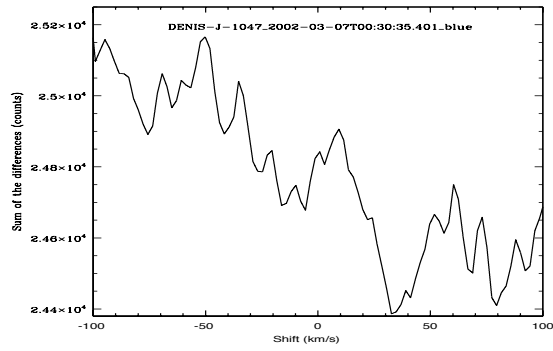
DENIS-P J0021.0-4244



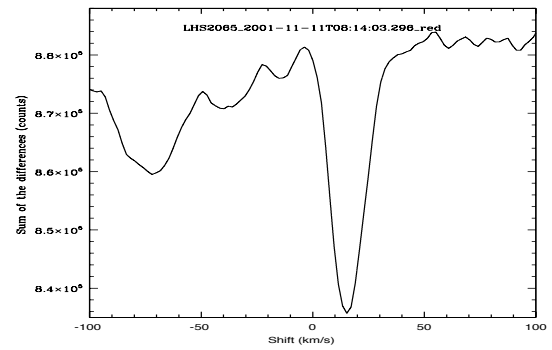
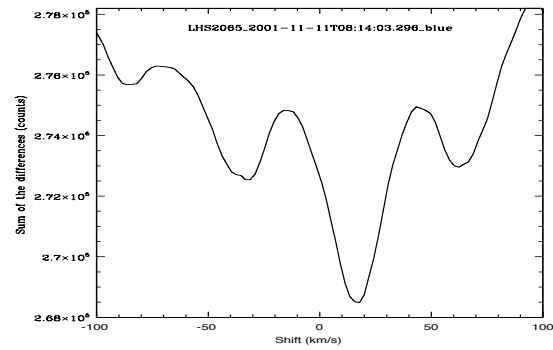


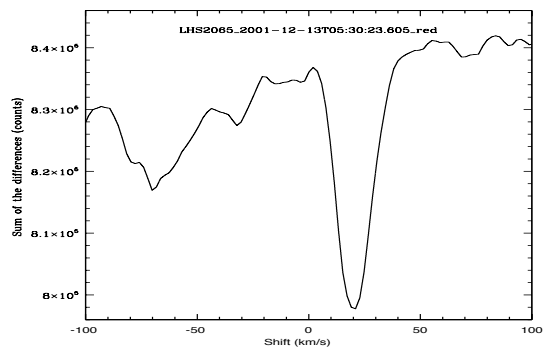
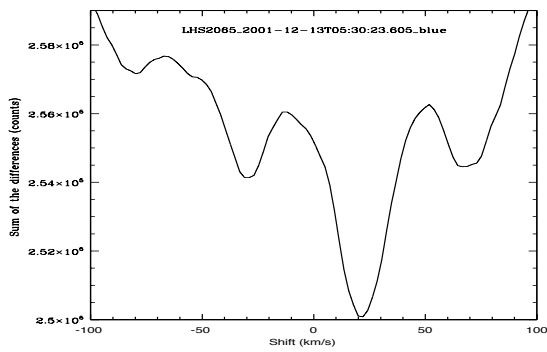
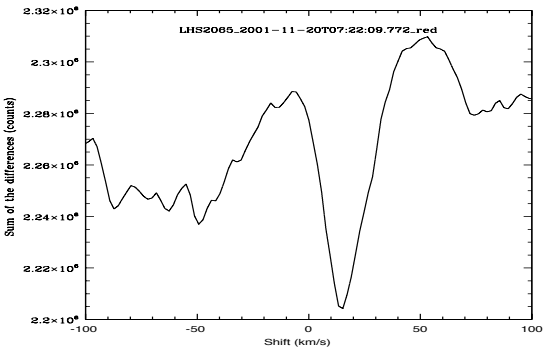
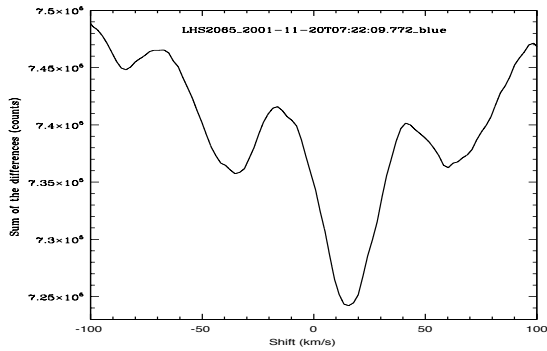
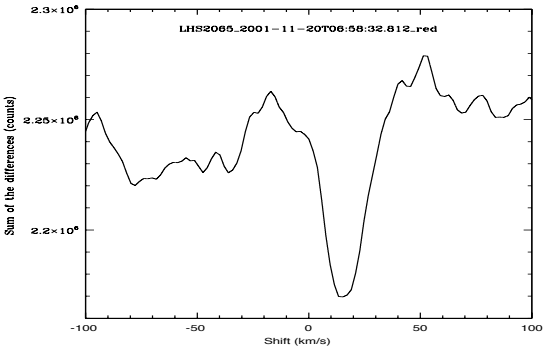
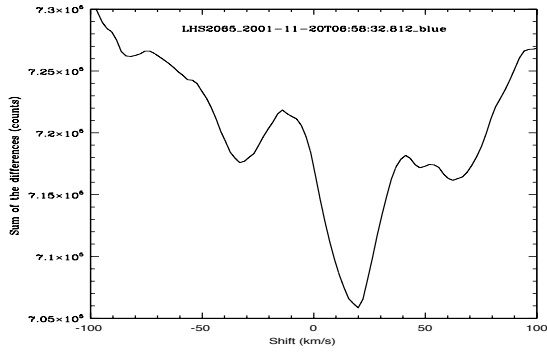
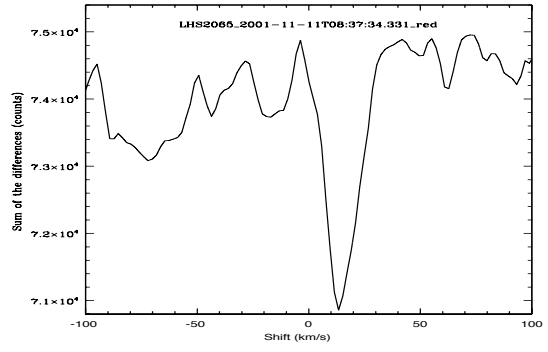
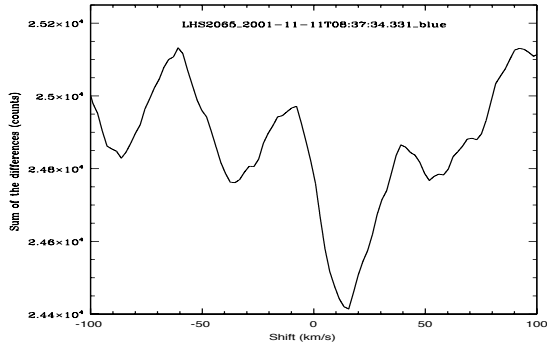
DENIS-P J1047.5-1815

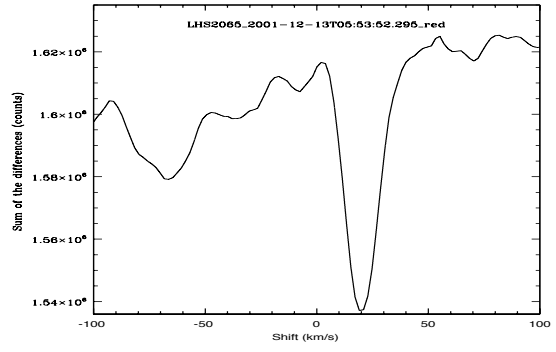
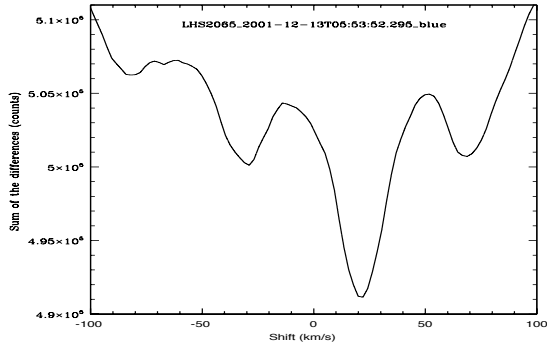




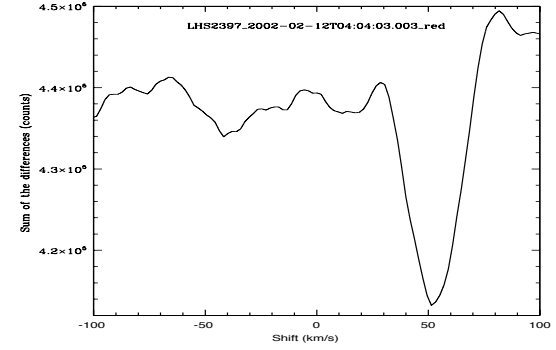
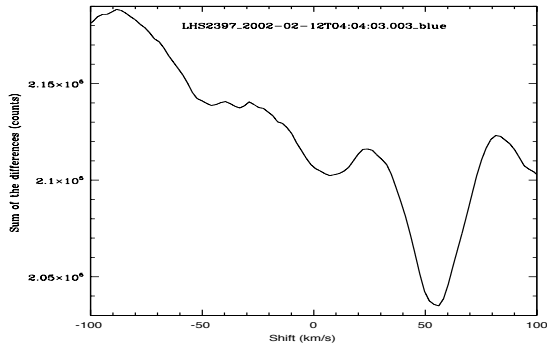
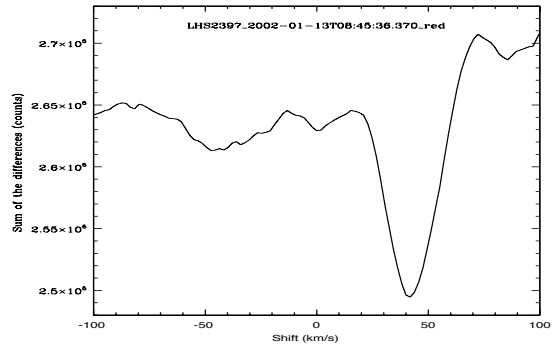
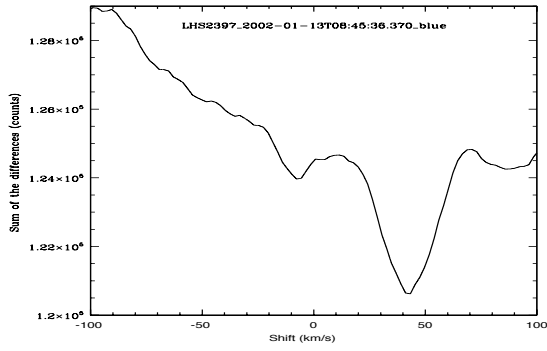
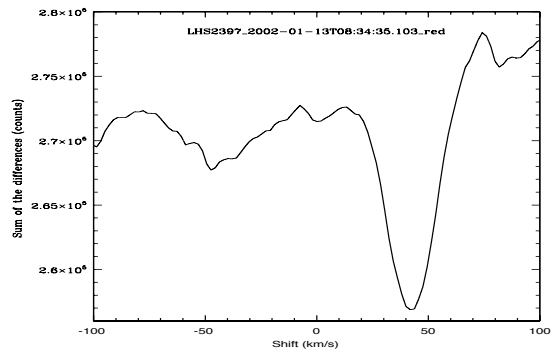
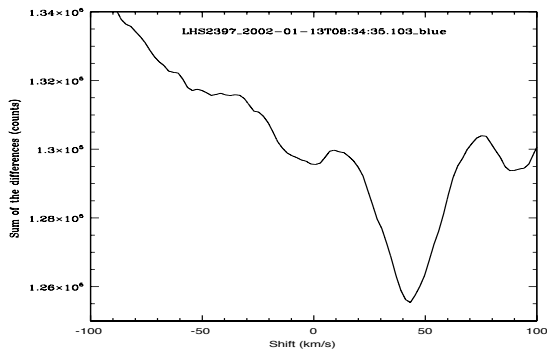
LHS 2065

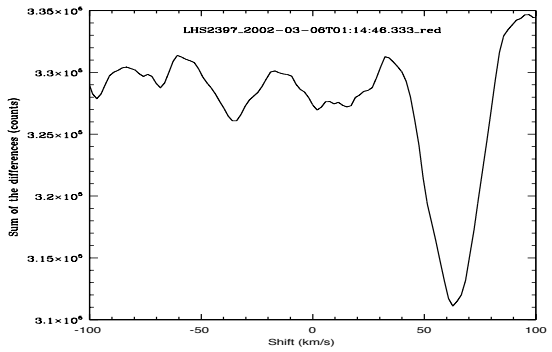
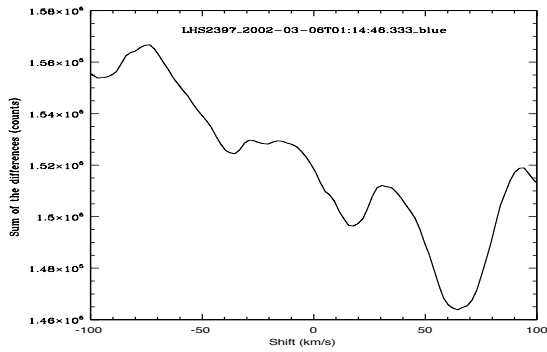
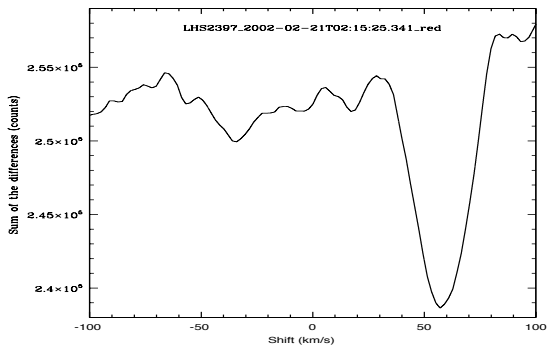
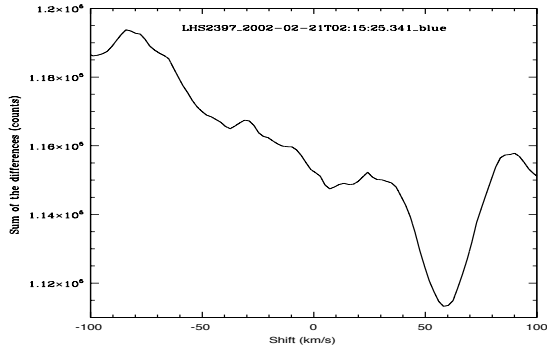
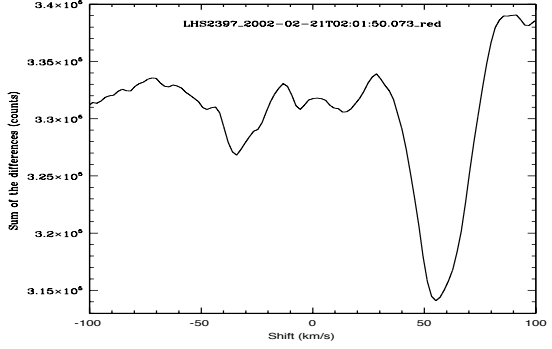
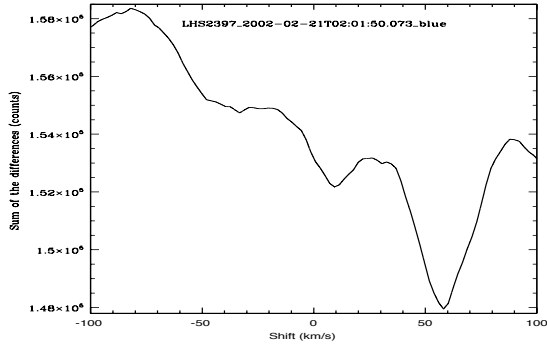
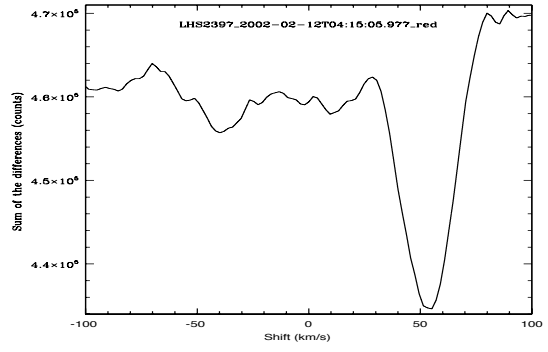
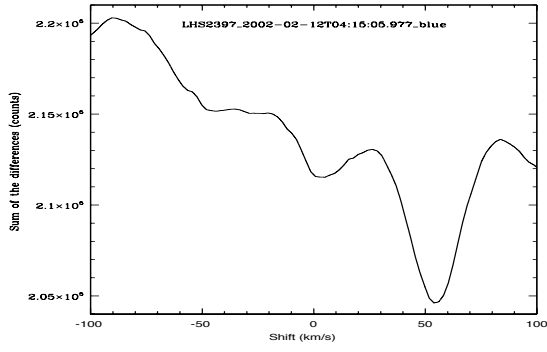


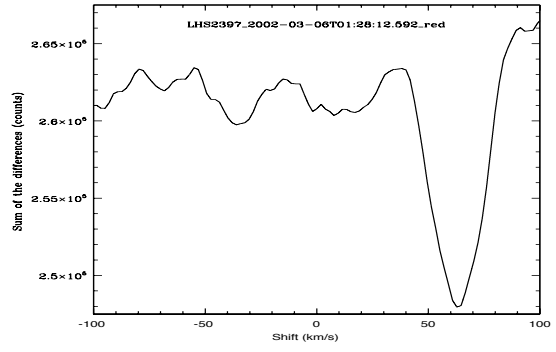
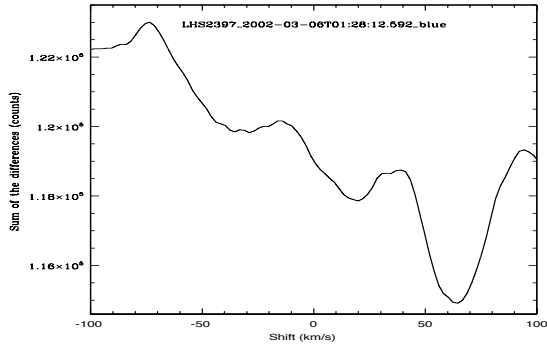




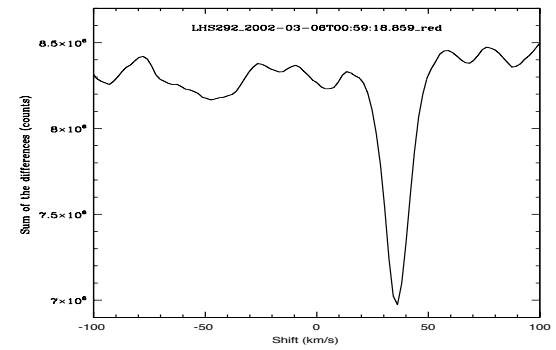
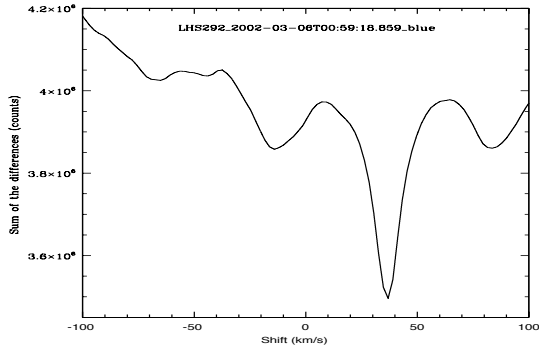
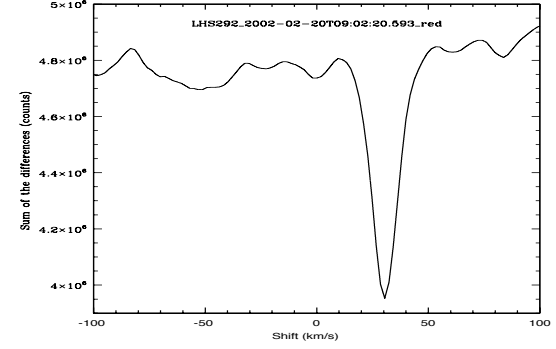
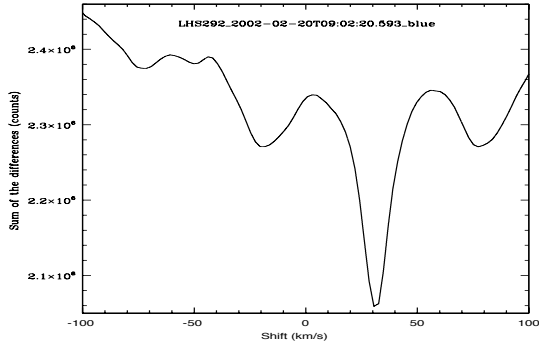
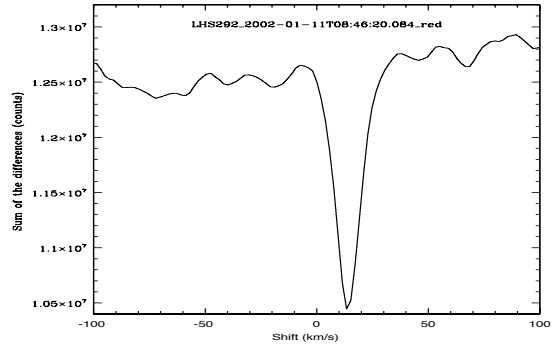
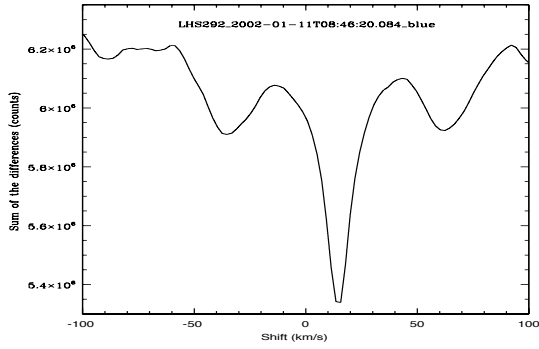
LHS 2397

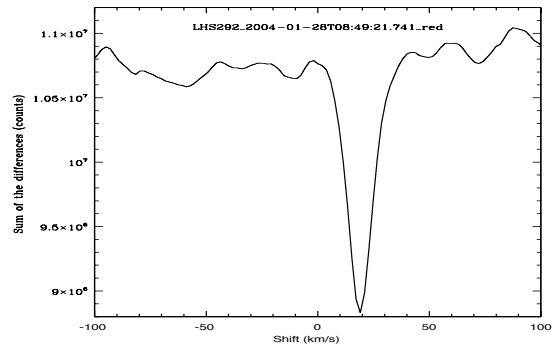
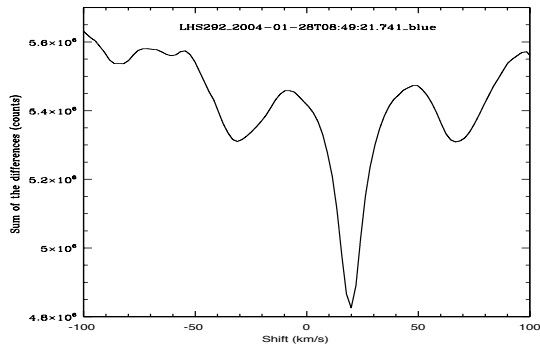
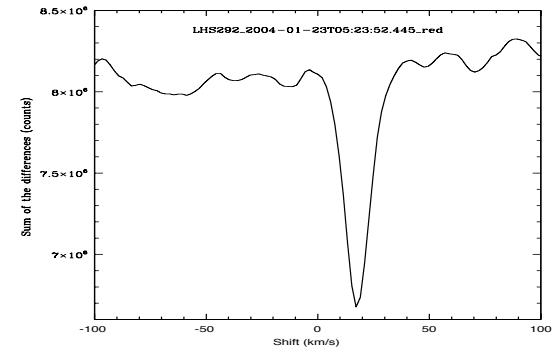
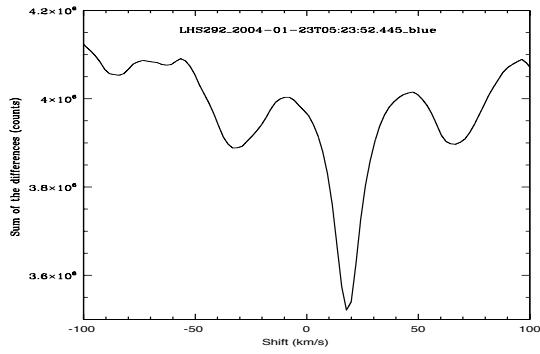
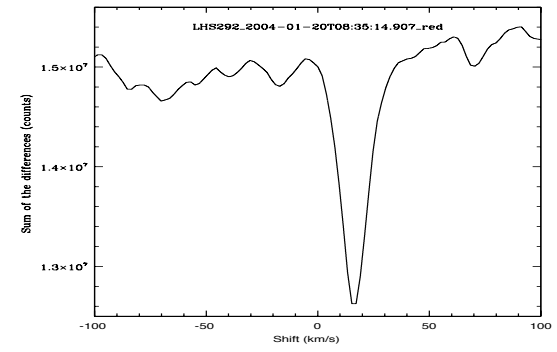
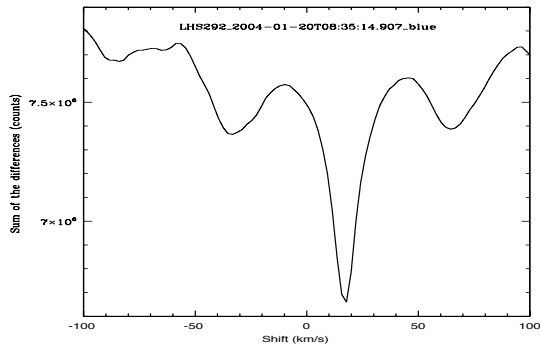
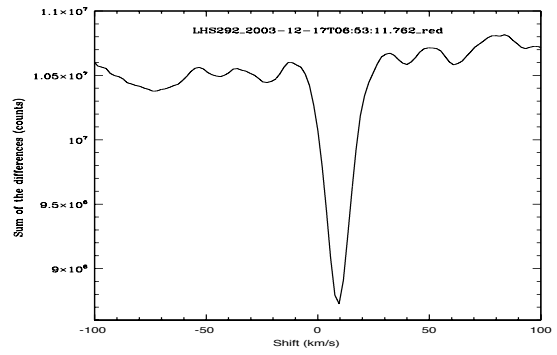
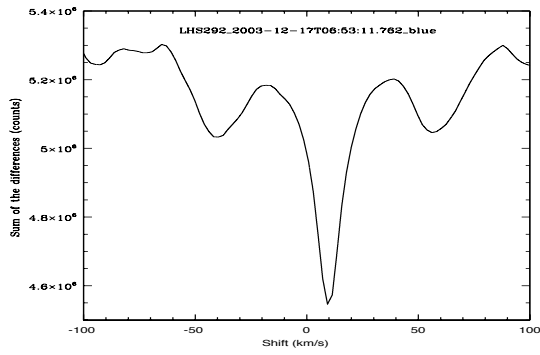


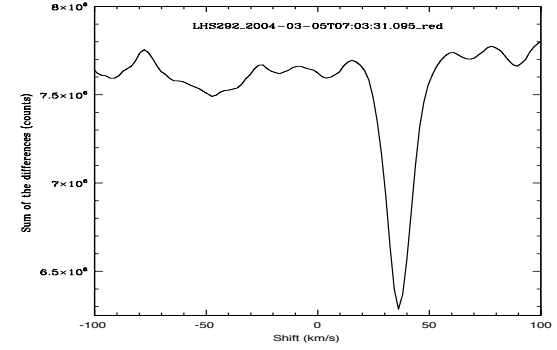
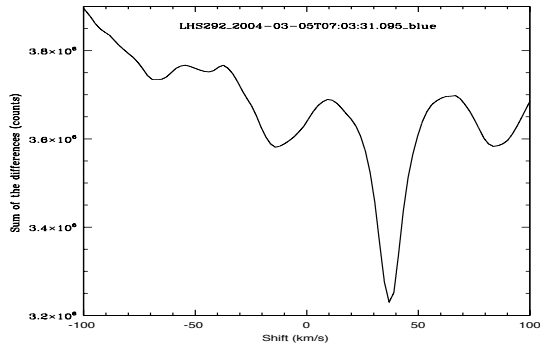
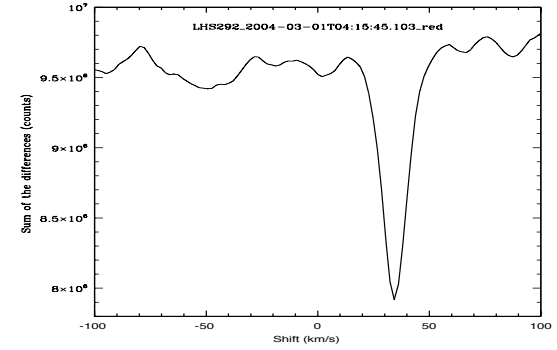
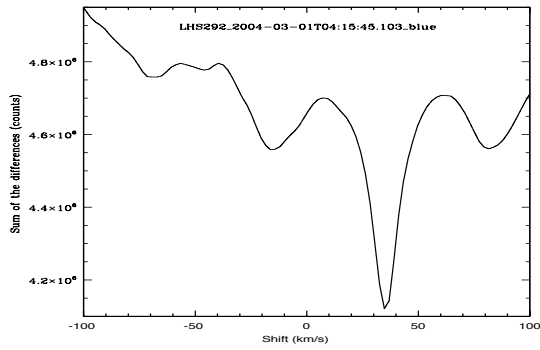
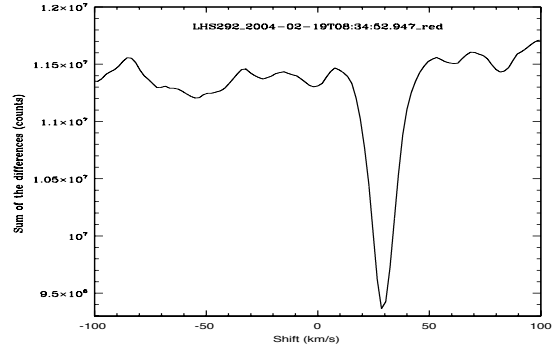
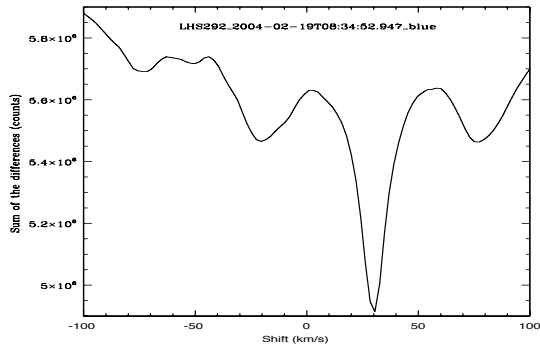




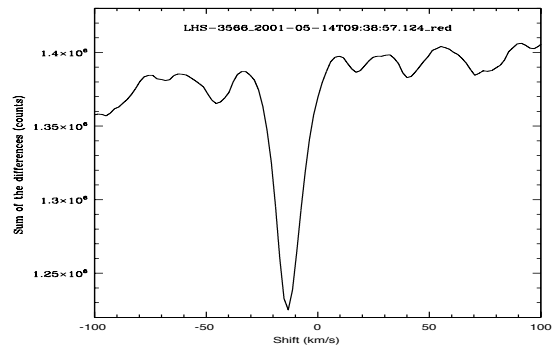
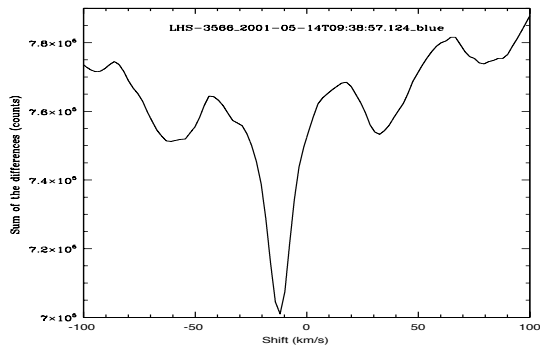
LHS 292

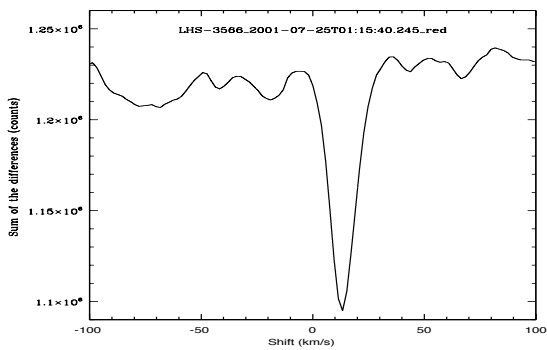
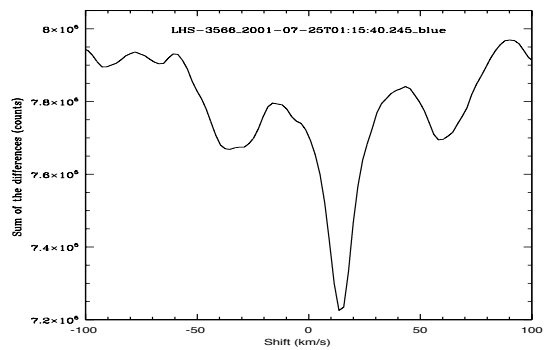
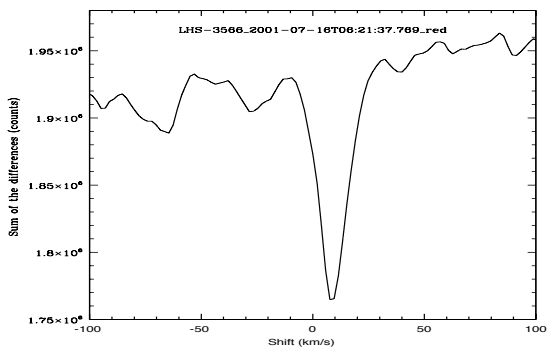
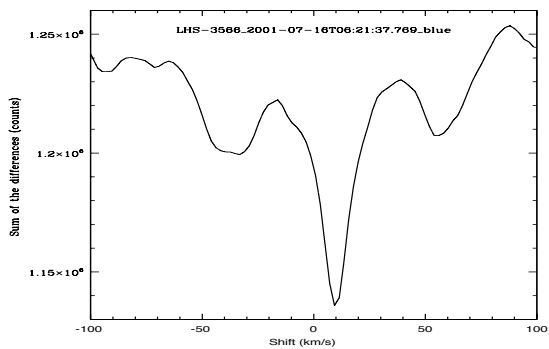
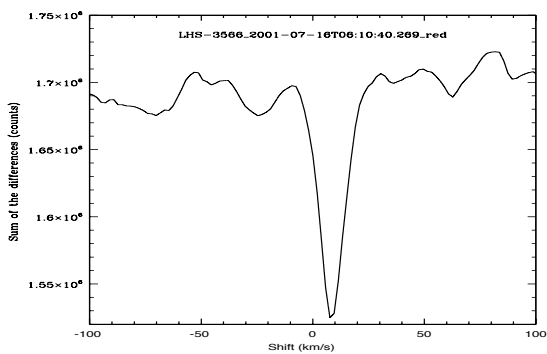
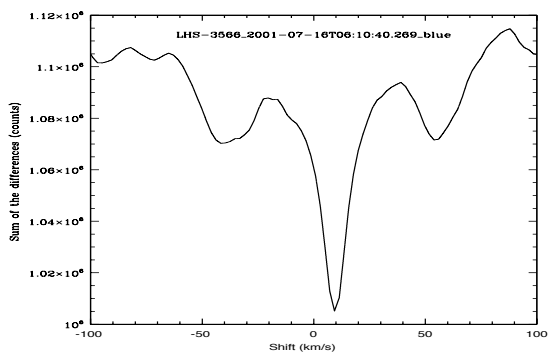
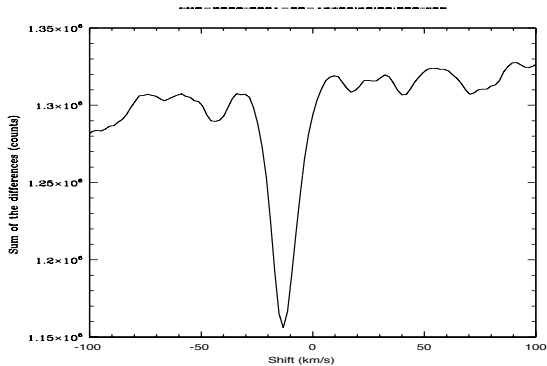
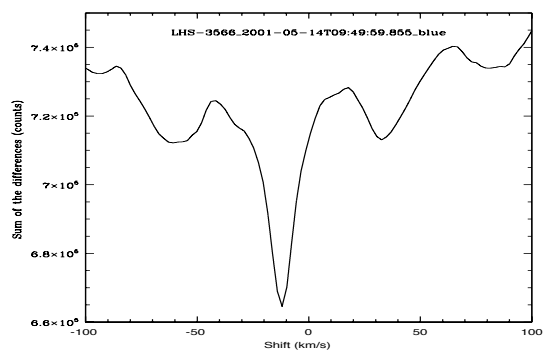


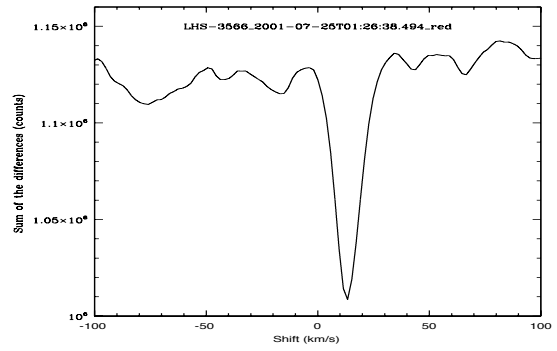
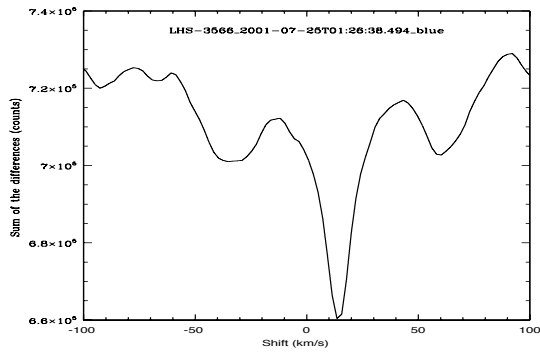




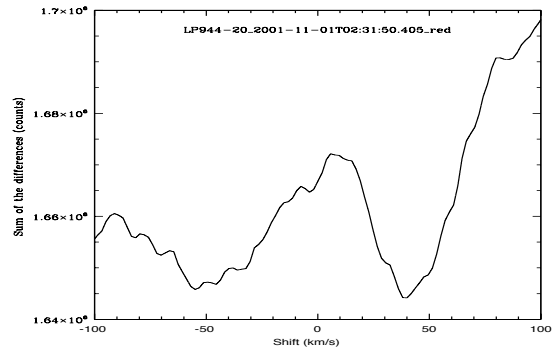
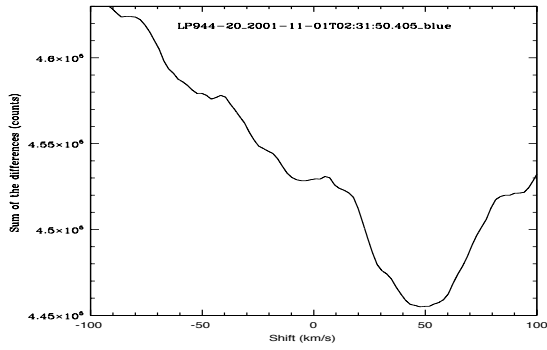
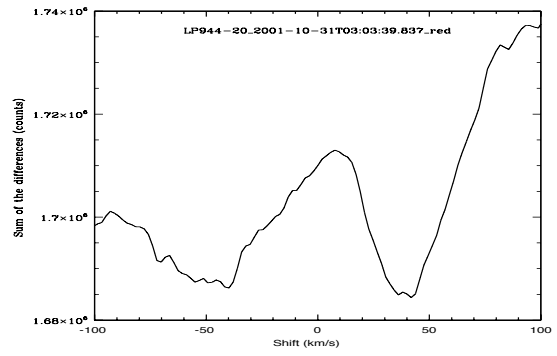
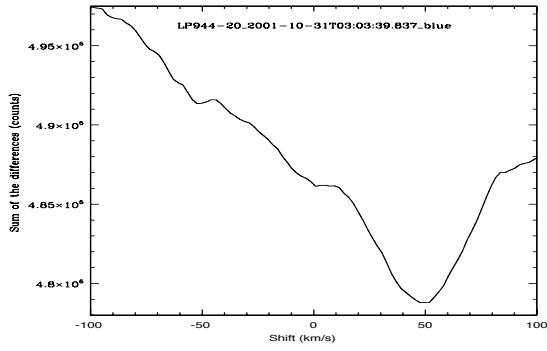
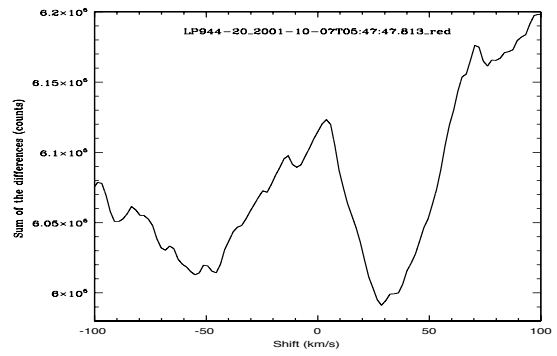
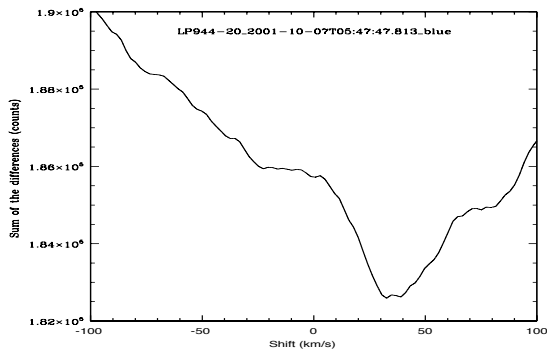
LHS 3566

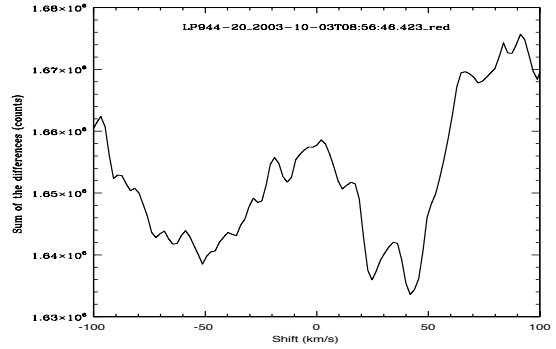
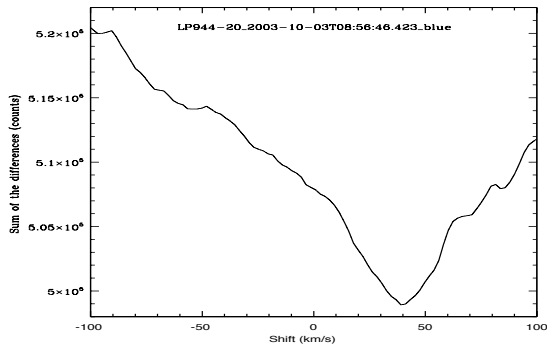
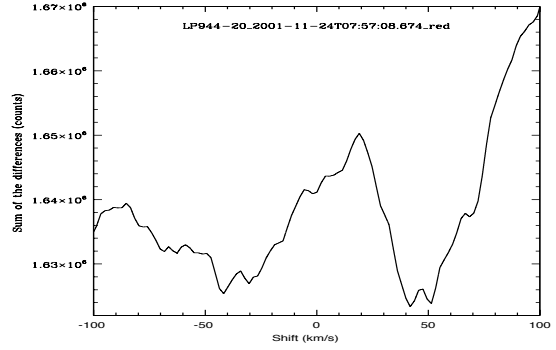
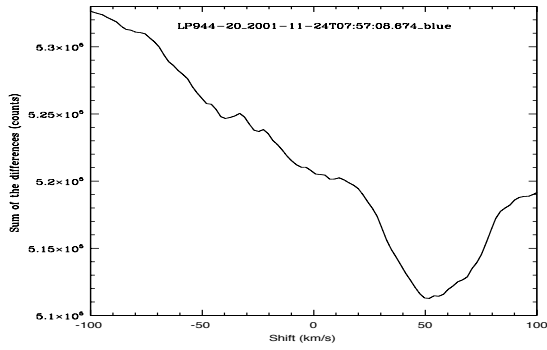
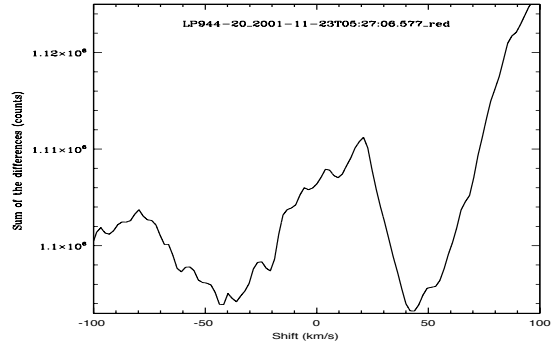
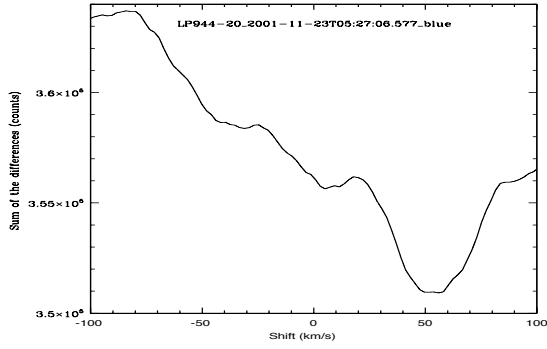
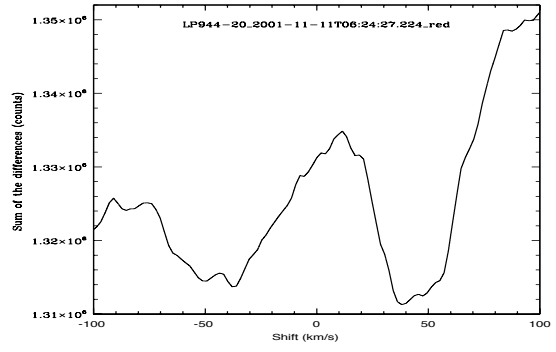
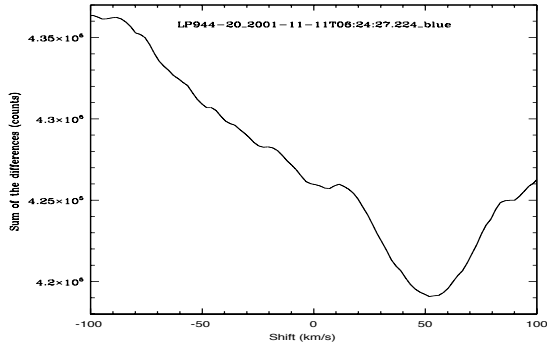


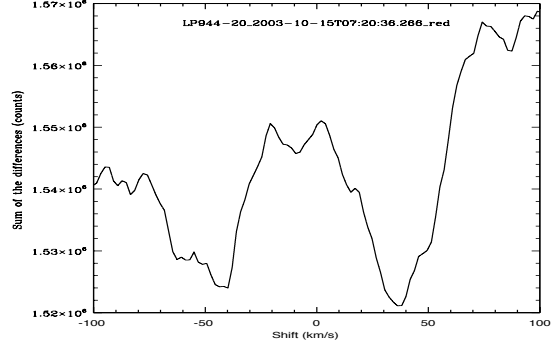
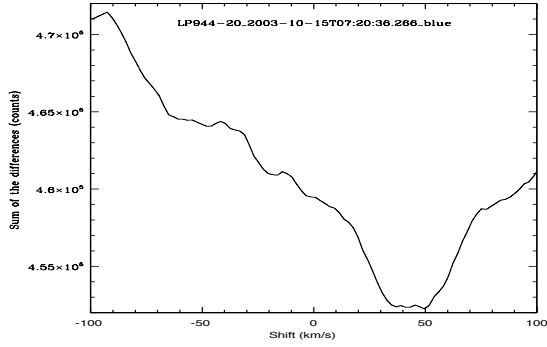
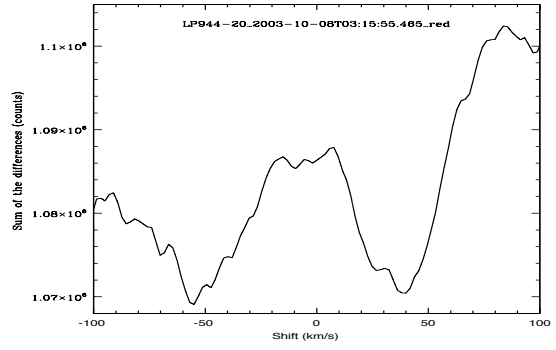
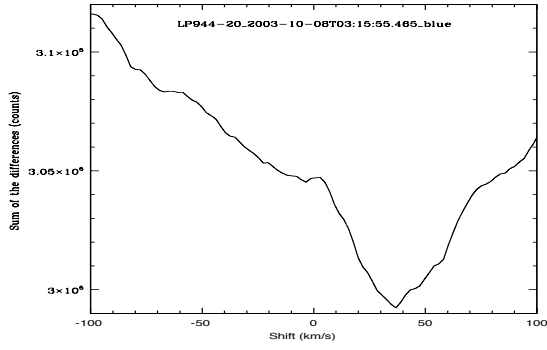
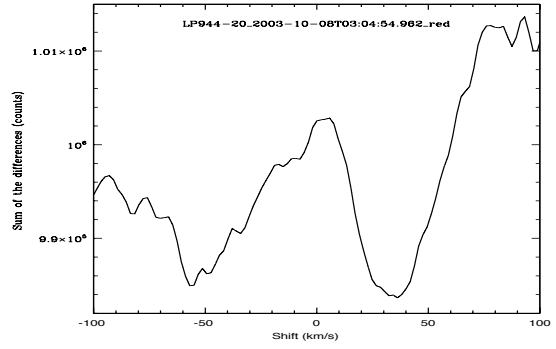
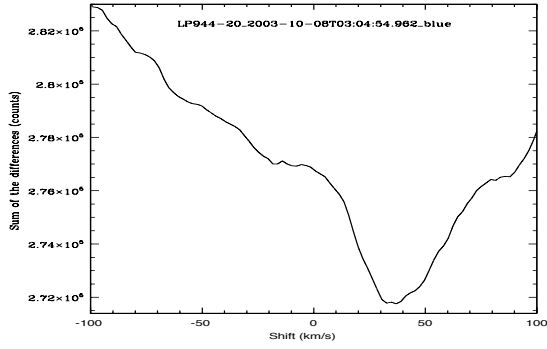
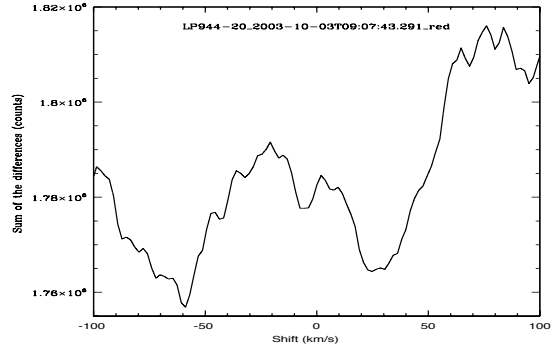
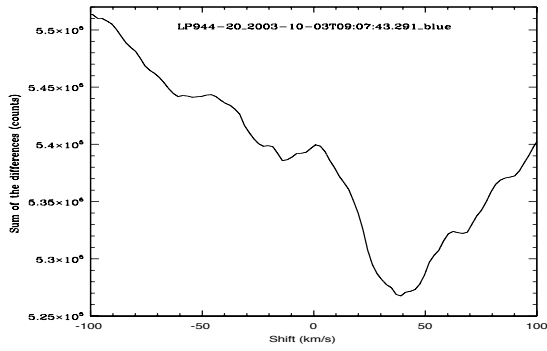


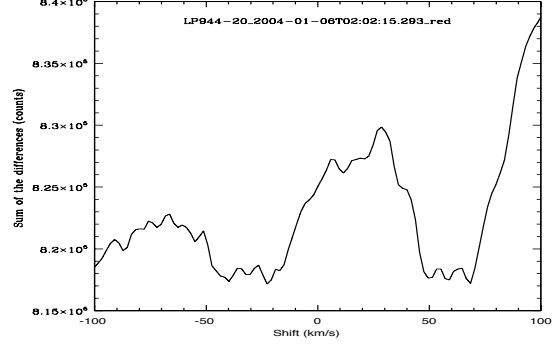
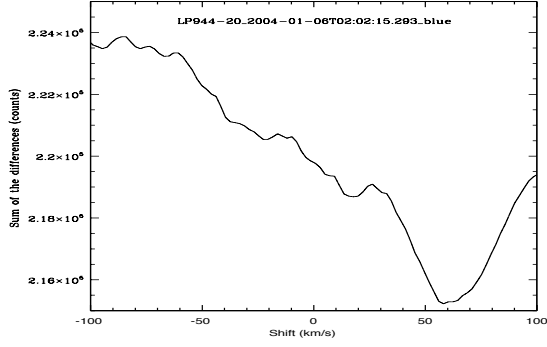
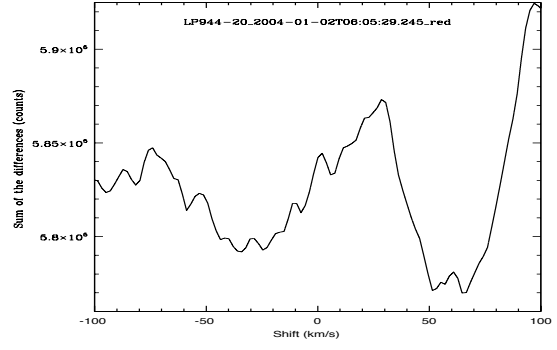
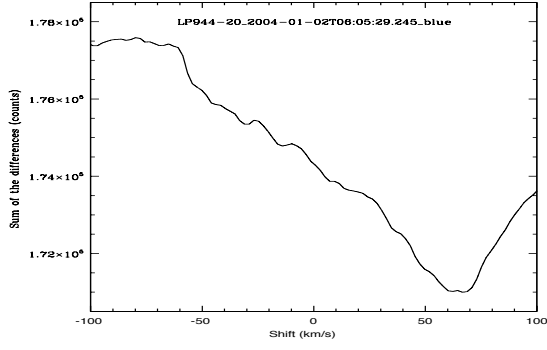
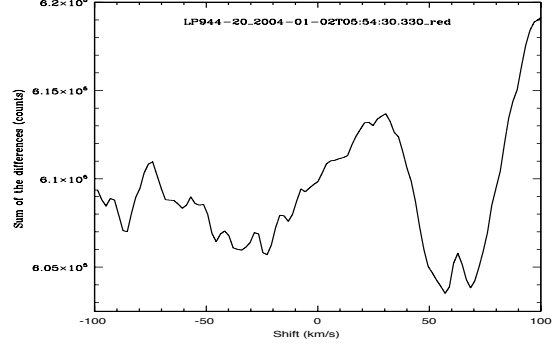
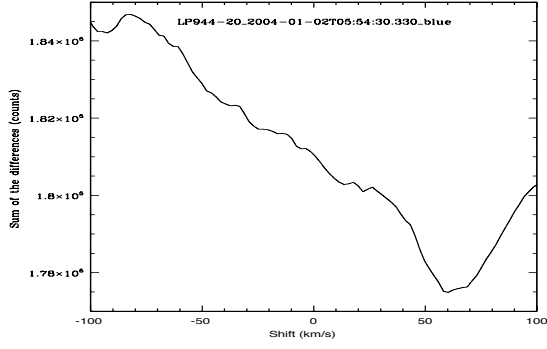
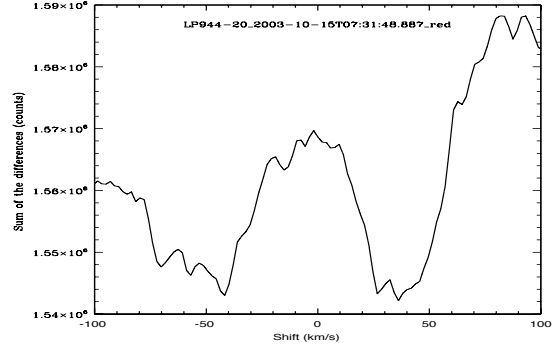
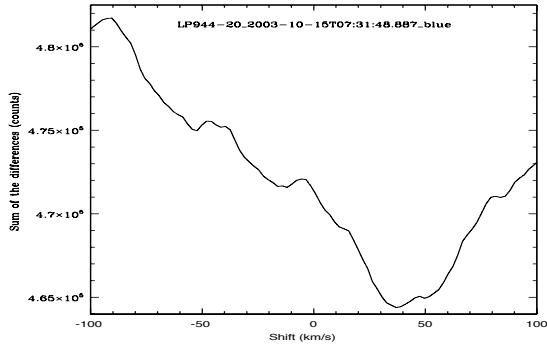


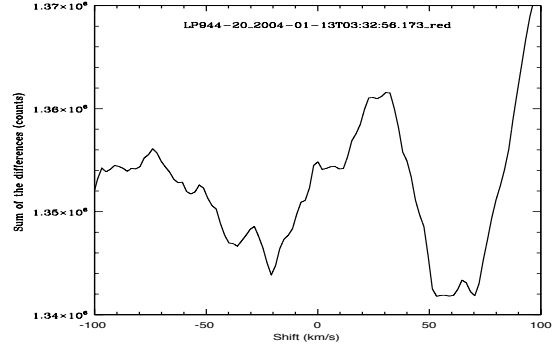
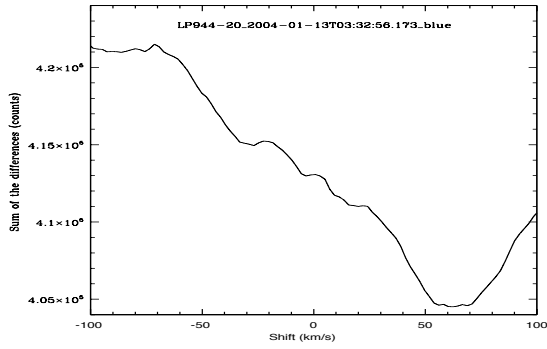
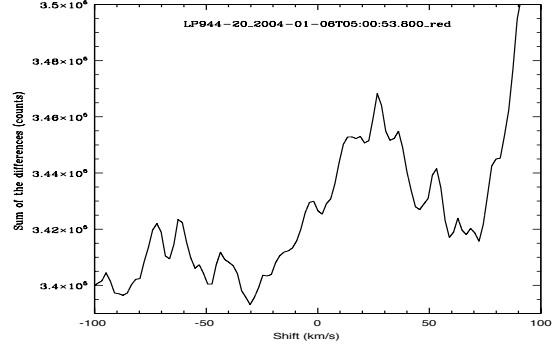
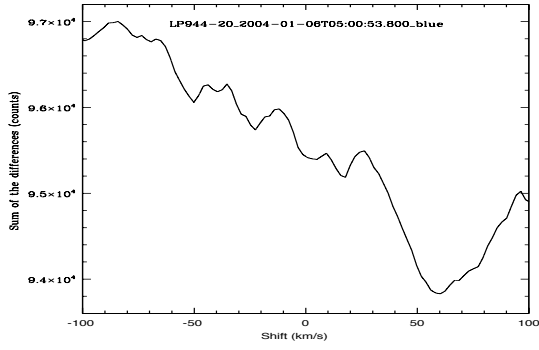
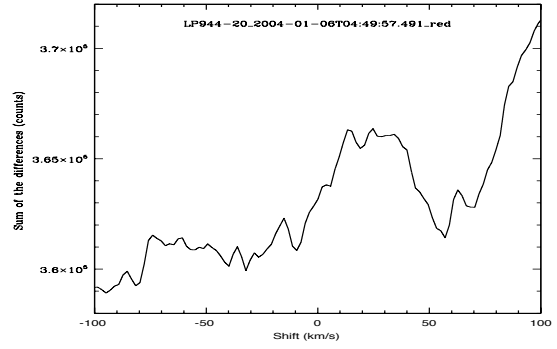
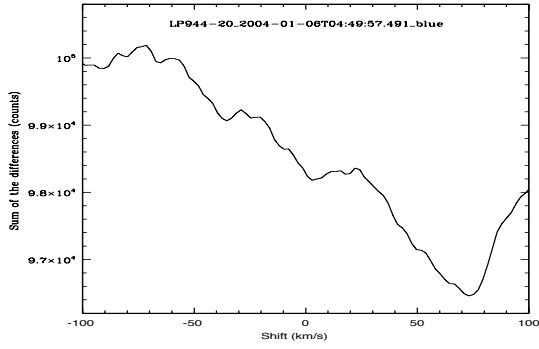
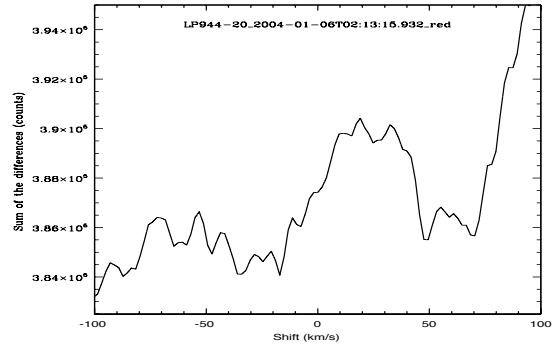
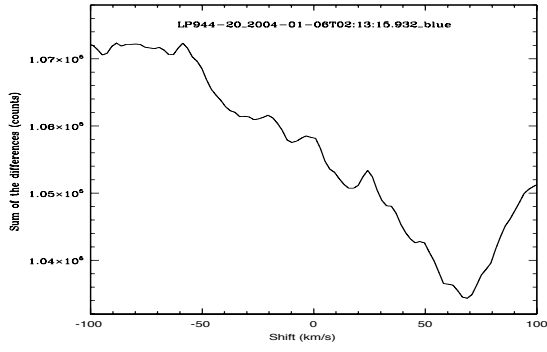
LP 944-20

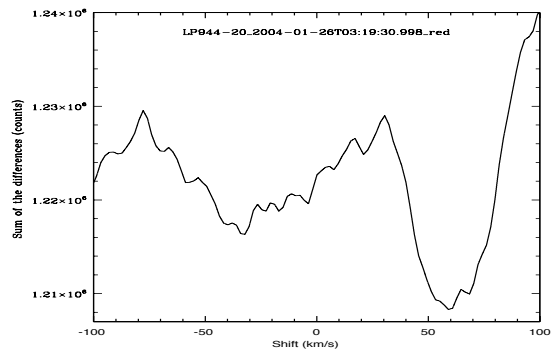
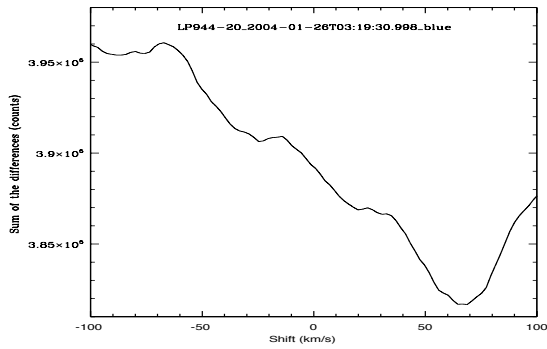
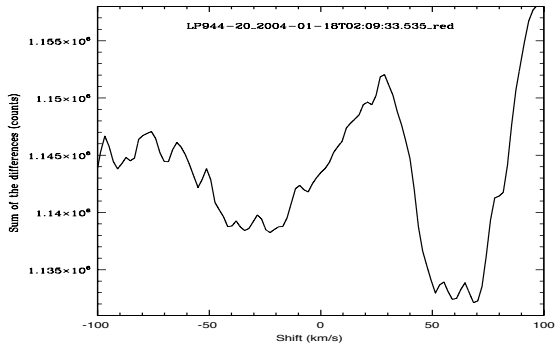
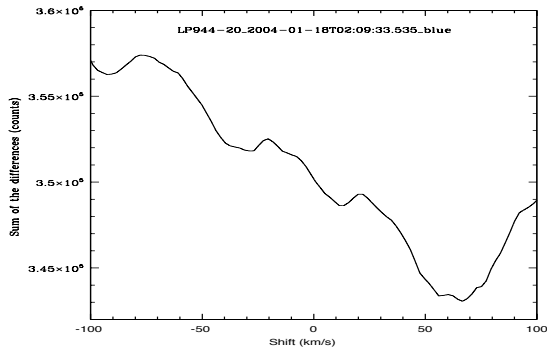
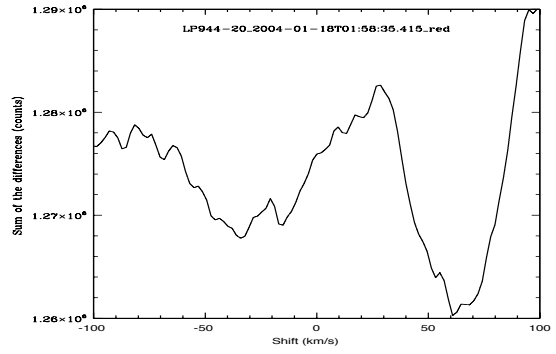
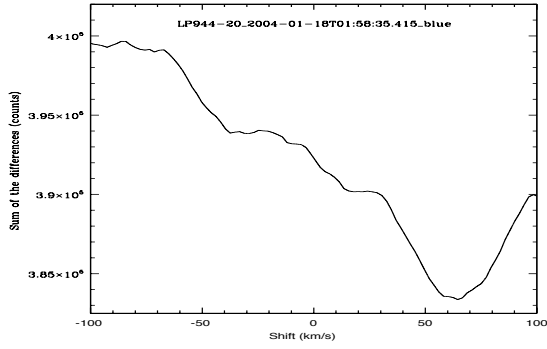
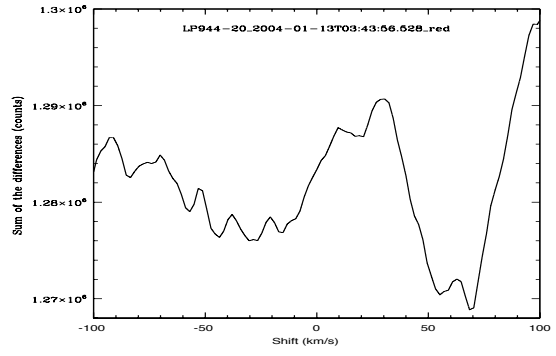
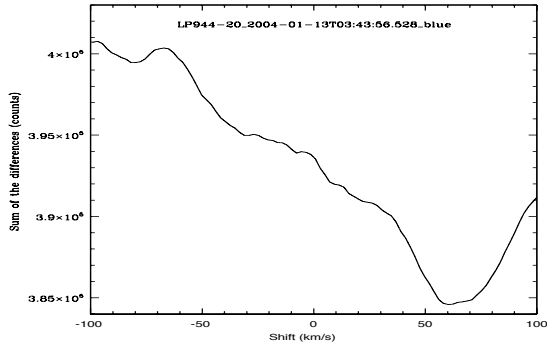




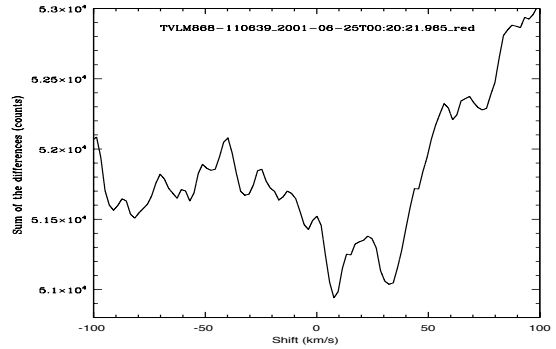
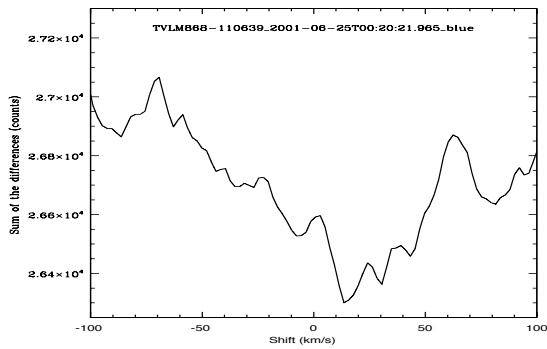
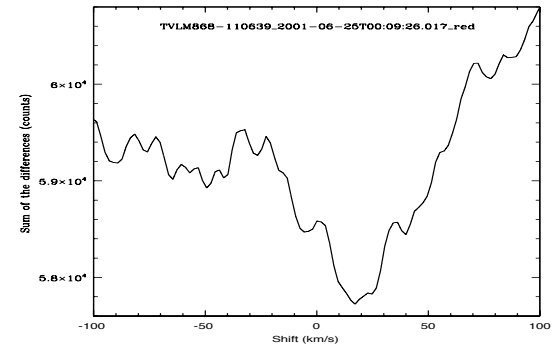
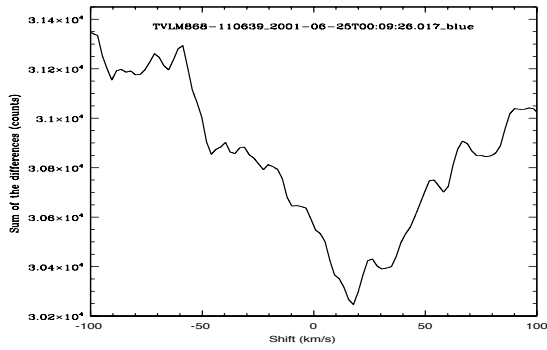
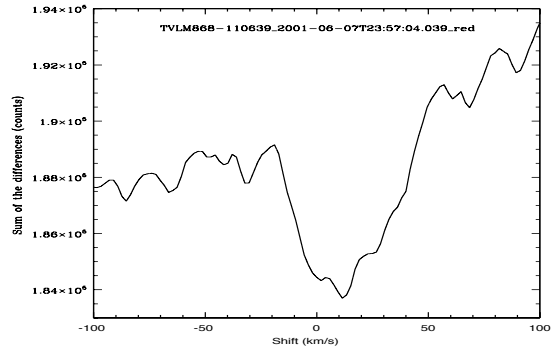
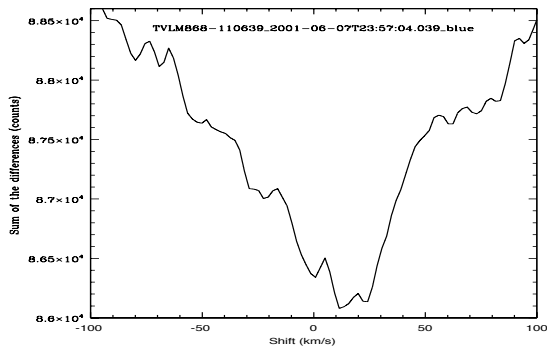
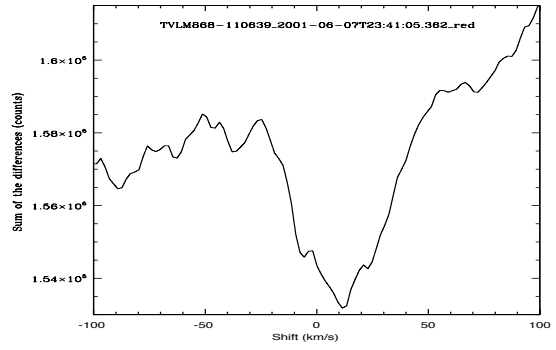
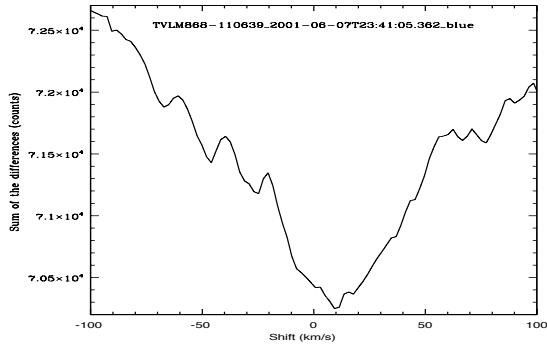


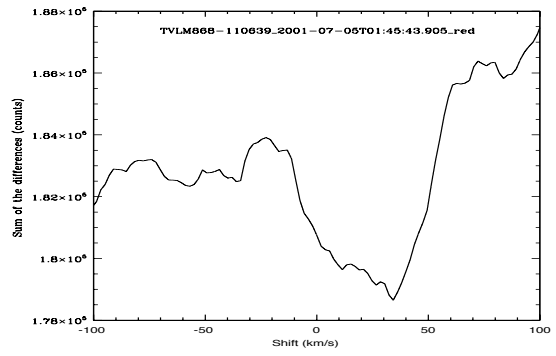
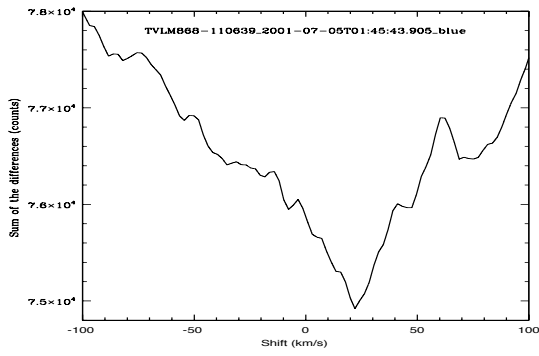
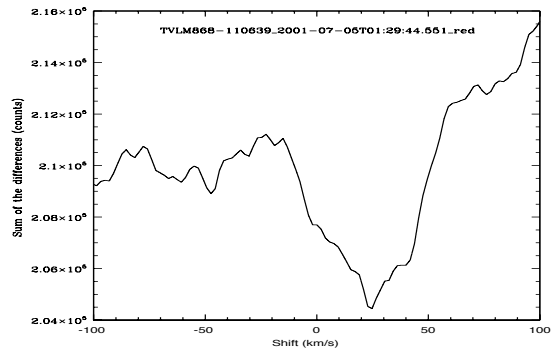
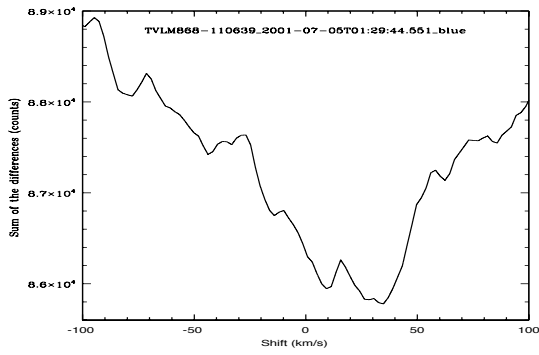




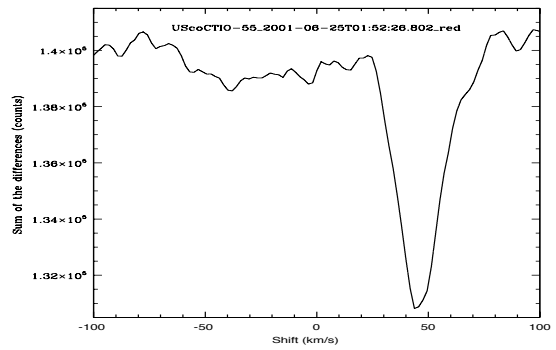
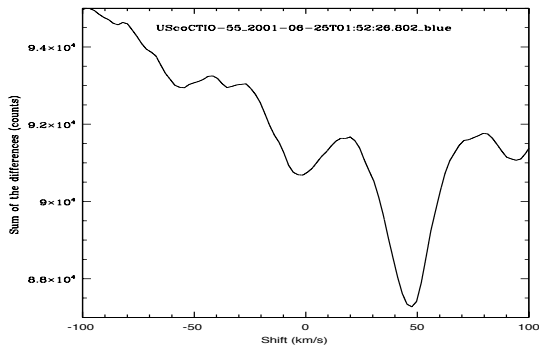
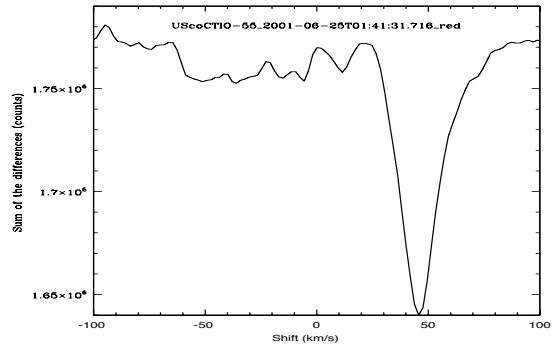
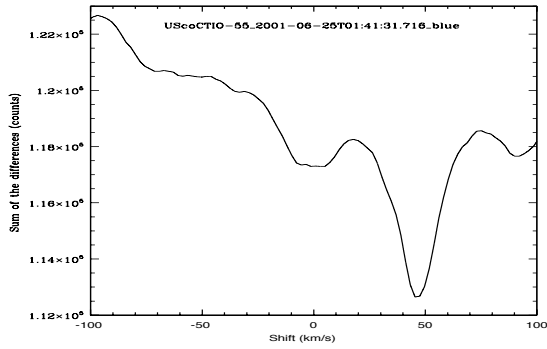


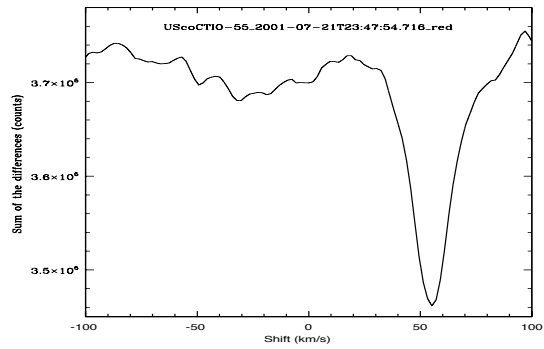
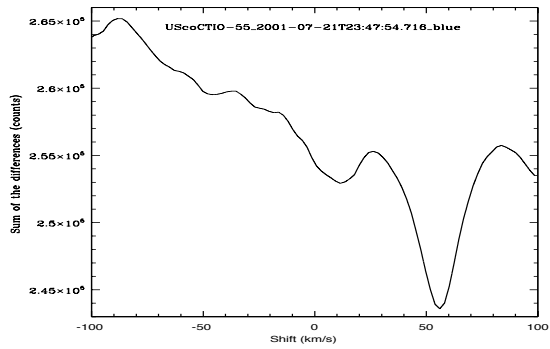
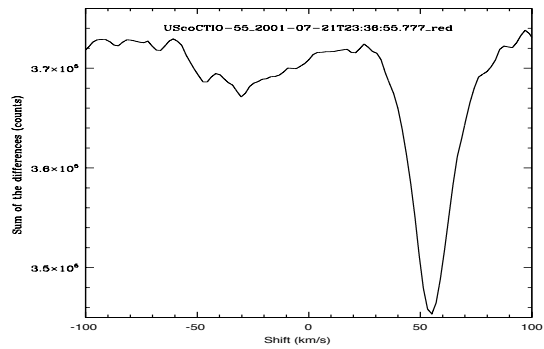
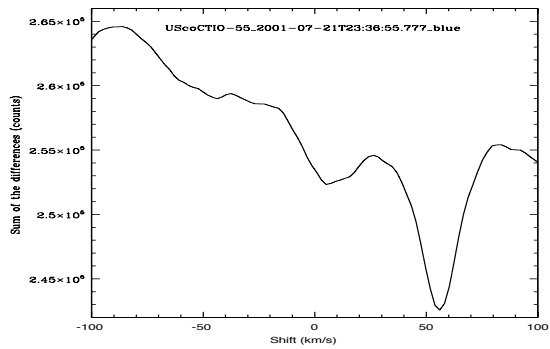
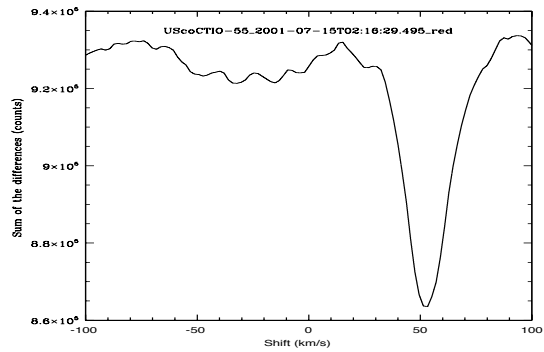
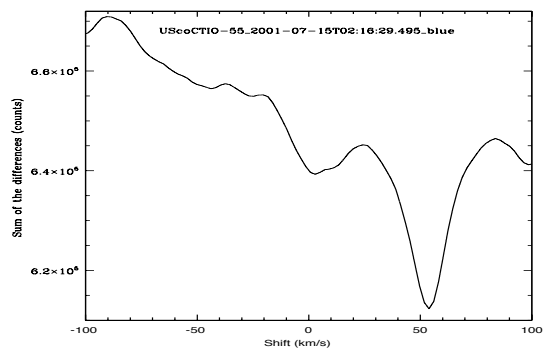
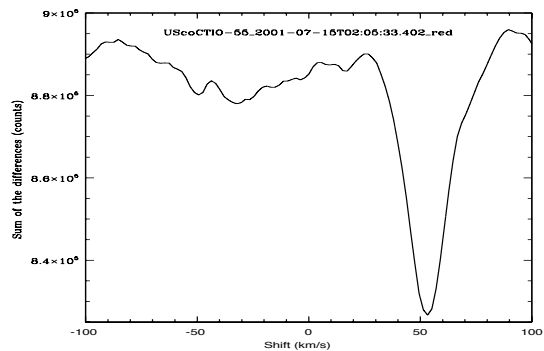
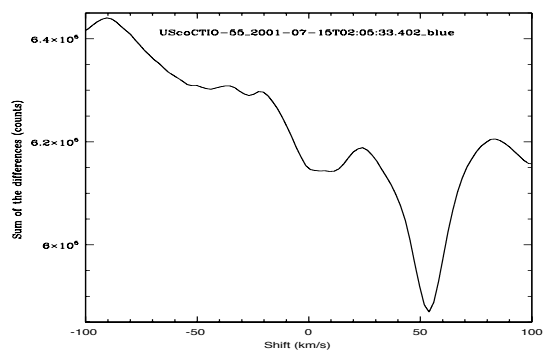
TVLM 868-110639



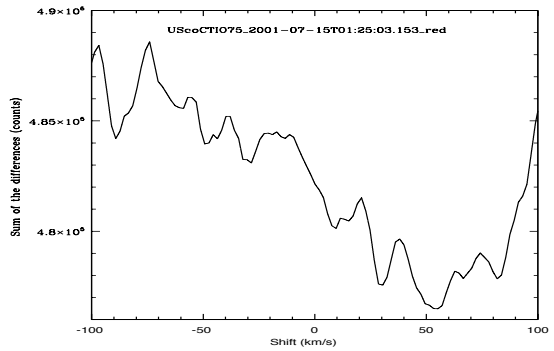
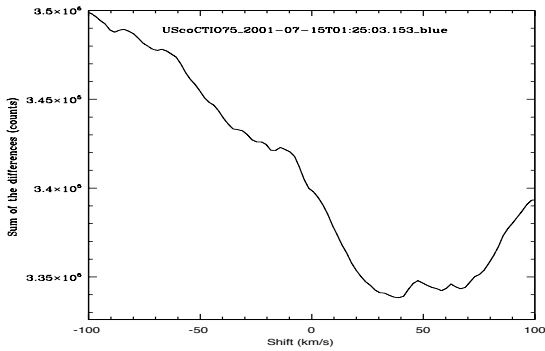
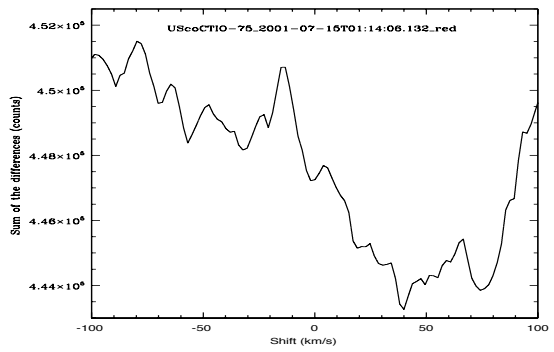
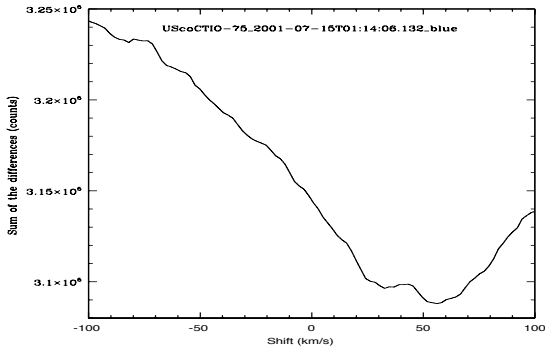
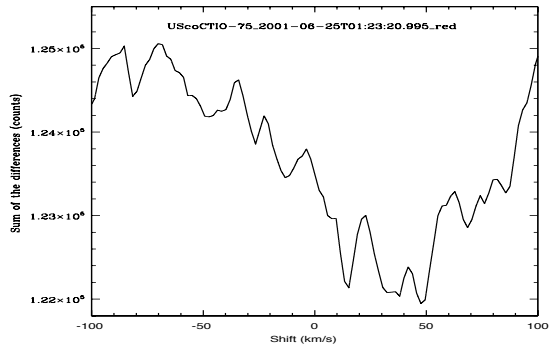
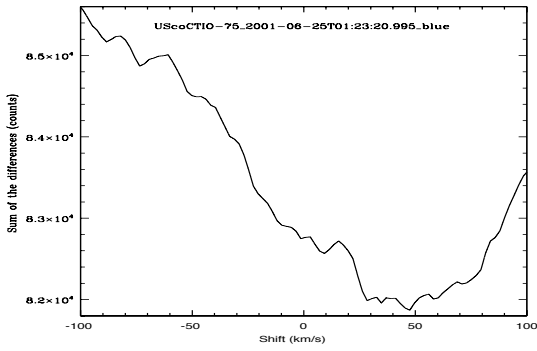
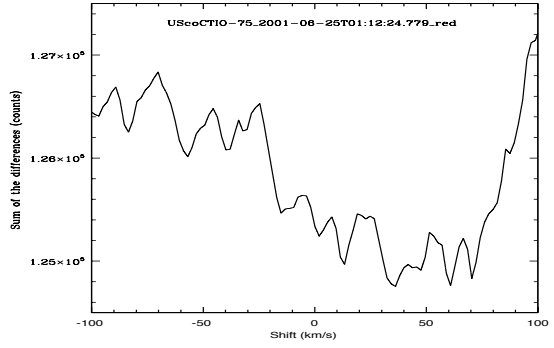
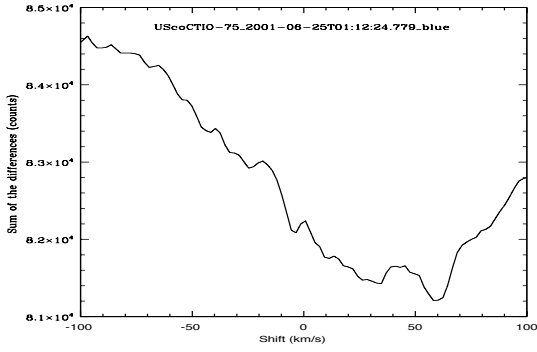


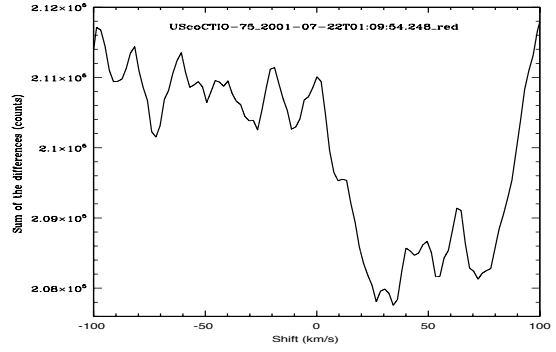
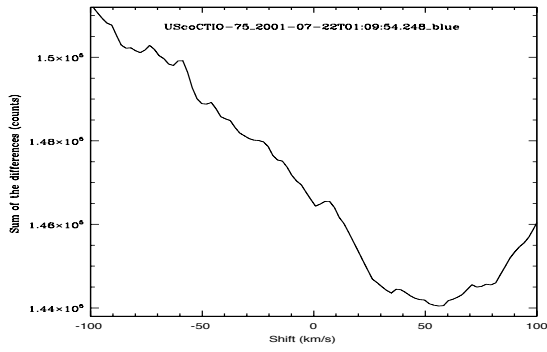
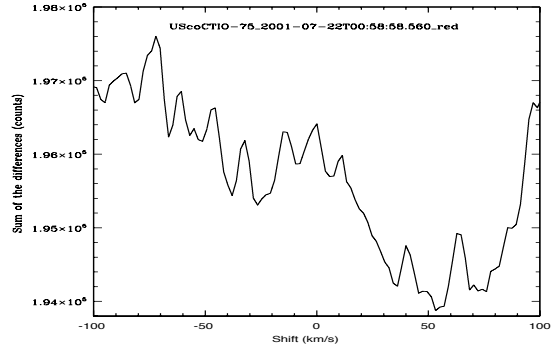
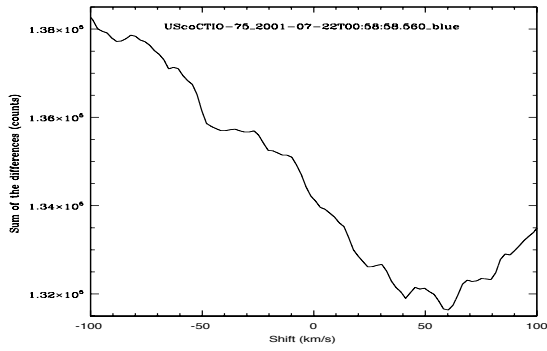
UScoCTIO 55



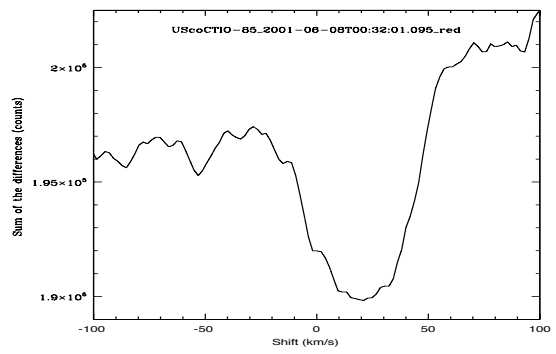
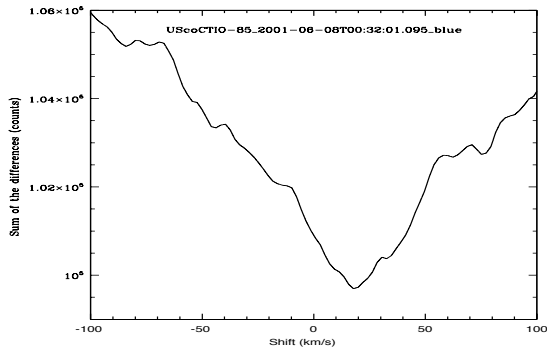
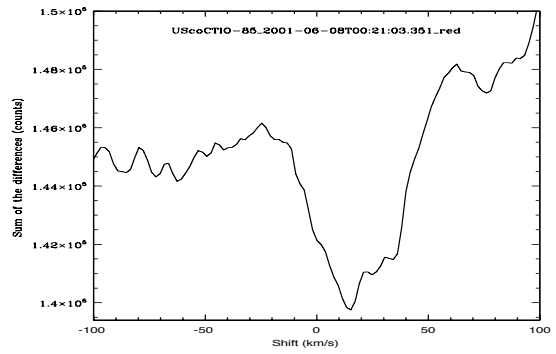
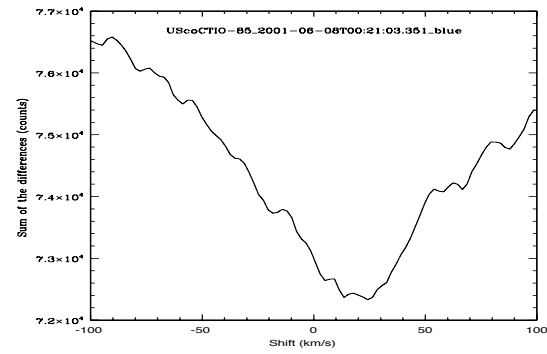


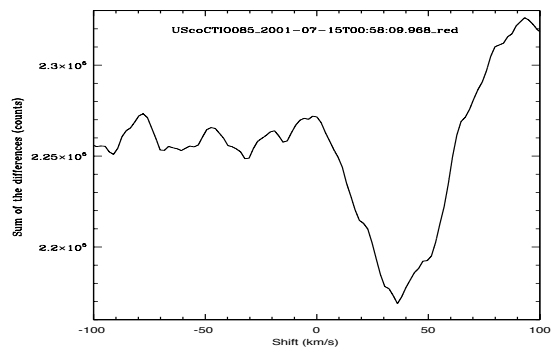
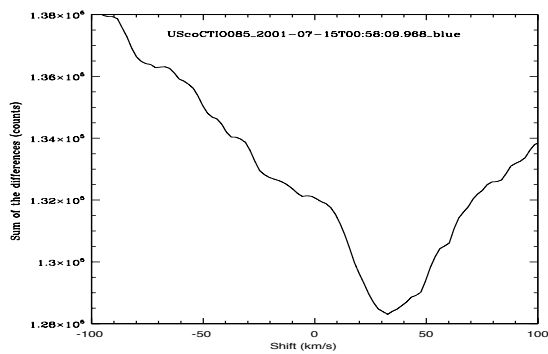
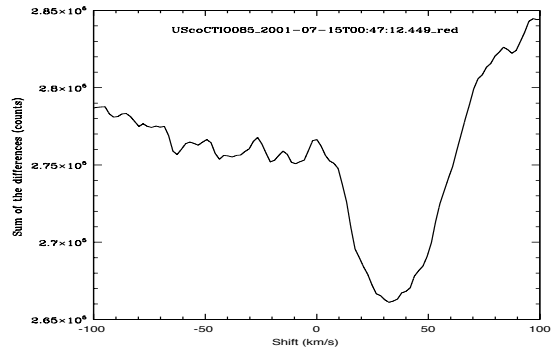
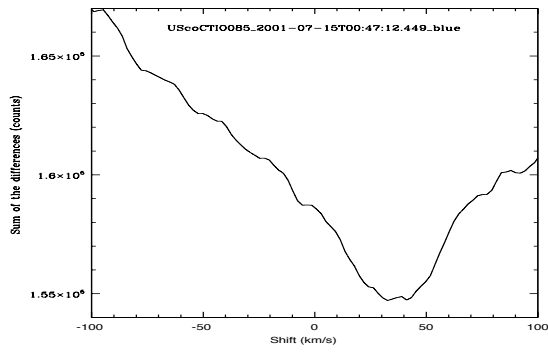
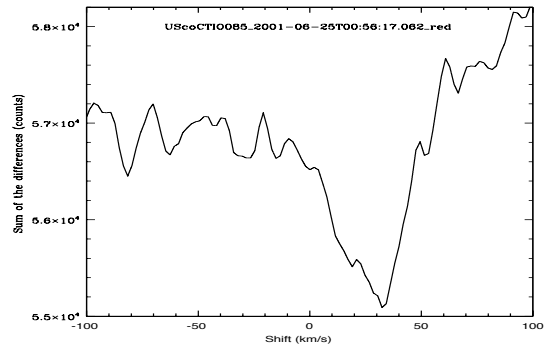
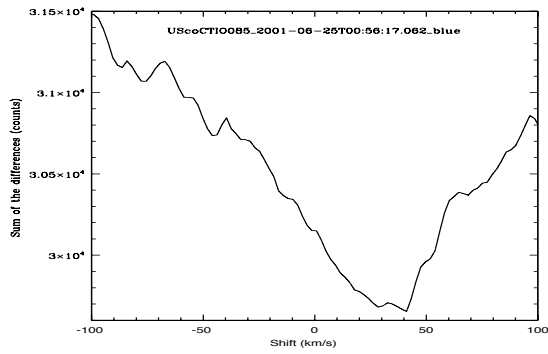
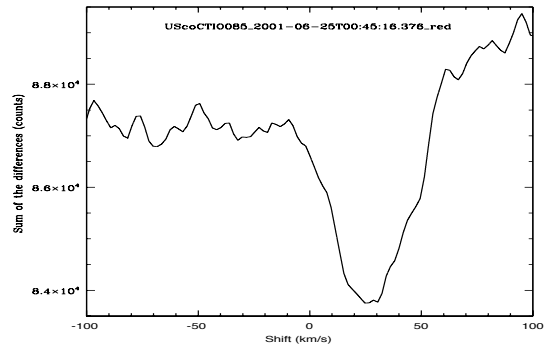
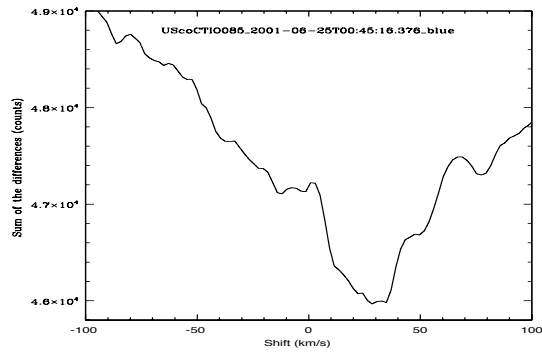
UScoCTIO 75



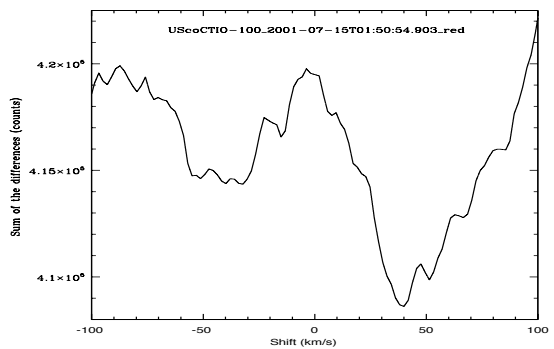
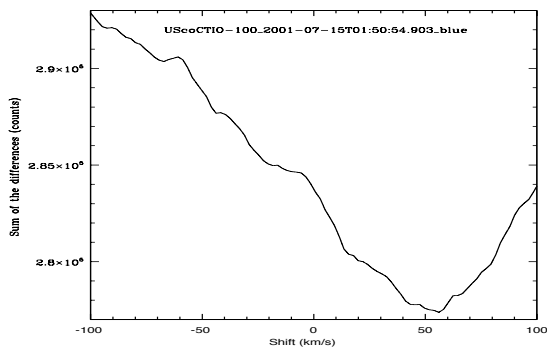
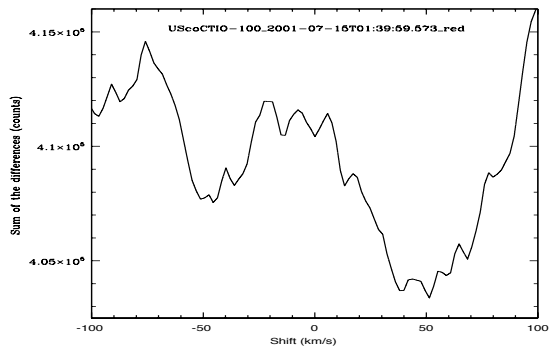
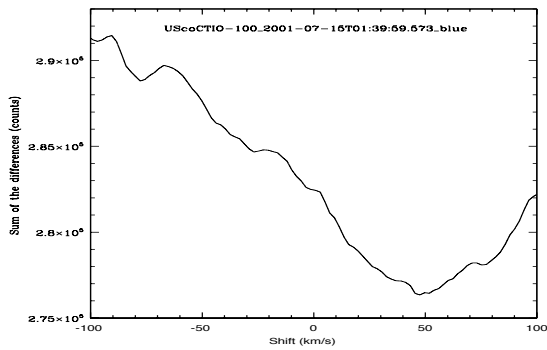
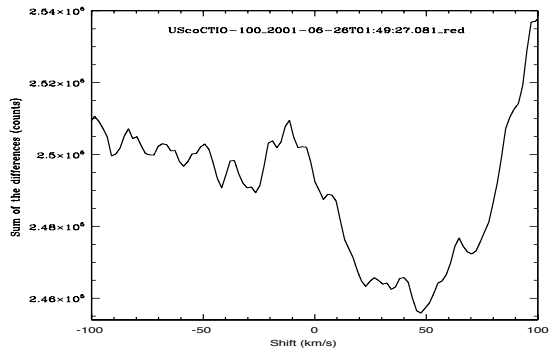
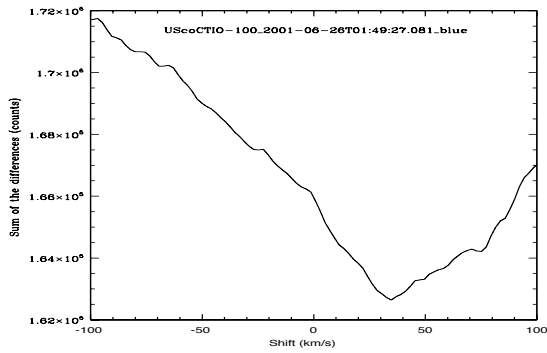
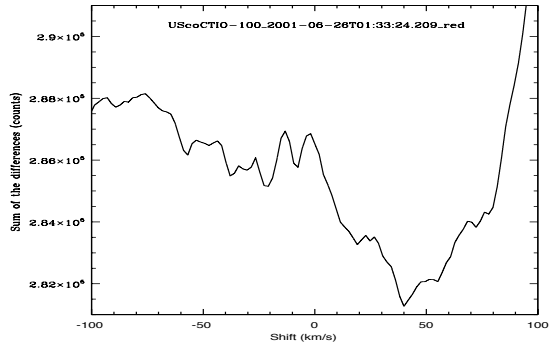
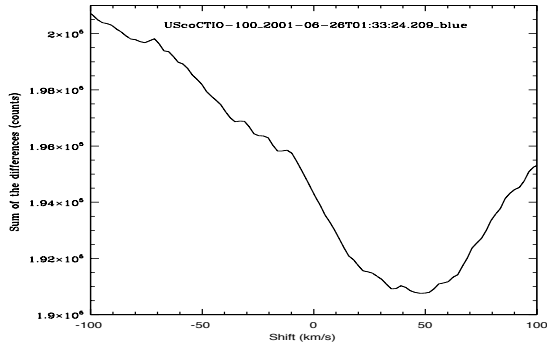


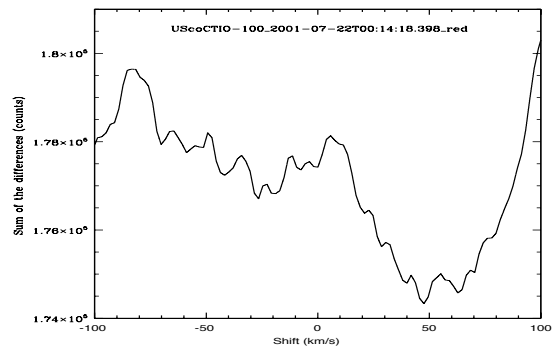
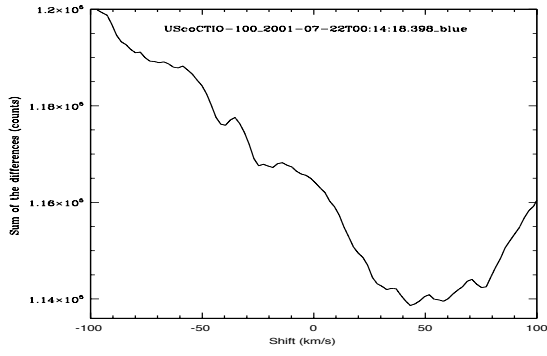
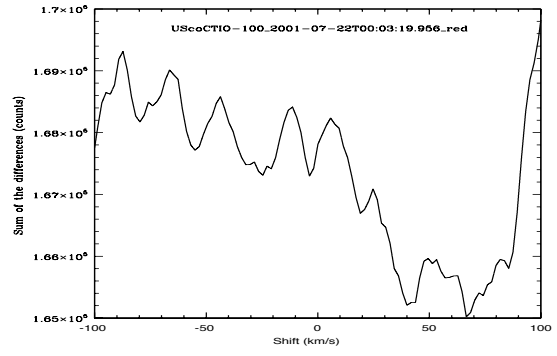
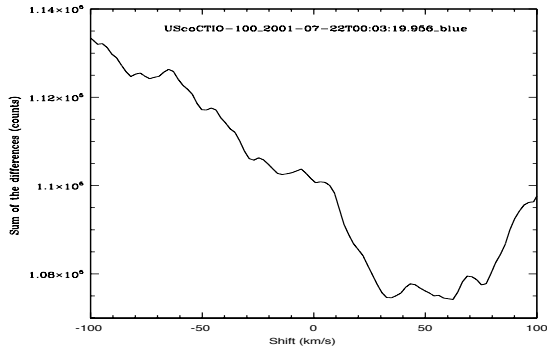
UScoCTIO 85





UScoCTIO 100





Bibliography

- Allard F., Hauschildt P. H., Alexander D. R., Starrfield S. 1997, *ARA&A*, 35, 137
- Armitage P. J., Bonnell I. A. 2003, *IAU*, 211
- Apai D., Pascucci I., Henning T., Sterzik M. F., Klein R., Semenov D., Guenther E., Stecklum B. 2002, *ApJ*, 573, 115
- Apai D., Pascucci I., Sterzik M. F., van der Blik N., Bouwman J., Dullemond C. P., Henning, T. 2004, *A&A*, 426, 53
- Apai D., Pascucci I., Bouwman J., Natta A., Henning T., Dullemond C. P. 2005, *Science*, 310, 834
- Bailer-Jones C., Brandner W., Henning T. 2006, *Sterne und Weltraum*, Jahrgang 45, Nr. 4, 34
- Balthasar H., Thiele U., Woehl H. 1982, *A&A*, 114, 357
- Baraffe I., Chabrier G., Barman T. S., Allard F., Hauschildt P. H. 2003, *A&A*, 402, 701
- Basri G., Martín E. L. 1999, *ApJ*, 118, 2460
- Basri G. 2000, *SciAm*, 282, 57
- Basri G., Reiners A. 2006, *AJ*, 132, 663
- Bate M. R., Bonnell I. A., Bromm V. 2002a, *MNRAS*, 332, L65
- Bate M. R., Bonnell I. A., Bromm V. 2002b, *MNRAS*, 336, 705
- Bate M. R., Bonnell I. A., Bromm V. 2003, *MNRAS*, 339, 577
- Bate M. R., Bonnell I. A. 2005, *MNRAS*, 356, 1201
- Berger E., Ball S., Becker K. M., Clarke M., Frail D. A., Fukuda T. A., Hoffman I.M., Kulkarni S. R., Mellon R., Momjian E. et al. 2001, *Nature*, 410, 338
- Berger E., Rutledge R. E., Reid I. N., Bildsten L., Gizis J. E., Liebert J., Martín E., Basri G., Jayawardhana R., Brandeker A., Fleming T. A., Johns-Krull C. M., Giampapa M. S., Hawley S. L., Schmitt H. M. M. 2005, *ApJ*, 627, 960
- Berger E. 2006, *ApJ*, 648, 629
- Billères M., Delfosse X., Beuzit J.-L., Forveille T., Marchal L., Martín E. 2005, *A&A*, 440, 55
- Boss A. 2001, *ApJ*, 551, 167
- Bouy H., Brandner W., Martín E. L., Delfosse X., Allard F., Basri G. 2003, *AJ*, 126, 1526
- Bouy H., Martín E. L., Brandner W., Zapatero-Osorio M. R., Béjar V. J. S., Schirmer M., Huélamo N., Ghez A. M. 2006, *A&A*, 451, 177
- Burgasser A., Kirkpatrick J. D., Reid I. N., Brown M. E., Miskey C. L., Gizis J. E. 2003, *ApJ*, 586, 512
- Burgasser A. J., Reid I. N., Siegler N., Close L., Allen P., Lowrance P., Gizis J. 2007, *prpl.conf.*, 427
- Chabrier G., Baraffe I., Allard F., Hauschildt P. H. 2000, *ApJ*, 542, 464

- Chabrier G., Baraffe I. 2000, *ARA&A*, 38, 337
- Chabrier G., Baraffe I., Allard F., Hauschildt P. H. 2005, astro-ph/0509798
- Chabrier G., Baraffe I., Selsis F., Barman T.S., Hennebelle P., Alibert Y. 2006, astro-ph/0602291
- Chauvin G., Lagrange A.-M., Dumas C., Zuckerman B., Mouillet D., Song I., Beuzit J.-L., Lowrance P. 2005, *A&A*, 438, 25
- Close L., Siegler N., Freed M., Biller B. 2003, *ApJ*, 587, 407
- Cruz K. L., Reid I. N. 2002, *AJ*, 123, 2828
- Delgado Donate E. J., Clarke C. J., Bate M. R. 2003, *MNRAS*, 342, 926
- Dobler W., Stix M., Brandenburg A. 2006, *ApJ*, 638, 336
- Duquennoy A., Mayor M. 1991, *A&A*, 248, 485
- Durney B. R., De Young D. S., Roxburgh I. W. 1993, *SoPh*, 145, 207
- ESO UVES User Manual, VLT-MAN-ESO-13200-1825, Issue 79, 09/06/2006
- ESO webpage, <http://www.ls.eso.org/lasilla/sciops/3p6/>, viewed 2006
- Forveille T., Ségransan D., Delorme P., Martín E. L., Delfosse X., Acosta-Pulido J. A., Beuzit J.-L., Manchado A., Mayor M., Perrier C., Udry S. 2004, *A&A*, 427, 1
- Freed M., Close L. M., Siegler N. 2003, *IAU*, 211, 261
- Gelino C. R., Marley M. S., Holtzman J. A. 2002, *ApJ*, 577, 433
- Golimowski D.A., Leggett S. K., Marley M. S., Fan X., Geballe T. R., Knapp G. R., Vrba F. J., Henden A. A., Luginbuhl C. B., Guetter H. H. et al. 2004, *AJ*, 127, 3516
- Golimowski D. A., Henry T. J., Krist J. E., Dieterich S., Ford H. C., Illingworth G. D., Ardila D. R., Clampin M., Franz O. G., Wasserman L. H. et al. 2004, *AJ*, 128, 1733
- Goodwin S. P., Whitworth A. P., Ward-Thompson D. 2004, *A&A*, 423, 169
- Goodwin S. P., Whitworth A. P. 2007, *A&A*, 466, 943
- Green R. M. 1985, *Spherical astronomy*, Cambridge University Press
- Grether D., Lineweaver C. H. 2006, *ApJ*, 640, 1051
- Guenther E. W., Wuchterl G. 2003, *A&A*, 401, 677
- Hester J. J., Scowen P. A., Sankrit R., Lauer T. R., Ajhar E. A., Baum W. A., Code A., Currie D. G., Danielson G. E., Ewald S. P. 1996, *AJ*, 111, 2349
- Jeffries R. D., Maxted P. F. L. 2005, *AN*, 326, 944
- Jiang Ing-Guey, Laughlin G., Lin D. N. C. 2004, *AJ*, 127, 455
- Joergens V. 2006a, *A&A*, 446, 1165
- Joergens V. 2006b, *A&A*, 448, 655
- Joergens V., Guenther E. 2001, *A&A*, 379, 9
- Joergens V., Neuhäuser R., Fernández M. 2004, *BaltA*, Vol. 13, 505
- Kenyon M. J., Jeffries R. D., Naylor T., Oliveira J. M., Maxted P. F. L. 2005, *MNRAS*, 356, 89
- Kirkpatrick J. D., Reid I. N., Liebert J., Cutri R. M., Nelson B., Beichman C. A., Dahn C. C., Monet D. G., Gizis J. E., Skrutskie M. F. 1999, *ApJ*, 519, 802
- Kirkpatrick J. D. 2005, *ARA&A*, 43, 195
- Klein R., Apai D., Pascucci I., Henning T., Waters L. B. F. M. 2003, *ApJ*, 593, 57
- Kraus A. L., White R. J., Hillenbrand L. A. 2005, *ApJ*, 633, 452
- Kumar S. S. 1963, *ApJ*, 137, 1121
- Kurosawa R., Harries T. J., Littlefair S. P. 2006, *MNRAS* 372, 1879

- Lin D. N. C., Laughlin G., Bodenheimer P., Rozyczka M. 1998, *Science*, 281, 2025
- Lin H., Rimmele T. 1999, *ApJ*, 514, 448
- Littlefair S. P., Dhillon V. S., Marsh T. R., Shahbaz T., Martín E. L. 2006, *MNRAS*, 370, 1208
- Luhman K. L. 2004a, *ApJ*, 614, 398
- Luhman K. L. 2004b, *ApJ*, 617, 1216
- Luhman K. L. 2005, *ApJ*, 633, 41
- Luhman K. L., Joergens V., Lada C., Muzerolle J., Pascucci I., White R. 2007, *prpl.conf.*, 443
- Marcy G., Butler R. P. 2000, *PASP*, 112, 137
- Martín E. L., Basri G., Brandner W., Bouvier J., Zapatero Osorio M. R., Rebolo R., Stauffer J., Allard F., Baraffe I., Hodgkin S. T. 1998, *ApJ*, 509, 113
- Martín E. L., Guenther E., Zapatero Osorio M. R., Bouy H., Wainscoat R. 2006, *ApJ*, 644, 75
- Mohanty S., Basri G., Shu F., Allard F., Chabrier G. 2002, *ApJ*, 571, 469
- Mohanty S., Basri G. 2003, *ApJ*, 583, 451
- Muzerolle J., Luhman K. L., Briceño C., Hartmann L., Calvet N. 2005, *ApJ*, 625, 906
- Nakajima T., Oppenheimer B. R., Kulkarni S. R., Golimowski D. A., Matthews K., Durrance S. T. 1995, *Nature*, 378, 463
- Oppenheimer B. R., Kulkarni S. R., Matthews K., Nakajima T. 1995, *Science*, 270, 1478
- Padoan P., Nordlund Å. 2002, *ApJ*, 576, 870
- Padoan P., Nordlund Å. 2004, *ApJ*, 617, 559
- Phan-Bao N., Martín E. L., Reyle C., Forveille T., Lim J. 2005, *A&A*, 439, 19
- Pollack J. B., Hubickyj O., Bodenheimer P., Lissauer J. J., Podolak M., Grennzwieg Y. 1986, *Ikarus*, 124, 62 (P96)
- Priest E. R. 1982, *Solar Magnetohydrodynamics* (Dordrecht:Reidel)
- Rebolo R., Martín E. L., Magazzu A. 1992, *ApJ*, 389, 83
- Rebolo R., Zapatero Osorio M. R., Martín E. L. 1995, *Nature*, 377, 129
- Reid I. N., Hawley S. L., Gizis J. E. 1995, *AJ*, 110, 1838
- Reid I. N., Kirkpatrick J. D., Liebert J., Gizis J. E., Dahn C. C., Monet D. G. 2002, *AJ*, 124, 519
- Reipurth B., Clarke C. J. 2001, *AJ*, 122, 432
- Ribas I. 2003, *A&A*, 400, 297
- Rutledge R. E., Basri G., Martín E. L., Bildsten L. 2000, *ApJ*, 538, 141
- Siegler N., Close L., Cruz K. L., Martín E. L., Reid I. N. 2005, *ApJ*, 621, 1023
- Sterzik M. F., Durisen R. H. 2003, *A&A*, 400, 1031
- Stahler S. W., Palla F. 2004, *The Formation of Stars*, WILEY-VCH Verlag GmbH & Co.KGaA
- Stassun K., Mathieu R. D., Valenti J. A. 2006, *Nature*, 440, 311
- Tinney C. G. 1996, *MNRAS*, 281, 644
- Tinney C. G. 1998, *MNRAS*, 296, 42
- Tinney C. G., Reid I. N. 1998, *MNRAS*, 301, 1031
- Tinney C. G., Tolley A. J. 1999, *MNRAS*, 304, 119
- Umbreit S., Burkert A., Henning T., Mikkola S., Spurzem R. 2005, *ApJ*, 623, 940

- Whitworth A. P., Goodwin S. P. 2005, *Astron. Nachr.*, Vol. 326, Issue 10, 899
- Whitworth A. P., Bate M. R., Nordlund Å., Reipurth B., Zinnecker H. 2007, *prpl.conf.*, 459
- Whitworth A. P., Stamatellos D. 2006, *A&A*, 458, 817
- Zapatero Osorio M. R., Béjar V. J. S., Martín E. L., Rebolo R., Barrado y Navascués D., Bailer-Jones C. A. L., Mundt R. 2000, *Science*, 290, 103

Selbständigkeitserklärung

Hiermit erkläre ich, dass ich die vorliegende Diplomarbeit selbständig und nur unter Verwendung der angegebenen Hilfsmittel und Literatur angefertigt habe.

Tautenburg, den 06/06/2007

.....
(Andrea Mehner)

Erklärung für die Bibliothek

Seitens der Verfasserin bestehen keine Einwände, die vorliegende Diplomarbeit für die öffentliche Nutzung in der Thüringer Universitäts- und Landesbibliothek zur Verfügung zu stellen.

Tautenburg, den 06/06/2007

.....
(Andrea Mehner)